

Search for Charged Higgs in $t\bar{t}$
Decay Products from Proton-Antiproton
Collisions at $\sqrt{s} = 1.96$ TeV

by
Ricardo Eusebi

October 2005

**Search for Charged Higgs in $t\bar{t}$
Decay Products from Proton-Antiproton
Collisions at $\sqrt{s} = 1.96$ TeV**

A Dissertation by
Ricardo Eusebi

Submitted in Partial Fulfillment
of the
Requirements for the Degree
Doctor of Philosophy
in Physics

Supervised by
Professor Paul Tipton
Department of Physics and Astronomy
The College Arts and Sciences
University of Rochester
Rochester, New York

October 2005

Acknowledgments

This dissertation is the final result of several years of investigation. Based on an old study, Paul L. Tipton, Andy Hocker, and I drafted the basic idea of this analysis. To Paul L. Tipton, my thesis advisor, I am deeply thankful for the guidance he provided me from the first day I arrived, for his fundamental knowledge of the physics involved in our problems, for consistently given me the chance to test my own ideas, for trusting me with large responsibilities such as the CMS burn-in design and construction, for teaching by example, for his support and patience during tough times and for his unyielding support in the last steps of my doctorate. Paul, I thank you for showing me how an advisor should be. The lesson is not forgotten, as in the near future I am planning to provide advice in a similar manner in which was given to me.

I am very thankful to Andy Hocker, my office-mate for more than three years, not only for providing an endless number of jelly-beans, but also for patiently answering my unlimited number of questions, teaching me the basics of the CDF detector and software, introducing me into the silicon radiation monitoring system, and in general for his always enthusiastic passion for physics and life.

The basic idea crafted by the three of us needed refinements, and this required the involvement of many more people; to all of them I am very thankful. I am specially grateful to Marcela Carena, who provided the theoretical expertise and help me in developing the formulae described in Appendix B. I am thankful to Eva Halkiadakis for helping me rewrite some paragraphs of the paper in a more concise way, and to Ulrich Husemann, for his comments on some chapters of this dissertation.

I am in debt to each person in the group of the University of Rochester at CDF, for allowing me to use their share of very powerful computing

farms. It is an excellent group and I will certainly miss them. To the vast cast of characters that forms the CDF collaboration, I can only say that I am looking forward to continue working with you, in CDF or in any other collaboration.

Of course, Crisha, I am deeply thankful to you. For always standing at my side when I needed you, for building a life in Naperville with me, for your immense commitment to your career that encouraged me to always keep going, for giving color to my life and for so many other important things.

I am also grateful to all of you that from far apart made me feel I was at home; Alejandra, Marcos, Andy and their respective families.

But I am most grateful to my parents. The education they gave me, the principles they taught me, their passion for travel and the understanding of other cultures, their way of life in Quilmes, and their long term support and encouragement find their way into the person I am now. To you I dedicate my doctoral dissertation.

A mis padres: Selma y Carlo

Da un bambino scemo

*“It is the mark of an educated mind to be able to entertain a
thought without accepting it”*

Aristotle

Preface

Curiosity is part of the human character. Since early times mankind has tried to understand and classify the world that surrounds us. It is in the classification process that one realizes that objects apparently similar can be distinguished and categorized into different groups according to a certain rule. The categorization process was then extrapolated from objects to ideas and abstract knowledge. Applied to the notion of distance, the categorization process planted then the question “*Is infinite divisibility possible*” and “*What are the fundamental constituents of matter?*”. Molecules and atoms, and later electrons, protons and neutrons appeared to be the end of the path for a long-lived question. Far from that, this path has currently led us to quarks, leptons and gauge bosons and it remains a mystery if the end of the path is close or even if it exists.

Ironically, when we thought that the end was just around the corner, the path took a strange turn. The things we have categorized so far can now be re-interpreted, and encompassed in larger theories that explain diversity as other sides of the same truth. The neatness of a single truth behind seemingly different processes is now the favorite sought-after model.

The curiosity that inspired our ancestors to question and understand nature still motivate us. The path has lead those of us who still ask the same question to a field that is now called Particle Physics.

Abstract

This dissertation reports the results of a search for charged Higgs bosons in the decays of $t\bar{t}$ pairs produced in $p\bar{p}$ collisions at a center-of-mass energy of 1.96 TeV. The search is performed on a data sample recorded by the upgraded Collider Detector at Fermilab and corresponding to an integrated luminosity of 193 pb^{-1} .

The search is based on the relative rates of events in the different $t\bar{t}$ decay channels. Results are obtained in the context of different models. In the context of the minimal supersymmetric extension of the Standard Model (MSSM), for which we fully account for radiative and Yukawa coupling corrections, regions in the $(m_{H^\pm}, \tan(\beta))$ plane are excluded. In the Tauonic Higgs Model in which the charged Higgs is assumed to decay exclusively to $\bar{\tau}\nu$, the $\text{BR}(t \rightarrow H^+b)$ is constrained to be less than 0.4 at 95% C.L. If no assumption is made on the charged Higgs decay, the $\text{BR}(t \rightarrow H^+b)$ is constrained to be less than 0.90 at 95% C.L. No evidence for charged Higgs production is found.

Contents

Curriculum Vitae	iii
Acknowledgments	v
Preface	ix
Abstract	xi
List of Tables	xvii
List of Figures	xix
1 Motivation	1
1.1 Motivation	1
2 Theoretical framework and present limits	5
2.1 The Standard Model	5
2.1.1 Introduction to SM particles and interactions	5
2.1.2 Lagrangian formulation of the SM	10
2.1.3 The Standard Model Higgs mechanism	17
2.1.4 Phenomenology	20
2.2 Two Higgs Doublet Model	22
2.2.1 Extended Higgs models	22

2.2.2	Introduction	23
2.2.3	Phenomenology	25
2.3	Supersymmetry and the MSSM	28
2.3.1	The hierarchy problem	28
2.3.2	Introduction to MSSM	30
2.3.3	Lagrangian formulation of the MSSM	33
2.3.4	MSSM Higgs mass eigenstates	36
2.3.5	Phenomenology	38
2.3.6	Benchmarks for the search of charged Higgs	44
2.4	Experimental limits to date	47
2.4.1	CLEO results	47
2.4.2	LEP results	48
2.4.3	FNAL results	50
	Bibliography	53
3	The Fermi National Accelerator Laboratory	61
3.1	The Fermi National Accelerator Laboratory	61
3.2	The Fermilab accelerator	62
3.2.1	The Proton Source	62
3.2.2	The main injector and recycler	67
3.2.3	The anti-proton source	68
3.2.4	The Tevatron	72
3.2.5	The beam structure	73
3.3	The CDF II detector	75
3.3.1	Overview of coordinate systems and coordinate variables	75
3.3.2	Tracking and vertexing	78
3.3.3	Calorimetry	94
3.3.4	Muon detectors	103
3.3.5	TOF	113

3.3.6	CLC	114
3.3.7	The trigger system and data flow	117
3.3.8	Data taking	124
3.3.9	Off-line data processing and datasets	125
3.4	Particle identification at CDF	129
3.4.1	Electron identification	129
3.4.2	Muon identification	135
3.4.3	Jet reconstruction	138
3.4.4	Tau reconstruction	141
3.4.5	Missing transverse energy	144
	Bibliography	147
4	Analysis	151
4.1	General strategy	151
4.2	Defining the search channels	154
4.2.1	The dilepton channel	155
4.2.2	The lepton+jets channel	157
4.2.3	The lepton+ τ_h channel	158
4.2.4	Backgrounds results	160
4.2.5	Removal of the overlap between channels	161
4.3	Event expectation	166
4.3.1	The efficiencies	170
4.3.2	Calculation of the raw Monte Carlo efficiencies	173
4.3.3	Interpolation of the raw Monte Carlo efficiencies	175
4.3.4	Width related corrections to the raw MC efficiencies	176
4.3.5	Efficiencies summary	182
4.4	Data-expectation comparison method	182
4.4.1	Bayesian statistics and Monte Carlo integration	184
4.4.2	MSSM	187

4.4.3	Tauonic Higgs model	191
4.4.4	Branching ratio independent model	192
	Bibliography	196
5	Results and Conclusions	197
5.1	Results	197
5.1.1	MSSM	197
5.1.2	Tauonic Higgs model	205
5.1.3	BR independent model	206
5.2	Conclusions	208
5.3	Future prospects	209
	Bibliography	213
A	Numeric integration	215
B	Radiative corrections to $\Gamma(t \rightarrow H^+b)$	217
B.1	QCD corrections	217
B.1.1	Renormalization Group improvement	219
B.2	SUSY corrections	220
B.3	Final Formulas	222
B.4	Conclusions	223
	Bibliography	224
C	Adding the $H^+ \rightarrow t^* \bar{b} \rightarrow Wb\bar{b}$ Decay to Pythia	225
C.1	Adding the decay to Pythia	225
C.2	Cross check of the implementation	226
	Bibliography	228

List of Tables

2.1	Fundamental interactions	6
2.2	Fundamental Particles in the Standard Model.	8
2.3	Supermultiplets of the MSSM	32
3.1	Dataset and trigger paths for the tight electron sample	127
3.2	Datasets and trigger paths for the tight muon sample.	127
3.3	Datasets and trigger paths for the plug sample.	128
3.4	Luminosity of datasets	128
3.5	Most significant hadronic tau decays	141
4.1	The top quark and Higgs boson decays	153
4.2	Results from published cross section measurements	155
4.3	Background estimation in published analysis	160
4.4	Signal overlap between channels	163
4.5	Background overlap between channels	165
4.6	Final background estimates in the exclusive channels	166
4.7	Common terms for the efficiency	172
4.8	Lepton-specific terms for the efficiency	174
4.9	Efficiency summary	183
5.1	Expected $t\bar{t}$ events in the ATLAS detector at LHC	210

List of Figures

2.1	SM Higgs production and decay	21
2.2	One-loop corrections to mass	28
2.3	MSSM diagrams causing flavor violation	35
2.4	$\text{BR}(t \rightarrow H^+b)$	39
2.5	$\text{BR}(t \rightarrow H^+b)$, dependence on μ	40
2.6	Charged Higgs branching ratios	41
2.7	Top and charged Higgs branching ratios	43
2.8	Widths of the top and Higgs	44
2.9	Lightest CP-even neutral Higgs	45
2.10	$b \rightarrow s\gamma$ diagram	48
2.11	Combined LEP results	49
2.12	CDF previous results	50
2.13	D0 previous results	51
3.1	The Cockcroft-Walton accelerator	63
3.2	The LinAc	65
3.3	The Booster	66
3.4	The Main Injector	67
3.5	The accumulator and debuncher	69
3.6	The debuncher and stochastic cooling	70
3.7	Accumulator orbit profile	71

3.8	Bunch structure	73
3.9	CDF lateral view	76
3.10	CDF tracking volume	79
3.11	COT super layers	80
3.12	COT cells	81
3.13	COT drift chamber	82
3.14	Silicon P and N type	83
3.15	Silicon p-n junction	84
3.16	Silicon modules	85
3.17	SVX bulkhead	87
3.18	L00 end view	88
3.19	Tracking: Aspect angle and seed construction	90
3.20	Tracking: Stereo reconstruction	92
3.21	Calorimeter	95
3.22	Calorimeter arch	96
3.23	Calorimeter CES chambers	98
3.24	Calorimeter central wedge light collection	99
3.25	Forward calorimeter section	101
3.26	Forward calorimeter wedges	101
3.27	Forward calorimeter Shower Maximum	102
3.28	Muon system $\eta - \phi$ coverage	106
3.29	CMU muon system	107
3.30	CMU cell details	108
3.31	CMP location	109
3.32	CMPX cells	110
3.33	CMX arches and IMU system	111
3.34	CMX layers	112
3.35	TOF bars	114

3.36	TOF performance	115
3.37	CLC location	116
3.38	CLC assembly diagram	116
3.39	CDF trigger	120
3.40	Tau identification cone	142
4.1	SM $t\bar{t}$ decays	152
4.2	Efficiency interpolation method	176
4.3	Top mass spectrum	179
4.4	Parameterization of top width	180
4.5	Method convergence Vs. number of iterations	186
4.6	Expected events for $m_{H^\pm}=120 \text{ GeV}/c^2$	189
4.7	Expected events for $m_{H^\pm}=140 \text{ GeV}/c^2$	190
4.8	Sensitivity results for the posterior probability density	193
4.9	Sensitivity results for the distribution of limits	195
5.1	MSSM results for benchmarks 1 and 2	198
5.2	MSSM results for benchmarks 3 and 4	199
5.3	MSSM results for the LEP benchmarks	200
5.4	Tauonic Higgs model results	205
5.5	BR independent model results	207
5.6	ATLAS expectation for benchmark 1 in 200 pb^{-1}	211
5.7	ATLAS expectation for the tauonic Higgs model in 200 pb^{-1}	211
C.1	Dalitz plot for the $H^+ \rightarrow t^*\bar{b} \rightarrow Wb\bar{b}$ decay	227

Chapter 1

Motivation

This chapter discusses the main unresolved aspects of contemporary physics and introduces some of the fundamental questions of particle physics that are, ultimately, the motivation for this analysis.

1.1 Motivation

During the past 50 years, particle physicists have developed an elaborate model of particles and interactions called the standard model. The model describes each particle by a field, which is simply an assignment of a quantity to every point in space-time. The standard model characterizes the ordinary matter around us and is supported by experiments with a high level of accuracy. With the assumption that the model is valid in the entire universe we have successfully predicted and understood astronomical observations of the past century.

As the 21st century begins, astrophysical and cosmological space observations have revealed that the picture of the universe based on the standard model is incomplete. The acceleration of the expansion rate of the universe is better explained by means of a yet undetected energy density that permeates the whole universe called “dark energy”. In addition astronomical evidence also shows that galaxies, and clusters of galaxies, have more mass than what is accounted for in ordinary matter, and the mass difference is

attributed to what is called “dark matter”. It is now believed that only 5% of the universe is made out of ordinary matter and that 95% of the universe is made out of something we do not understand.

It is a singular time in particle physics. Faced with the challenge to explain the constituents of ordinary matter, physicists constructed the standard model. Far from complete, and in light of the new data, the model leaves too many open questions; What is dark energy? What is dark matter? Why do the particles have the masses they have? In particular why neutrinos have so little mass? Are the forces unified at some high energy? Are there hidden symmetries beyond the ones in the current model? These are some of the most fundamental questions in contemporary physics.

The standard model is built by exploiting symmetry principles. The fundamental particles in the standard model are leptons, quarks, and bosons, and they can be categorized according to their symmetry properties. One of the symmetries of the standard model, called the “electro-weak” symmetry (EWS), predicts massless particles. We know that particles have masses and therefore we know the symmetry is broken. Within the standard model it is speculated that a single scalar field doublet breaks the symmetry, resulting in a single observable particle of unknown mass called the Higgs boson. To date, the standard model Higgs boson has not been observed, and the standard model mechanism of electroweak symmetry breaking (EWSB) is not yet confirmed. Other theories consider different mechanisms of EWSB. Some of them, with hidden symmetries, predict new particles that are natural candidates to solve the dark matter problem. They also predict the unification of forces at high energy, and even the dark energy puzzle could be understood if these theories are proven correct. The mechanism of EWSB is a key aspect to help answer some of the fundamental questions of contemporary physics.

The phenomenology of Higgs bosons provides direct insight into the structure of the Higgs sector and the mechanism of EWSB. Extensions of the standard model have been proposed with different Higgs phenomenologies. The simplest extension of the standard model Higgs sector is built by the introduction of another Higgs doublet resulting in a two-Higgs doublet model (2HDM). In these models EWSB results in five Higgs bosons, three of which are neutral (h^0, H^0, A^0) and two of which are charged (H^\pm).

Other extensions of the standard model include new symmetry principles in the basic theoretical formalism. One of such theories is called Supersymmetry. In supersymmetric theories the introduction of the new symmetry results in the introduction of extra particles. The minimal supersymmetric extension of the standard model includes a 2HDM sector. The 2HDM spectrum of observable Higgs particles is retained, and therefore the observation of a charged Higgs boson would provide unambiguous evidence of a mechanism of EWSB different than that predicted by the minimal formulation of the standard model.

One of the quarks of the standard model is named the “top” quark. This particle is also assumed to play an important role in EWSB. With a mass 40 times larger than the next heavy fermion its interaction strength with the Higgs field is very large. The Higgs boson(s), together with the top quark, are the main characters in the play of the EWSB. That is the driving force behind this analysis. We will search for charged Higgs production in association with top quarks with the hope that the search will help understand, or set stricter constraints, on possible mechanisms of EWSB.

Chapter 2 introduces the basic formalism of the standard model as well as commonly used extensions of it with special focus on the phenomenology of the Higgs sector. Chapter 3 describes the accelerator used to produce top quarks, and the detector used to detect them. Chapter 4 begins by

describing the procedures to identify and catalog pair-produced top events, and follows describing the analysis strategy to measure charged Higgs production. Chapter 5 presents the results, and this dissertation ends with concluding remarks and future prospects in the last part of Chapter 5.

Chapter 2

Theoretical framework and present limits

This chapter begins with the introduction of the Standard Model of particles and fields followed by a discussion of its inelegances and incompleteness as a motivation for the study of extensions to this theory. The two Higgs doublet model and Supersymmetry are then described with special focus on the charged Higgs sector and its associated phenomenology. The chapter concludes with the present experimental limits.

2.1 The Standard Model

Particle physics attempts to identify the fundamental constituents of matter and to understand the interactions between them. The currently accepted, experimentally favored, model of such constituents and interactions is called the “*The Standard Model of Particles and Fields*”, and will be referred throughout this dissertation as SM.

2.1.1 Introduction to SM particles and interactions

The SM fundamental particles are categorized into three groups; leptons, quarks and gauge bosons. These groups are described in detail in the following sections, however a quick description of their interactions is given here

in terms of their low energy behavior. There are four known forces governing the interactions of matter at low energies : strong, electromagnetic, weak and gravitational. The electromagnetic and weak are now understood as two expressions of the same electro-weak force. The connection between these two forces was one of the greatest achievements of this era. In this introduction, however, they are treated separately and a deeper description of the electro-weak theory is postponed to the next section. The properties of these four forces are shown in Table 2.1. The strength by which particles couple to fields is called the coupling constant.

Interaction	Mediator	Coupling Constant	Range (m)
strong	g	≤ 1	$\leq 10^{-15}$
electromagnetic	γ	$1/137$	∞
weak	W^\pm, Z^0	10^{-6}	10^{-18}
Gravitational	graviton	10^{-40}	∞

Table 2.1: Fundamental interactions. The particle acting as a mediator, the coupling constant and the range of the interaction are also shown.

The forces affect the different groups differently. The strong force is mediated by the exchange of gluons, and has a very short range of interaction. Quarks can interact via the strong force, which is ultimately responsible for the binding of quarks in neutrons, protons and other hadrons. The strong force is also responsible for the binding of neutron and protons between them, providing a general stability configuration to the atomic nuclei.

The electromagnetic force is felt by particles with net electric charge, and is mediated by the exchange of photons. The coupling of the electromagnetic force is about two orders of magnitude smaller than that of the strong force.

The weak force is mediated by the W^\pm and Z^0 gauge bosons, and with

the exception of gluons, interacts with all the other particles¹. This force plays a fundamental role in the neutron decay.

At last, the gravitational force interacts with any type of particle with a strength forty orders of magnitude smaller than the strong force. Its effects only become large when the interacting bodies have a large mass, as is the case in interplanetary systems.

Quarks and leptons

The fundamental particles of the SM are shown in Table 2.2. Quarks are fermions with spin $1/2$ and electric charge a fraction of that of the electron. There are six basic quarks arranged in three “generations”. The quarks have colorful names, such as up (u), down (d), charm (c), strange (s), top (t) and bottom (b). The last four quarks are unstable particles that decay into lighter quarks. The hadrons are further categorized into mesons and baryons, where the former are composed of a bound quark-antiquark and the latter of three quarks. Even though quarks have fractional charge the hadrons are formed such that they always have integer charge.

The fact that many bound states of quarks (which are fermions) appeared to be in contradiction with the Fermi statistics was overcome with the introduction of another degree of freedom, an intrinsic property of quarks called color. Three types of color, red (R), blue (B) and green (G) were necessary to satisfy experimental constraints from cross section ratios and pion decays [15]. The exchange of color charge between quarks is responsible for the strong force.

In general the antiparticle of a quark carries the anti-color of the quark. When hadrons are formed the quark content must be such that overall colorless hadrons are obtained. The quark colors are defined such that any

¹Whether the weak force interacts to gravitons is still an open question.

RGB, $\bar{R}\bar{G}\bar{B}$ or color-anticolor combination is colorless. This accommodates the experimental fact that many otherwise possible bound quark states have not been observed.

Generation			
I	II	III	
u	c	t	
Quarks			
d	s	b	
ν_e	ν_μ	ν_τ	
Leptons			
e	μ	τ	

Table 2.2: Fundamental Particles in the Standard Model.

Leptons are spin 1/2 particles. The electron (e), the muon (μ) and the tau (τ) have the electric charge of the electron. The electron-neutrino, (ν_e), the muon-neutrino, (ν_μ), and the tau-neutrino (ν_τ) have no electric charge.

The mass of the neutrinos has been recently found to be non-zero² [29]

All leptons interact via the weak force, but the charged leptons also interact electromagnetically. In analogy with the quarks, the leptons are arranged in three generations, with the first generation containing the stable particles.

For each particle in Table 2.2 there is an associated anti-particle not shown in the table.

² If the masses of the neutrinos are non-zero then right handed neutrinos must exist. However they will not interact with any of the gauge fields in the SM since they are not electrically charged and they are $SU(2)_L$ and $SU(3)_{color}$ singlet states.

Gauge bosons

Gauge bosons are integer spin particles. These particles are interchanged between particles to give origin to forces between them. Each gauge boson is associated with a fundamental interaction; the strong force is mediated by gluons, the electromagnetic force is mediated by photons, the weak force by the W^\pm and Z^0 bosons, and the gravitational force is believed to be mediated by massless gravitons. All these particles take part in the “transmission” of forces and are obtained in theoretical arguments by requiring “local gauge invariance”, thus the name of gauge bosons.

The strong force is carried by gluons and is responsible of the interaction between particles with color. Gluons themselves carry color, and are therefore capable of acting on another gluons. The strong force has a very distinctive feature; the force between colored particles increases with the distance between them. As two quarks pull away from one another, the energy becomes large enough that is energetically preferable to create a pair quark-antiquark from the vacuum in between the original pair than to sustain the original configuration. With the creation of the intermediate pair of quarks each original quark pairs itself with one of the newly created pair, and the distance between them is only half. This process is known as hadronization.

The electromagnetic force is carried by photons. Charge particles emit photons that are absorbed by other charged particles. To conserve energy the particle recoils when emitting the photon, and the particle absorbing it obtains its momentum. Because the photons do not carry charge they do not interact with other photons. The electromagnetic current will be derived in Section 2.1.2 in the context of gauge theories.

The weak force is a short range interaction. All fermions and massive gauge boson are subjected to the weak interaction. The short range of the interaction is accounted for by the heavy mass of the weak force

carriers, approximately 81 and 91 GeV/c² for the W^\pm and Z^0 bosons respectively. Charged currents are mediated by the W^\pm and neutral by the Z^0 boson. Current experiments show that the Z boson is only exchanged among fermions of the same generation, and have set very strict limits on the exclusion of flavor changing neutral currents (FCNC).

The weak force does not interact with right-handed particles. In the massless approximation a (left) right handed particle has the property that the spin is (anti) parallel to its momentum. For this reason the lepton and quarks are distinguished into left-handed doublets and right-handed singlets. Furthermore to explain strangeness-changing weak interactions the left-handed quarks are not arranged in their mass eigenstates, rather they are expressed as a linear combination of the physical quarks states through a non diagonal 3x3 mixing matrix named the CKM matrix in honor of Cabibbo, Kobayashi and Maskawa [16]. The weak neutral current is obtained from experiment as $J_\mu^{NC} = \bar{u}\gamma_\mu\frac{1}{2}(C_V - C_A\gamma^5)u$, where the values C_V and C_A depend on whether the u's are lepton or quarks. The general expression for the electro-weak currents will be obtained in Section 2.1.2.

The charge-parity-time theorem (CPT theorem) states that all interactions must respect a combined transformation of charge, parity and time reversal. The CKM matrix does not respect time reversal and thus, if the CPT theorem is to hold, the matrix is expected to allow for charge-parity (CP) violation. The conservation of CPT is consistent with all experimental observations, while CP violation has been determined in the decay of neutral kaons and b mesons [14].

2.1.2 Lagrangian formulation of the SM

In gauge field theory particles are described as quantized fields and their interactions are expressed in the Lagrangian density \mathcal{L} . The motivation to use

quantized fields lies in the fact that conserved quantities can be associated to symmetries. This is proven in the theorem of Noether [26], which states that each continuous symmetry of a system corresponds a conserved quantity. In a gauge field theory any continuous transformation in the field ψ that leaves unchanged the action (S) of the Lagrangian, defined as $S = \int \mathcal{L}(\psi, \delta\psi)dx$ is associated with a conserved quantity. The following sections derive the Lagrangian densities that are ultimately responsible for the forces as they are known to date.

Lagrangian formulation of quantum electrodynamics (QED)

The Dirac Lagrangian for a free spinor field is given by

$$\mathcal{L} = i\bar{\psi}\gamma^\mu\partial_\mu\psi - m\bar{\psi}\psi \quad (2.1)$$

The requirement of global invariance of the field results in charge conservation. Global invariance is obtained when the field is changed by the same amount in every point in space-time, e.g. the transformation $\psi(x) \rightarrow e^{iq\alpha}\psi(x)$ is a global transformation for any value of α . In group theory all the transformations of the type $\psi(x) \rightarrow e^{iq\alpha}\psi(x)$ obtained by changing the value of α are said to belong the global U(1) gauge group.

The SM however is based upon local (as opposed to global) gauge invariance. Local U(1) invariance is obtained when the Lagrangian is invariant to transformations of the type $\psi(x) \rightarrow e^{iq\alpha(x)}\psi(x)$ where now α depends on the space-time position x , i.e. the transformation is independent at each point in space-time. It is clear that the Dirac Lagrangian cited above is not invariant to this transformation. Introducing this transformation into the Dirac Lagrangian above results in

$$\mathcal{L}' = i\bar{\psi}\gamma^\mu(\partial_\mu + iq\partial_\mu\alpha)\psi - m\bar{\psi}\psi \quad (2.2)$$

If we insist on imposing invariance of the Lagrangian under local gauge

transformations we must seek a different derivative, one that transforms like ψ itself, i.e. $D_\mu\psi \rightarrow e^{iq\alpha(x)}D_\mu\psi$. This can be accomplished with the definition:

$$D_\mu \equiv \delta_\mu - iqA_\mu \quad (2.3)$$

$$A_\mu \rightarrow A_\mu + \frac{1}{q}\partial_\mu\alpha(x) \quad (2.4)$$

As long as A_μ transforms as Equation 2.4 the derivative D_μ will transform as $D_\mu\psi \rightarrow e^{iq\alpha(x)}D_\mu\psi$ and the Lagrangian defined as

$$\begin{aligned} \mathcal{L} &= i\bar{\psi}\gamma^\mu D_\mu\psi - m\bar{\psi}\psi \\ &= \bar{\psi}(i\gamma^\mu\partial_\mu - m)\psi + q\bar{\psi}\gamma^\mu\psi A_\mu \end{aligned} \quad (2.5)$$

is invariant with the local gauge transformation. The vector field A_μ introduced by demanding local phase invariance is called the gauge field. Hence, by demanding local invariance one is forced to introduced the gauge field, which couples to charged particles in the same was as the photon field does. If this field is to regarded as the physical photon field, a new term corresponding to the photon kinetic energy must be added to the Lagrangian. Because this new term must be invariant to the transformation of Equation 2.4 it can only involve the gauge invariant field tensor $F_{\mu\nu} \equiv \partial_\mu A_\nu - \partial_\nu A_\mu$.

The local invariant Lagrangian obtained in this way is then :

$$\mathcal{L}_{QED} = \bar{\psi}(i\gamma^\mu\partial_\mu - m)\psi + q\bar{\psi}\gamma^\mu\psi A_\mu - \frac{1}{4}F_{\mu\nu}F^{\mu\nu} \quad (2.6)$$

By requiring the Dirac Lagrangian for a free spinor field to be locally invariant under U(1) phase transformations, the Lagrangian for spinor fields interacting with the electromagnetic potential is obtained. The last two terms above appear in the classical Maxwell Lagrangian, where the charge density is identified with $J_\mu^m = q(\bar{\psi}\gamma_\mu\psi)$.

Lagrangian formulation of the electro-weak theory

The QED theory described above is derived by requiring $U_q(1)$ Lagrangian invariance, where the subindex “q” in $U_q(1)$ refers to the charge conservation that results from the symmetry³. The imposition of the symmetry leads to the introduction of the A^μ field.

With the same idea, the authors of GWS theory originally tried to explain the weak (neutral and charged) currents as resulting from the imposition of a weak symmetry group.

An isospin triplet of weak currents could be defined as

$$J_\mu^i(x) = \bar{\chi}_L \gamma_\mu \frac{1}{2} \sigma_i \chi_L \quad (2.7)$$

where σ_i are the usual Pauli spin matrices and $\chi_L = \begin{pmatrix} \nu \\ e^- \end{pmatrix}_L$ is the doublet of left-handed fermions. The current $J_\mu^3(x)$ represents the neutral current, while $J_\mu^1(x)$ and $J_\mu^2(x)$ are linear combinations of the positive and negative charged currents. For each current the corresponding charge (T^i) is obtained by integrating the 0th component of the charge over the space;

$$T^i = \int J_0^i d^3x \quad (2.8)$$

and it can be shown that the charges satisfy

$$[T^i, T^j] = i\epsilon_{ijk} T^k \quad (2.9)$$

The commutation relation between the charges indicates the nature of the symmetry generated by them; in this case $SU(2)_L$. The sub-index “L” reminds us of that the weak isospin current couples only to left-handed fermions.

³Formally it is said that q is related to Q, the charge operator that generates the $U_q(1)$ symmetry group of electromagnetic interactions.

However, the neutral current $J_\mu^3(x)$ as written in Equation 2.7 does not contain the right handed component experimentally found in data (J_μ^{NC}), and thus it does not show the V-A character of the weak neutral current. This is overcome by introducing the electromagnetic current J_μ^{em} which does couple to left and right fermions. Since neither J_μ^{NC} nor J_μ^{em} respect the $SU(2)_L$ symmetry two orthogonal combinations are formed that do have definite transformation properties. One combination will be J_μ^3 and will complete the weak isospin, the other is called j_μ^Y and is unchanged by $SU(2)_L$ and is thus a weak isospin singlet. The combination is done in such a way that

$$j_\mu^Y = \bar{\psi} \gamma_\mu Y \psi$$

where Y is the weak hypercharge defined by

$$Q = T^3 + \frac{Y}{2} \quad (2.10)$$

In this context the electromagnetic current is written as

$$j_\mu^{em} = J_\mu^3 + \frac{1}{2} j_\mu^Y$$

With the introduction of the electromagnetic interaction the symmetry group has been enlarged to $SU(2)_L \otimes U(1)_Y$. The $U(1)_q$ group of electromagnetism is now contained in it. Each group $SU(2)_L$ and $U(1)_Y$ couples with its own strength, and in addition to the electron charge, another coupling constant is needed to fully specify the electro-weak interaction.

In the language of field theory the $SU(2)_L \otimes U(1)_Y$ symmetry will introduce four gauge bosons; three of them (W_μ^i) are associated with the $SU(2)_L$ symmetry and coupled to weak isospin, and the other (B_μ) associated with $U(1)_Y$ coupling to weak hypercharge.

The standard model fermions are assigned to weak isodoublets (T=1/2) and isosinglets (T=0) as follows :

$T = 1/2$	$T = 0$	
$\begin{pmatrix} \nu \\ e \end{pmatrix}_L$	e_R	
$\begin{pmatrix} u \\ d \end{pmatrix}_L$	u_R	d_R

where the upper (lower) component of the doublet has $T^3 = +1/2$ ($-1/2$), and the isospin assignments for the second and third generation are identical.

The electro-weak Lagrangian density is

$$\mathcal{L} = gJ_\mu W^\mu + \frac{g'}{2}j_\mu^Y B^\mu \quad (2.11)$$

The physical bosons of the theory (W_μ^\pm, Z_μ and A_μ) are constructed from the $SU(2)_L \otimes U(1)_Y$ gauge bosons :

$$W_\mu^\pm = \frac{1}{\sqrt{2}} (W_\mu^1 \pm iW_\mu^2) \quad (2.12)$$

$$Z_\mu = W_\mu^3 \cos(\theta_W) - B_\mu \sin(\theta_W) \quad (2.13)$$

$$A_\mu = W_\mu^3 \sin(\theta_W) + B_\mu \cos(\theta_W) \quad (2.14)$$

where θ_W is defined such that $\tan(\theta_W) = g'/g$. Rewriting Equation 2.11 in terms of the physical bosons gives

$$\mathcal{L} = \frac{g}{\sqrt{2}} (J_\mu^- W^{\mu+} + J_\mu^+ W^{\mu-}) + \frac{g}{\cos(\theta_W)} (J_\mu^3 - \sin^2(\theta_W) J_\mu^{em}) Z^\mu + g \sin(\theta_W) J_\mu^{em} A^\mu \quad (2.15)$$

The last term in Equation 2.15 is the photon coupling to an electromagnetic current, and allows the identification of $g \sin(\theta_W)$ to the electron charge e . Writing out the currents explicitly,

$$J_\mu^\pm = \bar{\psi}_L \gamma_\mu \sigma^\pm \psi_L \quad (2.16)$$

$$J_\mu^3 = \bar{\psi}_L \gamma_\mu \sigma^3 \psi_L \quad (2.17)$$

$$J_\mu^{em} = \bar{\psi} \gamma_\mu Q \psi_L \quad (2.18)$$

Where Q is the charge operator and σ^i are the Pauli spin matrices.

If one examines the weak charged term and the weak neutral term (first and second terms in Equation 2.15) and re-interprets them in the context of the old V-A theory one finds

$$m_W = \left(\frac{g^2 \sqrt{2}}{8G_F} \right)^{1/2} = \left(\frac{e^2 \sqrt{2}}{8G_F \sin^2(\theta_W)} \right)^{1/2} \quad (2.19)$$

$$m_Z = \frac{m_W}{\cos(\theta_W)} \quad (2.20)$$

The first relatively accurate measurement of $\sin^2(\theta_W)$ of 0.23 ± 0.01 was obtained in 1981 using the rates of charged and neutral current reactions in low energy neutrino experiments. This quantity allowed the first prediction of the W^\pm and Z^0 boson masses to about 83 and 94 GeV/c² respectively. These bosons were first observed two years later by studying proton-antiproton collisions with the UA1 and UA2 detectors in the $Spp\bar{S}$ collider at CERN [37, 38]. The W^\pm was observed through its decay into a high energy lepton and missing transverse energy from the neutrino, and the Z^0 through its decay to a pair of charged leptons. The final measurement of the masses were in good agreement with the predicted values.

The introduction of the so called “Z factories”, electron-positron colliders tuned at the center of mass energy of the Z^0 boson, provided an solid confirmation of the GWS theory. The four detectors (OPAL, ALEPH, DELPHI, and L3) at the LEP circular collider at CERN recorded more than 16 million Z^0 boson events, and the SLD detector at SLAC over half a million with a partially polarized electron beam. The high statistics of the samples allowed for high-precision measurements of the boson properties, yielding excellent agreement with GWS theory.

Lagrangian formulation of quantum chromodynamics (QCD)

The theory for strong interactions is based on the $SU(3)_C$ symmetry group. The "C" refers to the quark's color and the three comes from its three possible degrees of freedom. The QCD Lagrangian is written as

$$\mathcal{L}_{QCD} = \sum_{color} i\bar{q}(\gamma^\mu D_\mu - m_q)q - \frac{1}{4}F_{\mu\nu}^\alpha F_{\alpha}^{\mu\nu} \quad (2.21)$$

where the quark fields q are :

$$\begin{pmatrix} q_1 \\ q_2 \\ q_3 \end{pmatrix} \quad (2.22)$$

The covariant derivative required to make the Lagrangian invariant to $SU(3)_C$ transformations is given by

$$D_\mu = \left(\partial_\mu - ig_s \frac{\lambda_\alpha}{2} A_\mu^\alpha \right) \quad (2.23)$$

The quantities $\frac{\lambda_\alpha}{2}$ are the generators of the $SU(3)_C$ group given by 3×3 traceless hermitian matrices, and A_μ^α are the gluons fields, with $\alpha = 1, \dots, 8$.

The energy of the gluon field is given by the last term in the Lagrangian where the gluon field strength tensor is

$$F_{\mu\nu}^\alpha = \partial_\mu A_\nu^\alpha - \partial_\nu A_\mu^\alpha + g_s f^{\alpha\beta\gamma} A_{\mu\beta} A_{\nu\gamma} \quad (2.24)$$

The third term represents the gluon-gluon interactions.

2.1.3 The Standard Model Higgs mechanism

In the electroweak theory any gauge boson mass term will enter the Lagrangian as $m_W^2 W^\mu W_\mu$. This term would destroy the $SU(2)_L \otimes U(1)_Y$ invariance unless the boson mass m_W is zero. This implies that all the bosons of the electroweak theory must have vanishing mass if the invariance is to

be kept. Thus, without any other mechanism, the electroweak theory lacks the ability to put mass into gauge bosons.

One could argue that invariance is required for aesthetics purposes only, and one could add such mass terms to the Lagrangian and ignore the symmetry breaking effects. This however inserts un-renormalizable divergences to all orders rendering the theory meaningless; invariance should be insisted upon.

The solution is to invoke a mechanism developed by Peter Higgs et al. [39]. In the Higgs mechanism a scalar field ϕ , with non-vanishing vacuum expectation value, is inserted into the theory of massless gauge bosons. To keep the Lagrangian invariant the field must belong to an $SU(2)_L \otimes U(1)_Y$ multiplet. The ϕ field will add a contribution \mathcal{L}_2 to the Lagrangian of the theory,

$$\mathcal{L}_2 = |D_\mu \phi|^2 - V(\phi) \quad (2.25)$$

In order to conserve the $SU(2)_L \otimes U(1)_Y$ invariance the covariant derivative D_μ must be

$$D_\mu = \partial_\mu + igT \cdot W_\mu + \frac{g'}{2} Y B_\mu \quad (2.26)$$

With the purpose of obtain a final theory in which the W^\pm and Z^0 bosons obtain mass while the electromagnetic field remain massless, the choice of 4 real scalar fields arranged in a doublet of complex scalar fields with hypercharge $Y=1$ is made;

$$\phi = \begin{pmatrix} \phi^+ \\ \phi^0 \end{pmatrix} \quad \text{with} \quad \begin{aligned} \phi^+ &\equiv (\phi_1 + i\phi_2)/\sqrt{2} \\ \phi^0 &\equiv (\phi_3 + i\phi_4)/\sqrt{2} \end{aligned} \quad (2.27)$$

Where the ϕ_i 's are four real fields. When the Higgs potential is minimized, the neutral component of the Higgs field acquires a vacuum expectation value (VEV). The phase of the Higgs field can be chosen such that VEV is

real and positive. The minimum of the Higgs field is represented by ϕ_0 ,

$$\phi_0 = \langle 0 | \phi | 0 \rangle = \frac{1}{\sqrt{2}} \begin{pmatrix} 0 \\ v \end{pmatrix} \quad (2.28)$$

A Lagrangian density with $V(\phi) = \mu\phi^\dagger\phi + \lambda(\phi^\dagger\phi)^2$ is chosen so as to have a minimum at $v = \sqrt{\mu^2/\lambda}$. Expanding the field ϕ around its VEV value,

$$\phi = \frac{1}{\sqrt{2}} \begin{pmatrix} 0 \\ v + h(x) \end{pmatrix} \quad (2.29)$$

introduce it into the Lagrangian of Equation 2.25, and rewrite the W_μ^i s and B_μ as a function of the physical bosons (see Equation 2.12 to 2.14), this gives :

$$\mathcal{L}_2 = \frac{1}{2}(\partial_\mu\phi)^2 + \left(\frac{gv}{2}\right)^2 W_\mu^+ W^{-\mu} + \frac{1}{2} \left(\frac{gv}{2\cos(\theta_W)} \right)^2 Z_\mu Z^\mu - \lambda v^2 h^2 + \dots \quad (2.30)$$

As a consequence of the VEV of the scalar field the symmetry has been broken resulting in W^\pm and Z^0 bosons with masses of $gv/2$ and $gv/(2\cos(\theta_W))$ respectively, and the photon remained massless as desired. In addition, the introduction of the scalar field also resulted in a new scalar boson with a mass of $\sqrt{2\lambda}v$. This boson is denoted h_{sm} and named the ‘‘Higgs’’ boson after Peter Higgs who was the first to understand this mechanism. It should be noted that while the value of v can be deduced from the W^\pm mass (yielding $v = 246$ GeV), the mass of the Higgs itself remains unknown since it includes the unknown value of λ .

The Higgs mechanism just described also provides a way to generate masses for the quarks and leptons. It is clear that the addition of a fermionic mass term such as $-m_e\bar{e}e = -m_e(\bar{e}_R e_L + \bar{e}_L e_R)$ is not gauge invariant, since e_L and e_R belong to different representations of SU(2) and have different U(1) hypercharges. But an invariant mass term can be written by including

a Yukawa-like coupling to the Higgs field ϕ ,

$$\mathcal{L}_3 = -\lambda_e \left[(\bar{\nu}_e, \bar{e})_L \begin{pmatrix} \phi^+ \\ \phi^0 \end{pmatrix} e_R + \bar{e}_R (\phi^-, \bar{\phi}^0) \begin{pmatrix} \nu_e \\ e \end{pmatrix}_L \right] \quad (2.31)$$

Using Equation 2.29 to break the symmetry gives

$$\mathcal{L}_3 = -\frac{\lambda_e}{\sqrt{2}} v (\bar{e}_L e_R + \bar{e}_R e_L) - \frac{\lambda_e}{\sqrt{2}} (\bar{e}_L e_R + \bar{e}_R e_L) h \quad (2.32)$$

$$= -m_e \bar{e} e - \frac{m_e}{v} \bar{e} e h \quad (2.33)$$

$$(2.34)$$

where $m_e = \frac{\lambda_e v}{\sqrt{2}}$.

This mechanism can be extended to all fermions. A fermion “f” will then acquire mass through interactions with the Higgs field via its coupling constant λ_f , which is proportional to the fermion’s mass, in contrast to the coupling to gauge bosons which are proportional to the squared masses.

Although the Higgs mechanism introduces a way for fermions to acquire mass, it does so at the price of inelegance. Since the values of λ_f ’s are arbitrary, the value of the fermion masses are not predicted. In fact, each coupling must be now tuned to achieve the experimentally measured fermion mass. Our theoretical ignorance of the origin of the fermion masses has now been merely re-interpreted as theoretical ignorance on the Higgs field coupling constants. This could be a strong indication that the SM is an incomplete theory.

2.1.4 Phenomenology

While the Higgs field endows mass to all the SM particles, a physical Higgs particle has yet to be found. The production cross section for SM Higgs at the Tevatron is shown in Figure 2.1(left) for different mechanisms. At the Tevatron (and at the future LHC) the main production mechanism is

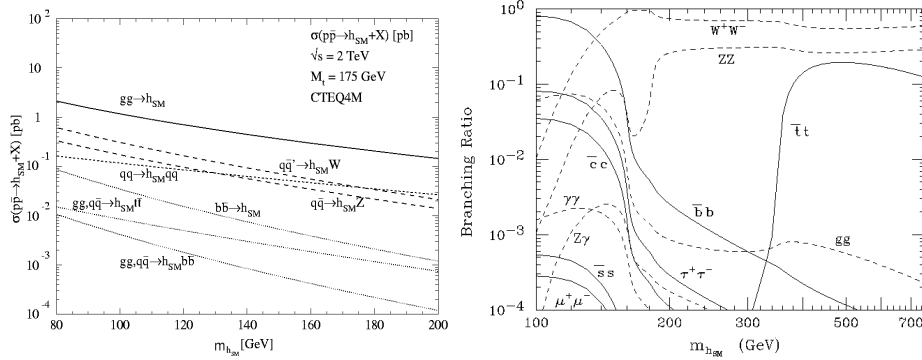


Figure 2.1: **Left:** Production cross section of SM Higgs as a function of its mass at Tevatron energies. The plot is taken from [19] and includes the complete NLO QCD corrections. The notation $q\bar{q} \rightarrow q\bar{q}h_{sm}$ refers to the both quark and antiquark radiating virtual bosons which then annihilate to produce the Higgs boson. **Right:** Branching ratios of the SM Higgs boson as a function of Higgs mass. Final states with two bosons (fermion-antifermion) are shown by solid (dashed lines). The $h_{sm}gg$, $h_{sm}\gamma\gamma$ and $h_{sm}Z\gamma$ vertices are generated at one-loop.

$gg \rightarrow h_{sm}$ (see references [20] and [21]). This is followed by the Higgsstrahlung mechanism $q\bar{q}l \rightarrow W^\pm h_{sm}$.

The notation $q\bar{q} \rightarrow q\bar{q}h_{sm}$ refers to the both quark and antiquark radiating virtual bosons which then annihilate to produce the Higgs boson. Vector boson fusion via $ud \rightarrow duh_{sm}$ and its charge-conjugate process are included.

The main decay modes of the SM Higgs boson are shown in Figure 2.1(right). The calculation of the branching ratios was done with the HDECAY program [17]. For Higgs masses below 135 the decay $h_{sm} \rightarrow b\bar{b}$ dominates followed by $h_{sm} \rightarrow \tau\bar{\tau}$ or gg . With masses above 135 GeV/c² the dominant decay mode is $h_{sm} \rightarrow WW^{(*)}$ ⁴

As mentioned above the largest Higgs boson production cross section is via $gg \rightarrow h_{sm}$ with the Higgs decaying to $b\bar{b}$ (WW^*) if the mass of the Higgs

⁴Below W^+W^- threshold one of the W bosons is virtual as indicated by the star.

is below (above) $135\text{GeV}/c^2$. The $b\bar{b}$ decay however is greatly obscured by the orders-of-magnitude larger QCD dijet background. The total integrated luminosity to come from the Tevatron is expected to be between 4fb^{-1} and 8fb^{-1} . For masses above $135\text{GeV}/c^2$ Tevatron Higgs searches in the channel $gg \rightarrow h_{sm} \rightarrow W^*W$ are accessible only with luminosities greater than 30fb^{-1} as shown by the study done in [24].

The most promising SM Higgs discovery mechanism at the Tevatron, given enough luminosity and for Higgs masses below $135\text{GeV}/c^2$, consists of Higgs-strahlung or $q\bar{q}$ annihilation into a virtual W (or Z) boson that radiates the Higgs boson to get on shell. The W (or Z) boson then decays leptonically and the Higgs boson decays $h_{sm} \rightarrow b\bar{b}$. These are indicated as $q\bar{q}t \rightarrow h_{sm}W$ and $q\bar{q} \rightarrow h_{sm}Z$ in Figure 2.1(left), and together sum up to 0.2 to 0.5 pb in the mass region between 100 and $135\text{GeV}/c^2$. An interesting feasibility study in this channel is shown in [25].

2.2 Two Higgs Doublet Model

2.2.1 Extended Higgs models

The choice of a scalar doublet for the Higgs field is based on the fact that it is the field with the minimum number of degrees of freedom that breaks the $SU(2)_L \otimes U(1)_Y$ symmetry. In this sense it is said that SM Higgs field is “minimal”. However, since there is no experimental evidence of the source of symmetry-breaking sector of the SM, it is instructive to take a look at more complex mechanisms.

There is a multitude of Higgs fields based on singlets, doublets, triplets, etc, that effectively result in massive fermions. However, any good Higgs mechanism candidate should, in addition to give masses to fermions and bosons, obey at least two important phenomenological constraints. The

first is the value of ρ , defined as

$$\rho = \frac{m_W^2}{M_Z^2 \cos^2(\theta_W)} \quad (2.35)$$

This value has been measured to be $\rho = 0.9998_{-0.0005}^{+0.0008}$ (see [3]). In the minimal SM Higgs sector the value is set to 1, as this is an automatically fulfilled condition to any Higgs sector with an arbitrary number of singlets or doublets. In more elaborated representations the condition $\rho = 1$ can only be achieved after a fine tuning of the parameters of the Higgs potentials.

The second constraint is the strict experimental limit obtained on flavor-changing neutral currents (FCNC). The absence of tree level FCNC is automatically achieved in the SM Higgs mechanism. In models with more than one Higgs doublet tree-level FCNC are absent if fermions of a given electric charge couple to no more than one doublet, as proven in a theorem by Glashow and Weinberg ([8]). In more elaborate models this can be effectively achieved by tuning the potential parameters so that Higgs bosons are very heavy, and then Higgs-mediated FCNC's are suppressed enough to be consistent with experimental limits.

The two Higgs Doublet model (2HDM), which automatically satisfies the $\rho = 1$ condition while preventing FCNC's, seems to be the simplest possible extension of the minimal SM Higgs mechanism. As will be shown in the next sections, the 2HDM is also the minimal form of electro-weak symmetry breaking that can also accommodate Supersymmetry.

2.2.2 Introduction

The 2HDM model assumes two complex, scalar doublets (ϕ_1, ϕ_2) with hypercharge $Y = 1$. It is clear then that the quantities $X_1 = \phi_1^\dagger \phi_1$, $X_2 = \phi_2^\dagger \phi_2$, $X_3 = \text{Re}(\phi_1^\dagger \phi_2)$ and $X_4 = \text{Im}(\phi_1^\dagger \phi_2)$ are $SU(2)_L \otimes U(1)_Y$ invariant.

The most general potential can then be written by means of the X_i 's as

follows[10] :

$$V = - \sum_{i=1}^4 \mu_i^2 X_i + \sum_{i<j=1}^4 b_{ij} X_i X_j \quad (2.36)$$

Where V depends on 14 real variables. After imposing CP invariance considerations the potential can be expressed in terms of only 8 parameters named $\lambda_{1,2\dots7}$, and ϵ ,

$$\begin{aligned} V = & \lambda_1(\phi_1^\dagger\phi_1 - v_1^2)^2 + \lambda_2(\phi_2^\dagger\phi_2 - v_2^2)^2 \\ & + \lambda_3 \left[(\phi_1^\dagger\phi_1 - v_1^2)^2 + (\phi_2^\dagger\phi_2 - v_2^2)^2 \right] \\ & + \lambda_4 \left[(\phi_1^\dagger\phi_1)(\phi_2^\dagger\phi_2) - (\phi_1^\dagger\phi_2)(\phi_2^\dagger\phi_1) \right] \\ & + \lambda_5 \left[\text{Re}(\phi_1^\dagger\phi_2) - v_1 v_2 \cos(\epsilon) \right]^2 \\ & + \lambda_6 \left[\text{Im}(\phi_1^\dagger\phi_2) - v_1 v_2 \sin(\epsilon) \right]^2 \\ & + \lambda_7 \left[\text{Re}(\phi_1^\dagger\phi_2) - v_1 v_2 \cos(\epsilon) \right] \left[\text{Im}(\phi_1^\dagger\phi_2) - v_1 v_2 \sin(\epsilon) \right] \end{aligned} \quad (2.37)$$

where the parameters $\lambda_{1,2\dots7}$ are real and positive. In particular the λ_7 can be eliminated by redefining the phases of the scalar fields (see [12]), and the parameter ϵ regulates the amount of CP violation in the Higgs sector. The potential is invariant to $\phi \rightarrow -\phi$ transformations which guarantees the absence of tree-level FCNC. It is also interesting to point out (see [13]) that only potentials with CP invariant minimum are consistent with the absence of FCNC in the fermionic sector.

If all $\lambda_{1,2\dots6}$ are non negative then the minimum of the potential is

$$\langle \phi_1 \rangle = \begin{pmatrix} 0 \\ v_1 \end{pmatrix} \quad \langle \phi_2 \rangle = \begin{pmatrix} 0 \\ v_2 e^{i\epsilon} \end{pmatrix} \quad (2.38)$$

which breaks the $SU(2)_L \otimes U(1)_Y$ symmetry down to $U(1)_q$. In this disertation it is assumed that there is no CP violation and the value of ϵ is consequently set zero.

The breaking of the electroweak symmetry results in five Higgs boson, three of which are neutral (h^0, H^0, A^0) and two of which are charged (H^\pm).

The masses of the physical Higgs states are obtained by diagonalizing the Higgs boson mass matrix $M_{ij}^2 = \frac{\partial^2 V}{\partial \phi_j \partial \phi_j}$, obtaining :

$$H^\pm = -\phi_1^\pm \sin(\beta) + \phi_2^\pm \cos(\beta) \quad (2.39)$$

$$A^0 = \sqrt{2} [-\text{Im}(\phi_1^0) \sin(\beta) + \text{Im}(\phi_2^0) \cos(\beta)] \quad (2.40)$$

$$H^0 = \sqrt{2} [(\text{Re}(\phi_1^0) - v_1) \cos(\alpha) + (\text{Re}(\phi_2^0) - v_2) \sin(\alpha)] \quad (2.41)$$

$$h^0 = \sqrt{2} [-(\text{Re}(\phi_1^0) - v_1) \sin(\alpha) + (\text{Re}(\phi_2^0) - v_2) \cos(\alpha)]$$

with masses

$$m_{H^\pm}^2 = \lambda_4(v_1^2 + v_2^2) \quad m_{A^0}^2 = \lambda_6(v_1^2 + v_2^2)$$

$$m_{H^0, h^0}^2 = \frac{1}{2} \left[M_{11} + M_{22} \pm \sqrt{(M_{11} - M_{22})^2 + 4M_{12}^2} \right]$$

where α , β and M_{ij} are defined as

$$\tan(\beta) = \frac{v_2}{v_1}$$

$$\sin(2\alpha) = \frac{2M_{12}}{\sqrt{(M_{11} - M_{22})^2 + 4M_{12}^2}}$$

$$\cos(2\alpha) = \frac{M_{11} - M_{22}}{\sqrt{(M_{11} - M_{22})^2 + 4M_{12}^2}}$$

$$M_{11} \equiv 4v_1^2(\lambda_1 + \lambda_3) + v_2^2\lambda_5$$

$$M_{22} \equiv 4v_2^2(\lambda_2 + \lambda_3) + v_1^2\lambda_5$$

$$M_{12} \equiv (4\lambda_3 + \lambda_5)v_1v_2$$

The mass of the H^0 boson is by construction greater than of h^0 . The quantity $v_1^2 + v_2^2$ is fixed by the W mass through $v_1^2 + v_2^2 = \frac{2m_W}{g}$, but the λ_i 's are arbitrary. Thus, the model has six free parameters, namely $\tan(\beta)$, α , and the physical masses of the Higgs bosons m_{H^\pm} , m_{A^0} , m_{H^0} and m_{h^0} .

2.2.3 Phenomenology

The couplings of the Higgs boson to gauge bosons can be expressed in terms of the SM Higgs coupling rescaled by factors depending on α and β . In

particular the relation between the Higgs coupling to di-bosons are

$$\frac{h^0 VV}{h_{sm} VV} = \sin(\beta - \alpha) \quad \frac{g_{H^0 VV}}{g_{h_{sm} VV}} = \cos(\beta - \alpha) \quad (2.42)$$

where V stands for W^\pm or Z and h_{sm} is the Higgs boson obtained in the Minimal Standard Model.

The coupling of Higgs boson to fermions depends on how the condition to avoid FCNC's mentioned in Section 2.2.1 is met. Two main models commonly used are named Type I and Type II. In a Type I 2HDM the first Higgs doublet ϕ_1 couples only to gauge bosons while the second one ϕ_2 couples only to quarks and leptons. The Type II model couples down-type fermions to ϕ_1 and up-type fermions to ϕ_2 exclusively.

This dissertation focus on Type II 2HDM models, since this is the model of the Higgs sector necessary in Supersymmetry as will be shown in the next section. The coupling of the 2HDM Higgs bosons to fermions, expressed in terms of the SM Higgs boson coupling to fermions, are as follows :

$$\begin{aligned} \frac{H^0 u\bar{u}}{h_{sm} u\bar{u}} &: \frac{\sin(\alpha)}{\sin(\beta)} & \frac{H^0 d\bar{d}}{h_{sm} d\bar{d}} &: \frac{\cos(\alpha)}{\cos(\beta)} \\ \frac{h^0 u\bar{u}}{h_{sm} u\bar{u}} &: \frac{\cos(\alpha)}{\sin(\beta)} & \frac{h^0 d\bar{d}}{h_{sm} d\bar{d}} &: \frac{-\sin(\alpha)}{\cos(\beta)} \\ \frac{A^0 u\bar{u}}{h_{sm} u\bar{u}} &: \cot(\beta) & \frac{A^0 d\bar{d}}{h_{sm} d\bar{d}} &: \tan(\beta) \end{aligned} \quad (2.43)$$

For a particular decay it is clear from equations 2.43 that α regulates the relative strength of the coupling between h^0 and H^0 via

$$\tan(\alpha) = \frac{g_{h^0 d\bar{d}}}{g_{H^0 d\bar{d}}} = \frac{g_{H^0 u\bar{u}}}{g_{h^0 u\bar{u}}} \quad (2.44)$$

The parameter β in the other hand regulates the relative strength between couplings to up and down fermions

$$\tan(\beta) \propto \frac{g_{h^0 d\bar{d}}}{\tan(\alpha) g_{h^0 u\bar{u}}}, \propto \frac{\tan(\alpha) g_{H^0 d\bar{d}}}{g_{H^0 u\bar{u}}}, \propto \sqrt{\frac{g_{A^0 d\bar{d}}}{g_{A^0 u\bar{u}}}} \quad (2.45)$$

Section 2.1.4 showed that the SM Higgs decays dominantly to the heaviest kinematically-available⁵ particles, as the coupling is proportional to their masses. In particular for $m_{h_{sm}} < 135 \text{ GeV}/c^2$ the decays $h_{sm} \rightarrow b\bar{b}, \tau\bar{\tau}$ are dominant.

In the 2HDM scenario these statements cannot be directly applied to the h^0 and H^0 decays, as one may naively expect. The α and β are free parameters and suitable choices of them may result in severe suppression of either the h^0 or H^0 decays to $b\bar{b}$ and $\tau\bar{\tau}$, balanced by an enhancement of the branching ratios into up-like fermions.

The charged Higgs boson couples to the up and down components of the fermionic doublet. This coupling is

$$g_{H^{\pm}u\bar{d}} = \frac{g}{2\sqrt{2}m_w} [m_u \cot(\beta)(1 + \gamma^5) + m_d \tan(\beta)(1 - \gamma^5)] \quad (2.46)$$

In terms of the third generation quarks, it is important to note that the bottom-mass (top-mass) term is enhanced for large (small) values $\tan(\beta)$. In these extreme cases of large and small values of $\tan(\beta)$ the coupling is proportional to the mass of the bottom and top quark respectively. When including corrections at tree level it is critical to correctly evaluate the masses at the energy scale of the corrections. Corrections of this type will be carried out in the context of Supersymmetry in the next section.

To finish the discussion of the Higgs sector it should be noted that 2HDM also provides vertices with two Higgs bosons. These vertices have both neutral and charged Higgs bosons, are taken from [11] and reproduced here

⁵Including also the decay to virtual particles whose on-shell masses may exceed that of the Higgs. The decay $h_{sm} \rightarrow W^*W$ is an example if the mass of the Higgs is below twice the mass of the W, see Figure 2.1.

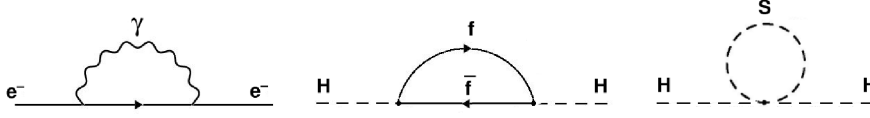


Figure 2.2: **Left:** One-loop contributions to the electron mass in QED. **Center:** Fermionic one-loop contribution to the Higgs mass. **Right:** Scalar one-loop contribution to the Higgs mass.

for reference:

$$\begin{aligned}
 g_{h^0 A^0 Z} &= \frac{g}{2\cos(\theta_W)} \cos(\beta - \alpha) & g_{H+W-h^0} &= \frac{g}{2} \cos(\beta - \alpha) \\
 g_{H^0 A^0 Z} &= \frac{g}{2\cos(\theta_W)} \sin(\beta - \alpha) & g_{H+W-H^0} &= \frac{g}{2} \sin(\beta - \alpha)
 \end{aligned}$$

The Feynman rules associated with a Type II 2HDM are also found in [11].

2.3 Supersymmetry and the Minimal Supersymmetric Standard Model

2.3.1 The hierarchy problem

The Higgs mechanism provides a successful model by which electroweak symmetry is broken allowing the gauge bosons and fermions of the SM to obtain mass. It is also through the Higgs that the most notable inelegance of the SM appears. The inelegance is called the ‘‘Hierarchy or naturalness problem’’ and is evident when considering radiative corrections to the Higgs mass.

The topic is introduced by analyzing the electron’s one-loop self energy diagram shown in Figure 2.2(left). The energy contribution to the electron

mass according to the QED theory is [26] :

$$m_e = m_e^0 \left[1 + \frac{3\alpha}{2\pi} \ln \left(\frac{\Lambda}{m_e^0} \right) \right] \quad (2.47)$$

where m_e^0 is the bare mass of the electron and Λ is the cutoff value of the integral that runs over the photon momenta. This integral is logarithmically divergent and passes its behavior to the correction of the electron mass.

The divergences in a theory are managed by what is called the renormalization process. This process is based on the assumption that SM parameters such as masses and coupling constants are, in fact, themselves divergent. What is really measured are not the bare parameters, but rather effective parameters that include bare parameters and their corrections according to the theory. In a sense, the renormalization process arranges the divergences in the coupling and the bare masses to exactly cancel the high-momentum infinities.

It is interesting to note that if taking Λ to be the entire mass of the universe ($\sim 10^{79}$ GeV) the shift in the electron mass is only $m_e \simeq 1.7m_e^0$. This shows that the normalization process of absorbing divergences into renormalized parameters is reasonable, at least when dealing with logarithmic divergences.

Let's consider now the fermion loop in the Higgs boson self-energy as shown in Figure 2.2(center). The correction to the mass of the Higgs boson due to this loop is [32]:

$$\delta m_h^2 = \frac{|\lambda_f|^2}{16\pi^2} \left[-2\Lambda^2 + 6m_f^2 \ln \left(\frac{\Lambda}{m_f} \right) + \dots \right] \quad (2.48)$$

In this case the correction is quadratic on the cut-off variable. Here, a conservative cut-off value such as the Planck scale (10^{19} GeV) would result in a mass correction 28 orders of magnitude larger than the expected physical mass of the Higgs of about $100 \text{ GeV}/c^2$. One may argue that this correction can be re-normalized into the bare mass of the Higgs boson, but this

still requires an enormous bare mass that gets canceled to one part in 10^{14} with the large corrections. Such a “fine-tuned” cancellation does not seem natural. This unattractive feature of the SM is known as the “gauge Hierarchy problem” and is common to all theories containing fundamental scalar particles [33] such as the minimal SM and the 2HDM.

2.3.2 Introduction to MSSM

It has been shown in the previous sections the key role that symmetry plays in the formal explanation of particles and fields. Following the same reasoning it is interesting to wonder whether the cancellations in the Higgs mass are the result of an underlying symmetry.

The cancellations in the Higgs physical mass due to a fermion loop is negative and quadratic in the cut-off value Λ as shown in Equation 2.48. If another fundamental scalar particle (S) were to exist the Higgs mass correction obtained from the diagram in Figure 2.2(right) would result in :

$$\delta m_h^2 = \frac{\lambda_S}{16\pi^2} \left[\Lambda^2 - 2m_S^2 \ln \left(\frac{\Lambda}{m_S} \right) + \dots \right] \quad (2.49)$$

Where the corrections are still quadratic but of opposite in sign of that in the fermion case. This is just a consequence of the Fermi/Bose statistics.

This suggests that a possible solution to the Hierarchy problem can be obtained if a symmetry relating fermions and bosons is considered. If each fermion in the SM is accompanied by two fundamental scalar particles such that the coupling to the Higgs field satisfies $|\lambda_S| = |\lambda_f|^2$ then the Λ^2 contributions in equations 2.48 and 2.49 would cancel. In fact, the cancellation occurs to every order in an unavoidable way once it is assumed that a symmetry relating fermions to bosons exists [32]. This kind of symmetry is called “Supersymmetry” and is generated by the Supersymmetry spinor operator

Q , and its hermitian conjugate Q^\dagger ⁶:

$$Q|boson \rangle = |Fermion \rangle \quad (2.50)$$

The single-particle states are put into irreducible representations called supermultiplets. Each supermultiplet contains fermion and boson states, which are commonly referred to as superpartners of each other. Because the Supersymmetry operator Q (and Q^\dagger) commute with the generators of the gauge transformation, the particles in the same supermultiplet have the same electric charge, weak isospin and color degree of freedom. Each supermultiplet contains the same number of fermionic and bosonic degrees of freedom.

Encompassed in Supersymmetry are many theories with different numbers of copies of the Q, Q^\dagger operators. The Minimal Supersymmetric Standard Model (MSSM) is that with a single set of Supersymmetry operators. Beyond the additional supersymmetric partners the MSSM has no additional fields.

In MSSM the Standard Model fermions and their spin-0 superpartners are arranged in chiral supermultiplets, whereas the Standard Model gauge bosons and their spin-1/2 superpartners in gauge supermultiplets. In general the supersymmetric partners are commonly denoted by putting tilde over their SM partner letter. Each supermultiplet contains a complex scalar ϕ_i and a left-handed Weyl fermion ψ_i . The names of the supersymmetric scalar partners is that of the SM fermionic partner with the prefix "s". The name of the supersymmetric fermionic partner is that of the SM bosonic partner with the suffix "ino". For example the supersymmetric scalar partner of the electron (e) is the selectron (\tilde{e}), and that of the neutrino (ν) is the sneutrino ($\tilde{\nu}$). The superpartner of the gluon (g) is the gluino (\tilde{g}), and that of the W

⁶The charge operator Q is denoted with the same letter, but no reference to it is done in the rest of the dissertation to avoid confusion.

boson, the Wino (\tilde{W}). When explicitly denoting the handedness, the partner of the e_R is the \tilde{e}_R , where it is clear that the subindex “R” denotes the handedness of its superpartner. The chiral and gauge supermultiplets with all the Particles of the MSSM are shown in Table 2.3.

Chiral supermultiplets			
superfield	spin-0 component	spin-1/2 component	$SU(3)_C, SU(2)_L, U(1)_Y$ representation
\hat{Q}	$(\tilde{u}_L, \tilde{d}_L)$	(u_L, d_L)	(3,2,1/6)
\hat{U}	\tilde{u}_R^*	u_R^\dagger	(3,1,-2/3)
\hat{D}	\tilde{d}_R^*	d_R^\dagger	(3,1,1/3)
\hat{L}	$(\tilde{\nu}, \tilde{e}_L)$	(ν, e_L)	(1,2,-1/2)
\hat{E}	\tilde{e}_R^*	e_R^\dagger	(1,1,1)
\hat{H}_u	(H_u^+, H_u^0)	$(\tilde{H}_u^+, \tilde{H}_u^0)$	(1,2,+1/2)
\hat{H}_d	(H_d^0, H_d^-)	$(\tilde{H}_d^0, \tilde{H}_d^-)$	(1,2,-1/2)
Gauge supermultiplets			
	spin-0 component	spin-1/2 component	$SU(3)_C, SU(2)_L, U(1)_Y$ representation
	\tilde{g}	g	(8,1,0)
	$\tilde{W}^\pm, \tilde{W}^0$	W^\pm, W^0	(1,3,0)
	\tilde{B}^0	B^0	(1,1,0)

Table 2.3: Supermultiplets of the MSSM. The multiplets of the second and third generation have been omitted for simplicity. The normalization in the hypercharge is such that $Q_{em} = T_3 + Y$, as opposed to the one used in Equation 2.10.

It is important to note that in the MSSM a two Higgs doublet model is used. This is necessary to achieve a theory free of triangle gauge anomalies. A necessary condition to this is $Tr[Y^3] = Tr[T_3^2 Y] = 0$, and it is clear that a single Higgs doublet with definite hypercharge will not satisfy it; it

is necessary to introduce another with opposite hypercharge. Furthermore Supersymmetry requires the H_u (H_d) Higgs doublet to couple to up-type (down-type) fermions exclusively. Therefore the MSSM contains a Type II 2HDM Higgs sector as mentioned previously.

2.3.3 Lagrangian formulation of the MSSM

The most general set of renormalizable non-gauge interactions for the Supersymmetric fields is determined by a single analytic function of the complex scalar fields called the superpotential and denoted by the letter W . The Lagrangian of the interaction can be expressed as a function of W in the form [32]:

$$\mathcal{L}_{int} = -\frac{1}{2}W^{ij}\psi_j\psi_j + W^i F_i + c.c. \quad (2.51)$$

Where the index “i” and “j” run over the supermultiplets and ψ_i represent the Weyl fermion of the “ith” supermultiplet. The F ’s represent auxiliary fields and together with W^{ij} and W^i are quantities that are related to the superpotential W by

$$F_i = -W_i^* \quad F^{*i} = -W^i \quad W^i = \frac{\partial W}{\partial \phi_i} \quad W^{ij} = \frac{\partial^2 W}{\partial \phi_i \partial \phi_j} \quad (2.52)$$

The superpotential obtained after requiring invariance has the general form

$$W = \frac{1}{2}M^{ij}\phi^i\phi^j + \frac{1}{6}y^{ijk}\phi_i\phi_j\phi_k \quad (2.53)$$

The term M^{ij} represents the symmetric mass matrix of the fermion fields and y^{ijk} is the Yukawa coupling of a supermultiplet’s scalar ϕ_k and two fermions $\psi_i\psi_j$, which is totally symmetric under interchange of i,j,k. In general the form of the superpotential is restricted by the supermultiplet content of the theory. In particular the superpotential of the MSSM is given by :

$$W_{MSSM} = \epsilon_{ij} \left(\hat{U}\mathbf{y}_u\hat{Q}^i\hat{H}_u^j - \hat{D}\mathbf{y}_d\hat{Q}^i\hat{H}_d^j - \hat{E}\mathbf{y}_e\hat{L}^i\hat{H}_d^j + \mu\hat{H}_u^i\hat{H}_d^j \right) \quad (2.54)$$

where the indexes i, j run over the $SU(2)$ representation, $\epsilon_{12} = -\epsilon_{21} = 1$ and $e_{11} = e_{22} = 0$. The dimensionless Yukawa coupling parameters y_u , y_d , and y_e are 3×3 matrices in family space. The variable μ is known as the Higgs mass parameter.

Another reason for the introduction of the second Higgs doublet is revealed when considering the masses of the up-type fermions. In the minimal SM the masses for the up-type are generated by means of the conjugate of the Higgs field. Supersymmetry requires that no conjugate scalar field appear in the superpotential, and the only way to give masses to the up-type fermions is through the introduction of a second doublet.

With the choice of superpotential written in Equation 2.54 the Lagrangian of Equation 2.51 is unbroken. Supersymmetry is clearly a broken symmetry because if the superpartner masses were degenerate with the SM ones they would have been already discovered.

The breaking of Supersymmetry must be achieved in such a way that it still provides a solution of the hierarchy problem. In particular is necessary that the relation $|\lambda_S| = |\lambda_f|^2$ continue to hold, otherwise quadratically divergent corrections will arise with the following form :

$$\delta m_h^2 = \frac{1}{8\pi^2}(\lambda_S - |\lambda_f|^2)\Lambda_{UV} \quad (2.55)$$

The breaking of Supersymmetry is then required to be “soft”, and is achieved by introducing the term

$$\begin{aligned} \mathcal{L}_{soft}^{MSSM} &= -\frac{1}{2} \left(M_1 \tilde{B}\tilde{B} + M_2 \tilde{W}\tilde{W} + M_3 \tilde{g}\tilde{g} \right) + c.c. \\ &- \left(\tilde{U} \mathbf{a}_u \tilde{Q} H_u - \tilde{D} \mathbf{a}_d \tilde{Q} H_d - \tilde{E} \mathbf{a}_e \tilde{L} H_d \right) + c.c. \\ &- \tilde{Q}^\dagger \mathbf{m}_Q^2 \tilde{Q} - \tilde{L}^\dagger \mathbf{m}_L^2 \tilde{L} - \tilde{U}^\dagger \mathbf{m}_U^2 \tilde{U} - \tilde{D}^\dagger \mathbf{m}_D^2 \tilde{D} - \tilde{E}^\dagger \mathbf{m}_E^2 \tilde{E} \\ &- m_{H_u}^2 H_u^* H_u - m_{H_d}^2 H_d^* H_d - (b H_u H_d + c.c.) \end{aligned} \quad (2.56)$$

where M_1 , M_2 and M_3 represent the bino, wino and gluino mass terms. The second line in Equation 2.56 contains the trilinear couplings \mathbf{a}_u , \mathbf{a}_d and

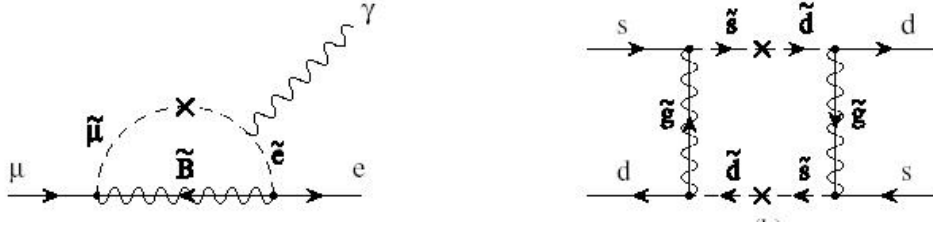


Figure 2.3: **Left:** MSSM contribution from slepton violation to the $\mu \rightarrow e\gamma$ decay. **Right:** Diagram contributing to the kaon sector.

\mathbf{a}_e , each a complex 3×3 matrix in family space. The third line contains the squark and slepton mass terms \mathbf{m}_Q^2 , \mathbf{m}_L^2 , \mathbf{m}_U^2 , \mathbf{m}_D^2 , and \mathbf{m}_e^2 , hermitian 3×3 matrices in family space. The last line represents the Supersymmetry-breaking contributions to the Higgs potential.

The most general MSSM that follows from Equation 2.56 contains 105 free parameters that determine masses, mixing angles and phases of the SUSY particles [48]. This large parameter space is already strongly restricted by experimental results. The $\mu \rightarrow e\gamma$ decay, which can happen via lepton flavor violation in the slepton sector as depicted in Figure 2.3(left) is severely constrained by experiment [34]. Similarly, contributions from Figure 2.3(right) affect the mixing $K \leftrightarrow \bar{K}^0$ [35][36]. A detailed list of relevant experiments and their consequences over the MSSM can be found in [32] and [19].

All these experimental constraints on FCNC and CP-violating effects can be accommodated by assuming that:

- The matrices \mathbf{m}_Q^2 , \mathbf{m}_L^2 , \mathbf{m}_U^2 , \mathbf{m}_D^2 , and \mathbf{m}_e^2 are “flavor-blind”. Consequently they are all proportional to the identity matrix. ($\mathbf{m}_Q^2 = m_Q^2 \mathbf{1}$, $\mathbf{m}_L^2 = m_L^2 \mathbf{1}$, etc.)
- The matrices \mathbf{a}_u , \mathbf{a}_d and \mathbf{a}_e , are proportional to the corresponding Yukawa coupling ($\mathbf{a}_u A_{u0} \mathbf{y}_u$, $\mathbf{a}_d A_{d0} \mathbf{y}_d$ and $\mathbf{a}_e A_{e0} \mathbf{y}_e$.)

- The complex components of M_1 , M_2 , M_3 , A_{u0} , A_{d0} , and A_{e0} are all set to zero. This requirement explicitly disallow any CP-violating effects coming from the supersymmetric spectrum of the theory. The only CP-violating phase comes from the CKM matrix.

With these simplifying assumptions, the number of variables needed to fully calculate the MSSM mass spectrum, and particle branching ratios is reduced to 14. These 14 real parameters can be chosen to be

$$\begin{aligned} &M_1, M_2, M_3, A_u, A_d, A_e \\ &m_Q, m_L, m_U, m_D, m_E \\ &\tan(b), m_{H^\pm}, \mu \end{aligned}$$

where the parameters m_{H_u} , m_{H_d} , and b in Equation 2.56 were replaced with the more phenomenologically familiar $\tan(\beta)$, m_{H^\pm} and μ .

2.3.4 MSSM Higgs mass eigenstates

The MSSM superpotential allows one to extract relationships between the general parameters of a Type II 2HDM derived in section 2.2.2. In particular, if considering only the fourth term in Equation 2.54, and adding the soft Supersymmetry-breaking potential of Equation 2.56, the following tree-level relations expressed in terms of the two independent variables m_A and $\tan(\beta)$ are obtained:

$$H^\pm = m_A^2 + m_W^2 \quad (2.57)$$

$$m_{H^0, h^0}^2 = \frac{1}{2} \left[m_A^2 + m_Z^2 \pm \sqrt{(m_A^2 + m_Z^2)^2 - 4m_Z^2 m_A^2 \cos^2(2\beta)} \right]$$

$$\frac{\tan(2\alpha)}{\tan(2\beta)} = \left(\frac{m_A^2 + m_Z^2}{m_A^2 - m_Z^2} \right) = \left(\frac{m_{H^0}^2 + m_h^2}{m_A^2 - m_Z^2} \right) \quad (2.58)$$

$$(2.59)$$

While the masses of A , H^0 and H^\pm could be arbitrarily large, Supersymmetry predicts the mass of the h^0 to be bounded by $m_{h^0} < |\cos(2\beta)|m_Z <$

m_Z . This striking prediction guarantees the mass of the lightest CP-even boson to be kinematically accessible at LEP2 !. Unfortunately, quantum corrections significantly weaken that limit.

The radiative corrections to the Higgs squared-masses have been computed using a variety of techniques, each with its own set of simplifying assumptions and renormalization schemes. Among them are calculations of the effective potential to one loop [40] [41], and two loops [42] [43]. Complete one-loop diagrammatic computations of Higgs masses are shown in [44] [45], and partial two-loop results in [46] [47].

The computation of the radiative corrections resulted in the strong modification of the upper bound of the light CP-even Higgs mass, as was first noted in [40]. Depending on the MSSM parameters the bound can be increased up to $135 \text{ GeV}/c^2$, to be compared with the Z mass bound obtained from tree-level calculations. In general the dominant effects arise from third generation quarks and squarks, as it will be seen after considering the third-generation squark mass eigenstates.

The mass eigenstates of squarks are determined by diagonalizing the mass squared matrix whose general expression is given in page 92 of reference [19]. Specifying the matrix for the third generation up-type squarks, in the $(\tilde{t}_L, \tilde{t}_R)$ basis, yields :

$$\begin{pmatrix} M_Q^2 + m_t^2 + \cos(2\beta) \left(\frac{1}{2} - \frac{2}{3} \sin^2(\theta_W) \right) m_z^2 & m_t(A_t - \mu \cot(\beta)) \\ m_t(A_t - \mu \cot(\beta)) & M_U^2 + m_t^2 - \frac{2}{3} \cos(2\beta) \sin^2(\theta_W) m_z^2 \end{pmatrix} \quad (2.60)$$

where A_t is the trilinear Higgs-stop coupling. The mixing angle that diagonalizes the mass matrix is denoted by $\theta_{\tilde{t}}$ and is defined as

$$\sin(\theta_{\tilde{t}}) = \frac{2m_t X_t}{m_{\tilde{t}_2}^2 - m_{\tilde{t}_1}^2} \quad X_t \equiv A_t - \mu \cot(\beta) \quad (2.61)$$

The masses of the stop quarks \tilde{t}_1 and \tilde{t}_2 are then calculated from M_Q, M_U, A_t, μ , and $\tan(\beta)$. It is also common to use the set M_Q, M_U, X_t, μ , and $\tan(\beta)$ where

the variable A_t is replaced by $X_t = A_t - \mu \cot(\beta)$. The mixing of the top-squark scalars is governed by θ_t , or equivalently X_t .

Finally, the radiative corrections to the lightest neutral Higgs are derived from the effective potential in the limit $m_A \gg m_Z$ and yield:

$$m_h^2 = m_z^2 \cos^2(2\beta) + \frac{3\alpha m_t^4}{4\pi \sin^2(\theta_W) m_W^2} \left[\ln \left(\frac{m_{\tilde{t}_1} m_{\tilde{t}_2}}{m_t^2} \right) + \left(\frac{m_{\tilde{t}_2}^2 - m_{\tilde{t}_1}^2}{4m_t^2} \sin^2(2\theta_{\tilde{t}}) \right)^2 \left(2 - \frac{m_{\tilde{t}_2}^2 + m_{\tilde{t}_1}^2}{m_{\tilde{t}_2}^2 + m_{\tilde{t}_1}^2} \ln \left(\frac{m_{\tilde{t}_2}^2}{m_{\tilde{t}_1}^2} \right) \right) + \frac{m_{\tilde{t}_2}^2 - m_{\tilde{t}_1}^2}{2m_t^2} \sin^2(2\theta_t) \ln \left(\frac{m_{\tilde{t}_2}^2}{m_{\tilde{t}_1}^2} \right) \right]$$

where the dependence in the top mass, the stops masses and the stop mixing is explicit.

2.3.5 Phenomenology

This dissertation considers charged Higgs production as a decay product of $t\bar{t}$ events. The associated phenomenology is discussed in this section in the context of the MSSM, with focus on the predictions of top and Higgs branching ratios.

The $t \rightarrow H^+ b$ branching ratio

With the inclusion of a two Higgs doublet came a physical charged Higgs boson. The phenomenology of the SM particles must then be modified to include the contributions that such a boson would generate. In particular the possibility of the top quark to decay to a charged Higgs and a b quark must be properly computed.

The width of the decay $t \rightarrow H^+ b$ was calculated including QCD corrections in [49]. An improved QCD correction was later developed in [50] where corrections involving the non-SM particle content of the SUSY spectrum (SUSY-Electroweak and SUSY-QCD) were also considered. These loop

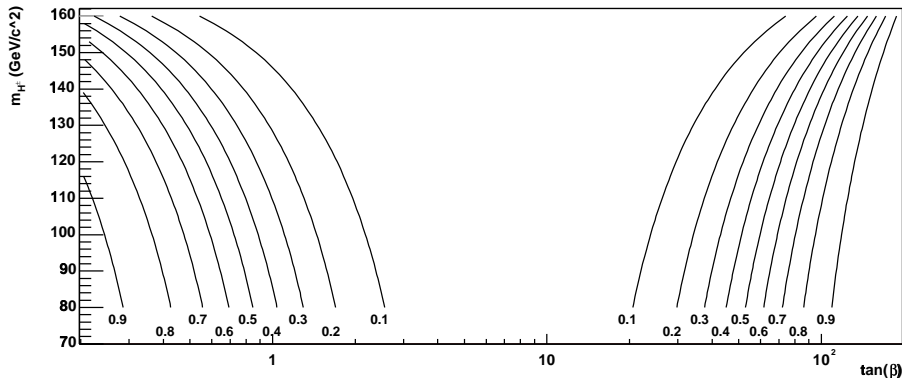


Figure 2.4: Contours of constant $\text{BR}(t \rightarrow H^+ b)$ in the $(m_{H^\pm}, \tan(\beta))$ plane.

corrections were developed in the large $\tan(\beta)$ approximation where they are expected to be significant. The search for charged Higgs, however, requires formulae valid to all values of $\tan(\beta)$. This improved computation was performed by M. Carena and R. Eusebi in [51] and described in Appendix B, resulting in an improved QCD, SUSY-Electroweak and SUSY-QCD corrections valid to all values of $\tan(\beta)$. These formulas are used to compute the $t \rightarrow H^+ b$ branching ratio as a function of MSSM parameters.

The typical behavior of $\text{BR}(t \rightarrow H^+ b)$ is shown in Figure 2.4. The figure shows contours of constant $\text{BR}(t \rightarrow H^+ b)$ in the $(m_{H^\pm}, \tan(\beta))$ plane. For a given mass of the charged Higgs, and as one moves from low to high values of $\tan(\beta)$, the $\text{BR}(t \rightarrow H^+ b)$ first decreases reaching a value very close to zero at $\tan(\beta) \simeq 7$, and then increases again as the large $\tan(\beta)$ region is reached. For a given $\tan(\beta)$ the $\text{BR}(t \rightarrow H^+ b)$ decreases the larger the mass of the charged Higgs. Thus, the regions of low and high values of $\tan(\beta)$, at low charged Higgs masses are characterized by a large $\text{BR}(t \rightarrow H^+ b)$, and are therefore the regions of most sensitivity for this analysis.

It is important to note the dependence of $\text{BR}(t \rightarrow H^+ b)$ on the MSSM parameters. One of the parameters that modifies this quantity the most

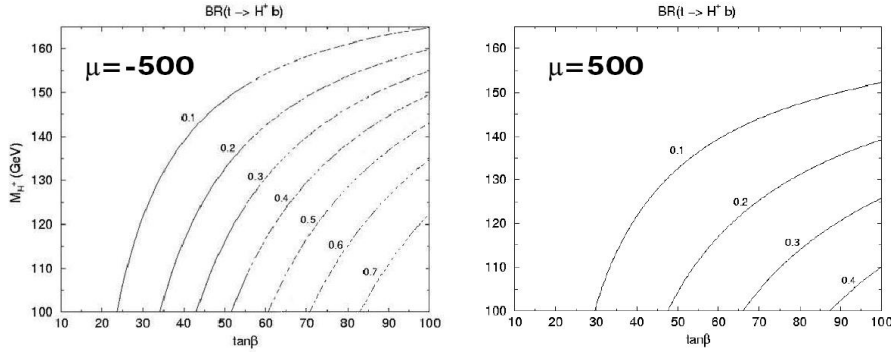


Figure 2.5: Contours of constant $\text{BR}(t \rightarrow H^+ b)$ in the $(m_{H^\pm}, \tan(\beta))$ plane, in the large $\tan(\beta)$ region for $\mu = -500 \text{ GeV}/c^2$ (left) and $\mu = 500 \text{ GeV}/c^2$ (right).

is μ , the Higgs mass parameter. This parameter directly modifies the top and bottom Yukawa couplings, and the $\text{BR}(t \rightarrow H^+ b)$ is proportional to the bottom coupling to the second power. A clear example of this is shown in Figure 2.5, where the large $\tan(\beta)$ region is shown for two sets of parameters only differing in the value of μ . Larger values of μ suppress the $\text{BR}(t \rightarrow H^+ b)$ while lower values enhance it. It is worth mentioning that the custom code used for the calculation of the $\text{BR}(t \rightarrow H^+ b)$ branching ratio contains the same corrections as CPsuperH, the program used to calculate the charged Higgs branching ratios described below.

The H^+ branching ratios

The charged Higgs branching ratios are computed using the program CPsuperH [18]. This is a recently developed computational package that calculates the mass spectrum and decay widths of the neutral and charged Higgs bosons in the MSSM with explicit CP violation. The machinery of CP violation is turned off in this dissertation, assuming that there are no new sources of CP violation in the MSSM sector.

The typical behavior of charged Higgs branching ratios are shown in

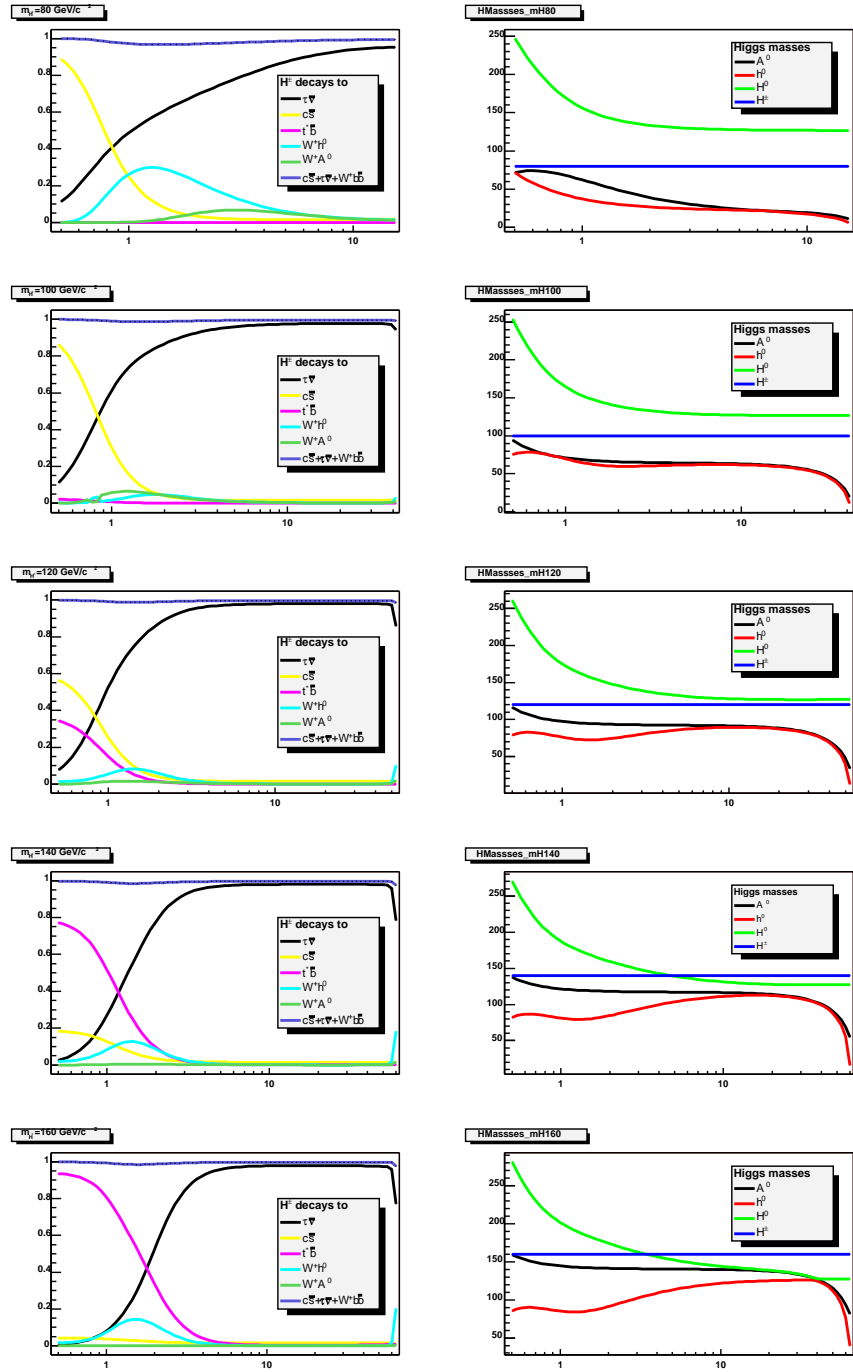


Figure 2.6: Branching ratios of charged Higgs (left column) and masses of the physical bosons (right column). The rows represent different masses of the charged Higgs.

Figure 2.6. The left column shows the branching ratios of the charged Higgs as a function of $\tan(\beta)$ for different masses of the charged Higgs. The plots show the branching ratio of charged Higgs decays to $c\bar{s}$, $\bar{\tau}\nu$, $t^*\bar{b}$, W^+h^0 , and W^+A^0 , where the last three result in $Wb\bar{b}$ final states with different kinematic topologies. The plots span the region in $\tan(\beta)$ in which CPsuperH can self-consistently calculate the mass eigenstates of the theory. Values of $\tan(\beta)$ in which CPsuperH report inconsistencies in the calculation of the Higgs sector are considered theoretically inaccessible.

At large values of $\tan(\beta)$ the decay $H^+ \rightarrow \bar{\tau}\nu$ dominates, regardless of the charged Higgs mass. At values of $\tan(\beta)$ around 1.0 all the decays have significant contributions. In the region of low values of $\tan(\beta)$ the decays $H^+ \rightarrow c\bar{s}$ and $H^+ \rightarrow t^*\bar{b}$ compete with each other, the latter being the dominant when the mass of the charged Higgs approaches that of the top.

The left column shows the sum of the charged Higgs branching ratios to $c\bar{s}$, $\bar{\tau}\nu$, and $Wb\bar{b}$ final states as a function of $\tan(\beta)$. The sum always exceeds 0.96 at any point in $\tan(\beta)$, showing that to the first order the approximation that the charged Higgs decays to only these particles is valid. The right column shows the masses of the physical boson as a function of $\tan(\beta)$.

The top and Higgs branching ratios : summary

The main features of the top and charged Higgs branching ratios are shown in Figure 2.7 as a function of $\tan(\beta)$ for different charged Higgs masses. The $t \rightarrow H^+b$ branching ratio is shown with a dashed line. At low and high values of $\tan(\beta)$ the top decay to charged Higgs is enhanced, while at values of $\tan(\beta)$ around 7 the ratio is almost zero, and the SM decay $t \rightarrow W^+b$ is recovered. For larger values of the charged Higgs mass the $t \rightarrow H^+b$ gets

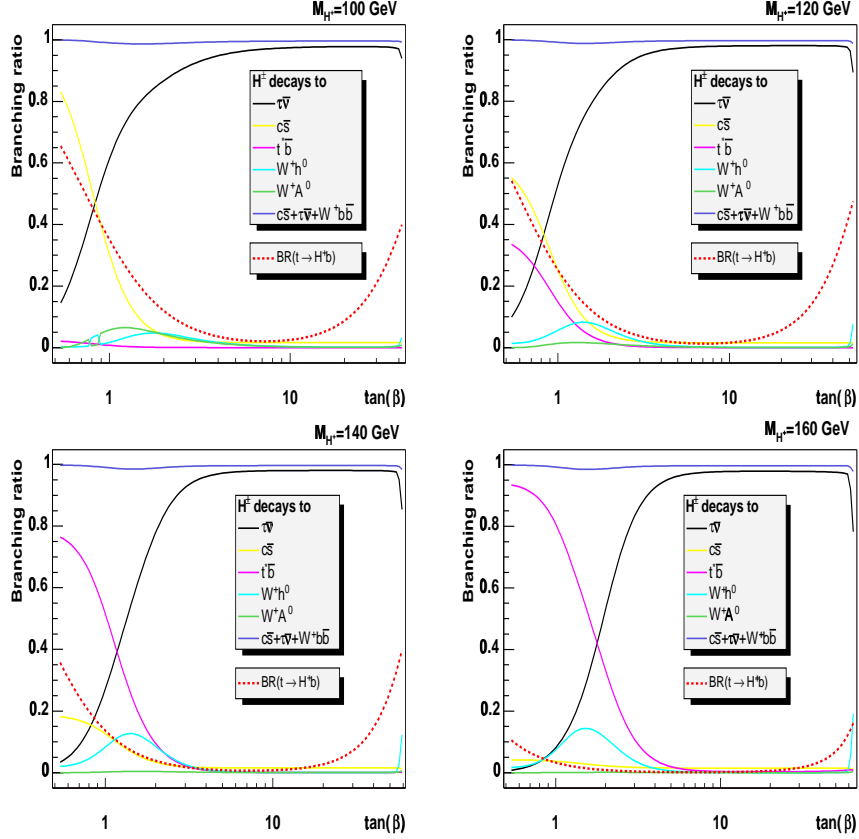


Figure 2.7: Summary of the top quark and charged Higgs branching ratios. The branching ratios are shown for benchmark 1 as a function of $\tan(\beta)$ and for Higgs masses of 100 GeV/c², 120 GeV/c², 140 GeV/c², and 160 GeV/c².

closer to zero for larger regions in $\tan(\beta)$.

The charged Higgs decays mostly to $c\bar{s}$ or $t\bar{b}$ at low values of $\tan(\beta)$ depending on the mass of the charged Higgs. The decays to W^+h^0 and W^+A^0 have their most sizeable contribution at values of $\tan(\beta)$ around one, but in this region all the decays contribute significantly. At large values of $\tan(\beta)$ the charged Higgs decays mostly to $\bar{\tau}\nu$.

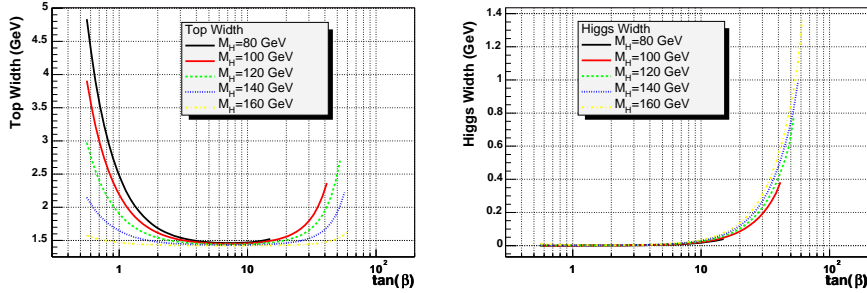


Figure 2.8: Widths of the top (left) and Higgs (right) as a function of $\tan(\beta)$ for different charged Higgs masses. The widths are calculated using the formulae and tools described above. The input parameters for CPsuperH are given by what is defined as “Benchmark 1” in section 2.3.6.

The top and Higgs widths

As shown above the MSSM predicts the width distribution of the top quarks and charged Higgs bosons. Figure 2.8 shows the top and charged Higgs widths as a function of $\tan(\beta)$ for different charged Higgs masses. The different lines span slightly different regions of $\tan(\beta)$ as the theoretically inaccessible region depends on the mass of the charged Higgs. In general, the higher the charged Higgs mass the larger the available $\tan(\beta)$ region. Both plots were made with a nominal mass of $m_t = 175 \text{ GeV}/c^2$. The top width shows a pronounced dependence with the mass of the charged Higgs. Although not shown in the figure, the charged Higgs width has a negligible dependence with the mass of the top in the range from $160 \text{ GeV}/c^2$ to $190 \text{ GeV}/c^2$.

2.3.6 Benchmarks for the search of charged Higgs

For the search of the lightest, CP-even, Higgs at LEP two sets of benchmark parameters were developed. These two benchmarks were named “maximal” and “minimal” mixing, referring to the top squarks mixing that maximizes

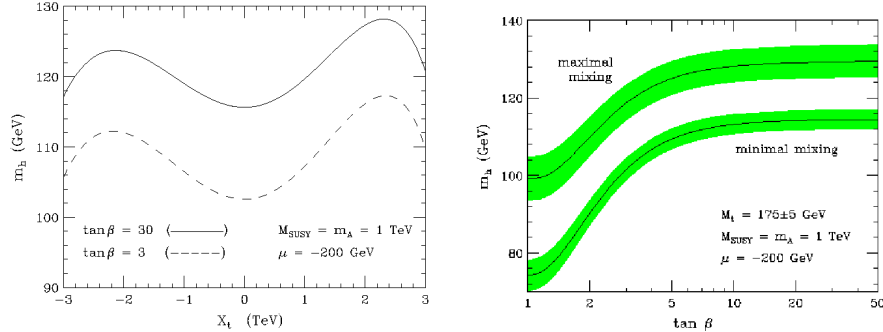


Figure 2.9: Extracted from reference [19]. The radiatively corrected mass of the lightest CP even neutral Higgs as a function of X_t (left figure) and $\tan(\beta)$ (right figure). In the right figure the central value of the shaded bands was obtained using $m_T = 175 \text{ GeV}/c^2$, while the upper (lower) edge of the bands correspond to $m_T = 180 \text{ GeV}/c^2$ ($m_T = 170 \text{ GeV}/c^2$).

and minimizes the neutral Higgs mass. The maximal and minimal benchmarks are obtained when $X_t = \sqrt{6}M_3$ and $X_t = 0$ respectively, as seen in Figure 2.9(left). The mass M_S represents the typical mass values of the particle spectrum. The mass of the lightest Higgs is shown in Figure 2.9(right) for these two benchmarks as a function of $\tan(\beta)$.

There is currently no standard benchmark specifically designed for the charged Higgs search. We will however build four specific benchmarks to specifically deal with top quarks decaying to charged Higgs, and our results will be interpreted in the context of these four benchmark. Two of these benchmarks differ only in the value of μ , the Higgs mass parameter introduced in Equation 2.54. It was shown in section 2.3.5 that the $t \rightarrow H^+b$ branching ratio is significantly affected by radiative corrections, and is especially dependent on μ . Two benchmarks are then built based on values of $\mu = -500 \text{ GeV}/c^2$ and $\mu = +500 \text{ GeV}/c^2$, where all the other parameters are of the order $M_{SUSY} = M_Q = M_U = M_D = 1000 \text{ GeV}/c^2$ and $A_t = 500 \text{ GeV}/c^2$.

It should also be noticed that the charged Higgs may decay to a neutral Higgs ($H^+ \rightarrow W^+h^0$) in certain regions of parameter space. In this situation it is interesting to combine the previous benchmarks with the minimal and maximal squark mixing sets of parameters used in the search of the light CP-even Higgs. The combination then results in 4 benchmarks :

Benchmark	μ (GeV/c ²)	X_t	Other parameters (GeV/c ²)
B1	-500	0	$M_1 = 0.498M_2; M_2 = M_3 = 1000$
B2	-500	$\sqrt{6}M_2$	$M_Q = M_U = M_D = M_E = M_L = 1000$
B3	500	0	$A_t = A_b, A_\tau = 500$
B4	500	$\sqrt{6}M_2$	

The proposed benchmarks were chosen because of their ability to increase or decrease the $t \rightarrow H^+b$ branching ratio and the mass of the lightest neutral Higgs independently, consequently increasing or decreasing the reach of this search. With this in mind it is then reasonable to expect, at some degree, that the results presented in this dissertation include or cover the real value of the parameters if the MSSM model is present in nature.

It should also be noted that this search makes no specific assumptions derived from any “organizing principle”, and it’s then based in the CP-conserving most general form of MSSM⁷

⁷The MSSM general parameter space is sometimes further reduced by invoking an “organizing principle”. Such a principle has some theoretical motivations, should comply to the current experimental limits, and constrains the MSSM’ parameter space. One of such principles is the “supergravity-inspired” MSSM. No such organizing principle is used in this dissertation.

2.4 Experimental limits to date

The search for a charged Higgs boson has been done in a large number of experiments in the past years. A brief review of these searches and their results is presented here.

2.4.1 CLEO results

The CLEO detector is located at the electron-positron collider known as CESR (Cornell Electron Storage Ring). With 2.01 fb^{-1} of data at a center of momentum energy of the $\Upsilon(4S)$ resonance, and 0.96 fb^{-1} at 60 MeV below the resonance, the CLEO collaboration has measured the $b \rightarrow s\gamma$ branching ratio [57]. The diagram of the decay is described by a penguin diagram in which a virtual W is exchanged in a loop with an up-like quark, and a photon is radiated from any of the lines as shown in Figure 2.10. The presence of a charged Higgs boson can interfere with the diagram taking the place of the W boson. If the charged Higgs belongs to a Type II 2HDM then the branching fraction of $b \rightarrow s\gamma$ is expected to increase [58]. This allows to set limits on the mass of the charged Higgs based on the measured branching ratio. The CLEO result limits the charged Higgs mass to be

$$m_{H^\pm} > \left(244 + \frac{63}{\tan(\beta)^{1.3}} \right) \text{ GeV}/c^2 \quad (2.62)$$

This limit, however, can be circumvented in Supersymmetry. If the chargino and scalar top are light their contribution can offset that of the charged Higgs [59]. In addition, higher-order calculations have shown that even in the context of the 2HDM these limits are also highly model dependent [60].

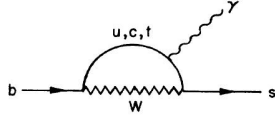


Figure 2.10: The $b \rightarrow s\gamma$ diagram

2.4.2 LEP results

The four experiments ALEPH, DELPHI, L3 and OPAL at the LEP e^+e^- accelerator searched for charged Higgs boson production via $e^+e^- \rightarrow H^+H^-$. The charged Higgs is assumed to decay only to $c\bar{s}$ and $\bar{\tau}\nu$, resulting in three possible decay modes of the H^+H^- pair. The combination of their results was carried out in [55] and expressed as a function of the branching ratio $\text{BR}(H^+ \rightarrow \bar{\tau}\nu)$ as shown in Figure 2.11(left). In the hadronic channel the sensitivity is suppressed at $m_{H^\pm} \sim m_{W^\pm}$ due to the large $e^+e^- \rightarrow W^+W^-$ background. A small regain of sensitivity at higher charged Higgs masses is signalled by the excluded “islands” above $83 \text{ GeV}/c^2$. The LEP results are then

$$m_{H^\pm} > 78.6 \text{ GeV}/c^2 \text{ at } 95\% \text{ C.L.} \quad (2.63)$$

In this dissertation these limits are reinterpreted in the context of the MSSM, and displayed in the $(m_{H^\pm}, \tan(\beta))$ plane as it is shown in Figure 2.11(right). For $m_{H^\pm} = 80 \text{ GeV}/c^2$ the MSSM predicts a significant branching fraction of the decay $H^+ \rightarrow W^+h^0$ as shown previously in Figure 2.6. This decay is not considered in the LEP results, and it is not clear how the limits would change if the decay was to be considered. Figure 2.6, however, also shows that the mass of the neutral Higgs boson is below $50 \text{ GeV}/c^2$ and the LEP results on the search for neutral Higgs have rule out values below $95 \text{ GeV}/c^2$.

In terms of the neutral Higgs boson no evidence was found at LEP [56]. As a consequence limits were set on possible MSSM parameters. The limits

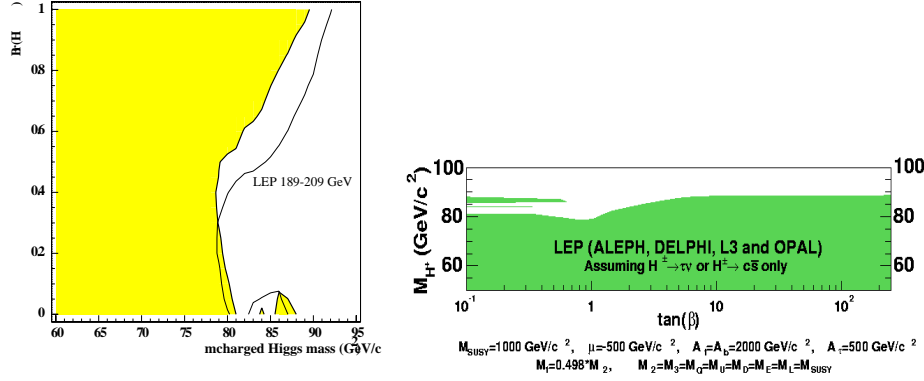


Figure 2.11: Left: The combined LEP results in the search for charged Higgs decaying to $c\bar{s}$ or $\bar{\tau}\nu$. The yellow region is the excluded region, and the line represents the sensitivity results. **Right:** The interpretation of the LEP results in the context of the MSSM. Benchmark 1 was used to translate from $BR(H^+ \rightarrow \bar{\tau}\nu)$ to $\tan(\beta)$.

on the mass of the lightest neutral Higgs depends on the MSSM parameters. For representative MSSM parameters the results are :

$$m_{H^0} > 91.0 \text{ GeV}/c^2 \quad m_{A^0} > 91.9 \text{ GeV}/c^2 \quad (2.64)$$

The LEP limits on neutral Higgs are beginning to put strong constraints against values of $\tan(\beta)$ less than a few. The low $\tan(\beta)$ region can only be consistent with low-energy SUSY if the squark masses of the third generation are in the order of TeV/c^2 , and the mixing parameters are also on that order [52]. In addition, the region of large values of $\tan(\beta)$ is consistent with the unification of the top and bottom Yukawa coupling at high energies in special models [53, 54]. These arguments encourage the interpretation of the results in a model that is valid at high $\tan(\beta)$ values, such as the tauonic Higgs model in which the charged Higgs decays exclusively to $\bar{\tau}\nu$.

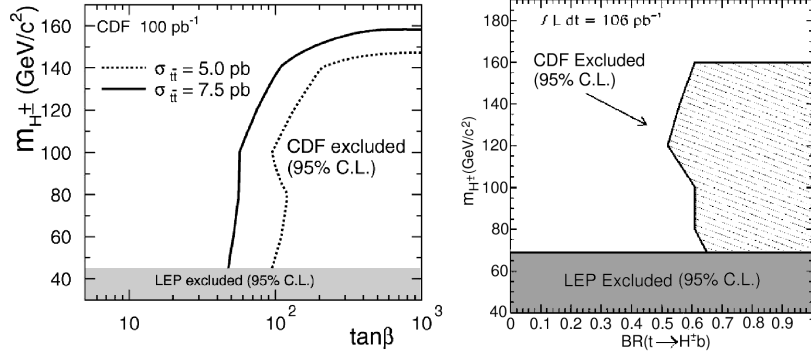


Figure 2.12: CDF Previous results assuming $\text{BR}(H^+ \rightarrow \bar{\tau}\nu)=1$. The left plot was extracted from [62] and quotes their results in term of $\tan(\beta)$ only. The right plot was extracted from [61] and also presents results in term of the $\text{BR}(H^+ \rightarrow \bar{\tau}\nu)$.

2.4.3 FNAL results

The CDF and D0 collaboration have also placed limits in charged Higgs production. The CDF searches have been performed in the $\tau_h + \cancel{E}_T + jets + \ell$ channel, where \cancel{E}_T is defined in 3.4.5, τ_h denotes the detection of a τ lepton through its decay to hadrons, and where $\ell = e$ or μ in [61] and $\ell = e, \mu$ or τ_h in [62]. In the framework of the tauonic Higgs model these searches set limits directly on $\text{BR}(t \rightarrow H^+ b)$ based on the measured production rate and interpret their results in terms of $\tan(\beta)$. The results of both these analyses are shown in Figure 2.12.

The D0 collaboration published their most recent search in the $\cancel{E}_T + jets + \ell$ channel, where $\ell = e$ or μ [63]. They obtain limits in the $(m_{H^\pm}, \tan(\beta))$ plane assuming that H^\pm decays to $\bar{\tau}\nu$, $c\bar{s}$ and $t^*\bar{b}$, the latter resulting in a $Wb\bar{b}$ final state. These limits utilize tree-level MSSM predictions of the $t \rightarrow H^+ b$ and charged Higgs branching fraction as a function of $\tan(\beta)$. Their results are shown in Figure 2.13 It is now known that higher-order radiative corrections significantly modify these predictions. The corrections strongly depend on the parameters of the model and are particularly large

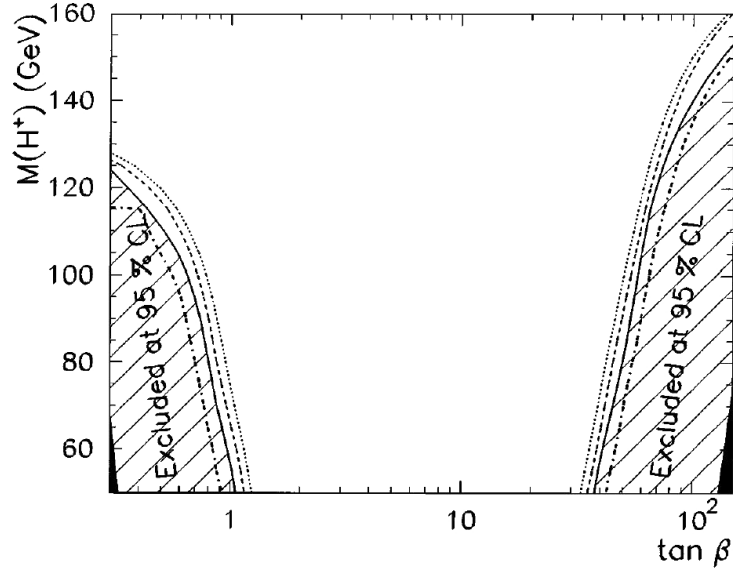


Figure 2.13: Previous results published by the D0 collaboration in [63]. The results assume the the charged Higgs decay to $c\bar{s}$, $\bar{\tau}\nu$, and $t^*\bar{b}$. The results are translated to the $(m_{H^\pm}, \tan(\beta))$ plane using tree-level MSSM calculations.

at high values of $\tan(\beta)$ [52]. In addition, it is also predicted that in the low $\tan(\beta)$ region, the charged Higgs has a sizable branching fraction to W^+h^0 , invalidating the implicit assumption that the charged Higgs decays only to $\bar{\tau}\nu$, $c\bar{s}$ or $t^*\bar{b}$.

Bibliography

- [1] Enrico Fermi, “*Versuch einer Theorie der β -Strahlen* ” Z. Phys. 88 161-177 (1934).
- [2] T. Lee and C. Yan “*Question of parity conservation in weak interactions*” Phys. Rev. 104, 254-258 (1956)
- [3] S. Eidelman et al., “*Review Of Particle Physics*” Phys. Lett. B592, 1 (2004)
- [4] C. Wu et al., “*Experimental test of parity conservation in β -decay*” Phys. Rev. 105, 1413-1415 (1957).
- [5] S. Glashow, Nucl. Phys. 22, 579 (1961)
- [6] S. Weinberg, Phys. Rev. Lett. 19, 1264 (1967)
- [7] A. Salam, Elementary Particle Theory, N. Svartholm, ed., Almquist and Wiksells, Stockholm, 367 (1968)
- [8] S. Glashow and S. Weinberg, Phys. Rev. D15, 1958 (1977)
- [9] S. Glashow, J. Illiopoulos, L. Miani “*Weak interactions with lepton-hadron symmetry*” Phys. Rev. D2 1285-1292 (1970).
- [10] R. Santos and A. Barroso, “*On the Renormalization of Two-Higgs-Doublet Models*” Phys .Rev. D56 (1997) 5366

- [11] J.F. Gunion, H.E.Haber, G. Kane and S. Dawson “*The Higgs Hunter’s Guide*”, Perseus Publishing, Cambridge, MA, (1990).
- [12] J.F. Gunion, H.E.Haber, G. Kane and S. Dawson “*Errata for the Higgs Hunter’s Guide*” hep-ph/9302272, (1993).
- [13] W. Hollik, “*Proc. of the Inter. Europhysics Conf. on High Energy Physics*” Brussels 1995,. J. Lemonne, C.V. Velde and F. Verbeure. Edts.World Scientific (1995) 921 and references therein.
- [14] J. Christenson, J. Cronin, V. Fitch, and R. Turlay “*Evidence for the 2π decay of the K_2^0 meson*” Phys. Rev. Lett. 13, 138-140 (1964).
- [15] Donald H. Perkins “*Introduction to High Energy Physics*”. Cambridge University Press, Cambridge, UK. 4th edition (2000).
- [16] M. Kobayashi and T. Maskawa, “*CP Violation in the renormalizable theory of weak interaction*”, Progr. Theor. Phys. 49, 652-657 (1973)
- [17] A. Djouadi, J. Kalinowski and M. Spira. Comp. Phys. Commun. 108 (1998) 56.
The HDECAY program is available from <http://people.web.psi.ch/spira/hdecay> .
- [18] J. S. Lee, A. Pilaftsis, M. Carena, S. Y. Choi, M. Drees, J. Ellis and C. E. M. Wagner ”CPsuperH: a Computational Tool for Higgs Phenomenology in the Minimal Supersymmetric Standard Model with Explicit CP Violation”, Comput. Phys. Commun. 156 (2004) 283. This program reports inconsistencies when the top or bottom yukawa couplings exceed the value of 2. The code was trivially modified to report such inconsistency when these quantities exceed the value of 4.
- [19] M. Carena and H.E. Haber “*Higgs Boson Theory and Phenomenology*”. Progress in Particle and Nuclear Physics 50 (2003) 63-152.

- [20] H. Georgi, S. Glashow, M. Machacek and D.V. Nanopoulos. Phys. Rev. Lett. 40 (1978) 692
- [21] A. Djouadi, M. Spira and P.M. Zerwas, “*Production of Higgs Bosons in Proton Colliders : QCD Corrections*”. Phys. Lett. B264 (1991) 440. See also S. Dawson, Nucl. Phys. B359 (1991) 283.
- [22] J. Aubert et al. “*Experimental observation of a heavy particle J* ” Phys. Rev. Lett. 33, 1404-1406 (1974)
- [23] J. Augustin et al. “*Discovery of a narrow resonance in e^+e^- annihilation*” Phys. Rev. Lett 33, 1406-1408 (1974)
- [24] T. Han, A.S. Turcot and R.J. Zhang. “*EXPLOTING $H \rightarrow W^*W^*$ DECAYS AT THE UPGRADED FERMILAB TEVATRON*” Phys. Rev. D59 (1999) 093001.
- [25] A. Stange, W. Marciano and S. Willenbrock “*HIGGS BOSONS AT THE FERMILAB TEVATRON.*” Phys. Rev. D49 (1994) 1354; D50 (1994) 4491.
- [26] Brian Hatfield “*Quantum Field Theory of Point Particles and Fields* ” Addison-Wesley, Reading, MA (1992).
- [27] S. Herb et al. “*Observation of dimuon resonance at 9.5 Gev in 400 proton-nucleus collisions*” Phys. Rev. Lett.39,252-255 (1977).
- [28] C. Rubbia et al. “*Experimental observation of the intermediate vector bosons W^+ , W^- and Z^0* ” Rev. Mod. Phys. 57, 699-722 (1985)
- [29] C. Athanassopoulos et al. “*Evidence for $\nu_\mu \rightarrow \nu_e$ Neutrino oscillations from LSND*”, Phys. Rev. Lett. 81, 1774-1777 (1998)

- [30] F. Abe et al., “*Observation of the top quark production in $p\bar{p}$ collisions with the Collider Detector at Fermilab*”, Phys. Rev. Lett. 74, 2626-2631 (1995).
- [31] S. Abachi et al., “*Observation of the top quarks*”. Phys. Rev. Lett. 74, 2632-2637 (1995).
- [32] Stephen P. Martin “*A SUPERSYMMETRY PRIMER.*” hep-ph 9709356 (1999)
- [33] Daniel E. Ryan “*Direct Searches for Scalar LeptoQuarks at The Run II Tevatron* ” Thesis dissertation CDF Note 7425
- [34] R. Barbieri and L. J. Hall “*SIGNALS FOR SUPERSYMMETRIC UNIFICATION* ”. Phys. Lett. B338, 212 (1994)
- [35] B.A.. Campbell “*SUPERSYMMETRY AND NEUTRAL FLAVOR NONCONSERVATION*”. Phys. Rev. D28, 209 (1983).
- [36] J. Hagelin, S. Kelley and T. Tanak “*SUPERSYMMETRIC FLAVOR CHANGING NEUTRAL CURRENTS: EXACT AMPLITUDES AND PHENOMENOLOGICAL ANALYSIS.*”. Nucl. Phys. B415, 293 (1997).
- [37] UA1 Collaboration, G. Arnison et al., Phys. Lett., B122, 103 (1983)
- [38] UA2 Collaboration, M. Banner et al., Phys. Lett., B122, 476 (1983)
- [39] P. W. Higgs, Phys. Lett. 12, 132 (1964)
- [40] Y. Okada, M. Yamaguchi and T. Yanagida, “Upper Bound Of The Lightest Higgs Boson Mass In The Minimal Supersymmetric Standard Model,” Prog. Theor. Phys. **85**, 1 (1991).
- [41] J. R. Ellis, G. Ridolfi and F. Zwirner, “On radiative corrections to supersymmetric Higgs boson masses and their implications for LEP searches,” Phys. Lett. B **262**, 477 (1991).

- [42] R. J. Zhang, “Two-loop effective potential calculation of the lightest CP-even Higgs-boson mass in the MSSM,” *Phys. Lett. B* **447**, 89 (1999) [arXiv:hep-ph/9808299].
- [43] A. Brignole, G. Degrassi, P. Slavich and F. Zwirner, “On the two-loop sbottom corrections to the neutral Higgs boson masses in the MSSM,” *Nucl. Phys. B* **643**, 79 (2002) [arXiv:hep-ph/0206101].
- [44] P. H. Chankowski, S. Pokorski and J. Rosiek, “Charged and neutral supersymmetric Higgs boson masses: Complete one loop analysis,” *Phys. Lett. B* **274**, 191 (1992). A. Yamada, “Radiative corrections to the Higgs masses in the minimal supersymmetric standard model,” *Phys. Lett. B* **263**, 233 (1991). A. Dabelstein, “The One loop renormalization of the MSSM Higgs sector and its application to the neutral scalar Higgs masses,” *Z. Phys. C* **67**, 495 (1995) [arXiv:hep-ph/9409375].
- [45] D. M. Pierce, J. A. Bagger, K. T. Matchev and R. j. Zhang, “Precision corrections in the minimal supersymmetric standard model,” *Nucl. Phys. B* **491**, 3 (1997) [arXiv:hep-ph/9606211].
- [46] R. Hempfling and A. H. Hoang, “Two loop radiative corrections to the upper limit of the lightest Higgs boson mass in the minimal supersymmetric model,” *Phys. Lett. B* **331**, 99 (1994) [arXiv:hep-ph/9401219].
- [47] . S. Heinemeyer, W. Hollik and G. Weiglein, “QCD corrections to the masses of the neutral CP-even Higgs bosons in the MSSM,” *Phys. Rev. D* **58**, 091701 (1998) [arXiv:hep-ph/9803277]. *Phys. Rev. Lett.* **440**, 296 (19yy).
Eur. Phys. J. **9**, 343 (19yy).
- [48] S. Dimopoulos and D. Sutter, *Nucl. Phys. B* **452**, 496 (1995)

- [49] Andrzej Czarnecki and Sacha Davidson, “ QCD corrections to the charged Higgs boson decay of a heavy quark”, Phys. Rev. D 48, 4183 (1993)
- [50] M. Carena, D. Garcia, U. Nierste and C.E.M. Wagner, Phys. Lett. B499 (2001) 141.
- [51] R. Eusebi and M. Carena “*Radiative Corrections to $\Gamma(t \rightarrow H^+b)$ valid to all values of $\tan(\beta)$.*” CDF Note 7348.
- [52] M. Carena, J. Ellis S. Mrenna, A. Pilaftsis and C.E.M. Wagner “*Effective Lagrangian for the anti- t b H^+ interaction in the MSSM and charged Higgs phenomenology*”, Nucl. Phys. B577,88-120 (2000), hep-ph/9912516.
- [53] G. W. Anderson, S. Raby, S. Dimopoulos and L. J. Hall, “*Precise predictions for $m(t)$, $V(cb)$, and $\tan \beta$* ”, Phys. Rev. D47,3702-3706 (1993), hep-ph/9209250.
- [54] L. J. Hall, R. Rattazzi and U. Sarid, “*The Top quark mass in supersymmetric $SO(10)$ unification*”, Phys. Rev. D50,7048-7065 (1994), hep-ph/9306309.
- [55] LEP Higgs Working Group for Higgs boson searches, “*Search for Charged Higgs bosons: Preliminary Combined Results Using LEP data Collected at Energies up to 209 GeV*”, hep-ex/0107031 (2001)
- [56] LEP Higgs Working Group, “*Searches for the neutral Higgs bosons of the MSSM: Preliminary combined results using LEP data collected at energies up to 209-GeV*”,(2001), hep-ex/0107030.
- [57] Alam, M. S. et al. CLEO collaboration, “*First measurement of the rate for the inclusive radiative penguin decay $b \rightarrow s$ gamma*”, Phys. Rev. Lett., 74, 2885-2889 (1995).

- [58] T. G. Rizzo, “ *$b \rightarrow s\gamma$ IN THE TWO HIGGS DOUBLET MODEL*”, Phys. Rev. D38, 820 (1988).
- [59] S. Bertolini et al., Nucl. Phys. B294,321 (1987); Y. Okada, Phys. Lett. B 315, 119 (1993).
- [60] F. Borzumati and C. Greub, Phys. Rev. D 58, 074004 (1998); Phys. Rev. D 59, 057501 (1999).
- [61] T. Affolder et al., “*Search for the charged Higgs Boson in the decays of top quarks pairs in the $e\tau$ and $\mu\tau$ channels at $\sqrt{s} = 1.8$ TeV*”, Phys. Rev. D., 62,012004, (2000), hep-ex 9912013.
- [62] F. Abe et al.”,”*Search for Charged Higgs Boson Decays of the Top Quark using Hadronic Decays of the Tau Lepton*”, Phys. Rev. Lett.,79,357 (1997).
- [63] B. Abbott et al. “*SEARCH FOR CHARGED HIGGS BOSONS IN DECAYS OF TOP QUARK PAIRS*”, Phys. Rev. Lett.,82, 4975 (1999), hep-ex/9902028.

Chapter 3

The Fermi National Accelerator Laboratory

In this chapter the experimental apparatus used for the search of charged Higgs bosons is described. The chapter begins by describing the Fermi National Accelerator Laboratory, and the chain of accelerators that conforms the Tevatron. It follows with a detailed description of the CDF II detector, and concludes with the particle identification criteria used at CDF.

3.1 The Fermi National Accelerator Laboratory

The Fermi National Accelerator Laboratory (Fermilab) is located 30 miles West of Chicago, Illinois. Fermilab, originally named the National Accelerator Laboratory, was commissioned by the U.S. Atomic Energy Commission under a bill signed by President Lyndon B. Johnson on November 21, 1967. On May 11, 1974, the laboratory was renamed in honor of 1938's Nobel Prize winner Enrico Fermi, one of the preeminent physicists of the atomic age. Universities Research Association (URA), a consortium of 90 leading research-oriented universities in the United States, Canada, Japan, and Italy has built and operated the facility since its founding.

The laboratory is currently the home of a large diversity of projects mostly related to high-energy physics, including CDF, DO, Dark Energy

Survey, Pierre Auger Observatory, Sloan Digital Sky Survey, MINERvA, MiniBooNE, MINOS, NOvA and NuTeV to mention a few. Many of these experiments take advantage of Fermilab's Tevatron, currently the world's highest-energy particle accelerator.

3.2 The Fermilab accelerator

The Fermilab accelerator is a chain of circular and linear accelerators used to accelerate protons and antiprotons to the world's record energy of 0.98 TeV as measured in the laboratory reference frame. The complexity of the machines involved in the accelerating process is enormous but the description of underlying physics is often simple and their basics principles can be summarized explained. In this section I describe the components and accelerators that comprise the Fermilab Accelerator complex.

The Fermilab accelerator [1] accelerates particles using a chain of 8 accelerators which can be divided into 4 groups according to their functionality. These groups are named **The Proton Source**, **The Anti-proton Source**, **The Main Injector and Recycler** and the **Tevatron**.

3.2.1 The Proton Source

The Proton Source is composed of the Cockcroft-Walton, Linac and Booster accelerators, and it is where the accelerating process begins. All the protons that are used in the Fermilab accelerator come from a simple "C" size cylinder of compressed hydrogen gas (H_2). The hydrogen is used to fill a chamber which, by means of high voltage, provides a source of negatively ionized ions of hydrogen. The high voltage strips the electrons from the neutral hydrogen atoms and while the electrons go to the anode, the protons are collected by a cathode plate made of cesium. The low work function of the cesium easily releases electrons to the adjacent protons. Eventually one of the re-

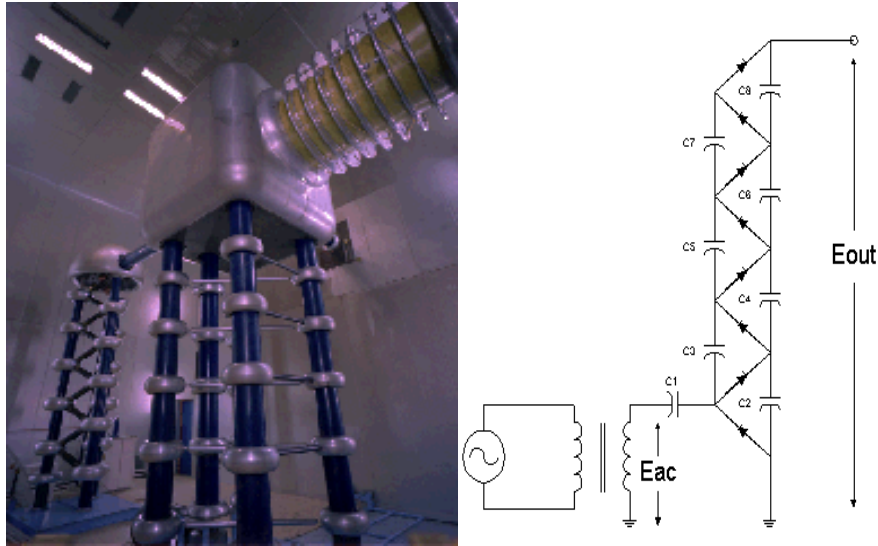


Figure 3.1: The Cockcroft-Walton accelerator. **Left:** Two big structures are shown. The Cockcroft-Walton accelerator itself (to the left, in second plane) providing 750 kV DC to the hydrogen chamber (metallic cube atop insulator tower in first plane). **Right:** Electric diagram of the Cockcroft-Walton voltage multiplier.

cently electron-stripped hydrogen atom (i.e. proton) strikes a proton out of the surface of the cesium plate allowing it to take off with two electrons. This negatively charged hydrogen atom is now accelerated by the anode and proceeds to the next accelerator stage.

The voltage used in the hydrogen chamber is provided by a Cockcroft-Walton voltage multiplier. This is a multistage diode/capacitor voltage multiplier providing 750 kV DC at low current. The charge collection mechanism of the Cockcroft-Walton is derived from the electric scheme of Figure 3.1(right). The actual room housing the Cockcroft-Walton multiplier and the hydrogen chamber is shown in Figure 3.1(left).

The negative hydrogen ions coming from the Cockcroft-Walton are fed into the Linac [2]. The word “Linac” stands for linear accelerator and consists of a series of drift tubes aligned in the accelerating direction and sepa-

rated by small gaps as shown in Figure 3.2. Radio-Frequency (RF) is applied to these drift tubes such that when the particles are traversing in between the drift tubes they increase their energy by an amount proportional to the peak-to-peak voltage of the RF signal. The length of the drift tubes and the RF frequency and phase are synchronized so that when the particles are between drift tubes the electric field between them is always maximum and in the same direction. The particles gain the same amount of energy each time they pass through a drift-tube gap and so the gain of energy while traversing the Linac is proportional to the number of gaps. The beam is said to be “bunched” since the particles should now be traveling in a close spacial region for the accelerating scheme to work: particles that pass through the gap when the RF field is in opposite direction are decelerated. The current Linac is 130 meters long, has an RF frequency of 805 MHz and an electric field of about 3 Megavolt/meter and brings the beam to 400 MeV in pulses of 20 ms length before injection into the Booster. A typical Linac pulse contains 4000 bunches, and a typical bunch contains 1.5 billion particles.

The booster [3] will now strip the H^- ions coming from the Linac of the two extra electrons and increase the beam energy. The LinAc provides a pulse of total length of 20 ms, and since the booster circumference is only 2.2ms long the use of a multi-turn injection process is necessary.

The system takes advantage of the fact that H^- and protons have opposite charge and almost identical mass since the mass of the electrons is negligible compared to that of the proton. The hydrogen ions are then injected to the booster via a bending magnet and “merge” to the existing proton beam, if any, see Figure 3.3(right). This mixed beam of protons and H^- is then passed through a thin Carbon foil. The Carbon foil is thin enough as to not significantly scatter the beam, but thick enough as to effectively strip the electrons out of the hydrogen ions, leaving the beam a rather

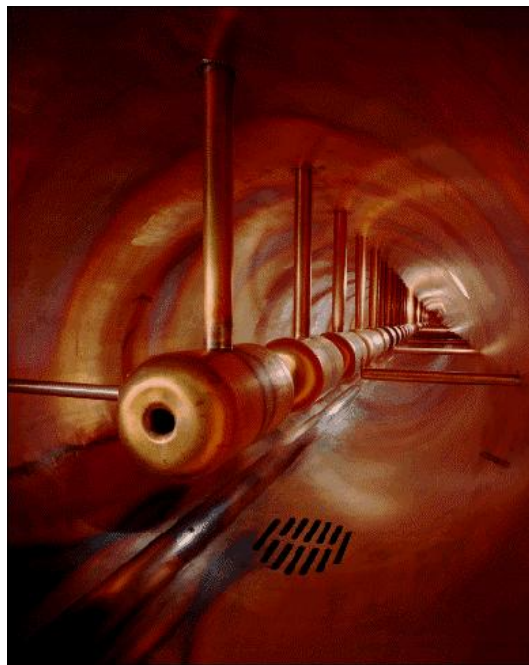


Figure 3.2: The Linac. A photograph showing the drift tubes in which the RF is applied. The whole space must be kept a ultra low vacuum.

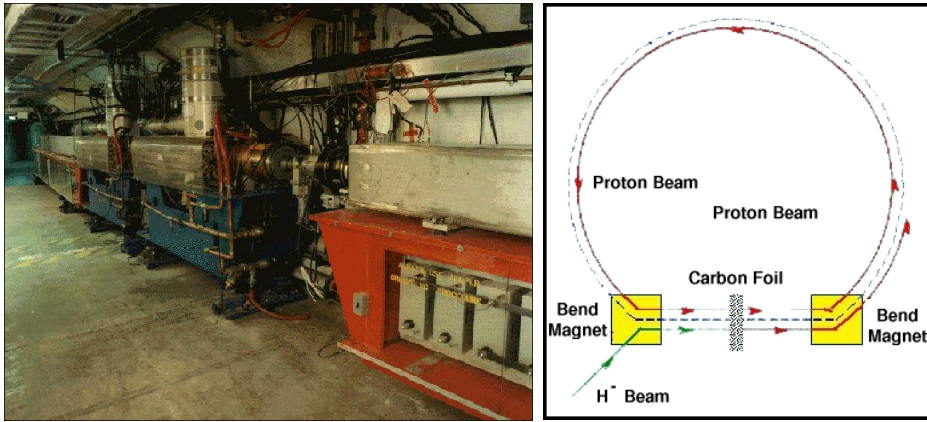


Figure 3.3: The Booster. **Left:** The photograph shows the RF cavities in the left side margin and the bank of capacitor inside the orange girder in the right side. **Right:** The diagram shows how the beam of H^- coming from the Linac is stripped and compacted in the Booster.

pure beam of protons. These protons are now forced to a circular trajectory by means of dipole magnets, completing the circle when they re-enter the bending magnet. After all the bunches from the Linac are into the Booster the ramping process begins. As with any synchrotron the Booster increases the energy by turning the RF cavities on while increasing the magnetic field in the dipole magnets so as to keep up with the larger momentum of the particles. The inductance of the Booster magnets is balanced by banks of capacitors (inside the orange girder in the photo of Figure 3.3(left)) to form a 15 Hz resonant circuit with a Q of about 10. The Booster is 475 meters in circumference and accelerates the protons from the Linac energy of 400 MeV to 8 GeV in a period of 0.033 seconds. The beam goes around the Booster around 16,000 times.



Figure 3.4: **Left:** Aerial view of the Main Injector (first plane) and the Tevatron (second plane). **Right:** Main Injector Tunnel. The lower magnets are part of the Main Injector, the upper green magnets part of the Recycler.

3.2.2 The main injector and recycler

Protons at 8 GeV from the Booster are injected into Fermilab's Main Injector [4]. The Main Injector (see Figure 3.4) is the 8th largest synchrotron in world, and it has two important functions that are carried out at different times.

The first one is the acceleration of 8 GeV protons coming from the Booster to 120 GeV for the purpose of having a high energy beam with which antiprotons can be generated¹. The generated antiprotons are stored in the Accumulator with an energy of 8 GeV until their use is required. The details on how antiprotons are produced and accumulated is discussed in section 3.2.3.

The second function is to accelerate the 8 GeV protons from the Booster, and later the 8 GeV antiproton from the Accumulator to 150 GeV for final injection into the Tevatron ring. The ramp up process takes about 1.5 seconds.

The Recycler [5] is a fixed-energy storage ring placed in the Main Injec-

¹This beam is also partly used in fixed target experiments which are not discussed here.

tor tunnel directly above the Main Injector beamline, near the ceiling (see Figure 3.4(right)). The purpose of the Recycler is to further increase the luminosity of the Tevatron Collider over the luminosity goals of the Main Injector by itself.

The Recycler consists of a ring of steel cases holding bricks of magnetized strontium ferrite mounted on steel hangars. The use of permanent magnets removes the need for expensive conventional iron/copper magnets along with their power supplies, cooling water system, and electrical safety systems. The Recycler is currently being commissioned and will function as a post-Accumulator ring. As the stack size in the Accumulator ring increases, there comes a point when the stacking rate starts to decrease. By emptying the contents of the Accumulator into the Recycler periodically, the Accumulator is always operating in its optimum antiproton intensity regime.

Originally the main role of the Recycler, and what would be by far the leading factor in luminosity increase, was to act as a receptacle for antiprotons left over at the end of Tevatron stores. Due to technical difficulties it is not clear at the moment if the Recycler would ever be used on a regular basis for that purpose, and so the name Recycler would become misleading.

It is worth mentioning that the few times the Recycler was used to store antiprotons from the accumulator the luminosity reached record values as high as $1.01 \cdot 10^{32} \text{ cm}^{-2}\text{s}^{-1}$.

3.2.3 The anti-proton source

The antiproton source [6][7] consist of The Target Station, The Debuncher, and The Accumulator.

The bunched beam of 120 GeV protons from the Main Injector is directed, every 1.5 seconds, to a Nickel Target where antiprotons are pro-

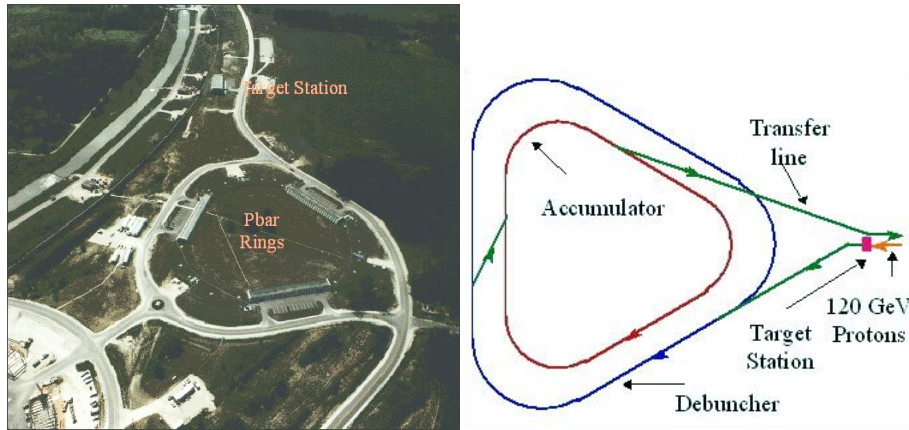


Figure 3.5: **Left:** Aerial view of the Accumulator and Debuncher site. **Right:** Schematic diagram. The Debuncher takes the antiprotons from the target, reduces their momentum spread and pass it to the Accumulator.

duced along a myriad of other particles. A Lithium lens² is used in order to focus the antiprotons and other particles in a beam. The antiprotons are separated from the other particles in the beam by the use of a pulsed magnet, effectively acting as charge-mass spectrometer. The strength and direction of the magnetic field is tuned to allow only antiprotons to pass the spectrometer and be directed to the Accumulator via The Debuncher.

The spread in energies of the antiprotons coming of the target would result in a very inefficient injection to the Accumulator due to its limited momentum aperture. The antiprotons need to be stabilized and their momentum spread reduced in order to enter the Accumulator efficiently: that is the purpose of the Debuncher. The Debuncher uses the technique of RF bunch rotation and adiabatic debunching and exchanges the large energy spread and narrow time spread³ into a narrow energy spread and large time spread. The antiprotons with higher energy travel on the outside of the De-

²A cylindrical piece of Lithium through which an axial current is passed

³The beam of protons is bunched when hitting the target and so are the produced secondary particles.

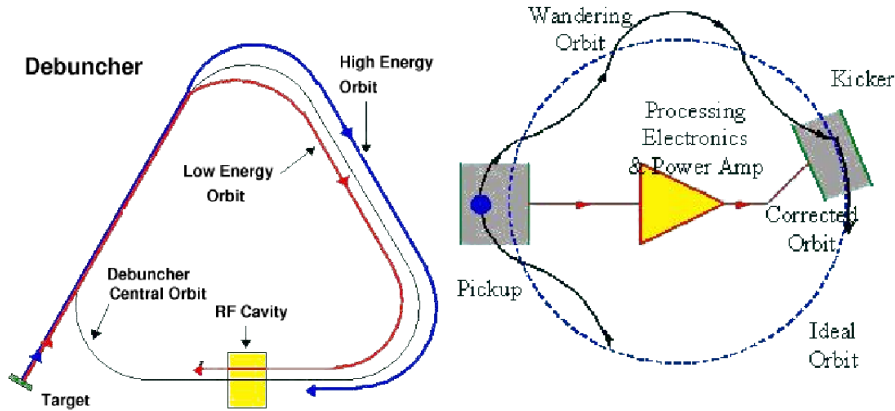


Figure 3.6: Basic functioning of the Debuncher (left) and of the Stochastic Cooling (right).

buncher ring, while the lower energy ones will travel on the inside of the ring. Thus the lower energy antiprotons arrive at the RF cavity before the higher energy ones because of the difference in path lengths around the accelerator, see Figure 3.6(left). After many turns (about 100 milliseconds) the momentum spread is narrow enough, the time spread is large (i.e. the beam is not bunched anymore), and the beam is almost ready to be transported to the Accumulator.

However, since the Main Injector takes 1.5 seconds to provide a new pulse and only 0.1 seconds were needed in the debunch process the rest of the time is spent in Stochastic Cooling, a process in which the beam is monitored for position or momentum in one part of its trajectory and the information is used “on fly” to correct the trajectory or momentum by applying a correcting pulse. See Figure 3.6 (right). After doing this, and just before the new pulse of particles comes from the target, the antiprotons are passed to the Accumulator.

The function of the Accumulator, as its name implies, is to accumulate antiprotons. This is accomplished by stacking successive pulses of antipro-

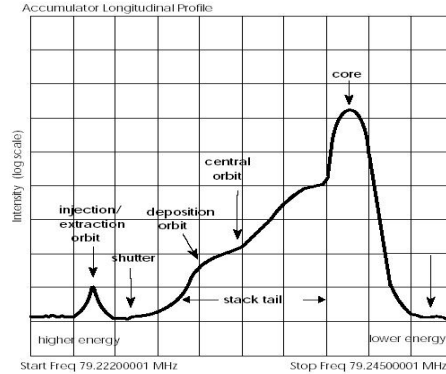


Figure 3.7: Accumulator profile. Display of the Accumulator’s beam distribution. It shows the intensity (proportional to the number) of antiprotons versus the revolution frequency which relates to the horizontal position.

tons from the Debuncher over long periods of time, up to several days. The accumulation process is an interesting one and it is worth mention in more detail. Essentially the antiprotons from the debuncher are injected in an 8 GeV injection/extraction orbit. This orbit is about 150 MeV more energetic (and with a 80 mm larger radius) than the core orbit of 7.85 GeV of the Accumulator where the bulk of the accumulated antiprotons are. Once in the injection orbit a RF frequency captures the beam and proceeds to decelerate the beam by approximately 60 MeV to the edge of the stack tail. The RF is slowly turned off as the edge of the tail is approached, see figure 3.7 to get a visual reference. The stack tail momentum cooling system now acts on the antiprotons. This system decelerates the beam towards the stack core which is a 7.85 GeV. After about 30 minutes the antiprotons in the stack tail have been decelerated into the domain of the core orbit. This process continues for hours or days until the desired Accumulator intensity is reached.

When the transfer of antiprotons to the Main Injector is needed an RF system with harmonic number 4 is energized with a frequency correspond-

ing to that of the core orbit, thus capturing a portion of the beam into four buckets⁴. Then the RF is increased raising the energy of the captured antiprotons up to 8 GeV, the energy of the extraction orbit. In this orbit another RF system kicks in, re-bunching the beam into 11 or so bunches suitable for capture by the Main Injector's RF. A Kicker then bends the beam to a beamline out of the Accumulator and to the Main Injector, where they are accelerated to an energy of 150 GeV as described in the previous section. Once the energy of the particles is 150 GeV the beam is transported to its final destination: The Tevatron.

3.2.4 The Tevatron

The Tevatron [8] is the final stage in the acceleration process. It receives 150 GeV (anti)protons from the Main Injector, and then accelerates them to the final energy of 980 GeV. The Tevatron ring is a circular beam pipe of one kilometer radius. Its total circumference of about 6.3 Km holds 816 dipolar, superconducting magnets made of niobium-titanium alloy wire. These magnets are kept at a temperature of 4.3 K by what is currently the largest cryogenic system in the world, capable of supplying 1000 liters/hour of liquid helium at 4.2 K. and capable of absorbing heat at a rate of 23 kW while maintaining a temperature of 4.6 K. At 980 GeV energy the magnetic field of the dipolar magnets is 4.2 Tesla, the current draw of the coils being 4000 Amperes.

Interleaved with the dipole magnets are 204 quadrupole magnets that

⁴A bucket is a stable phase space region in which particles can be captured and accelerated by the RF cavities. A group of particles captured in a bucket is called a bunch. A bucket may or may not contain a bunch.

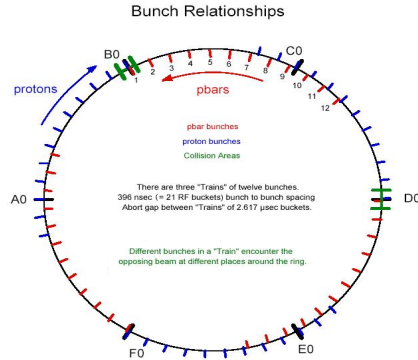


Figure 3.8: Bunch structure in 36x36 mode. Proton bunches go clockwise and are shown as blue marks outside the ring. Antiprotons go counter-clockwise and are shown as red marks inside the ring. Detectors are placed at B0 and D0 points.

focus⁵ the beam to achieve peak luminosity.⁶

The RF system of the Tevatron consist of an array of 8 RF cavities running at the frequency of 53.03 MHz. This frequency does not need to be changed during the ramping since the very small velocity difference of the protons at 150 GeV and 980 GeV. It takes 9 cycles to fill the Tevatron with 36 bunches of protons (or antiprotons), and takes about 40 seconds to ramp the energy from 150 GeV to 980 GeV. The typical number of protons (antiprotons) in a bunch is about 27×10^{10} (33×10^9).

3.2.5 The beam structure

During RunIIa the Tevatron is operated in 36x36 mode, which refers to the number of bunches of protons and antiprotons respectively. The beam configuration is shown in Figure 3.8. The 36 bunches are distributed in three trains of 12 bunches each. The bunches in a train are separated by 21 RF

⁵The quadrupoles are generally used in pairs. The transverse directions are called x and y , the first quadrupole focus in x while defocus in y , and the second focus in y while defocussing in x . The net effect is that of focusing in both, x and y .

⁶The definition of luminosity is postponed to 3.3.6.

buckets (396 ns). The trains are separated by a 139-bucket gap (2617 ns) called the abort gap. If protons and antiprotons were orbiting in a central orbit (as depicted in Figure 3.8) collisions will occur at many points ⁷. The points marked B0,D0 and F0 would have the maximum number of collisions (12) per turn. However detectors are located only at the B0 and D0 points and collisions produced at other points in the ring are wasted. To avoid this inefficient use of beam a new twist is added to the configuration. Once all the proton bunches are injected, and before loading the antiprotons a set of electro-static separators are used to create a pair of non-intersecting helical closed orbits with protons in one strand and the antiprotons to be loaded in the other. The helical configurations prevents the collisions between the beams all along the ring. Antiprotons are then injected in their strand of the helix. With the two beams in the Tevatron the ramping up to 980 GeV is done. After some procedures to clean up the beam halo are finished the injection helix is set to collision helix. This mode uses separator bumps close to the interaction points and phases the helix so that the proton and antiproton beams collide only at the center of the detectors. The bunch crossing occurs every 396 ns.

There are two detectors in the Tevatron ring located at the points marked B0 and D0. The detector used in this analysis is located at B0 and it's called CDF, the **C**ollider **D**etector at **F**ermilab.

⁷The calculation goes as follows: An observer located at, say B0, will see the collision of proton bunch N to antiproton bunch N, with N from 1 to 12. Close around B0 there are $(12-1) \times 2$ collisions. So the total for B0 is $(12-1) \times 2 + 1 = 23$. Since there are three trains the total number of collision points is 69.

3.3 The CDF II detector

Since the first operation of the Tevatron the CDF detector has undergone many changes. The current detector, used in what is called Run II of data taking, is called CDF II. For simplicity of notation through this entire book I refer to the CDF II detector either as CDF or CDF II.

This section starts with an overview of the CDF II coordinate systems and continues with the hardware description of the detector.

The most important CDF II detector sub-systems for this analysis can be grouped in three categories, according to both, the functionality and the localization in the detector. The innermost system is the integrated Tracking System and consists, from inside out, of the Silicon Vertex Detectors, the Central Outer Tracker and the Solenoid. Outside and surrounding the Integrated Tracking system is the Calorimetry system, and consists of the central and forward electromagnetic and hadronic calorimeters. The last system is the Muon Chambers, and is the most outward system in the detector.

In addition the Time of Flight system and the Cerenkov Luminosity Counter system are described.

The description of the detector is not intended to be rigorous and it is made with the only intention of clarifying the process with which data used in this analysis is obtained. Not all the subsystems are described, and the description of the ones that are is not necessarily complete. A more detailed description of all the components can be found in [9].

3.3.1 Overview of coordinate systems and coordinate variables

The Cartesian coordinate system of CDF is defined as a right-ternary $(\hat{x}, \hat{y}, \hat{z})$ with its origin at the center of the detector which roughly coincides with

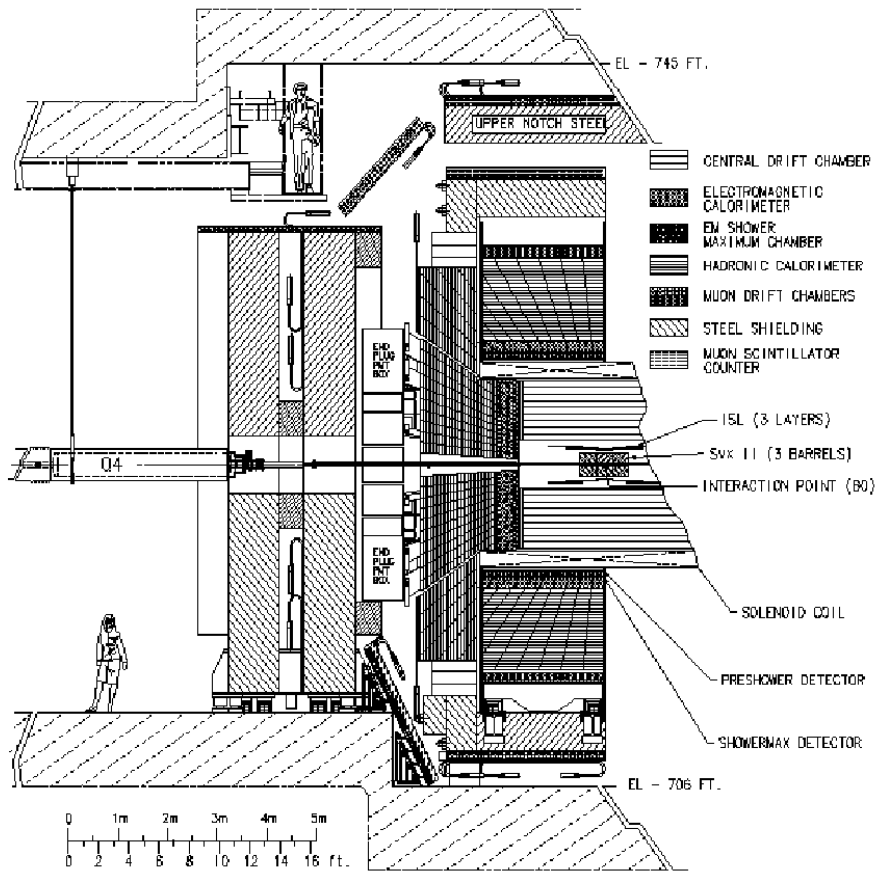


Figure 3.9: The CDF II lateral view.

the nominal collision point of the bunches.

The detector (see figure 3.9) has cylindrical symmetry along the \hat{z} axis and reflection symmetry around the (\hat{x},\hat{y}) plane. The \hat{z} direction is defined along the beampipe such that protons move in the positive \hat{z} direction. The \hat{y} direction is defined transversal to the \hat{z} direction with its positive side pointing up to the zenith of the detector. The \hat{x} direction is then chosen to complete the right ternary, pointing its positive side outwards the ring, parallel to the horizon.

The symmetry of the detector and the fact that the colliding beams are not polarized often makes it convenient to work in cylindrical $(\rho_{\perp},\phi,\hat{z})$ or polar (ρ,ϕ,θ) coordinate systems. In the cylindrical system the ρ_{\perp} is defined transverse to the \hat{z} axis. The azimuthal angle ϕ is defined in the (\hat{x},\hat{y}) plane with $\phi = 0$ in the positive side of the \hat{x} axis. The \hat{z} is defined as in the Cartesian system. The polar angle θ is counted from the positive direction of the \hat{z} axis.

Another coordinate system often used is (ρ,ϕ,η) obtained by replacing in the polar system the θ coordinate by the η , the pseudo rapidity. The variable η is defined from θ as

$$\eta = -\log \left[\tan \left(\frac{\theta}{2} \right) \right]$$

and is the relativistic limit of the rapidity ζ , defined as

$$\zeta = \frac{1}{2} \log \left(\frac{E + p_z}{E - p_z} \right) \underset{p \rightarrow E}{=} -\log \left[\tan \left(\frac{\theta}{2} \right) \right] = \eta$$

The importance of this coordinate system resides in the fact that, while the (anti)proton's energy is accurately measured, the energy of the partons involved in the fundamental interaction follows the parton distribution function [10] and is not known on an event-by-event basis. Thus the imbalance in the longitudinal momenta of the interacting partons often results in large

boosts along the z axis⁸. The variable ζ transforms linearly with boost in the \hat{z} direction, so ζ intervals are invariant under such a boost. As it is described later on, some sub-detectors in CDF II are divided in region with constant Δ_η .

The global CDF II coordinate system is anchored to the Central Outer Tracker (COT), which is part of the Tracking system as described in the next section. The position of all other sub-detectors are measured with respect to the COT reference frame and this information is stored in alignment tables. Positions in a sub-detector are typically measured in the local reference frame and then converted into the global CDF II coordinate system via the proper alignment table.

3.3.2 Tracking and vertexing

The trajectory of particles can give valuable information about the kinematics of a physical process, including charge sign and good momentum resolution if magnetic fields are present. The process of reconstructing a particle trajectory is known as *tracking*. In this section I describe the sub-detectors that form the integrated tracking system of the CDF II detector as shown in Figure 3.10, followed by a brief overview of the basics in tracking reconstruction.

Solenoid:

All the tracking systems are contained in a superconducting solenoid of 1.5m in radius and 4.8m in length. The solenoid provides a very homogeneous magnetic axial field of 1.4 Tesla inside a useful volume of 2.8m in diameter and 3.5m along the $-\hat{z}$ direction. In normal operating conditions its current

⁸ The transverse momentum of the (anti)protons is negligible, and so is then the momentum of their partons according to the parton distribution functions.

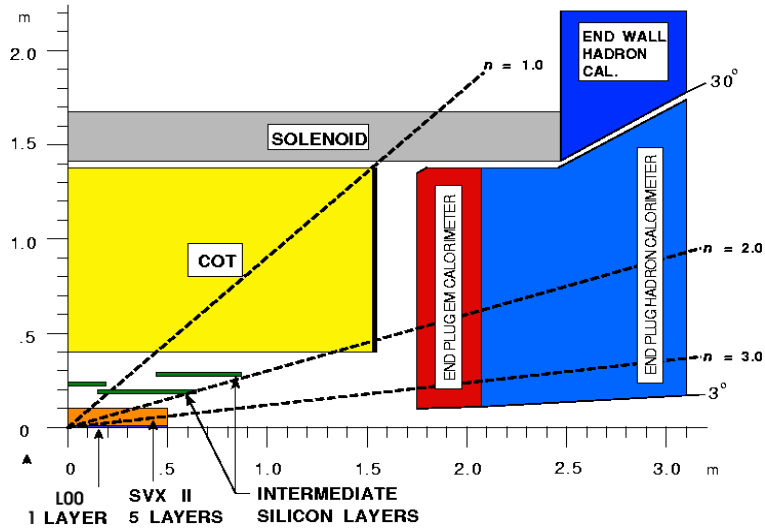


Figure 3.10: Longitudinal view of the CDF II tracking volume. Its main components are the Solenoid, the Central Outer Tracker (COT), and the silicon micro-strip detectors ISL, SVX, and L00.

consumption is about 4650 A. Inside the solenoid and in direct contact with it the Central Outer Tracker is located.

Central Outer Tracker (COT):

As mentioned in section 3.3.1 the COT position defines the global CDF II reference frame and it is the main component of the tracking system. It is located inside the solenoid in the region of $|Z| < 155$ cm and between the radii of 44 and 132 cm. The COT is a cylindrical multi-wire open-cell drift chamber. It consists of 8 superlayers made each of a large number of cells as shown in Figure 3.11. Each cell is either an “axial” or a “stereo” cell. Superlayers 1,3,5,7 (2,4,6,8) are made completely of “stereo” (“axial”) cells. The main difference between these two type of cells is their orientation: “axial” cells are placed in a straight longitudinal direction, parallel to the \hat{z} direction at constant ϕ , while that the “stereo” cells are obtained from

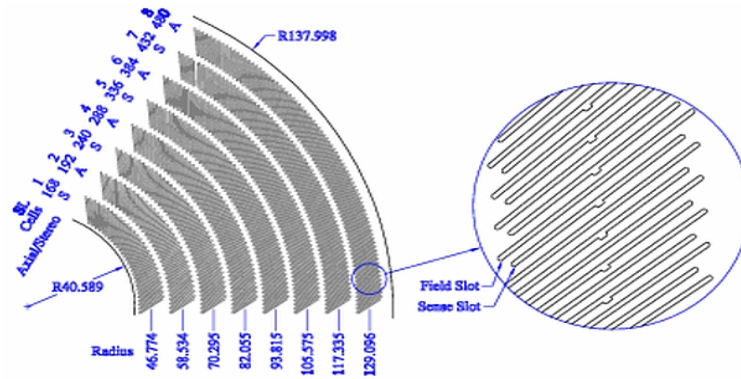


Figure 3.11: Schematic diagram of the 8 layers in quadrant of the COT. The number of cells, the radius from the center to the beampipe and the type (Stereo or Axial) is shown for each superlayer.

an axial cell in which the two end-plates have been rotated with respect to each other. In such a cell each wire is rotated by six cells from the east end-plate to the west end-plate. Together with the “axial” cells the “stereo” cells provide information of the \hat{z} position of the hit.

Each cell has an approximate size of about 2 cm by 10 cm and with a length of 310 cm spans the whole longitudinal direction of the COT.

The COT is filled with 50:50:1.7 Argon-Ethane-Isopropyl alcohol mixture as the active medium. The open-cell configuration means that all the cells share the active gas in the COT volume. Due to wire aging problems the active gas is now being continuously recirculated at a rate of 400 SCFH, and the addition of fresh gas is such that the gas is completely replaced every 15 hours.

A transverse view of three cells in superlayer 2 is shown in Figure 3.12. The cells are separated from each other by field panels made of golden plated mylar. Inside the cell wires run along its longitudinal direction, some of them are potential wires introduced to shape the electric field while the others are sense wires from which the information of the particle’s trajectory

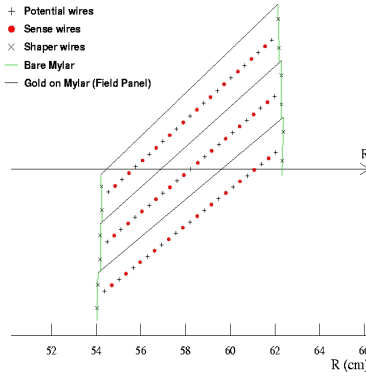


Figure 3.12: Schematic diagram of three cells in Superlayer 2 of the COT.

can be inferred.

When a charged particle passes through the gas it leaves a trail of ionization electrons. These electrons drift towards the sense wires by virtue of the electric field created by the field panels and potential wires (see Figure 3.13(left)). Once near the sense wires the electrons get strongly accelerated because of the local $\frac{1}{r}$ electric field producing more ionization in a process known as avalanche. The signal of this wire is further analyzed and depending on the charge collection the wire is said to be “hit”. The time it takes from the moment the collision was expected to occur to the time the signal was detected gives information about the distance between the particle’s trajectory and the sense wire. The high voltage applied to the COT is such that the electric field drift is about 1.9 kV/cm. The drift velocity is about 54 $\mu\text{m}/\text{ns}$.

In addition to the electric field due to the cell’s field panel the solenoid magnetic field permeates the COT volume. In such crossed fields charged particles originally at rest move in the plane perpendicular to the magnetic field at an angle α with respect to the electric field as shown in Figure 3.13(right). This angle is known as the Lorentz angle and depends on the magnitude of the fields and the properties of the active medium. In

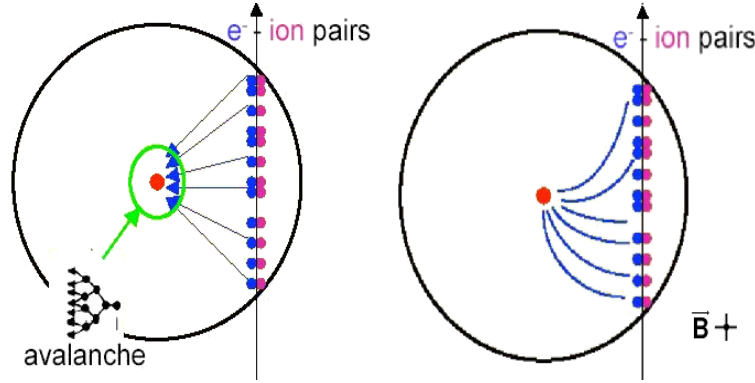


Figure 3.13: Schematic diagram of a single-wire drift chamber. The diagrams show the trail of ionization electrons left by the passage of a charged particle and the drift of the electrons with and without (right and left) the presence of a magnetic field.

the COT $\alpha=35^\circ$. This is the reason that all the cells are tilted 35° in the COT geometry, so ionization electrons will drift in the ϕ direction which is perpendicular to high P_T tracks optimizing the overall resolution of the COT. The single “hit” position resolution of the COT has been measured to $140 \mu\text{m}$, resulting into the transverse momentum resolution of

$$\frac{\Delta_{P_T}}{P_T} = 0.15\% \frac{P_T}{[\text{GeV}/c]}$$

Silicon vertex detectors:

At CDF II there are three silicon-based detectors named L00, SVX and ISL. They differ in size, radius and number of active elements, but they all use silicon micro-strip technology. This enable us to measure the position of secondary vertexes, like those produced in the decay of long lived hadrons such as B mesons with excellent resolution, in fact 10 times better than would be obtained with the COT only. The silicon micro-strip detectors were used for the first time in a hadronic accelerator by CDF during Run I of data taking [11].

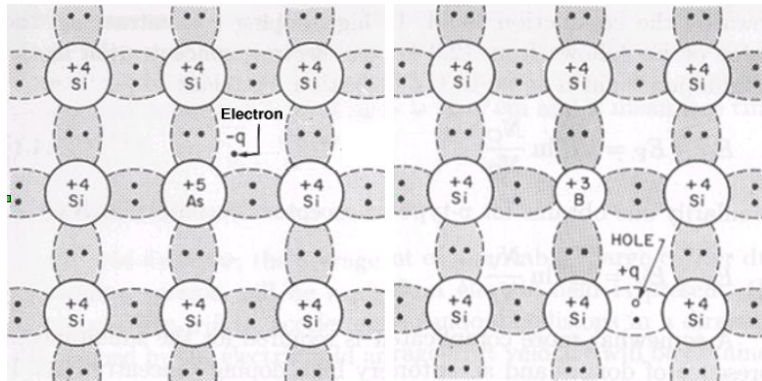


Figure 3.14: Impurities in the Silicon crystalline structure added to obtain n-type (left) and p-type (right) silicon.

The silicon detector takes advantage of the ionization products left by the passage of a charged particle. The semi-conductor properties of the Silicon (semi-conductor since the energy gap between valence band and the conduction is small), allows the electron-holes produced by ionization to drift apart by means of an applied electric field. However in pure silicon the charge carriers outnumber the charge produced in the ionization process by 4 orders of magnitude so the electron-hole pairs quickly recombine. In order to accurately measure the ionization signal it is essential to deplete the free charge carriers in the ionization volume.

This is accomplished by exploiting the properties of the p-n junction. A p-n junction is the union of Silicon n-type and Silicon p-type. Silicon n-type is obtained by adding impurities of donor ions like Phosphorus or Arsenic in the molecular structure of the silicon crystal as shown in Figure 3.14(left). The donors introduce energy levels close to the conduction band, resulting in electrons as the majority carriers. Silicon p-type is obtained by introducing acceptor ions like Boron in the silicon crystal (see Figure 3.14,right). This acceptors introduce energy levels close to the valence band, resulting in holes as the majority carriers. The process of adding donors/acceptors to

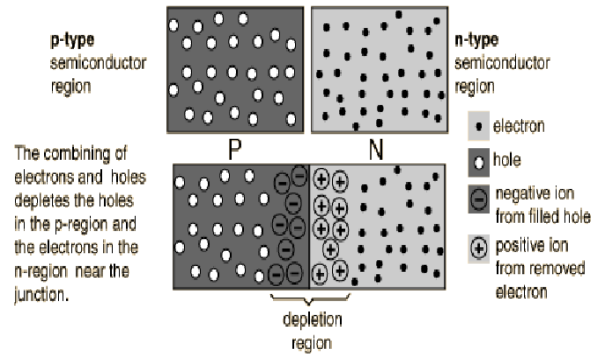


Figure 3.15: Junction of p-type and n-type silicon materials.

an otherwise pure material is refer to as “doping”.

When brought together to form a p-n junction, the gradient of electron and holes densities results in a migration of majority carries out of the junction. The junction is now left with net charge of opposite sign on each side, but otherwise depleted of majority carriers as shown in Figure 3.15. The region near the junction is called the depletion zone. In this zone the electron-hole pairs produced by ionization will drift along the field lines generated by the net charges. The depletion zone can be enlarged by applying a reversed bias voltage. The depletion zone can extend to different lengths in each side of the junction depending on the concentration of the impurities in each side. In silicon detectors it is common to use a highly doped p-type (p^+) silicon and a lightly doped n-type (n^-) silicon that constitutes the bulk of the detector; in this case the depletion zone extends mostly in the volume of the n^- type silicon.

The depletion width is a function of the bulk resistivity, charge carrier mobility and the magnitude of the reverse bias voltage. The bias voltage at which the whole volume of the silicon is depleted is called the depletion voltage.

At CDF three types of modules made of silicon detectors are used. The

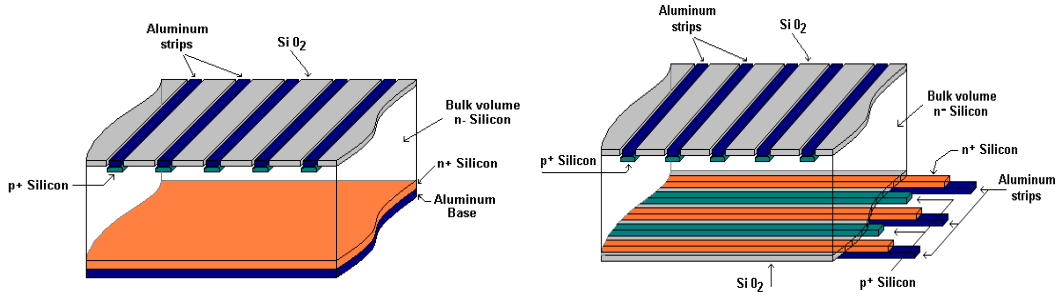


Figure 3.16: **Left:** Silicon strip detector used for $(\rho - \phi)$ hit position identification. **Right:** Silicon strip 90° detector used for $(\rho - \phi - z)$ hit position identification.

first one is made by laying micro-strips of p^+ type silicon over a n^- bulk of silicon, see Figure 3.16(left). The side of the silicon opposite to the p^+ strips is a highly doped n-type substrate (n^+). If the strips lie parallel to the \hat{z} direction the module allows $(\rho - \phi)$ position identification. The second type called a 90° stereo and is similar to the first one with the added work of replacing the n^+ substrate with n^+ strips that run perpendicular to the \hat{z} direction allowing the measurement of the hit in the \hat{z} direction, thus fully determining the position of the hit, see Figure 3.16(right). The third type is called a small angle stereo and it is essentially a $(\rho - \phi)$ that lies quasi-parallel at an angle of only 1.2° with respect to the \hat{z} direction. This type is used by overlapping it with a $(\rho - \phi)$ module, thus allowing the determination of the complete hit position, with only worst resolution in the \hat{z} position than a module of type two. Between SVX, ISL and L00 the three type of modules are used.

The signal is usually detected in a small amount of consecutive strips. The hit position is determined by weighting the strip position to the amount of charge collected by each. With this method the single hit resolution at CDF is about $12 \mu\text{m}$.

SVX The silicon modules are supported with Rohacell foam in as-

semblies called ladders. Each ladder support double-sided silicon modules, where in each side lies a string of 4 modules connected to each other by wire bonds, thus quadrupling the length of the strips. Twelve of these ladders are set in a semi-circular configuration to form a layer that surrounds the beam pipe at a certain radius. The ladders are supported by two beryllium bulkheads the design for which is shown in Figure 3.17. Special attention has been put in precisely machine the bulkhead for an accurate positioning of the ladders. The bulkhead provides support for 60 ladders in 5 concentric layers, conforming a 29 cm long SVX barrel. The SVX is built by placing three barrels along the beampipe. Layers are numbered from 0(innermost) to 4 (outermost). Layers 0,1 and 3 combine $(\rho - \phi)$ modules in one side with 90° stereo in the other side. Layers 2 and 4 combine $(\rho - \phi)$ modules in one side with small angle stereo in the other. The single hit resolution of SVX is about $12 \mu\text{m}$. The large number of channels require that much of the electronics be mounted closed to the modules. This results in a better signal-to-noise ratio of the hit signal but also in an additional multiple scattering due to the extra material in the volume.

ISL Consists of three layers as shown in Figure 3.10 . In the central region ($|\eta| \leq 1$) a single layer is placed at a radius of 22 cm. Two more layers are located in the region $1 \leq |\eta| \leq 2$ at radii of 20 cm and 28 cm. The layers are double-sided with $(\rho - \phi)$ in one side and small angle stereo modules in the other. In order to reduce the total number of channels to 268,800 only one out of two channels is read. The ISL single hit resolution is about $20 \mu\text{m}$.

L00 Consists of a single-sided layer of 12 ladders and is shown in Figure 3.18. Six of the ladders lie at a radius of 1.35 cm and the other six at 1.62 cm from the beamline. Each ladder is made out of 6 sets of two wire-bonded modules each, spanning 95 cm in the \hat{z} direction. The layer is

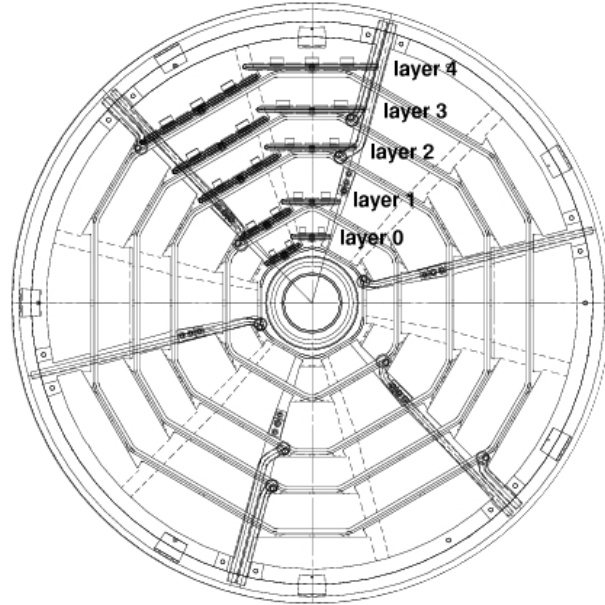


Figure 3.17: End view of the SVX silicon bulkhead. The placement of ladders is shown in two adjacent wedges.

supported by a carbon-fiber structure.

In addition, L00, SVX and ISL have dedicated cooling lines running at a nominal temperature of -6°C . Special effort is put into aligning the Silicon detectors to the beam, as opposed to the COT. This is because a small misalignment of the COT, while not significantly changing the track information obtained with it, can affect the impact parameter⁹ of the tracks, which is obtained using Silicon hit information and is used for triggering purposes, introducing a dependence on the ϕ coordinate.

Special effort is put into aligning the Silicon detectors to the beam, as opposed to the COT. The impact parameter¹⁰ of a track is obtained using Silicon hit information and is used for triggering purposes. A small misalignment of the COT does not result in a severe track misreconstruction.

⁹Distance to closest approach of the track to the beam, as explained in the next section

¹⁰Distance to closest approach of the track to the beam, as explained in the next section

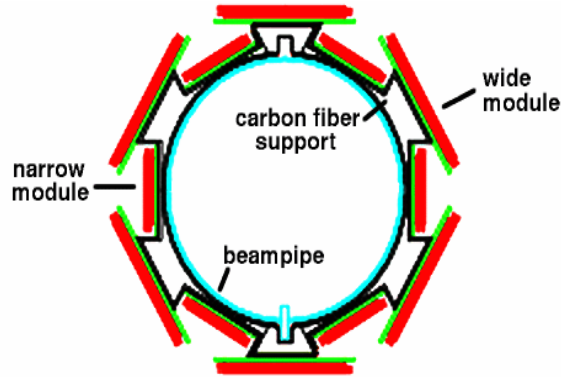


Figure 3.18: End view of the L00 detector.

But if the Silicon were aligned to the COT, and thus were also misaligned too, the impact parameter (and the trigger) would obtain a dependence on the ϕ coordinate, which is non-desirable.

Tracking and pattern recognition

Tracking Parameterization: In the plane perpendicular to an homogeneous magnetic field, such as the one provided by the CDF solenoid, the trajectory of a charged particle follows a circular pattern. The longitudinal component of the particle's momentum is not modified by the axial magnetic field, thus in three spacial dimensions the trajectory of charged particles are helices. In three spacial dimensions the helices can be parametrized with the use of five parameters, which for convenience are chosen as:

C : the signed helix curvature defined as $C = \frac{sign(q)}{2R}$, where R is the radius of the circle in the transverse plane and q is the charge of the particle.

z_0 : the position of the point in the \hat{z} axis which is closest to the track.

d_0 : signed quantity defined as $d_0 = sign(q)(r_C - R)$ where r_C is the position of the center of the circle in the transverse plane. Its magnitude is the distance from z_0 to the closest point in the track.

ϕ_0 : direction of the transverse momentum of the particle in the point to closest approach to the \hat{z} axis.

$\cot(\theta)$: the ratio of the longitudinal to the transverse momentum ($\frac{P_z}{P_T}$)

Pattern Recognition: Track reconstruction begins with the use of COT data. The algorithm is described in detail in [12], and it is cited here for reference. The algorithm starts by finding in each superlayer the so called 3-hit seeds. A seed consist of hits in three consecutive wires, from which the aspect angle (α) is constructed and cut upon. The aspect angle is defined as $\sin(\alpha) = \hat{v} \cdot \hat{p}$ as shown in Figure 3.19(left), where \hat{p} is the track direction and \hat{v} is the drift direction. The aspect angle is calculated only with the information from the first and third wire. If the aspect angle is greater than 50° the seed is considered faulty and dropped.

To build a seed the algorithm starts with a hit on an inner wire of a cell and searches for hits on the next two immediate outer wires, in either the same cell or in its immediate neighbors. For each initial hit there are at most 5 possible seeds due to the possible combinations of hit wires, as shown in Figure 3.19(right). For each seed the four drift sign combinations are used to calculate the aspect angles. The combinations passing the aspect angle cut are ordered in ascending slope. The final list of seeds is obtained after requiring that the time of the hit in the second wire is within a small time interval relative to the expected time in the second wire calculated with the first and third wire information. The time interval is 15 ns ($800 \mu\text{m}$) if the first and third hit of the seed are the same side and in the same cell, 25 ns otherwise.

All seeds passing this requirement are considered good and are used to search for hits on the remaining wires of the superlayer. Each seed that gives origin to a collection of hits in a superlayer forming a segment of a particle's track is called a segment. To build the segment each seed is fit

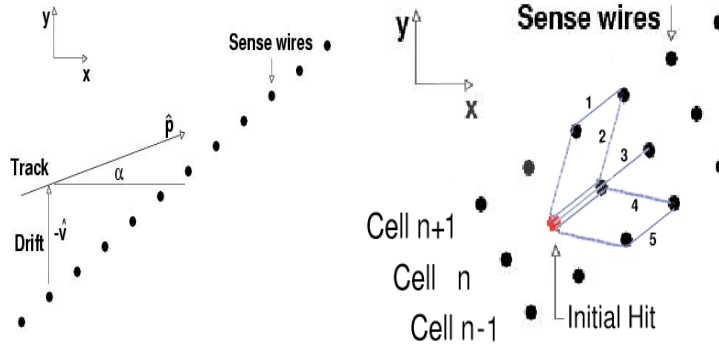


Figure 3.19: Left: Definition of the aspect angle for a cell in the COT. The nominal drift in the case of equal cell tilt angle and Lorentz drift angle is shown. **Right:** Possible combinations for a 3-hit seed.

to a line that defines the path for the hit search. For each hit wire on the path the time of the hit is compared to the expected time, and the hit is added to the segment only if the the time difference is within 20ns. The procedure is repeated until all the wires in the superlayer are reached. After all the segments in a superlayer are found a list of segments is compiled and ordered in decreasing number of hits.

The next step is to obtain axial tracks (i.e. tracks without any \hat{z} coordinate information) by linking the segments from the axial superlayers. The algorithm (named Segment Linking, or SL) starts by creating an initial set of tracks from the segments in the outer superlayer (SL8) assuming no impact parameter, and calculating its expected position and angle in the next inner axial superlayer (SL6). For each segment in the inner axial superlayer SL6 a search is done for those segments in SL8 whose expected position at SL6 matches the SL6 segment. The segments are matched if the angle between the expected track at SL6 (extrapolated from the SL8 segment) and the segment in SL6 is less than 0.05 rad, and the position is less than a specific threshold. If multiple matches are found for a given SL6 segment the best

match is chosen based on the one with the smallest angular difference. Once the segments are linked the track is fit using only information from these two superlayers, obtaining the curvature, the d_0 , the ϕ_0 , and the covariance matrix.

The information from the rest of the axial superlayers(SL4 and SL2) is now included by linking the tracks made from SL8 and SL6 to the segments in SL4 and SL2. The procedure is similar to that used in linking the SL8 segments to the SL6 segments, except that now the extrapolation path takes into account the d_0 parameter and covariance matrix of the tracks. The tracks extrapolated to SL4 and SL2 are compared to the segments found in those superlayers, and the matching is done requiring an angle difference less than 0.05 rad and a position difference less than 4 times the error of the extrapolated track. If a link is found the segment is added to the track and the track is refit to include the new segment information.

In addition to the SL algorithm, a second track-reconstruction method named *Histogram linking, or HL* is run in parallel in order to get the maximum reconstruction efficiency out of the two methods. Essentially this algorithm starts by seeking segment with at least 8 hits and curvature greater than 0.008. The segment is then extrapolated defining a search path. For each layer the distance between the hit and the extrapolated segment is histogrammed. All the layers are then summed up to obtain global histogram. The bin with the most hits defines the position of the track candidate. If the bin has more than 10 entries(hits) a track is made.

At this point axial tracks were obtained by two different algorithms: SL and HL. Now the stereo pattern recognition is applied.

The stereo pattern algorithm starts by matching stereo segments to existing axial tracks. For each segment in the outer stereo superlayer a stereo fit is performed to the axial track. The stereo fit is done starting with a

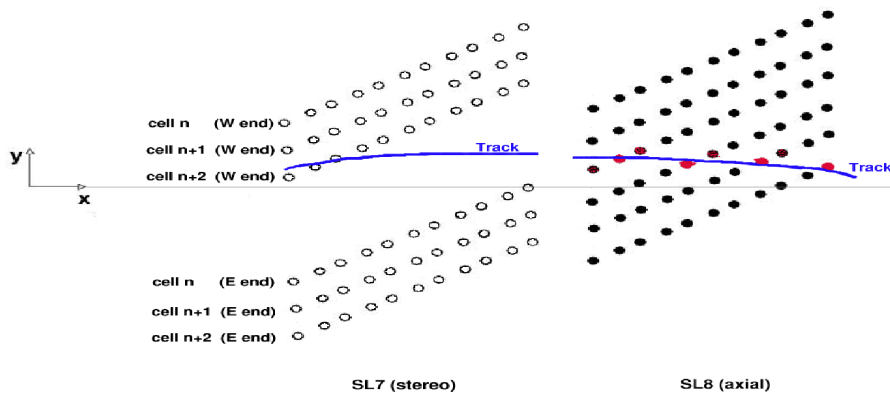


Figure 3.20: Stereo track reconstruction. A few cells of SL8 and SL7 are shown. The ϕ position of the cells in SL8 does not change as a function of the z coordinate. The cells number n , $n+1$ and $n+2$ are shown as a function of their z position. An axial track is first reconstructed from the hits (sense wires in red) in SL8. Another track is reconstructed with full z information from the hits in SL7. If the stereo track matches the axial track (as it happens in the diagram) the axial segment is appended to the stereo track and a new fit is performed.

value of $z_0 = \cot(\theta) = 0$, the z_0 and $\cot(\theta)$ obtained as a result of the fit are then fed as the input for a new fit, iterating up to ten times. All the stereo segments with $|z_0| \leq 175$ cm enter the list of candidate stereo matches. If there are no such segments in the outer stereo superlayer the next inner superlayer is searched. As before, these segment candidates are used to search for matching segments in the next inner stereo superlayers. A set of matching segments should have ϕ differences less than 0.01 rads. The matching stereo segments are then used to search for matching segment in the inner stereo superlayers. Other algorithm are applied at this stage to recover stereo information for axial tracks that have failed the stereo-matching algorithm.

At this point the fit of the three axial parameters and two stereo parameters of the track were done independently. The next step is to perform a full 5-parameter fit. Only tracks with at least two stereo hits and 12 axial hits are fit. The fit is defined to be a success only if all the following apply:

$$\begin{aligned} |C| &\leq 0.1 \\ |d_0| &\leq 150 \text{ cm} \\ |z_0| &\leq 300 \text{ cm} \\ |\cot(\theta)| &\leq 4 \end{aligned}$$

The final step is to remove residual hits from the track (i.e. hits on wires to which the track distance was larger than 600 microns ¹¹) and make a final refit. If the new fit fails, the track keeps its old parameters. The final list of COT-only tracks is then made by carefully removing duplicate tracks obtained from the SL and HL algorithms.

The most complete track is obtained when the silicon detector hits are added to the COT track information. In general, and depending on the

¹¹These hits are likely redundant and poorly measured

specifics of the analysis, both COT only or COT+SVX tracks are used.

The COT+SVX track collection is made starting from the COT-only tracks and extrapolating each track through the Silicon SVX detector from the outer layers to the inner ones. At each layer the error matrix of the track parameters is updated to reflect the amount of material traversed. The silicon hits close¹² to the extrapolated track are added to the track and a refit is performed. Each time a hit is appended a new track candidate is generated. Each of these tracks is further extrapolated until all the layers of the detector are searched. From the full list of track candidates associated with one COT track the best one is selected based on the number of hits and quality of the fit. The typical position resolution of a COT+SVX track is about $40\ \mu\text{m}$ for d_0 and $70\ \mu\text{m}$ for z_0 .

3.3.3 Calorimetry

Surrounding the Tracking volume and outside the solenoid is located the calorimetry system. The CDF calorimetry system features 4 sub-systems; the “Central”, “Wall”, “Forward or Plug”, and “MiniPlug” calorimeters, providing energy measurement in the region $|\eta| \leq 3.4$ as shown in Figure 3.21.

This section describes the mechanical and geometrical design of the CDF calorimeters.

Central calorimeter

The Central calorimeter has a cylindrical shape surrounding the beam pipe along the \hat{z} direction. It is made by the union of two cylindrical pieces that join at $z=0$ and extend over either side of \hat{z} direction covering the region $|\eta| \leq 1.1$ as shown in Figure 3.21. Each of these cylindrically-shaped pieces

¹²The closeness of a hit to an extrapolated region is defined in terms of the error in the position of the extrapolated track

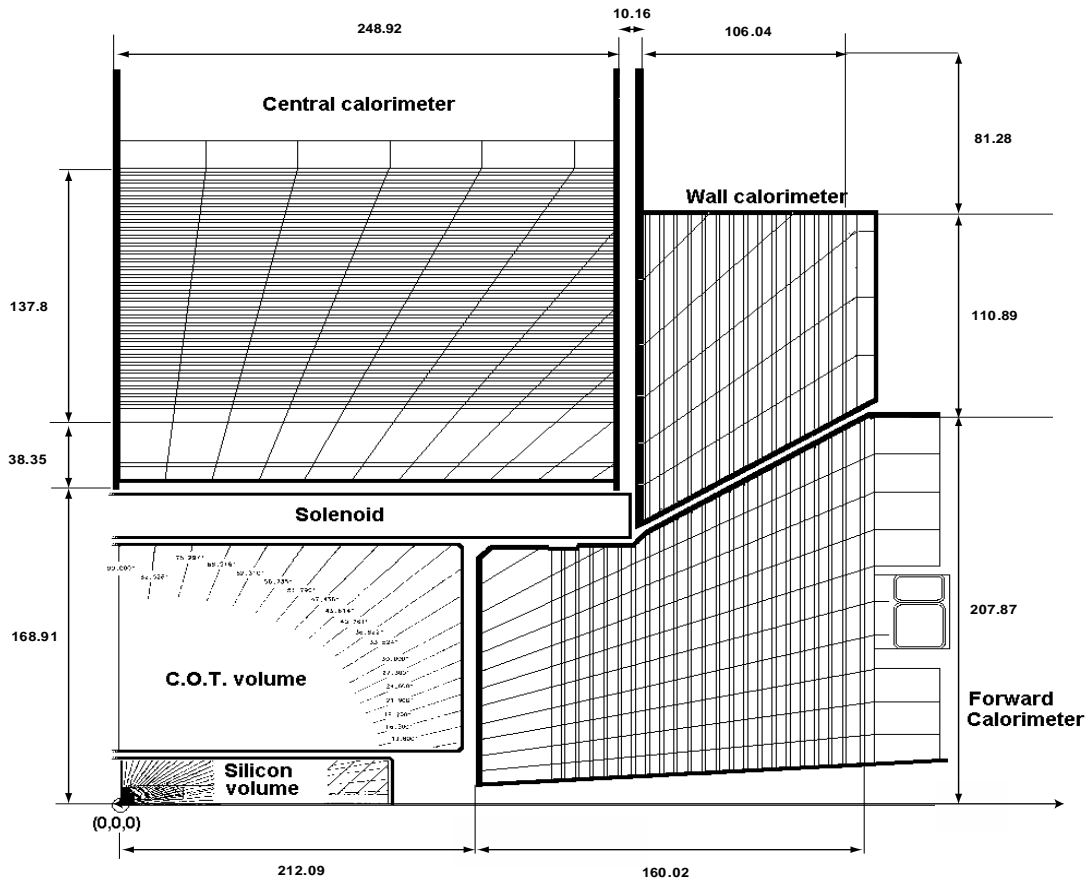


Figure 3.21: Calorimeter sub-systems. The schematic diagram shows a quadrant of the CDF detector. The CDF detector features four calorimeters, the “Central”, the “End Wall”, the “Forward or Plug” and the “MiniPlug” calorimeter (not shown). All lengths are in centimeters.

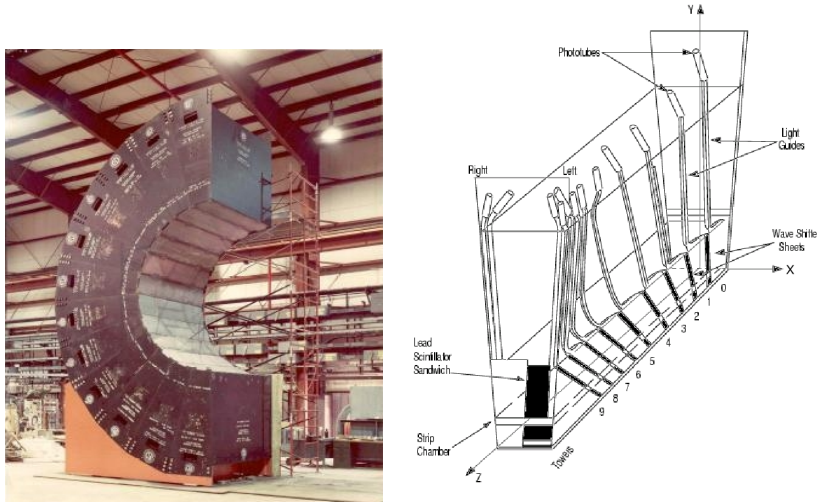


Figure 3.22: Left: Construction stage of one arch. It contains 12 wedges and constitutes a quarter part of the central calorimeter. **Right:** Schematic diagram of one central wedge.

is in turn composed of 24 wedges in two so called arches with 12 wedges each. Each wedge spanning 15° in azimuth. The Figure 3.22(left) shows the construction stage of one arch.

All the wedges are identical with the exception of one in which a hole has been made in order to obtain a path through which cables and wires of different sub-systems can reach the exterior of the detector. The typical geometry of the wedge is shown in Figure 3.22(right).

The wedge has length along the \hat{z} direction of 249 cm and spans from a inner radius of 172 cm to a radius of 345 cm.

In each wedge the inner 35 cm features the electromagnetic part (CEM, **C**entral **E**lectro **M**agnetic), while the outer rest is used to place the hadronic calorimeter CHA (**C**entral **H**Adronic).

The CEM and the CHA are sampling calorimeters. They are built by stacking layers atop each other. Each layer is made of two components

carefully chosen to obtain the most accuracy for the type of measurement wanted. The CEM has 31 layers of polystyrene scintillator (SCSN-38) sheet of 5 mm thickness together with a lead sheet of 3.175mm thickness. The CHA is made of 32 layers of 2.54 cm iron thickness with 1 cm thick scintillator. While the iron and lead are single-piece sheets running along the \hat{z} direction, the scintillator is cut and isolated in several pieces (or tiles) along the \hat{z} direction. In each layer the size of the different pieces vary, so that when looking from the interaction point the same piece number in all the layers are in line at the same η coordinate, thus forming what is called projective towers, as is clearly seen in Figure 3.21.

The light from all the pieces of scintillator that form the same tower is collected together, but for the CEM and CHA separately so to obtain, after suitable signal conditioning and calibration, a single energy measurement in each CEM tower and each CHA tower. The segmentation in the CEM matches that of the CHA, i.e. the η values of the center of the towers matches in both calorimeters. The difference between the center of two consecutive towers is a very constant $\delta_\eta = 0.11$.

The CEM has ten projective towers. The total radiation length for a particle traveling from the origin through the first tower ($\eta \leq 0.11$) is about $18 \chi_0$, but this amount changes if the particle travels at an angle, as it does when passing higher η towers. To keep the radiation length constant across all the towers in a wedge, a fraction of the lead sheets has been replaced with a regular plastic sheet. This portion increases with the η tower, such that the last tower has approximately a total of 20 lead sheets versus the 31 that can be found in the first tower.

The capabilities of the CEM are enhanced by the implementation of two extra detection systems in the wedges' CEM volume; a proportional chamber named CPR (**C**entral **P**Reradiator) located just in front to the

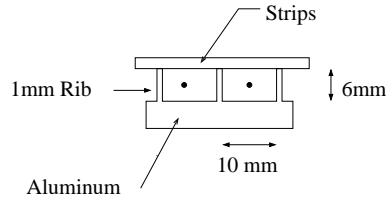


Figure 3.23: Chambers of the central electromagnetic shower detector.

CEM, and a Proportional strip detector (CES) at about $7 \chi_0$ in the tower. The interaction of particles with the solenoid and tracking material before entering the calorimeter results in soft shower profiles that are measured in the CPR. This serves as a discriminator to distinguish between pions, conversion electrons and electrons coming from the primary vertex, and can help to reduced the electron background, as resulted in the Run I top quark analysis[13] by a factor of 2. The CES is a two-dimensional shower profile detector located at the expected shower maximum of $7 \chi_0$. It is made of wires running along the \hat{z} direction and strips orthogonal to them (see Figure 3.23). It provides valuable information used in the identification of electrons and photons. The position measurement can be matched to existing tracks while the transverse shower profile can be used to separate single photons from the two photon decays of π^0 s.

When the particles of the shower pass through the scintillators they emit light. In the CEM the light going out of the thin edge of the scintillator is collected by a flat panel of Y7 Polymethylmethacrylate (Y7 PMMA) transverse to the scintillators of the tower. Two such panels are used for each CEM tower in either sides of the wedge. The upper edge of the panel is molded such that it smoothly converges into a squared 3 cm by 3 cm section optically coupled to a long rod that extends radially passing the CHA and ending in a PMT. The light collection design is shown in Figure 3.24 for the CEM and the CHA. The energy deposited in a CEM tower is then obtained

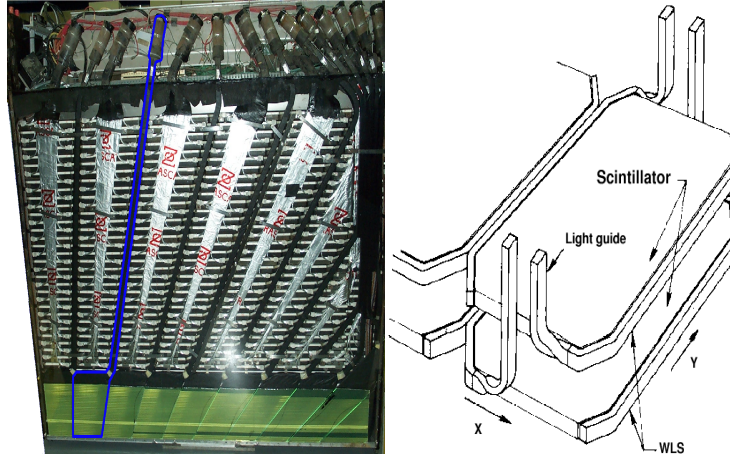


Figure 3.24: Left: A detailed picture of the side of a central calorimeter wedge. The light is collected from the CEM by the flat panels at the bottom and redirected via a square light guide to the PMT in the upper side. In the CHA the light is collected from each tile and guided upwards to merge to a PMT. **Right:** Detail of the light collection in CHA scintillator tile.

by adding the information of both tower's PMTs. The PMMA also acts as a wave shifter, reducing the frequency of the light emitted by the SCSN-38 scintillator to that optimum for the Photo Multiplier Tubes (PMT). The energy resolution of the CEM is measured to be $1.7\% + \frac{13.5\%}{\sqrt{E}}$

The CHA light collection is slightly different. The light coming out of each scintillator tile is collected by a two square-shaped light guides that surrounds the tile as shown in Figure 3.24(right). In each hadronic tower the light guides from one wedge side are joined together and extended until reaching the PMT. Details of this can be seen in Figure 3.24(left). As with the CEM, the light in the CHA is collected using two PMTs per tower. The energy resolution of the CHA is $\frac{80\%}{\sqrt{E}}$ when the CHA tower information is combined with the WHA.

Out of the ten CEM towers only 8 are properly projected into the CHA, the other two projecting outside the CHA from the far \hat{z} side. The total

interaction absorption length for the first tower is about $4.7\Lambda_0$, but the higher η towers project outside the CHA from the side before completing this length. This is completed by a set of towers located in the WHA (**W**all **H**adronic), as explain in the next section.

Wall hadron calorimeter

The WHA extends the hadronic towers of the CHA to roughly complete $4.7\Lambda_0$ per tower. The material components of the layers in the WHA are the same as the CHA. The physical characteristics however are different, as the WHA towers are made of layers that lie parallel to the (\hat{x},\hat{y}) plane, and thus are perpendicular in orientation to those of the CHA as it is shown in Figure 3.21. The WHA uses 15 layers of 5 cm iron and 1.0 cm scintillator.

Forward calorimeter

The forward calorimeters are placed surrounding the beam pipe at 172 cm in the \hat{z} axis at either sides of the interaction point (see Figure 3.25 and Figure 3.21). It provides coverage in the region $1.1 \leq \eta \leq 3.6$. As with the central calorimeter the forward has an electromagnetic (PEM) and a hadronic (PHA) section. As before both sections are made of stacked layers of scintillator and lead (for the PEM) or scintillator and iron (for the PHA). The layer orientation follows that of the WHA where the layers lie in the (\hat{x},\hat{y}) plane. In the transverse plane the calorimeter is sectioned in 12 pieces of 30° in ϕ called wedges. The section of a wedge is shown in Figure 3.26 where the tower segmentation can be appreciated. The lines define the boundaries of the scintillator tiles. The tiles at the same position in different layers define the projective towers. The forward calorimeter covers the region $1.1 \leq \eta \leq 3.6$ with 12 towers for a given angle ϕ .

The PEM has 23 layers composed of 4.5mm lead and 4mm scintillator

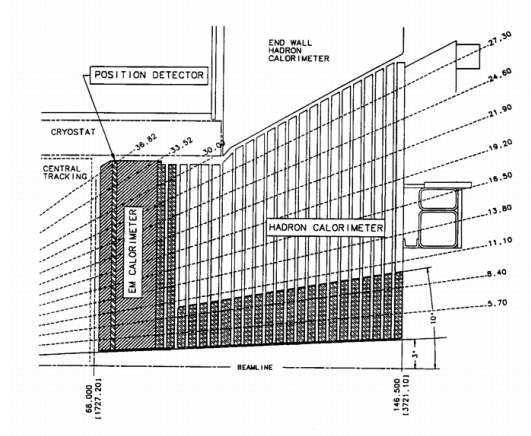


Figure 3.25: The forward calorimeter section. Detailed diagram showing the location of the electromagnetic and hadronic calorimeter, the shower maximum detector and the tower segmentation.

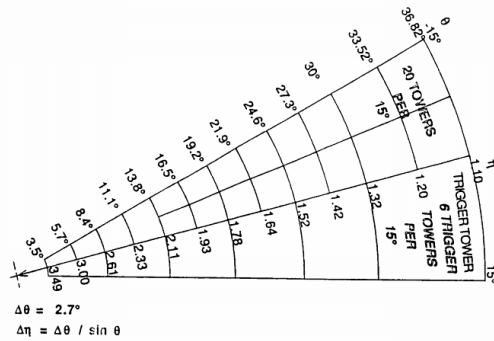


Figure 3.26: The section of a wedge in the forward detector. The physical scintillator tiles in the region $-15^\circ < \theta < 0^\circ$ are repeated but not shown in the region $0^\circ < \theta < 15^\circ$, where the diagram shows the logical towers used in the trigger system.

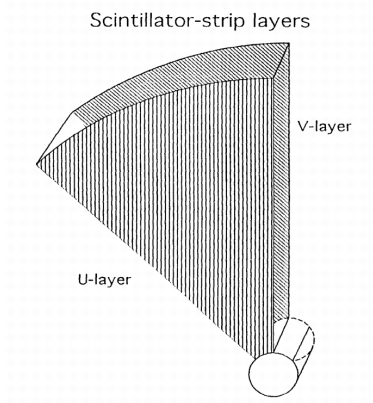


Figure 3.27: The U and V layers that conform the Shower maximum detector (PES) of the Plug forward Calorimeter.

type SCSN38 each, resulting in about $21\chi_0$ at normal incidence. The PHA has also 23 layers of 5.08 cm iron and 6mm scintillator resulting in about $7\Lambda_0$ ¹³. The energy resolution of the PEM is $1\% + \frac{16\%}{\sqrt{E}}$

The light is collected from the scintillator tiles by a wavelength shifting fiber (WLS) embedded in the scintillator. One fiber per tile is used, adding up to 40 fibers per layer per wedge. All the fibers of a single projective tower in the PEM are joined together in the tower's PMT. The same is done for the PHA towers, resulting in 480 PMT's for the PEM and another 480 for the PHA.

The PEM is also implemented with a shower maximum detector (PES) similar to the one implemented in the CEM. This 2-D position sensitive detector is placed at a depth of $6\chi_0$ inside the PEM calorimeter, and helps discriminate between electrons and di-gamma decays of π^0 's. The PES covers a circular area of 2.6m in diameter at 1.8m from the origin of the detector. It is divided into 8 sections of 45° in ϕ , thus spanning three PEM wedges. Each sector (see Figure 3.27) contains two layers (named U and

¹³In addition the PEM material adds about $1\Lambda_0$ to the total interaction length.

V for reasons beyond my understanding) of 5mm pitch scintillator strips. These layers are held together with 3.175mm thick lexan material. The strips in the U and V layers lie at a 45° crossing angle allowing the 2-D position identification.

In order to reduce the occupancy of the strips expected from the underlying event the U and V layers are both divided into an upper and lower segments corresponding to $1.13 \leq \eta \leq 2.60$ and $2.60 \leq \eta \leq 3.50$ respectively. This η division line matches the PEM calorimeter inter-tile boundary. The occupancy expected in the lower segment is two to four times that of the upper one, but more segmentation is impractical if not physically impossible. The strips connects to a WLS fiber that carries the light to a channel in a Multiple Anode PMT (MAPMT) for readout.

It should also be mentioned that the scintillator of the first layer of the PEM is 10mm thick (as opposed to 4mm thick) and made out of BC408, a different scintillator type that yields about 1.6 times more light than SCSN38, the one used throughout the rest of this calorimeter. The larger thickness of the scintillator sheet and the larger light yield allow this layer to be used as a preradiator (PES), providing a good discriminator between gamma and π^0 's. This layer is read out separately and all the fibers read out using Multiple Anode PMT's (MAPMT).

3.3.4 Muon detectors

Most particle detection systems are not specific to one particle. While the CEM is sensitive to electrons it also detects photons. The detection of a shower in the CEM does not undoubtedly indicates the nature of the original particle. Similar statements can be made about the CHA and the tracking sub-systems. The properties of muons on the other hand, allow for a clear, often unmistakable identification.

The large mass of the muon compared to that of the electron for example, results in a $\frac{M_{e\ell}^2}{M_{m\mu}^2} \sim \frac{1}{40000}$ relative suppression of electromagnetic bremsstrahlung[16], the primary process by which electromagnetic showers are created. Muons, as electrons, are weakly interacting particles and so they are not subjected to the strong interaction with atomic nuclei that could result in hadronic showers. Yet the mass of the muon is smaller than most of the other particles, and thus its decay to other particles that may interact hadronically is, unlike the lepton τ , kinematically forbidden, resulting in the muon's long decay time. While the net result is the muon's ability to pass through larger amounts of matter without interacting than any other charged particle, its only possible identification handles left must rely on its mass and charge properties.

CDF takes advantage of such properties by locating (track) detectors of charged particles behind large quantities of absorber. The only charged particle with the ability to pass through such absorbers with high efficiency is a muon, so a "hit" in this charged particle detector is often¹⁴ a clear enough indication of a muon.

The CDF muon system is typically in the form of drift chambers stacked in a few layers to reconstruct the particle's track information. In the muon system a pair of adjacent stacks is called a tower, and the portion of a reconstructed track is called a *stub*. The timing information is obtained, when possible, by placing a scintillator in front of the drift chambers.

In an event by event basis there are, however, other processes that could mimic a muon with "hits" in the muon system. This processes include:

- Real muons from cosmic rays, which are (of course) not coming from the primary vertex. Those out of time with the collision are ignored.

The rest are typically vetoed in offline calculations with the help of

¹⁴See ahead for muon misidentification sources.

the COT track information.

- Particles that, due to statistical fluctuations, do not interact in the absorber or interact in the last portion of it, starting a late shower that extends outside of the absorber and into the muon system. This process is called in the field “punch-through” fake muons.
- Particles that interact in the beam pipe and are deflected towards a muon system. These particles are typically out of synch with the time of the collision by about 30 to 40 ns.
- Particles originally coming from the primary collision that interact in the beam pipe. These are not so much out of synch, and increase with η due to the larger number of interaction lengths.

To minimize these effects, CDF requires that the stub matches a COT track in order for the stub to be considered left by a muon. The use of larger absorbers to reduce some of these contributions is not always advised. First, because the effects of multiple Coulomb scattering grow with the traversed material, resulting in tracks reconstructed at the muon system that do not represent the original muon direction, and thus do not match the corresponding COT track. Second the muon also loses (little) energy while traversing the absorber. The minimum transverse momentum value (p_T) at which a muon will not pass the absorber is called the rangeout threshold. The rangeout threshold is at CDF in general very small compared to high p_T muons this dissertation is interested in.

At CDF four such charged particle detection sub-systems form the overall CDF muon detection system. These systems are named CMU (**C**entral **MU**on Detector), CMP (**C**entral **MU**on **uP**grade), CMX (**C**entral **MU**on **eX**tension), and IMU (**I**ntermediate **MU** Detector). The coverage of all these systems is shown for reference in Figure 3.28, and a more detailed

description can be found in the following sub-sections.

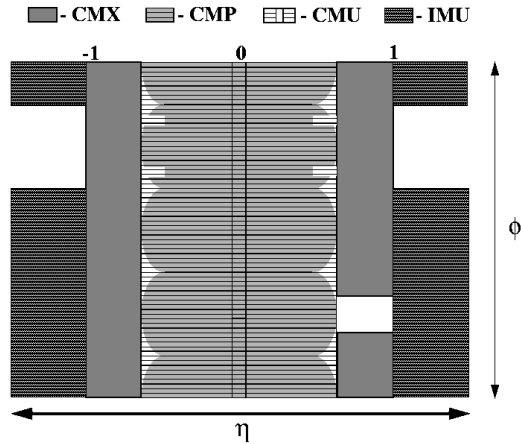


Figure 3.28: The coverage in $\eta - \phi$ coordinates is shown for the Muon system.

CMU

The Central muon system shown in Figure 3.29, is housed in the Central calorimeter wedges illustrated in section 3.3.3. As the central calorimeter it has a cylindrical shape and is located at a minimum radius of 347 cm. The calorimeter serves as the absorber and the muon rangeout threshold is about $1.4\text{GeV}/c$, in most part due to the heavy calorimeter material.

Due to geometrical and mechanical constraints only 12.6° (out of the 15° total) of the wedge are instrumented, leaving a 2.4° gap between chambers in consecutive wedges. A central gap of about 18 cm is also presented between chambers in east-side and west-side wedges. Figure 3.30. In each wedge the CMU system is segmented into three sections of 4.2° each as shown in Figure 3.29. Each section consists of four stacked layers of drift chambers. Each layer has four single-wire drift cells. The cells run along the \hat{z} direction and are filled with a mixture of Argon-Ethane-Isopropyl in 50:50:1.7 proportions providing a drift velocity of about $54 \mu\text{m}/\text{ns}$. Each sense wire

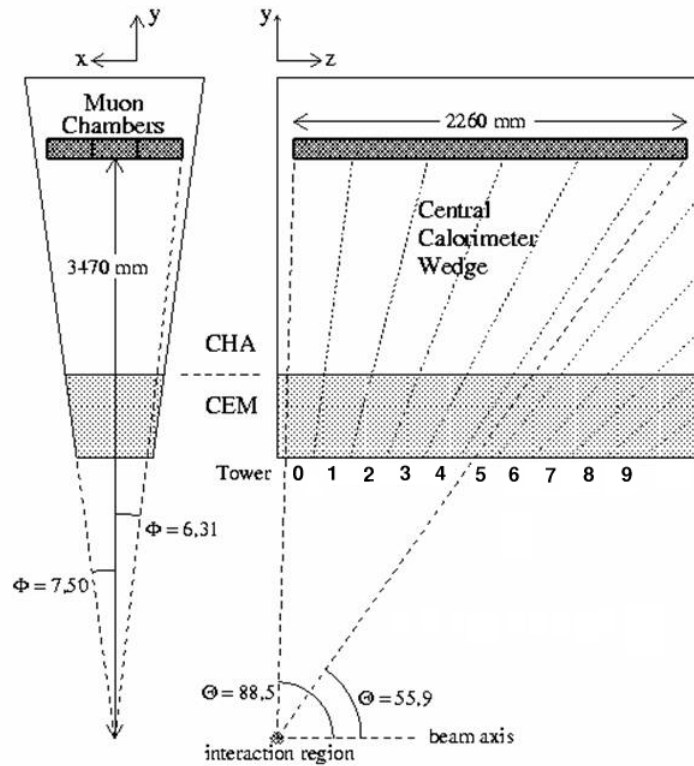


Figure 3.29: The CMU muon chambers are located in the Central Calorimeter wedge geometry, at a larger radius than the CHA.

is attached to a TDC to get timing information.

The cells are made of aluminum and held at -2500V while the sense wires are held at $+2325\text{V}$. The upper two layers have slightly larger cells than the lower two, resulting in a slight offset of the sense wires between layers of up to 2mm in the outer cells. This allows us to resolve the two-fold ambiguity characteristic of drift chambers of which side of the wire the track passed through.

The CMU system also provides the z coordinate of the track by the charge division method. This method essentially consists of collecting the charge in both ends of the wire. Due to the wire resistivity the charge will

differ according to the z position of the track. If Q_1 and Q_2 are the collected charges at both ends of the wire, the position z_0 of the track from the end in which Q_1 was collected is $z_0 = L \times \frac{Q_1 - Q_2}{Q_1 + Q_2}$ where L is the total length of the wire.

The clever CMU design connects wires of adjacent cells together in one end in order to perform charge division to find the z coordinate of the hit.

The two most significant limitations in the CMU system performance are: A) the short length of the absorber in front of it, i.e the calorimeter. With only $5.5\chi_0$ the showers generated in the CHA are often extended beyond it reaching the CMU system and producing “fake” muon signals. And B) the gaps between wedges, which add up to 57.6° or 16% of the 2π ϕ coverage.

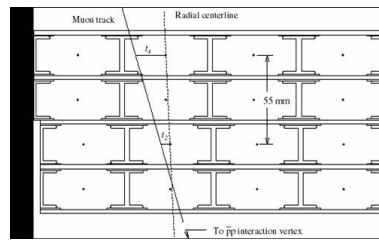


Figure 3.30: One CMU section (of the three) located in a central calorimeter wedge. The details of the cell are shown. The black line on the left is the lateral wall of the wedge.

CMP

The CMP (or **C**entral **M**uon **uP**grade) is designed to improve upon both limitations of the CMU system. Outside the detector and in the sides of an imaginary rectangular box another set of muon scintillator-chambers is located, see Figure 3.9 .

These chambers are preceded by a heavy steel absorber that adds $2.3\chi_0$ for a total of $7.8\chi_0$. With this additional absorber the rangeout threshold reaches only $2.2\text{GeV}/c$, and is still well below typical muon energies from

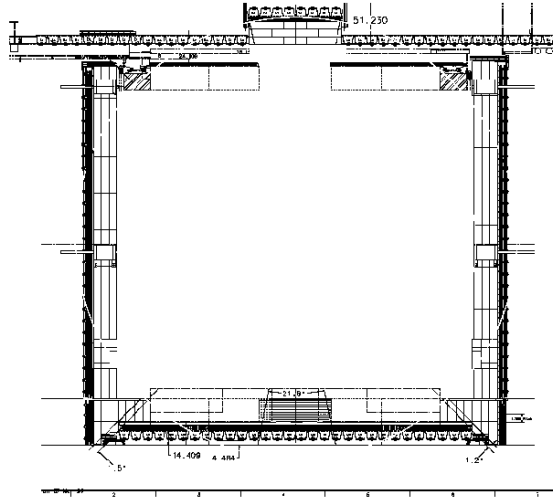


Figure 3.31: Positioning of the CMP system in the CDF detector hall.

electro-weak sources. As can be seen in the diagram of Figure 3.31 and Figure 3.9, some portions of the system take advantage of already present steel, like the upper and lower solenoid return yokes, and so all the sections may not lie in the same plane.

The CMP also provides full coverage in ϕ . Due to its rectangular geometry the η coverage depends on the ϕ coordinate, as seen in Figure 3.28; it is roughly about $\|\eta\| \leq 0.6$.

The CMP system is based on single wire drift chambers 2.5 cm by 15 cm and 640 cm long as shown in Figure 3.32. The chambers are arranged in four layers with half-cell staggering between them. Behind the cell a scintillator system (named CSP **C**entral **S**ciintillator **u**Pgrade) provides timing information. As with the CMU, each wire is read by a single TDC.

With the inclusion of the CMP system a new handle for the evaluation of the number of CMU “fake” muons due to “punch-through” is at hand. In order to obtain cleaner samples of muons it is now common practice to require that CMU hits have a corresponding CMP hit, in addition to match

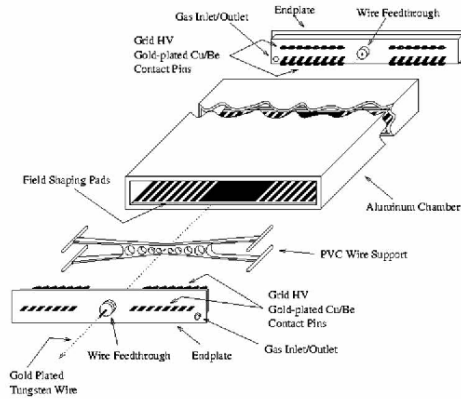


Figure 3.32: Drift chambers used in the CMP and CMX muon detector systems. The wire supports are used only in CMP.

a COT track. These muons are informally called CMUP muons.

While the CMP provides for a better discriminator of muons than the CMU alone, its η coverage is limited, and a big fraction of muons get lost in uninstrumented regions at larger η .

CMX

The CMX (Central Muon eXtension) enlarges the coverage of the muon system, providing extra coverage in the region $0.6 \leq \eta \leq 1$, while slightly overlapping in the region $\eta = 0.6$ with the CMU. The CMX consists of a pair of arches at each end of the detector. The arches are retractable to allow maintenance operations. In each side the CMX chambers follow the surface of an imaginary cone whose apex lies in the \hat{z} axis further away from the detector. See Figure 3.33 to see the arches during the detector assembly period. The aperture angle of the cone is about 45° .

The two arches are complemented with two more chamber arrays at the top and bottom, which are not shown in Figure 3.33. While the upper chamber is made of the same components as the arches the lower one has



Figure 3.33: The CMX arches in the detector hall. The arches are still to be complemented at the top and bottom to give a full ϕ coverage. The rest of the CDF detector is yet to be put in between them. Part of the IMU system is also shown surrounding the yellow toroids.

a finer segmentation. In the arches and the upper chambers the CMX is segmented in wedges, each spanning 15° in ϕ . Each wedge is composed of 8 layers of a 180 cm long version of the drift chambers used in the CMP. The layers are staggered as shown in Figure 3.34 so that all particles will traverse at least 4 layers, in order to accurately reconstruct the track.

While no additional steel was added in front of this detector the large angle from the interaction point through the calorimeter, solenoid yoke, and support structures yields considerably more absorber material than in the central region.

The CMX is also implemented with scintillators in what is called the

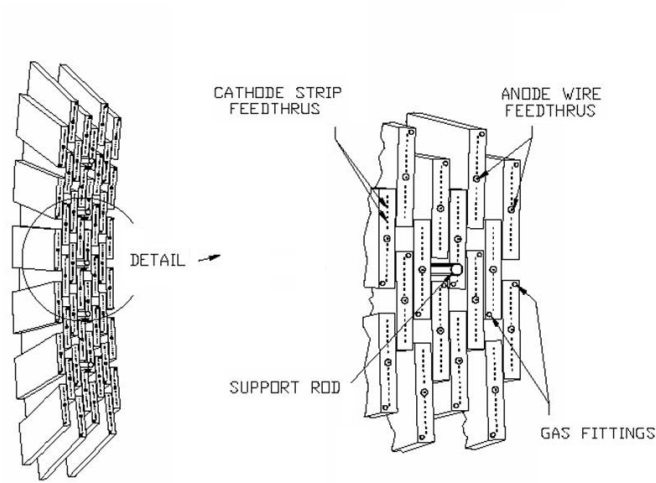


Figure 3.34: The eight-layer CMX drift chamber system.

CSX (**C**entral **S**cintillator **eX**tension). In the arches the scintillators are installed both in the inside and outside of the chamber and are half-cell staggered. Each scintillator is read by a single PMT.

In the lower chambers scintillators are placed in only one side, and read with two PMT's from both ends to allow the computation of a mean-time.

IMU

The IMU (**I**ntermediate **MU**on system) covers the region $1.0 \leq |\eta| \leq 2.0$. It is motivated by the introduction of high η tracking systems (as ISL). The heart of the detector is a system similar to the CMP/CSP that is mounted on the other side of the forward toroids at each side of the detector. The IMU is then behind about 6 to 20 interaction lengths of steel (see Fig3.33), on average more than the CMP. There is additional pinwheel of counters between the toroids and on the endwall that are used for triggering.

As always muons are identified with stubs in the chambers. The counters provide a time stamp that must coincide with the pinwheel counter.

The toroids are retractable to allow for service work in the plug and other systems, but in normal data taking conditions are pushed next to the detector.

3.3.5 TOF

The TOF (**T**ime **O**f **F**light) is dedicated to measure the time of flight of the particles generated in the primary interaction. The TOF system consist of 216 scintillator bars 279 cm long arranged in a cylindrical geometry. The bars have a square cross section with an approximate side of 4 cm, and occupy the space between the COT and the cryostat of the solenoid (see Figure 3.35) at a radius of 138 cm. The bars are made of plastic scintillator BC-408, which provides a fast rise time and long decay time while having a bulk attenuation length of about 380 cm. The bars are placed next to each other providing full coverage in ϕ and covering $|\eta| \leq 1.0$.

Each end the bars are coupled to Winston cone light guides attached to fine mesh PMTs. The PMT's are located *in situ* and thus embedded in the solenoid's 1.4 T magnetic field. This reduces the PMT's gain to about 2×10^4 , about 500 less than if no magnetic field is present. To increase signal, a custom made amplifier with a gain of about 15 was appended to the output of the PMT.

The TOF measures the time of flight of the particle from the moment the interaction occurs to the moment the particle traverses the TOF bars. The time of the interaction is determined by the tracks in the event and the TOF system provides the time at which the particle passed through a bar, taking into account necessary corrections. The difference between these two times is the time of flight of the particle.

Since the length of the track between these two points is known from the tracking systems, the TOF provides a direct measurement of the particle's

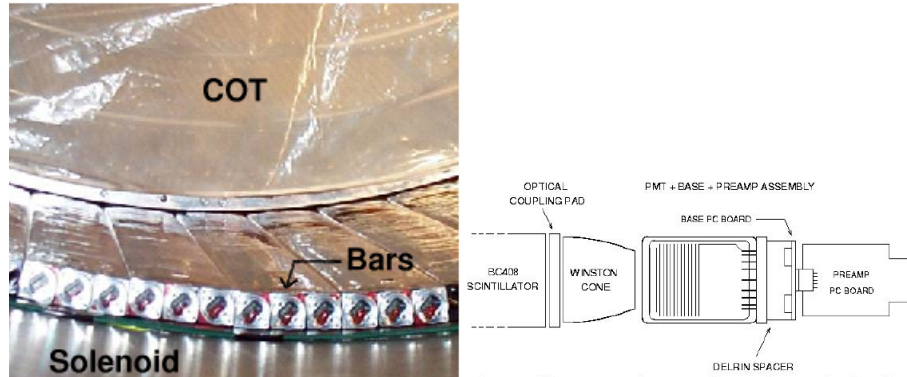


Figure 3.35: **Left:** TOF bars installed in the lower portion, between the superconducting solenoid (surface below) and the COT structure (above). **Right:** Detail of the read out design of the TOF bars.

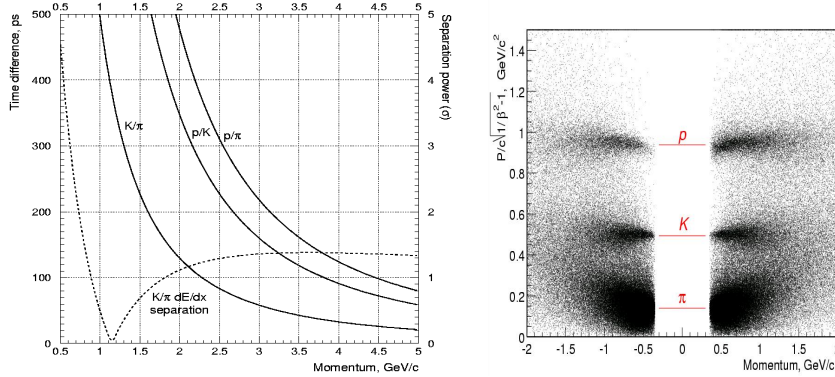
velocity. For a given momentum the smaller the time difference, the larger the velocity and the smaller the mass. The mass can be directly calculated from $m = \frac{p}{c} \sqrt{\frac{c^2 t^2}{L^2} - 1}$ where p and L are the momentum and length of the particle's track and t is the time of flight of the particle obtained from the TOF. In Figure 3.36(left) the expected time of flight difference between charged π , K and p relative to one another is shown as a function of momentum. The time difference between pairs of particles is translated into particle ID separation power assuming 100ps resolution. The performance of the TOF with early data is shown in Figure 3.36(right)

A more detailed description of the construction details is given in [17] and of its expected performance and impact in physics analysis in [18]

3.3.6 CLC

The CLC (Cerenkov Luminosity Counter) is located at each side of the detector in the 3° gap between the plug calorimeter and the beam pipe as shown in Figure 3.37. It spans from 184 cm to 405 cm in the \hat{z} axis.

It measures the average number of interactions per bunch crossing (μ).



Expected time of flight difference (in ps) between charged π , K and p relative to one another as a function of momentum and separation power assuming 100ps resolution. The dashed line shows the K/π separation from dE/dx measurement by the COT.

TOF reconstructed mass versus momentum. The data clusters around the charged π , K and p masses with a 60:30:10 proportion. Data from Tevatron store 860 (12/23/2001).

Figure 3.36: TOF performance

This information allows the computation of the instantaneous luminosity \mathcal{L} from: $\mu f_{bc} = \sigma_{p\bar{p}} \mathcal{L}$, where f_{bc} is the frequency of bunch crossing in the Tevatron and $\sigma_{p\bar{p}}$ is the total $p\bar{p}$ cross section of about 100mb at the Tevatron's $\sqrt{S} = 1.96$ TeV.

To measure μ the CLC takes advantage of Cherenkov radiation, the effect in which particles at velocities higher than the speed of light in the medium radiate light in a fixed angle (δ) with respect to its momentum. The angle (δ) depends on the refraction index of the medium (n) and particle's velocity such that $\cos(\delta) = \frac{1}{n\beta}$, and $\beta = v/c$.

The CLC is composed of an array of Cherenkov counters in the shape of long cones (cone-modules). These are made of 2 layers of aluminized mylar

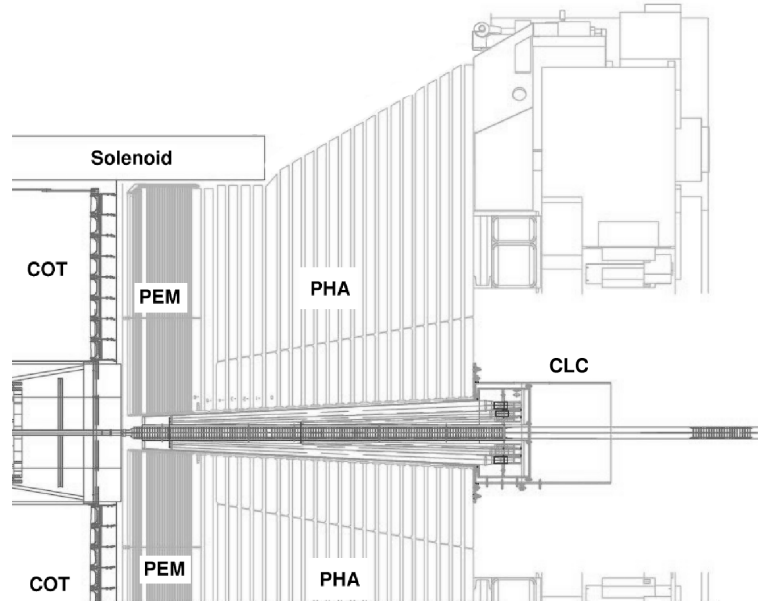


Figure 3.37: The CLC is located in the 3° gap between the plug calorimeter and the beam pipe.

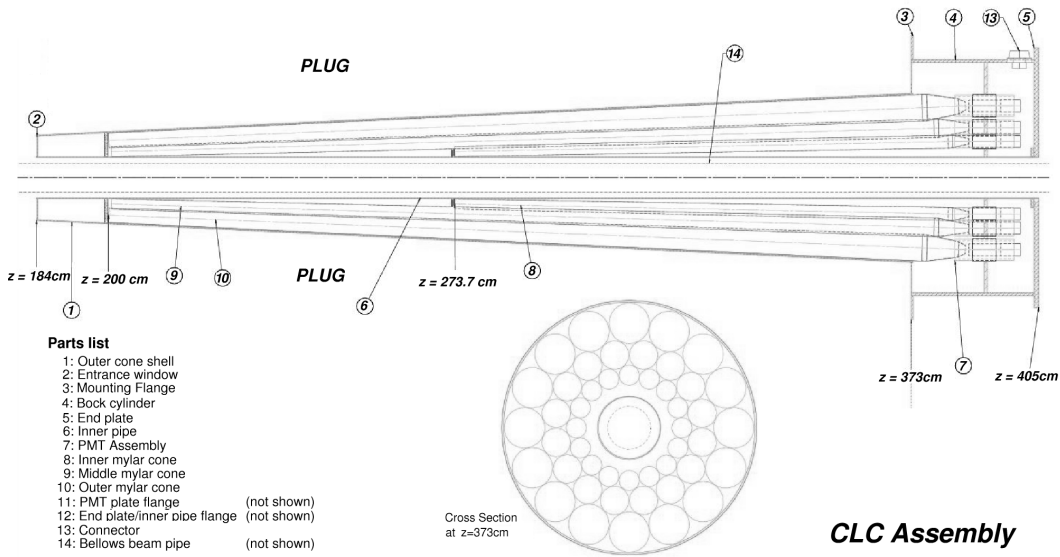


Figure 3.38: The CLC Assembly diagram. The cross section view at $z=373$ cm is also shown.

rolled into a conical shape, and have in one end a light collector that directs the light to a PMT, and in the other a glued plastic cap. There are three types of cone-modules arranged in three concentric (and conic) layers with 16 cones each. The full CLC consists then of 48 conical counters per detector side. See Figure 3.38

The cones are supported by two plates, one at 390 cm from the detector center just outside the volume of the forward calorimeter, and the other located inside the volume of the detector at about 184 cm from the detector center. These plates align and support the cones such that it has a good projective geometry with respect to the nominal collision point. The CLC is filled with isobutane gas at about 14.7 psig pressure. The conical geometry makes the CLC sensitive to particles coming from the collision point.

More detailed information on the CLC is found in [19] and [20].

3.3.7 The trigger system and data flow

As mentioned in section 3.2.5 the proton and antiproton bunches cross every 396 ns. With the current Tevatron luminosities of order $4 \times 10^{31} \text{ cm}^{-2}\text{s}^{-1}$ this results in about 1.6 interactions per bunch crossing, i.e 1.6 interactions every 396 ns or about 2.5 Million events/second.

There are two main reasons for which recording all the produced events is not feasible. First, with an average event size of about 100 kiloBytes, it will require throughput and storage capabilities of 250 GibaBytes/second, and there is currently no technology with such capabilities. Second, even if such technology existed the detector is not fast enough to read out and transfer all the information before the next bunch crossing occurs. It typically takes about 2 ms for a complete CDF detector readout, but there is only 0.4 ms between bunch crossing.

However, the majority of the produced events are of little interest to

the current CDF physics program. Most of these events are proton and antiproton passing right through each other with a low amount of momentum transferred between the interacting partons. Only occasionally there will be a hard parton-parton collision with large transverse momentum outgoing particles. The non-elastic, soft interacting events are typically called “minimum bias events”. The minimum bias event¹⁵ has a production cross section of order 10 mb, and is typically used for calibration purposes.

The CDF physics program is focused on much more rare events, with production cross sections typically smaller than $100 \mu\text{b}$. This is more than three orders of magnitude smaller than the total $p\bar{p}$ cross section. The $t\bar{t}$ production cross section, of special interest to this dissertation, is about 6.7 pb or nine orders of magnitude smaller than the minimum bias production cross section!

The two above problems are circumvented by the implementation of the CDF trigger system, which selectively reads out and stores only those events considered of interest. A schematic diagram of the CDF trigger system is shown in Figure 3.39(Left).

The CDF global trigger system has a three-level structure. The Level-1 trigger filters out the vast majority of the events without any interesting signatures. Since this level takes up to $5.5 \mu\text{s}$ to reach an accept/reject decision, the front-end electronics is equipped with a 14-event deep buffer to accommodate new events while the Level-1 decision is taken. The accepted events are further analysed by the Level-2 trigger.

The Level-2 trigger takes more time and adds more information to take a further decision about the event. If accepted, the full information of the detector subsystems is read out and passed to the Event Builder. There

¹⁵Some of the most popular models associate minimum bias events with non-diffractive inelastic interactions.

the different fragments of information from the different sub-detectors is collected, reordered and concatenated to build a single unit of information containing all the information for the event. The Event Builder then passes the full event directly to Level-3.

Level-3 then takes the final decision and, if accepted, the event is transferred to the Consumer Server Logger (CSL), a local mass storage system that temporarily stores the events. The CSL ultimately transfers the information to the Fermilab Feynman Computing Center (FCC) where is written to tape. If the connection between the CSL and the FCC were to break the CSL can store up to 8 hours of information before reaching its maximum storage capacity.

The CDF trigger system is described in detail in [22]. A detailed Description of the CSL and FCC can be found at [21].

In the following subsections a more detailed description of the parts that comprise the CDF Trigger system are discussed, with special emphasis on those that are relevant to this analysis.

Level-1 trigger system

A block diagram of the Level-1/Level-2 trigger system is shown in Figure 3.39. These trigger levels are managed by the Trigger Supervisor Interface (the box marked TSI/CLK in the figure), which also provides a global clock. The Level-1 is a synchronous trigger system. Every bunch crossing this trigger reads out the event information from the detector, stores it in the pipeline and makes a decision on an earlier event. The decision is taken based on “primitives”, a fast and rudimentary reconstruction of the raw sub-detector information. The Level-1 trigger uses primitives made from measurements of energy in the calorimeters (Central, Wall, and Plug), tracks in the COT, stubs in the muon systems (CMU, CMP and CMX) and,

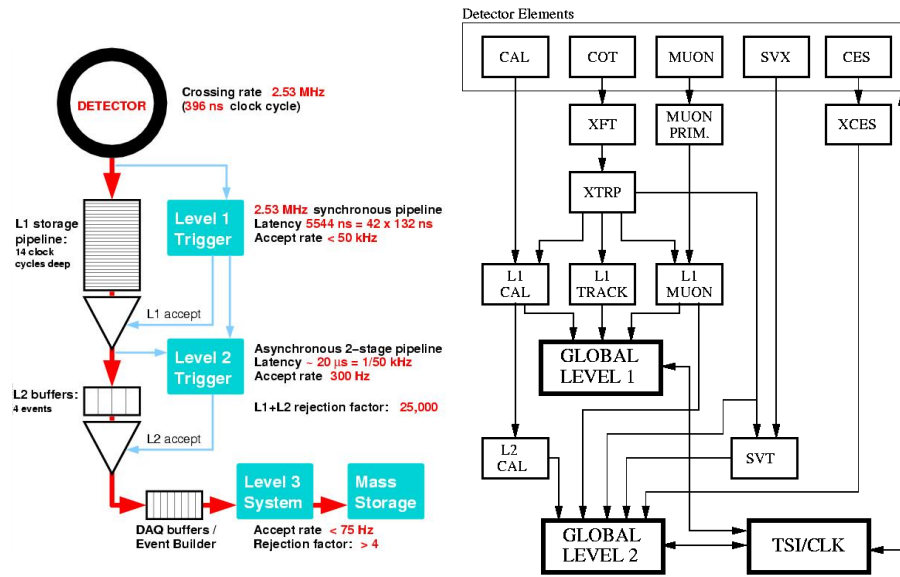


Figure 3.39: Left: Schematic diagram of the CDF global Trigger system. Right: Detailed block diagram of Level 1 and Level 2 trigger.

not shown in the Figure, coincidence hits in the CLC for minimum bias trigger and Time of Flight information. The first three are shown in Figure 3.39(right) as the boxes labeled L1-CAL, L1-TRACK, and L1-MUON respectively.

The L1-CAL information sets an array of 8 bits per each 15° wedge, representing 8 momentum thresholds per wedge. Track extrapolation is done using look-up tables so that tracks crossing wedge boundaries are handled correctly.

The L1-Muon basically informs what muon towers have fired¹⁶, and makes use of the real granularity of the muon sub-detector systems, as opposed to logical (typically bigger) granularity units.

These primitives are often combined to form electron, muon or jet objects, that are later to take part in the trigger decision process.

¹⁶ A muon tower is said to have fired if at least one of the stacks has a stub. See section 3.3.4 for details of tower and stubs.

In general Tracking reconstruction, even when done rudimentarily, is more complex to achieve than the reconstructions of primitives based on Calorimeter and muon information. The extra complexity of the tracking is shown in Figure 3.39(right) by the boxes labeled XFT and XTRP whose function is explained next.

XFT

XFT stands for eXtremely Fast Tracker, and is an online track processor to identify charged particles¹⁷ in the COT in time to take part in the Level-1 decision making process. The processor uses the information of the 4 axial superlayers only.

The identification algorithm basically consists of two steps: Segment finding and segment linking. The segment finding portion classifies all the COT hits into either prompt hits (drift time $< 44\text{ns}$) or delayed (drift time between 44ns and 132ns). Then in each superlayer a set of predefined patterns of prompt/delayed hits are applied to find all the segments. These predefined patterns were obtained assuming impact parameter equal to zero. The track's charge is then determined by the ϕ position and the track's slope in both the two outermost axial superlayers. The slope and the ϕ position conform a "pixel". The segment linking is then perform by matching all those pixels that appear to be part of the same track. If 4 or more pixels are found and an estimate of the track parameters is obtained. The tracks found by the XFT are passed to the XTRP and a copy is made to be used later in Level-2 if the event were to pass Level-1.

XTRP

¹⁷A minimum transverse momentum of 1.5GeV is required

The XTRP is the eXTRaPolator unit. It performs a quick extrapolation of the XFT tracks to other sub-detector systems such as calorimeter and muon chambers. This allows for a better identification of real physics objects (or particles) such as electron, jets and muons, as opposed to detector objects such as tracks, showers in the calorimeters, etc.

An algorithm that uses a particular logical combination of the primitives is called an individual (Level-1) trigger. These individual triggers are designed based on the desired event final state, or equivalently on the physics process to be studied. To cover the CDF physics program 64 individual triggers are implemented.

The Level-1 trigger system makes a decision for each of the 64 individual triggers, while also taking a global Level-1 decision. If the event is accepted the event information is passed to the Level-2 system together with the 64 bits representing the accept/reject decision for the individual triggers.

The Level-1 trigger accepts is less than 50 kHz, much smaller than the total input rate of 2.5MHz.

Level-2 trigger system

The Level-2 trigger is an asynchronous system that processes events as they are passed in from Level-1. The Level-2 decision is based on Level-1 primitives as well as in more accurately processed information from the Calorimeter, and extra information from the shower maximum strip chambers (CES) and the axial strips of the Silicon vertex detector (SVX). These are indicated in Figure 3.39(right) by the boxes labeled L2CAL, XSEC and SVT.

The L2CAL hardware uses the trigger tower provided by L1CAL and further calculates the total energy of the clusters by summing the energy of the towers that comprise it. The clusters are obtained by finding “seed” (energy above a “seed” threshold) and “shoulder” towers (which are con-

tiguous to the seed tower, above a “shoulder” threshold and below the “seed” threshold).

The need for L2CAL also arises from the fact that jets are not fully contained in Level-1 trigger towers, and thus the Level-1 threshold must be set to much lower values than the jet energy. But this also results in rates too high for the Level-3 processing, so the L2CAL provides a reduction in the jet trigger rates by calculating the total cluster energy (which should be close to the jet energy) and allowing a filter based on that. The L2CAL hardware also provides total transverse energy and transverse missing energy.

The XSEC hardware takes the information of the CES and generates a bitmap of strips with energy above a certain threshold. Then the XFT tracks, extrapolated by the XTRP, are matched with the bitmap to produce electron candidates.

The SVT system significantly improves upon the XFT track parameters. It extrapolates the XFT track primitive inside the SVX volume and recalculates the track parameters, this time adding the impact parameter information which is not present in the XFT primitives. It uses only the information of the axial strips of the SVX. The impact parameter is an indication of a displaced vertex, which is a strong and clean signature in many physics processes.

At the moment the data used in this analysis was taken the number of possible individual triggers for Level-2 was 128. This number was recently increased to 192. The Level-2 global decision is taken and if accepted the event is transferred to the Event Builder[23] and then to Level-3, together with the Level-1 and Level-2 primitives and individual trigger bits.

The Level-2 hardware takes less than $30 \mu\text{s}$ to make the global decision, and with the implementation of a set of 4 event buffers the total acceptance rate is below 300 Hz.

Level-3 trigger system

The Level-3 trigger system is a large array of conventional PCs running the Linux operational system. The farm is further composed of 16 sub-farms of identical structure. Each sub-farm is composed of a converter node and an array of 12 or more processor nodes. The subfarms are arranged such that two of them share an output node.

The event comes from Level-3 directly to the converter nodes of one of the sub-farms. There the ordered fragments of the event are combined into a unit of data call the event record. The event record is then the only information for a particular event. The converter choose a processor node in its own sub-farm and delivers the event record to it for analysis. In the processor event reconstruction is performed and the final trigger requirement is applied. The reconstruction process allows for more accurate information and detailed trigger requisits in the individual Level-3 triggers, currently more than 300.

If the event is accepted the processor sends it to the sub-farm's output node, where is subsequently tranfered to the CSL for temporary storage and ultimately is tranfered to the Feynman Computing Center to be written to tape.

The total Level-3 accept rate is about 75 Hz, as compared to the 300Hz input rate.

3.3.8 Data taking

From the operational point of view the data taking occurs in three basic steps. First, the detector is “set up”, this implies the initialization of the crates and front-end electronics and the download of settings to specialized electronic components for calibration and other purposes. The second step is actual data-taking which occurs in a very much automatic way and could

last in principle as long as the operator decides. There is a number of reasons to finish data-taking such as the approaching end of store, detector hardware or software problems, etc.

The data collected from the moment the detector is set up until the the data taking finishes is called a run, and is characterized by a single integer number. Each time the detector is setup the run number is incremented by one. In certain runs sub-detector systems could have malfunctioned, be turned off or be in a general bad state. When a run is finished, it is always properly marked to indicate the overall status of the sub-detectors systems. This information is later used to decide what runs to exclude (if any) from the data analysis. The list of runs to be considered good is called the good run list and strongly depends on the sub-detectors used in a particular analysis.

3.3.9 Off-line data processing and datasets

During data taking, the events passing Level-3 are further categorized into either of ten streams denoted with the letters A to J. All the streams are being written to tape simultaneously in a continuous flow from the detector as data is being taken.

To analyze the data further off-line processing needs to be done. The most important processing is called production. The production process unpack all the data banks and generates the collection of physics objects such as tracks, electrons, muons, jets, vertices etc. This is done in a very elaborate and time consuming way, unlike the rudimentary reconstruction that Level-3 performs.

The output of the production process is further subdivided into 35 datasets. In addition, and in order to reduce the size of the sample and for this analysis purposes only, further filtering is applied resulting in what

I call primary datasets. Secondary datasets are also obtained from the primary ones by applying additional requirements. The name of the datasets used in this dissertation, as well as the individual trigger requirements, are specified in Tables 3.1 to Table 3.3.

In general the “tight” electron (those with very strict electron identification cuts) sample is obtained from the bhel08 and bhel09 datasets. These datasets require any of the triggers listed in Table3.1, requiring the electron to shower in the central calorimeter, and with a total energy greater than 18 GeV. The primary sample is an intermediate sample obtained by requiring “loose” (as opposed to “tight”) electron identification cuts. The final sample is obtained in turn from the primary by requiring “tight” electron cuts. A more precise definition of “tight” and “loose” cuts is given in Section XXX (to be defined).

Similarly the “tight” muon sample is obtained from bhmu08 and bhmu09 datasets, in which “tight” muon identification cuts are required. This sample triggers require stubs located in the CMUP or CMX sub-detector systems. The stubs should also match a track in the COT with transverse momentum greater than 18 GeV.

A third dataset is made from the bpe08 and bpe09 datasets, and is used to collect events triggered by what is called a “Phoenix” (or PHX) electron. PHX electrons are forward with a $\eta \geq 1.1$. They deposit energy in the Plug electromagnetic calorimeter and have several hits in the Silicon Vertex detector (both SVX and ISL). The trigger requirements are missing transverse energy above 15 GeV, a cluster of energy in the PEM and a successfully reconstructed track from the cluster to the event’s primary vertex.

These dataset were produced with version 4.8.4 of the production executable. However, since that version of the executable was found to lack the right calorimeter constants, all the calorimeter dependent quantities were

re-produced with version 4.11.1 of the production executable.

electron sample provenance		
dataset type	name	filtering/requirements
L3 trigger	<i>bhel08/09</i>	ELECTRON70_L2_JET ELECTRON_CENTRAL_18 ELECTRON_CENTRAL_18_NO_L2 W_NOTRACK W_NOTRACK_NO_L2 Z_NOTRACK
primary	<i>btop0g/0j</i>	loose CEM electron cuts
secondary	tight electron	≥ 1 tight electron (baseline CEM e cuts)

Table 3.1: Dataset and trigger paths for the tight electron sample.

muon sample provenance		
dataset type	name	filtering/requirements
L3 trigger	<i>bhmu08/09</i>	MUON_CMUP18 MUON_CMX18
primary	<i>btop1g/1j</i>	loose muon cuts
secondary	tight muon	≥ 1 tight muon (baseline μ cuts)

Table 3.2: Datasets and trigger paths for the tight muon sample.

The tight electron, tight muon, and plug datasets represent data taken between March 2002 and September 2003. After selecting only good runs in which the detector status is believed to be in good operating conditions¹⁸ the total integrated luminosity ranges from 150 pb⁻¹ to 193 pb⁻¹, depending

¹⁸Good run list used is located at [24]. Runs with CSL and SVX beamline problems were removed from all lists by hand.

plug sample provenance		
dataset type	name	filtering/requirements
L3 trigger	<i>bpel08/09</i>	MET_PEM_L1_EM8_&_MET15_v4 MET_PEM_v10 PLUG_ELECTRON_20_v5 PLUG_Z_v3
primary	<i>unnamed</i>	MET_PEM_L1_EM8_&_MET15_v4 MET_PEM_v10

Table 3.3: Datasets and trigger paths for the plug sample.

on the detector requirements, as detailed in Table 3.4.

Sample	Luminosity (pb^{-1})
CEM/CMUP	193.5 ± 11.6
CEM/CMUP and CMX	175.3 ± 10.5
CEM/CMUP and SVX	161.6 ± 9.7
CEM/CMUP and CMX and SVX	149.8 ± 9.0

Table 3.4: Luminosity of datasets. Summary of integrated luminosity for some sub-detectors. The left column indicates the sub-detector systems that were in good working conditions during the data-taking process. The right column shows the integrated luminosity of the data obtained under such conditions. Other sub-detector systems were always working such as the COT tracking system and all the calorimeters.

3.4 Particle identification at CDF

The collision of proton and antiprotons can result in the generation of a large variety of final states particles. In particular, this dissertation considers final states coming from $t\bar{t}$ decay products, that are therefore highly energetic. This section describes the requirements, imposed on the information gathered from different sub-detectors, to efficiently identify the different particles in the high energy range.

The electron identification criteria is described first, followed by muon identification and jet reconstruction criteria. The section ends by describing the imbalance of transverse energy that can be used to identify the presence of neutrinos escaping the detector. The cuts described in this section will be referred to as “standard” in the rest of this dissertation. More detailed information about CDF particle identification can be found in [25].

3.4.1 Electron identification

High energy electrons can be identified by a high- P_T track in the drift chamber and large energy depositions in electromagnetic calorimeters. The geometry of the CDF detector imposes the categorization of electrons in two types according to the calorimeter in which the deposition takes place.

Central electrons

Central electrons traverse the central part of the detector, $|\eta| < 1.1$, leaving a high- P_T track in the COT and depositing their energy in the CEM calorimeter. To identify central electrons the following requirements are applied:

- $E_T = E \cdot \sin(\theta) > 20 \text{ GeV}$

The total electromagnetic energy deposited by the electron in the CEM

cluster (E) multiplied by the $\sin(\theta)$ of the COT track pointing to the seed tower of the cluster. The electron cluster is formed of a seed EM tower, defined as the tower where most of the energy is deposited, and a number of shoulder towers, which are added to the seed tower until the maximum cluster size is reached. The largest cluster spans two towers in pseudorapidity and one tower in azimuth. The energy E is corrected to account for non-linear effects and known differences in response between the different towers, as measured from $Z \rightarrow e^+e^-$ candidates.

- $P_T > 10 \text{ GeV}/c$

The transverse momentum of the COT track. The resolution of the track is improved by constraining the track to originate from the beam line position.

- $E_{had}/E < 0.055 + 0.00045 \cdot \text{GeV}^{-1} \cdot E_{total}$

The ratio of the energy deposited in the hadronic calorimeter cluster to what is deposited in the electromagnetic cluster. The second term in the right hand side compensates for inefficiency of the cut at very high energies, as the electron shower leaks into the hadronic calorimeter.

- $E/P < 2$

Ratio of the electromagnetic calorimeter energy to the momentum of the track as measured from the COT track. This cut helps reducing the number of jets that fake electrons. These jets typically contain a π^0 that deposits its energy in the electromagnetic calorimeter. This cut also helps discard those electrons that radiated a high energy photon. The photon is typically collinear with the electron track and generally deposits its energy in the same calorimeter tower and therefore the cluster energy does not differ much from the original energy of the

electron. The P_T of track however does significantly changes, and the ratio E/P can be much larger than one.

- $L_{shr} < 0.2$

This quantity uses the lateral shower profile and compares it to what is expected from electromagnetic showers. It is defined as

$$L_{shr} = 0.14 \sum_i \frac{E_i^{\text{measured}} - E_i^{\text{expected}}}{\sqrt{(0.14\sqrt{E})^2 + \sigma_{E_i^{\text{expected}}}^2}} \quad (3.1)$$

where the index i runs over towers, E_i^{measured} is the energy measured in tower i and E_i^{expected} is the energy expected from test beam data. The error in the energy measurement is represented by $0.14\sqrt{E}$ and $\sigma_{E_i^{\text{expected}}}^2$ is the uncertainty in the energy estimate. Typically L_{shr} is a two-tower sum. Any extra particles accompanying the one responsible for the main EM shower will tend to add to the energy in adjacent towers and make L_{shr} a larger number.

- $-3.0 \text{ cm} < Q \cdot \Delta x < 1.5 \text{ cm}; |\Delta z| < 3 \text{ cm}$

The distance between the COT track extrapolated to the CES, and the best matching CES cluster is represented by Δx and Δx . This requirement imposes a close match between the two. The cut on Δx has been multiplied by the charge of the track, Q , and it is asymmetric in $r - \phi$ to account for possible photon bremsstrahlung in the direction of the outside of the track.

- $\chi_{strip}^2 < 10$

This quantity compares the shower profile in the shower maximum detector, CES, with the shower profile obtained from test beam electrons.

- $|z_{vertex}| < 60 \text{ cm}$

The position in z of the primary vertex interaction. The z_{vertex} is

determined by the intersection of the track with the beam axis. The longitudinal spread of the event vertex about the nominal interaction point $z = 0$ is a Gaussian with $\sigma = 26$ cm. The vertex position is required to be within 2σ to avoid tracks to pass through uninstrumented regions of the detector.

- Track quality cuts

A well reconstructed track should have at least 7 hits in each of three axial and three stereo superlayers of the COT.

- Fiduciality

This variable requires that the electron is reconstructed in a region of the CDF detector that is well instrumented.

- Not a conversion

The interaction of photons with the detector material can result in the conversion of electron-positron pairs. These conversions can be identified by the presence of another electron candidate with opposite charge near the electron candidate. If both tracks are close on ϕ at the point of conversion the event is flagged as conversion and rejected as a whole.

- Calorimeter isolation: $E_T^{iso} / E_T^{cluster} < 0.1$

The ratio of transverse energy in the electromagnetic and hadronic calorimeter in a cone of radius $\Delta R = \sqrt{(\Delta\eta)^2 + (\Delta\phi)^2} \leq 0.4$ excluding the electron cluster energy to the electron cluster energy. This cut rejects electrons that are not isolated from hadronic activity, including those coming from semi-leptonic quark decays.

The efficiency of the central electron identification cuts is determined from $\gamma/Z^* \rightarrow e^+e^-$ data sample. Events were required to have oppositely

charged electrons, with a invariant mass of the electron pair in a $\pm 15 \text{ GeV}/c^2$ range from the nominal Z mass. One electron was required to pass all the tight cuts, while the other was used to obtain the efficiency of the cuts. The central identification efficiency was found to be $\epsilon_{data} = (82.5 \pm 0.2)\%$. The same calculation using Monte Carlo yields $\epsilon_{MC} = (85.5 \pm 0.5)\%$. To compensate for differences in the reconstruction in data and MC a scale factor of $\epsilon_{data}/\epsilon_{MC} = 0.965 \pm 0.006$ is applied to correct acceptances obtained from MC.

Plug electrons

Electron candidates depositing energy in the PEM calorimeter are called *plug electrons*. To identify plug electrons the following requirements are applied:

- $1.2 < |\eta| < 2.0$

The PEM allows the identification of electromagnetic clusters of energy at pseudorapidities up to $|\eta| < 2.5$. Electron candidates with $|\eta| > 2$ have, however, a large charge misidentification rate and the cut $|\eta| < 2.0$ is required. This requirement has a small effect in the acceptance of $t\bar{t}$ events since these are mostly central.

Plug electrons identified solely in a cluster in the forward calorimeter are called PEM electrons. The charge misidentification rate of PEM can be very large as forward electrons may not traverse a large part of the COT, and track information is limited. The track efficiency is improved by using an algorithm named the Phoenix algorithm [26].

The algorithm starts by associating a track with energy observed in the PEM cluster. The track is constrained at the primary vertex and at the center of the cluster. Two tracks are constructed based on the two possible charges of the electron. The algorithm next looks for hits

in the silicon that matches the tracks. If hits are matched the track is reconstructed. If both track are reconstructed the one with the best goodness of fit is taken. Electrons candidates with a cluster in the PEM and a Phoenix track are called PHX electrons.

- $E_T > 20$ GeV

The transverse energy of the PEM cluster, which is limited to two towers in pseudorapidity and two towers in azimuth, must be greater than 20 GeV.

- $E_{had}/E < 0.05$

Similar to the central electron requirement.

- $U_{5 \times 9} \geq 0.65$ and $V_{5 \times 9} \geq 0.65$

The variables $U_{5 \times 9} \geq 0.65$ and $V_{5 \times 9} \geq 0.65$ are isolation variables for the shower maximum detector. They are independently applied to both the U and V layers. The clustering in each layer is performed by ordering strips in decreasing energy with the highest-energy strips used as seeds. The PES cluster has a fixed width of nine strips. The quantities $U_{5 \times 9}$ and $V_{5 \times 9}$ represent the ratios of energy sum in the central 5 strips to the total energy in all the nine strips.

- $\chi_{3 \times 3}^2 < 10$

This variable compares the energy distribution in the 3×3 PEM towers around the seed tower to what was obtained from test beam electrons by means of a χ^2 test statistics.

- $|\Delta R_{PES}| < 3$ cm

This variable compares the position of the shower obtained from the $\chi_{3 \times 3}^2$ fit to the intersection of the centroids in the layers U and V. The difference in pseudorapidity $\Delta\eta$, and in azimuth $\Delta\phi$, determines $(\Delta R_{PES})^2 = (\Delta\eta)^2 + (\Delta\phi)^2$.

- $N_{hits}^{Si} \geq 3$
The number of hits in the silicon.
- $|z_{vertex}| < 60$ cm
Same as the central electron requirement.
- Calorimeter isolation: $E_T^{iso}/E_T^{cluster} < 0.1$
Same as the central electron requirement.

The plug electron identification efficiency is determined from $\gamma/Z^* \rightarrow e^+e^-$ data sample. A central electron and a plug electron are required with the invariant mass of the two-electron system in a $30 \text{ GeV}/c^2$ window around the Z mass. The plug electron identification efficiency is found to be $\epsilon_{data} = (65.1 \pm 0.8)\%$. The same calculation in Monte Carlo yields $\epsilon_{data} = (74.9 \pm 0.2)\%$. To compensate for differences in the reconstruction in data and MC a scale factor of $\epsilon_{data} = (65.1 \pm 0.8)\% \epsilon/\epsilon_{MC} = 0.87 \pm 0.01$ is applied to correct acceptances obtained from MC.

3.4.2 Muon identification

Muons are minimum ionizing particles which penetrate large amount of material with little energy loss. They passage through the detector is characterized by a track in the COT, little energy deposition in the calorimeter, and hits in the muon chambers.

Muons at CDF are categorized by the detector region through which they pass. In this dissertation only the CMU, CMP, and CMX sub-detectors are used. Those reconstructed in the CMU detector are called CMU muons, and so on. Muons reconstructed in both the CMU and CMP detectors are called CMUP muons. In particular, central tracks that are not expected to pass through any of the muon detectors are called Central Minimum Ionizing

Objects or CMIO muons. They are also called stubless muons, to indicate that no stub was reconstructed in the muon detector.

The following requirements are applied to muons:

- $P_T > 20 \text{ GeV}/c$ The transverse momentum of the COT beam-constrained track.

- $|z_0| < 60 \text{ cm}$

The z-position of the track.

- $d_0 < 0.2 \text{ cm}$ for tracks with no silicon hits

$d_0 < 0.02 \text{ cm}$ for tracks with silicon hits

The impact parameter d_0 is the distance of z_0 to the closest point in the track. This selection is of course used for the default muon track, i.e. without the beam constraint requirement. This cut forces the muon to originate from the nominal interaction point, and substantially reduces cosmic muons that entered the detector in the time window of the collision.

- Track quality tracks

Identical to the electron quality tracks.

- $E_{em} \leq 2 \text{ GeV} + \max(0, 0.0115(P - 100 \text{ GeV}/c))$

It requires the energy deposited in the electromagnetic calorimeter to be very small. A small change is introduced for muons with $P > 100 \text{ GeV}/c$.

- $E_{had} \leq 6 \text{ GeV} + \max(0, 0.0280(P - 100 \text{ GeV}/c))$

Requires the energy deposited in the hadronic calorimeter to be smaller than that of strongly interacting jets.

- $E_{em} + E_{had} > 0.1 \text{ GeV}$ for stubless muons only

Stubless muons are required to have non-zero energy deposition in the

calorimeter to limit background from electrons escaping the detector through non-instrumented regions of the calorimeter.

- $|\Delta X|_{CMU} \leq 3$ cm, $|\Delta X|_{CMP} \leq 5$ cm and $|\Delta X|_{CMX} \leq 6$ cm

The distance in the $r - \phi$ plane between the COT track extrapolated to the stub segment, and the position of the reconstructed stub for the muons in different sub-detectors. The requirements are weaker for CMP and CMX since the muons traverse more material and suffer greater deflections due to multiple scattering.

- Fiduciality

This variable requires that the track of the muon candidate extrapolates to the proper muon chamber. For stubless muons it requires the track to pass through well instrumented regions of the CDF detector and through no muon sub-detector.

- $\rho_{COT} > 140$ cm

The radius at which the track leaves the COT. This track is used for CMX only, as tracks may leave the COT from the side. In general, data and Monte Carlo simulation do not agree for $\rho_{COT} \leq 140$ cm due to the data bias introduced by the XFT trigger which requires the track to have hits in at least 4 COT superlayers. Data and Monte Carlo agree for $\rho_{COT} > 140$ cm.

- Isolation: $E_T^{iso} / P_T < 0.1$

The quantity E_T^{iso} is the energy of calorimeter towers in the cone of $\Delta R = 0.4$ without including the tower associated with the track.

- Not a cosmic muon

Muons coming from cosmic background are identified as dimuon events with an angular separation close to 180° in ϕ . Cosmic rays enter the

detector at random times and random locations. As cosmic muons traverse the detector they leave energy in the calorimeter, traverse through the COT leaving a single track that is reconstructed as two and leaves energy in the calorimeter as it goes out. The time difference between the energy deposited in both ends of the hadronic calorimeters can be analyzed to identify cosmic muons. In addition, a cut in the impact parameter of the track efficiently identify cosmic muons. Events in which a cosmic muon is tagged are rejected.

As with electrons the muon identification efficiencies are measured using the $\gamma/Z^* \rightarrow \mu^+\mu^-$ data sample. One muon is required to have strict cuts and is associated with the Level-1 trigger. The other muon is chosen to be fiducial (i.e. the track points to the proper sub-detector) and examined to see if passes all the identification cuts.

3.4.3 Jet reconstruction

In a typical $p\bar{p}$ collision quarks and gluons are created. These carry color charge and are therefore subjected to the hadronization process described in **XXX**. After this process the original parton results in a stream of colorless particles. These particles are collimated along the direction of the original parton and, after traversing the tracker, deposit their energy in a cluster of towers in the calorimeter detector. This stream of particles is called a *jet*.

The jets are reconstructed from the energy deposited in the calorimeter towers with an algorithm called *jet clustering*. This algorithm starts by identifying the seed tower as the one with the largest calorimeter energy. The cluster of towers within the cone $\Delta R = \sqrt{(\Delta\eta)^2 + (\Delta\phi)^2} = 0.4$ from the center of the seed tower are identified. The cone size $\Delta R = 0.4$ is chosen to include most of the jet energy without including a large contribution from other event activity.

After the cluster is formed, the shower center in the plane (η, ϕ) of the calorimeter is determined as follows:

$$\eta_{centroid} = \frac{\sum_i E_T^i \eta^i}{\sum_i E_T^i} \quad \phi_{centroid} = \frac{\sum_i E_T^i \phi^i}{\sum_i E_T^i} \quad (3.2)$$

where the sum runs over the towers in the cluster and η^i (ϕ^i) represent the η (ϕ) coordinate of the center of the tower. After the position of the shower is calculated a new cone is defined centered in the new coordinates and the calculation is repeated for the new cluster. This process is then iterated until the cluster remains unchanged.

The transverse energy of the jet is determined as

$$E_T^{raw} = \sqrt{\left(\sum_i E_i \sin(\theta_i) \cos(\phi_i)\right)^2 + \left(\sum_i E_i \sin(\theta_i) \sin(\phi_i)\right)^2} \quad (3.3)$$

where E_i is the total energy in tower i . This quantity represents the energy deposited in the cluster, and does not includes corrections to account for detector effects or other physics processes, and is thus referred to as *raw*.

The corrected value of the jet E_T is derived from the raw value E_T^{raw} using a set of multiplicative and additive correction factors resulting in corrected values that are close to the energy of the initial parton. The corrections are given by the following relation:

$$E_T = (E_T^{raw} \times f_{rel} \times f_{time} \times f_{scale} - E_T^{MI}) \times f_{abs} - E_T^{UE} + E_T^{OC} \quad (3.4)$$

The seven factors are briefly explained below, (more detailed information can be found in [25]).

1. Relative correction, f_{rel} .

This factor takes into account the relative tower-to-tower differences in calorimeter response.

2. Time dependent correction, f_{time} .

The calorimeter response evidenced a decline with time. This correc-

tion factor depends on the date of the event was recorded and properly assign a multiplicative factor to account for that.

3. Energy scale correction, f_{scale} .

This factor account for the non-linear response of the calorimeter.

4. Multiple Interaction, E_T^{MI}

With current luminosities one interaction per bunch crossing is expected on average. The distribution follows Poisson statistics, and in a particular event this number can be larger, and the physics process under study may have an overlapping minimum bias event. The energy of the minimum bias event may fall in the jet clustering cone, and must be subtracted. This is calculated in an event-by-event basis.

5. Absolute energy correction, f_{abs}

This factor corrects the energy of the jet to that of the original parton that generated it. It includes nuclear absorption and particle leakage effects that can reduce the total energy measured in the jet cluster.

6. Underlying event correction, E_T^{UE}

Extra energy can be deposited in the jet cluster that is not coming from the original parton. This energy can be originated from spectator partons, beam-beam soft interactions or beam remnants.

7. Out of cone corrections, E_T^{OC}

Part of the energy of the initial parton may fall outside the cone resulting in a underestimation of its energy. This quantity is obtained from MC simulation of the physics process in study.

Each level of correction has a systematic error associated with it, and the combination of them result in the total systematic uncertainty of the jet E_T measurement.

X_h	$BR(\tau \rightarrow X_h \nu_\tau)$ (%)	$B_i / \sum_j B_j$ (%)
h^-	11.75	18.3
$h^- \pi^0$	25.86	40.4
$h^- h^+ h^-$	10.01	15.6
$h^- 2\pi^0$	9.39	14.7
$h^- h^+ h^- \pi^0$	4.53	7.1

Table 3.5: Most significant hadronic tau decays. The quantity h^\pm represents π^\pm 's or a K^\pm 's. The second column are the tau branching ratios to the different decay modes.

3.4.4 Tau reconstruction

Tau reconstruction refers to the process of identification of a hadronically decaying tau by its decay products. The hadronic decay of a lepton tau proceeds as $\tau \rightarrow X_h \nu_\tau$, where X_h can be π^\pm or K^\pm or some short-lived intermediate resonance that decays to final states including π^\pm , π^0 , K^\pm or K^0 . Table 3.5 lists the most significant hadronic decays of taus.

The fraction of tau decays containing K^\pm 's is much smaller than that containing π^\pm and therefore all the charged tracks are considered pions in the tau reconstruction process.

The decay products of high energy taus travel in a direction collimated around the tau momentum. The reconstruction algorithm starts by finding a seed calorimeter tower with transverse energy greater than 6 GeV. Then neighboring towers with energy larger than 1 GeV are added to the cluster. Because the cluster is expected to be narrow no more than 6 tower are allowed in the cluster. The algorithm then defines the seed track as the highest momentum track pointing to the calorimeter cluster. All other tracks inside a signal cone of 10° around the seed track, and whose z_0 position is

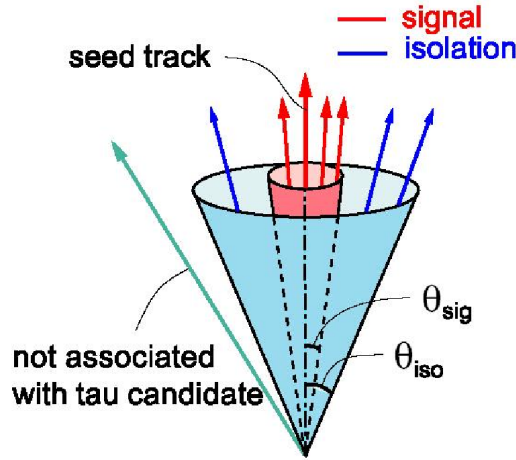


Figure 3.40: Tau identification cone, and isolation annulus. This particular set of track would not pass the tau cuts as there are tracks in the isolation annulus.

close to that of the seed track, are associated with the tau candidate. Other tracks outside the signal cone and inside a larger cone of 30° are treated as isolation tracks. The region between 10° and 30° is called the isolation annulus. The signal cone and isolation annulus are depicted in Figure 3.40 for a non isolated tau candidate. More detailed information about the tau reconstruction algorithm is found in [27].

The neutral pions decay to diphoton around 98.8% of the time. The neutral pions coming from highly energetic tau's (e.g. tau's from the decay of W's or Z's) have typical energies larger than 10 GeV. For these high energy pions the angular separation between the two photons is very small, and the clusters of energy deposited in the calorimeter are generally overlapped and identified as one. The identification of a π^0/γ is done by a cluster in the shower max detector, CES. The CES cluster is required to have certain energy distribution and to have no track pointing to its center to reduce contamination from real electrons. The four momentum of the π^0 can be reconstructed assuming the vertex to be at the z_0 of the seed track. A de-

tailed description of π^0 reconstruction is given in [28]. The four momentum of the hadronic system can be calculated from the momentum of the tracks and the π^0

The following is the set of extra requirements imposed over the tau candidates as found above:

- $\pi^0 + \sum_{tracks=i} P_T^i > 15 \text{ GeV}/c$
requires the energy of the π^0 and the tracks to be greater than 15 GeV/c.
- $|z_0| < 60 \text{ cm}$
Same as with electrons.
- $|d_0| < 1 \text{ cm}$
requires the impact parameter of the seed track to be less than 1 cm.
- $M_{tracks+\pi^0} < 1.8 \text{ GeV}/c^2$
Invariant mass of the tracks and π^0 to be less than the tau mass.
- Calorimeter Isolation : $\Delta R = 0.4 \text{ GeV}/E_T^{cluster} < 0.06$
The ratio of the calorimeter energy in a cone of ΔR minus the energy of the cluster to the energy in the cluster.
- Track isolation :
 - tracks in isolation annulus =0
No tracks in the isolation annulus.
 - π^0 's in the isolation annulus =0
No π^0 in the isolation annulus.
- Track in signal cone < 4
- $|\sum_{tracks=i} q^i| = 1$
The magnitude of the sum of the track charges must add up to one.

- μ veto : $E_T^{calorimeter}/\text{seed track } P_T > 0.5$
Muon veto
- e veto : $E_T^{had\ calorimeter}/\text{seed track } P_T > 0.15$
Electron veto
- Seed track quality cuts
Same as for electrons.
- $9\text{ cm} < Z_{CES}^{seed\ track} < 216\text{ cm}$
The Z position of the CES cluster to be localized in the most sensitive CES region.

3.4.5 Missing transverse energy

Although with an unknown magnitude, the momentum of the initial partons is known to be in the beam direction. Momentum conservation thus requires that the energy of all the final states balances in the plane transverse to the beam line.

Many interesting physical processes have neutrinos in their final state. Neutrinos escape the detector carrying significant amounts of energy, and the identification of the presence of a neutrino is possible by the detection of imbalance in the transverse energy. The transverse energy, E_T , is a 2D vectorial quantity defined as:

$$\vec{E}_T^{raw} = \sum_{cal.\ towers} E_i^{raw} \sin(\theta_i) \vec{n}_i \quad (3.5)$$

where the sum is over all the calorimeter towers, E_i^{raw} is the raw energy of each tower, θ_i is the polar angle to the center of the tower, and \vec{n}_i is a transverse unit vector pointing to the center of the tower.

The value of \vec{E}_T^{raw} defined above has to be corrected on an event-by-event basis. The first correction is related to the muons in the event. The

amount of energy deposited by muons in the calorimeter is significantly less than the energy they carry. The estimation based on the calorimeter is then corrected to include the energy of the muon as measured by its track information. A second correction is related to the jets in the event. Since the jet cluster energy is corrected as explained above, in the calculation of the \vec{E}_T^{raw} the raw energy of towers in the cluster has to be replaced by their corrected energies. The corrected resulting transverse energy is referred to as \vec{E}_T .

Since the energy is assumed to be balanced it is often more useful to talk in term of the “missing energy” defined simply as $\vec{E}_T = -\vec{E}_T$. If neutrinos are present in the final state, the \vec{E}_T indicates the direction and magnitude of the vectorial sum of the neutrinos transverse energy in the event.

Bibliography

- [1] Fermilab Beams Division, “*Run II Handbook*” http://www-bdnew.fnal.gov/pbar/run2b/Documents/RunII_handbook.pdf
- [2] Fermilab Beams Division, “*Fermilab Linac Upgrade. Conceptual Design*” <http://www-lib.fnal.gov/archive/linac/fermilab-lu-conceptualdesign.pdf>, (1989).
- [3] Fermilab Beams Division, “*The Booster rookie book*”
http://www-bdnew.fnal.gov/operations/rookie-books/Booster_PDF/Booster_TOC.html
- [4] Fermilab Beams Division, “*The Main Injector rookie book*”
http://www-bdnew.fnal.gov/operations/rookie-books/Main_Injector_PDF/Main_Injector.html
- [5] Fermilab Beams Division, “*Recycler design report*”
FERMILAB-TM-1991, <http://www-lib.fnal.gov/archive/1997/tm/TM-1991.html>
- [6] Fermilab Beams Division, “*The antiproton source rookie book*”
http://www-bdnew.fnal.gov/pbar/documents/PBAR_Rookie_Book.PDF,(1999).
- [7] Fermilab Beams Division, “*Another antiproton source rookie book*”
http://www-bdnew.fnal.gov/operations/rookie-books/Pbar_PDF/Pbar.html
- [8] Fermilab Beams Division, “*The Tevatron rookie book*”
http://www-bdnew.fnal.gov/operations/rookie-books/Tevatron_PDF/TeV_Rookie_Book.htm

- [9] CDF Collaboration, “*The CDF II detector. Technical design report*”. FERMILAB-Pub-96/390-E, (1996)
- [10] J. Bjorken and E. Paschos, “*Inelastic $e-p$ and $\gamma-p$ scattering and the structure of the nucleon*”. Phys. Rev. 175(1975)
- [11] D. Amidei et al, “*The Silicon Vertex Detector of the Collider Detector at Fermilab*”. NIMPR A350,73 (1994).
- [12] Chris Hays, et al, “*The COT Pattern Recognition Algorithm and Offline Code*”, CDF note 6992.
- [13] F. Abe et al. Phys. Rev. D50 (1994) 2296.
- [14] G. Acoli et al. “*The CDF central muon detector*” Nucl. Instr. & Meth., Volume A,268, 63-67 (1988)
- [15] CDF Collaboration, “*The 1992 CDF muon system upgrade*” CDF Note 2858 (1994)
- [16] J.D. Jackson “*Classical Electrodynamics*” John Wiley and Sons, 1999, pg715.
- [17] CDF Collaboration “*Proposal for Enhancement of the CDFII Detector: An Inner Silicon Layer and A Time of Flight Detector*”
<http://www-cdf.fnal.gov/upgrades/PAC/p909.ps>
- [18] CDF Collaboration “*Update to Proposal P-909: Physics Performance of the CDFII Detector with An Inner Silicon Layer and A Time of Flight Detector*”
http://www-cdf.fnal.gov/upgrades/btb_update_jan99.ps
- [19] CDF Collaboration “*Luminosity Monitor Based on Cherenkov Counters for P Anti-P Colliders*”
Nucl. Instr. & Meth., Volume A,441, 366-373 (2000)

- [20] CDF Collaboration “*The CDF Run II Luminosity Monitor*”
Nucl. Instr. & Meth., Volume A,461, 540-544 (2001)
- [21] M. Shimojima et al. “*CONSUMER-SERVER/LOGGER SYSTEM FOR THE CDF EXPERIMENT.*”
IEEE Trans. Nucl. Sci. Vol 47, page 236 (2000)
- [22] H. Frisch et al. “*Conceptual Design of a Deadtimeless Trigger for the CDF Trigger Upgrade*”
CDF Note 2034 (1994)
- [23] K. Anikeev et al. “*Event Builder and Level-3 for acs*”
CDF Note 5793, (2001)
- [24] See <http://www-cdf.fnal.gov/internal/dqm/goodrun/v4/goodv4.html>
- [25] Andrew G. Ivanov, “*Search for Anomalous Kinematics of Top Dilepton Events in $p\bar{p}$ Collisions at $\sqrt{s} = 1.96$ TeV*”. Ph.D. thesis. University of Rochester. (2004)
- [26] J. Goldstein et al., “*Silicon Tracking for Plug Electrons*” CDF Note 5970 (2002).
- [27] A. Anastassov et al., “*Search for neutral MSSM Higgs boson(s) in the $\tau\tau$ decay channel*” CDF Note 7622 (2005).
- [28] A. Anastassov, “*Non-isolated π^0/γ reconstruction*” CDF Note 6688 (2003).

Chapter 4

Analysis

This chapter begins by defining the strategy used to search for charged Higgs bosons in $t\bar{t}$ decay products. Next, the implementation of the strategy and all its details are discussed in what constitutes the core of this dissertation. The chapter concludes defining the format in which the results will be presented.

4.1 General strategy

At the Tevatron top quarks are produced mainly in pairs ($t\bar{t}$). In the SM the top quark decays almost exclusively to W^+b , and $t\bar{t}$ events are categorized in channels according to their final state given by the decays of the W 's. Table 4.1 shows a graphical representation of the distribution of $t\bar{t}$ events in different final states. The x and y axes represent the branching ratios of W^+ and W^- decays to e , μ , τ and hadrons. The labeled regions are the different channels, and their areas represent the fraction of $t\bar{t}$ events in each channel. A description of each channel follows:

- The largest fraction of $t\bar{t}$ events decay into the “all-hadronic” final state, characterized by a large number of jets obtained after the hadronization process of the quarks. Although this channel provides a large sample, these $t\bar{t}$ events are very difficult to distinguish from other processes resulting in hadronic final states. Typical cross section measurements in this channel have a signal over background ratio (S/B) of events of

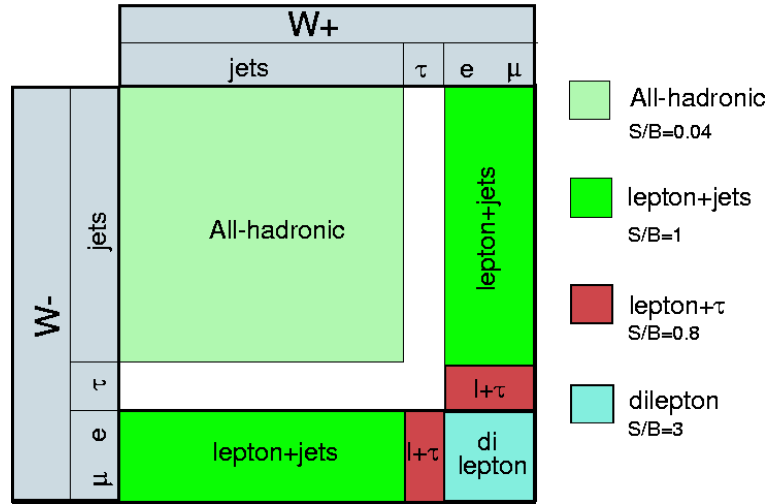


Figure 4.1: Graphical representation of the distribution of $t\bar{t}$ events in different final states. The $t\bar{t}$ decays to $W^+bW^-\bar{b}$. The decay modes of the W^+ are represented by the x axis and those of the W^- by the y axis.

about 0.04.

- The second largest channel is called “lepton+jets”, and its final state is characterized by one lepton (electron or muon), four jets, and significant missing transverse energy from the undetected neutrino. The typical cross section measurement in the “lepton+jets” channel has a S/B of about 1.0. Throughout this chapter the word lepton refers only to electron or muons; unless explicitly stated it does not include taus.
- The third largest channel is called “dilepton”, and it possesses two leptons, two jets, and large transverse missing energy in its final state. It has a significantly lower rate than the lepton+jets channel but is the cleanest channel available with a S/B of about 3.
- The last channel is called the “lepton+ τ_h ”, and requires an electron or muon, one tau lepton decaying hadronically (τ_h), two jets and missing

top	H ⁺
$\hookrightarrow W^+b$	$\hookrightarrow c\bar{s}$
$\hookrightarrow H^+b$	$\hookrightarrow \bar{\tau}\nu$
	$\hookrightarrow t^*\bar{b}$
	$\hookrightarrow W^+h^0$

Table 4.1: The top quark and Higgs boson decays assumed in this dissertation

transverse energy. The S/B in this channel is about 0.8.

Under the assumption that a charged Higgs is present, other decay modes may become available. If the mass of the charged Higgs is below that of the top, the decay $t \rightarrow H^+b$ can be sizable and compete with the SM decay $t \rightarrow W^+b$. As described in Section 2.3.5, the charged Higgs in turn can decay into a variety of final states as shown in the Table 4.1.

Given a certain $t\bar{t}$ production cross section the presence of a charged Higgs significantly modifies the expectations of the number of events in all the above-mentioned channels. As an example, if the charged Higgs were to decay 100% to $\bar{\tau}\nu$, an excess of the number of events in the lepton+ τ_h channel with respect to what is expected from SM would be observed. This would also result in a deficit in the lepton+jets and dilepton channels, as more events would be distributed to tauonic channels than in the SM. On the other hand, if the charged Higgs were to decay to $c\bar{s}$ 100% of the time, we would expect to see an increase in the hadronic channel, and a decrease in all the others. Depending on the top and Higgs branching ratios, the number of expected events in different decay channels can show an excess or deficit with respect to SM expectations.

The general strategy is then to look at certain “search” channels, and use different models to predict the expected number of events in each. These

numbers are then compared to the observed number of events, and depending on the results of the comparison we can either observe or exclude the model's Higgs production at some confidence level.

The next sections describe the search channels, the calculation of the number of expected events for a generic model, and the method of comparison between the observed and expected number of events in each channel.

4.2 Defining the search channels

The CDF collaboration has recently reported measurements of the $t\bar{t}$ production cross section in the dilepton channel [1], the lepton+ τ_h channel [2], the lepton+jets with one or more tagged jets [3], and the lepton+jets with two or more tagged jets [3]. These measurements were carried out under the assumption $\text{BR}(t \rightarrow H^+b)=0$ and use data samples corresponding to an integrated luminosity of up to 193 pb^{-1} . Each measurement agrees with the theoretical SM $t\bar{t}$ cross section expectation within its uncertainty, providing no direct evidence for non-SM physics.

These four cross section analyses are “counting experiments”, i.e. they compute the $t\bar{t}$ production cross section ($\sigma_{t\bar{t}}^{\text{prod}}$) based on the number of candidates passing their selection cuts (N^{obsv}), the number of SM-expected background events (n^{back}), and the integrated luminosity times efficiency of detection of $t\bar{t}$ decay products assuming SM decays (ϵ_{WW}). The production cross section $\sigma_{t\bar{t}}^{\text{prod}}$ is then computed for a particular channel k from the following equation:

$$N_k^{\text{obsv}} = \sigma_{t\bar{t}}^{\text{prod}} \epsilon_{WW,k} + n_k^{\text{back}} \quad (4.1)$$

The results from which these analyses calculate the cross section are shown in Table 4.2.

Channel	n^{back}	N^{obsv}	SM expected events
dilepton	2.7 ± 0.7	13	10.9 ± 1.4
lepton+jets, ≥ 1 tags	23.1 ± 3.0	57	64.0 ± 4.4
lepton+jets, ≥ 2 tags	1.3 ± 0.3	8	10 ± 1
lepton+ τ_h	1.3 ± 0.2	2	2.3 ± 0.3

Table 4.2: Results from published cross section measurements [1, 2, 3]. The expected number of SM events is calculated assuming $\sigma_{t\bar{t}}^{\text{prod}} = 6.7_{-0.9}^{+0.7}$ pb.

We will take advantage of these studies and their results, and use these four channels for the search for charged Higgs bosons in $t\bar{t}$ decay products. The next three subsections give a brief overview of the selection requirements for each search channel. The fourth subsection presents the background expectation for the four analyses. The need for a trivial modification to the selection requirements is explained in the last subsection, together with the changes in the background expectation for each channel.

4.2.1 The dilepton channel

The dilepton channel requires events to pass the following requirements:

- Presence of two standard leptons (e or μ), where standard refers to the definition given in Section 3.4. One of the leptons is required to be either CEM, PHX, CMUP or CMX. The other other can be CEM, PHX, CMUP, CMX, NICEM, NICMUP, NICMX, CMU, NICMU, CMP, NICMP, CMIO. The prefix “NI” stands for “Non Isolated”, indicating that the isolation requirement does not need to be fulfilled. Dilepton events in which both leptons are identified as PHX are not considered. A dilepton event can be classified in one of 41 possible different categories according to the sub-detectors in which the leptons

are identified.

- At least two jets with $E_T > 15$ GeV corrected up to and including level 5, and $|\eta_{jet}| < 2.5$.
- $\cancel{E}_T > 25$ GeV, where the \cancel{E}_T has been corrected for the muons in the event and the corrections in the jets energy. If $25 \text{ GeV} < \cancel{E}_T < 50 \text{ GeV}$ then the angle between the \cancel{E}_T and the nearest jet in the transverse plane should be greater than 20° .
- If the event has a dilepton invariant mass between 76 and 106 GeV/ c^2 and there are jets in the event the following requirements are applied to reduce the background contribution from the Drell-Yan processes:
 - If the angle between the nearest jet and the \cancel{E}_T is less than 10° then the event is rejected.
 - If the angle between the nearest jet and the \cancel{E}_T is less than 90° the the events is vetoed if $jet_{sig} < 8$ GeV. The jet significance jet_{sig} is defined as:

$$jet_{sig} = \frac{\cancel{E}_T}{\sqrt{\sum_i E_T^{jet_i} \cdot \hat{\cancel{E}}_T}} \quad (4.2)$$

where the sum is carried over those jets which angle to the \cancel{E}_T is less than 90° , and $\hat{\cancel{E}}_T$ represents a unit vector in the direction of the \cancel{E}_T in the transverse plane.

- $H_T > 200$ GeV. The large mass of the top results in larger transverse momentum than in background processes. The variable H_T is the sum of the transverse energy in the event and is defined as

$$H_T = \cancel{E}_T + \sum_{jets} E_T^{jet} + \sum_{electrons} E_T^{electron} + \sum_{muons} E_T^{muon} \quad (4.3)$$

- Opposite sign of both leptons.

When computing the efficiency to detect $t\bar{t}$ event using Monte Carlo an extra cut, based on generator level information, is imposed. The event is required to contain two leptons coming from the respective bosons (either W 's or charged Higgs). This cut guarantees that the efficiency comes directly from the signal part of $t\bar{t}$ decays, and exclude the efficiency coming from other processes such as jets faking leptons that are already accounted for in the background calculation.

4.2.2 The lepton+jets channel

The event selection for the lepton+jets channel requires the following:

- One standard lepton (e or μ), where standard refers to the definition given in 3.4. The lepton is required to be either CEM, CMUP or CMX. A lepton+jets event can be classified in one of 3 possible different categories according to the sub-detector in which the lepton is identified.
- At least three jets with $E_T > 15$ GeV corrected at level 4 and $|\eta_{jet}| < 2.0$.
- $\cancel{E}_T > 20$ GeV, where the \cancel{E}_T has been corrected for the correction to the jet energies and the muons in the event. If $25 \text{ GeV} < \cancel{E}_T < 50 \text{ GeV}$ then the angle between the \cancel{E}_T and the nearest jet in the transverse plane must be greater than 20° .
- Dilepton veto. The event is vetoed if two leptons are found.
- Z veto. The event is vetoed if the lepton and a second object form an invariant mass with energy between 76 GeV and 106 GeV. If the lepton is an electron, the other object can be an electromagnetic object, a jet

or a track of oppositely charged particle. If the lepton is a muon, the other object can be a minimum-ionizing track of opposite charge with various loose requirements.

- Cosmic veto. The event is vetoed if it is identified as cosmic.
- Conversion veto. The event is vetoed if the lepton is an electron identified as coming from a photon conversion.
- QCD veto. To reduce the QCD background, the angle between the \cancel{E}_T and the nearest jet is required to be between 0.5 and 2.5 radians if $\cancel{E}_T < 30$ GeV.
- At least one b-tagged jet. At least one of the jets must be tagged by the secondary vertex algorithm described in section 3.3.2.

The events passing this selection criteria can be further categorized according to the number of tagged jets. We refer to the lepton+jets sample with one or more tags as lepton+jet, ≥ 1 tags and to the lepton+jets sample with two or more tags as lepton+jet, ≥ 2 tags.

4.2.3 The lepton+ τ_h channel

The lepton+ τ_h channel requires the following cuts:

- One standard lepton (e or μ), where standard refers to the definition given in Section 3.4. The lepton is required to be either CEM, CMUP or CMX. A lepton+ τ_h event can be classified in one of 3 possible different categories according to the sub-detector in which the lepton is identified.
- One hadronically decaying tau candidate passing the standard cuts for taus.

- Opposite sign. Requires the charge of the lepton to be opposite to the sum of the charges of the particles in the tau signal cone.
- At least two jets. Both jets are required to be in the region $|\eta_{jet}| < 2.0$. One of them is required to have $E_T > 25$ GeV and the other $E_T > 15$ GeV. None of the jets should match the lepton or the tau. Jets are corrected to level 5.
- $\cancel{E}_T > 20$ GeV.
- Z veto: If $65 \text{ GeV}/c^2 < M_{\text{lepton},\tau_h} < 115 \text{ GeV}/c^2$ then the event is vetoed if $\Delta\phi_{\text{lepton},E_T} + \Delta\phi_{\tau_h,E_T} + \Delta\phi_{\text{lepton},\tau_h} < 0.4$. For events in which the mass of the lepton- τ_h system is between 65 GeV and 115 GeV, veto the event if the \cancel{E}_T is in between the lepton and the hadronic tau in the transverse plane. This cut targets the $\gamma^*/Z \rightarrow \tau\tau$ +jets background in which one τ decays leptonically and the other decays hadronically. In this case the missing energy arises from the neutrinos in the leptonic and in the hadronic tau decays, and the \cancel{E}_T is expected to lie in between the lepton and the hadronic tau momentum in the transverse plane.
- $H_T > 205$ GeV. The total transverse energy of the event.

When computing the efficiency to detect $t\bar{t}$ event using Monte Carlo simulation an extra cut, based on generator level information, is imposed. The event is required to contain a hadronically decaying tau and a lepton coming from the respective bosons (either W's or charged Higgs). As in the dilepton channel this cut guarantees that the efficiency comes directly from the signal part of $t\bar{t}$ decays, and excludes the efficiency coming from other processes such as jets faking leptons that are already accounted for in the background calculations.

4.2.4 Backgrounds results

The total expected number of background events is given in Table 4.2. The contribution from different physics processes to the total in each channel is shown in Table 4.3. These numbers are extracted from the different publications [1, 2, 3]. The SM background in the dilepton and lepton+ τ_h channels is composed dominantly by QCD fakes and Drell-Yan processes. The background in the lepton+jets, ≥ 1 tags is dominated by QCD fakes, mistags, and W plus heavy flavor production (W + $c\bar{c}$ or (W + $b\bar{b}$)). The requirement of two tagged jets in the lepton+jets, ≥ 2 tags channels strongly suppress fakes from QCD background, and only mistags and W plus heavy flavor dominate the background in this channel.

Background source	dilepton	lepton+jets events		lepton+ τ_h
	events	Tags ≥ 1	Tags ≥ 2	events
$Z/\gamma^* \rightarrow e\bar{e}$	0.36±0.27			
$Z/\gamma^* \rightarrow \mu\bar{\mu}$	0.07±0.3			0.05±0.03
$Z/\gamma^* \rightarrow \tau\bar{\tau}$	0.42±0.13			0.26±0.07
ZZ		0.04±0.01		
WW	0.51±0.19	0.34±0.06		0.14±0.02
WZ	0.23±0.09	0.32±0.07	0.03±0.014	0.02±0.01
QCD Fake	1.1±0.45	6.8±1.7		0.83±0.19
Mistag		5.8±0.8	0.22±0.03	
W{bb,cc,c}		6.6±1.3	0.52±0.15	
Single Top		1.3±0.2	0.17±0.04	
Total	2.7±0.7	21.2±2.5	0.94±0.16	1.3±0.21

Table 4.3: Background estimation in published analysis. The numbers are taken from [1, 2, 3].

4.2.5 Removal of the overlap between channels

As will be shown later, the search for charged Higgs requires the event selection for the different search channels to be exclusive. While the exclusivity between lepton+jets and dilepton is guaranteed by virtue of the “dilepton veto” cut in the lepton+jets selection, the candidates for the lepton+jets, ≥ 2 tags are (clearly) a subset of those for the lepton+jets, ≥ 1 tags. In addition, no effort has been made to guarantee exclusivity of the lepton+ τ_h channel with either the lepton+jets or dilepton channels. In the context of the SM, where top quarks decay mainly to Wb, the overlap of events is very small since lepton+ τ_h events are rare compared to dilepton and lepton+jets. However, the overlap becomes an important effect when the tau content of the top sample is enhanced by the presence of a charged Higgs.

In this analysis extra requirements are applied to each channel in order to force the association of every event to a single channel only. The removal between the “ ≥ 1 tag” and “ ≥ 2 tags” lepton+jets channels is performed by demoting the “ ≥ 1 tag” channel to require exactly one tag, “= 1 tag”. The lepton+jet channels = 1 tag and ≥ 2 tags are then exclusive by construction. The overlap with the lepton+ τ_h event selection is removed by applying a lepton+ τ_h veto cut in the dilepton and both lepton+jets event selections, thus keeping the lepton+ τ_h acceptance and background unchanged. This veto cut is chosen because it does not reduce the already small acceptance of the lepton+ τ_h event selection. We implement this new cut by running the lepton+ τ_h selection code as a veto for events passing the standard dilepton and lepton+jets selections. The acceptance and background contribution to each of these exclusive channels must therefore be recalculated.

As a motivation we show next the level of overlap of the cross sections when used as their were originally defined, i.e. without the lepton+ τ_h cut veto. Then we proceed to recalculate the background expectations in each

channel when the extra lepton+ τ_h cut is applied. The four search channels are then defined as dilepton, lepton+jet, = 1 tag, lepton+jet, ≥ 2 tags and lepton+ τ_h , where the dilepton and lepton+jets event selections contain the lepton+ τ_h veto cut.

Original overlap

We are interested in the amount of events the original dilepton or lepton+jets event selections share with the lepton+ τ_h . We express this amount as a fraction (F) of the total number of events passing the given event selection. Thus a value of $F_{dilepton}$ close to 1 indicates a strong overlap in which most events passing the standard dilepton event selection also pass the lepton+ τ_h event selection, and a value of zero indicates null overlap. The quantity F also represents the fraction of events that are removed when the lepton+ τ_h veto is implemented.

$$F_k = \frac{\# \text{ Ev. passing both lepton+}\tau_h \text{ and event selection } k}{\# \text{ Ev. passing event selection } k}$$

where k is dilepton, lepton+jets, = 1 tag, or lepton+jets, ≥ 2 tags. Table 4.4 shows the overlap in acceptance for each of ten different decay modes for a charged Higgs mass of 120 GeV/ c^2 . Note that the table shows the results for the lepton+jets with exactly one tag.

In the SM decay mode $t\bar{t} \rightarrow W^+bW^-\bar{b}$ the overlap is less than 1.5% in any of the shown channels, as indicated in the first row of the table. In decays involving a charged Higgs the overlap in acceptance between the dilepton and the lepton+ τ_h is very small, reaching a maximum of $(1.1 \pm 0.7)\%$ in the $t\bar{t} \rightarrow H^+bH^-\bar{b} \rightarrow \bar{\tau}\nu b\tau\bar{\nu}\bar{b}$ decay chain. The lepton+jets, = 1 tag shows a stronger overlap as one would expect. The maximum overlap in this channel, of about 12%, occurs for the $t\bar{t} \rightarrow H^+bH^-\bar{b} \rightarrow \bar{\tau}\nu b\tau\bar{\nu}\bar{b}$, followed by $t\bar{t} \rightarrow H^+bW^-\bar{b} \rightarrow \bar{\tau}\nu bW^-\bar{b}$ with 8.7% and $t\bar{t} \rightarrow H^+bH^-\bar{b} \rightarrow \bar{\tau}\nu bW^-\bar{b}\bar{b}$

with 6.4%. The same pattern is observed in the lepton+jets, ≥ 2 tags analysis with an even stronger overlap of up to 15 %.

$t\bar{t} \rightarrow b\bar{b}+$	$F_{dilepton}$	$F_{lepton+jets,=1\ tag}$	$F_{lepton+jets,\geq 2\ tags}$
$W^+W^-(SM)$	0.001 ± 0.001	0.011 ± 0.002	0.015 ± 0.004
$H^+W^- \rightarrow \bar{\tau}\nu W^-$	0.002 ± 0.002	0.087 ± 0.004	0.101 ± 0.009
$H^+W^- \rightarrow c\bar{s}W^-$	$\equiv 0$	≤ 0.0002	≤ 0.0008
$H^+W^- \rightarrow t^*\bar{b}W^-$	≤ 0.0007	0.007 ± 0.001	0.008 ± 0.002
$H^+H^- \rightarrow \bar{\tau}\nu\tau\bar{\nu}$	0.011 ± 0.007	0.12 ± 0.01	0.15 ± 0.02
$H^+H^- \rightarrow c\bar{s}s\bar{c}$	$\equiv 0$	$\equiv 0$	$\equiv 0$
$H^+H^- \rightarrow t^*\bar{b}\bar{t}^*b$	≤ 0.002	0.003 ± 0.001	0.006 ± 0.002
$H^+H^- \rightarrow c\bar{s}\tau\bar{\nu}$	$\equiv 0$	≤ 0.0004	≤ 0.002
$H^+H^- \rightarrow c\bar{s}\bar{t}^*b$	$\equiv 0$	≤ 0.0003	≤ 0.0008
$H^+H^- \rightarrow \bar{\tau}\nu\bar{t}^*b$	0.009 ± 0.004	0.064 ± 0.004	0.074 ± 0.006

Table 4.4: Signal overlap between channels. For ten decay modes of a $t\bar{t}$ event (1st column), this table shows the overlap fraction of the lepton+ τ_h analysis with the dilepton (2nd column), lepton+jets,= 1 tag (3rd column) and lepton+jets, ≥ 2 tags (4th column). The fields in which the analysis veto every event by looking at generator level information is marked with “ $\equiv 0$ ”. If the number of events passing both analyses is zero we assume 1 has passed both and set a limit by marking the field with a “ \leq ” character.

New background estimates

The background expectations for the four original cross section event selections were given in Table 4.3. Because of the addition of extra cuts to achieve exclusivity between the channels, the background estimates need to be recalculated.

As a first step the overlap between the lepton+jets ≥ 1 tags and ≥ 2 tags

channels is removed. The task is simplified by the fact that the lepton+jets, ≥ 2 tags events are a subset of the lepton+jets, ≥ 1 tags and so the signal and background can be subtracted in order to obtain an exactly 1 tag channel from the 1 or more tags one, thus leaving the ≥ 2 tags background unchanged. The results of this subtraction are shown in Table 4.5 for the background.

As the second step the fraction of overlap between the backgrounds in the lepton+ τ_h and the other channels is identified. The overlap is estimated by running over the proper Monte Carlo background samples evaluating the fraction of overlap ($F_{dilepton}$, $F_{lepton+jets,=1\ tag}$ and $F_{lepton+jet+\geq 2\ tags}$) with the lepton+ τ_h channel. Table 4.5 shows the fraction of overlap for the different backgrounds in each channel. When the different analyses use different datasets to estimate their backgrounds the average of the overlap is quoted. In general, the level of overlap is driven by the jet-to- τ_h fake ratio. This ratio is the fraction of “fakeable” jets that fake a hadronically decaying tau, where “fakeable” jets are defined as those with E_T above 15 GeV, $E_{Had} > 0.15\sum_i P_i$, number of tracks in tau cone < 4 and track charge in tau cone $= \pm 1$. This ratio was measured in [4] as a function of the transverse energy of the jets from the samples JET20, JET50 and JET70. These samples require at least one jet with transverse energy larger than 20, 50 and 70 GeV respectively. The measurement yields a jet-to- τ_h fake ratio of about 1%.

The background contribution to the exclusive event selections is then obtained by multiplying each original background estimate by $(1 - F)$. For example the original WW contribution to the lepton+jets, = 1 tag analysis is 0.34 ± 0.06 (see Table 4.5). Multiplying by $(1 - F) = 1 - 1/135 = 134/135$ yields 0.34 ± 0.06 within errors. Correcting all backgrounds in each analysis and adding them up results in the new total background estimates shown in Table 4.6. Note that the dilepton and lepton+jet, ≥ 2 background estimates

Background	dilepton		lepton+jets, = 1 tag		lepton+jets, ≥ 2 tags	
		F_{dilep}		$F_{l+jets1}$		$F_{l+jets2+}$
$Z/\gamma^* \rightarrow e\bar{e}$	0.36±0.27					
$Z/\gamma^* \rightarrow \mu\bar{\mu}$	0.07±0.3	0/26				
$Z/\gamma^* \rightarrow \tau\bar{\tau}$	0.42±0.13	0/232				
ZZ			0.04±0.01			
WW	0.51±0.19	0/749	0.34±0.06	1/135		
WZ	0.23±0.09	0/369	0.29±0.07	0/265	0.03±0.01	0/14
QCD Fake	1.1±0.45	0.0037	6.8±1.7	1/246		
Mistag			5.6±0.8		0.22±0.03	
W{bb,cc,c}			6.1±1.3		0.52±0.15	
Single Top			1.1±0.2		0.17±0.04	
Total	2.7±0.7		20.3±2.5		0.94±0.1	

Table 4.5: Background overlap between channels. The column labeled “F” at the right of each channel shows the fraction of overlap with the lepton+ τ_h event selection using the dataset indicated in parenthesis in the left column. If two datasets are indicated, the first one is used in the dilepton and the second in the lepton+jets analyses.

did not change at all, and the only change was in the lepton+jets, = 1 tag by a negligible amount. The smallness of the overlap fraction results in a negligible correction to the backgrounds, and could be regarded as covered by the present errors which are at least an order of magnitude larger.

Background Summary				
	dilepton	lepton+jets = 1 tag	lepton+jets ≥ 2 tags	lepton+ τ_h
Total Background	2.7 ± 0.7	20.3 ± 2.5	0.94 ± 0.10	1.30 ± 0.21

Table 4.6: Final background estimates in the exclusive channels, after the removal of the overlap.

4.3 Event expectation

The expected number of events in channel k is:

$$\mu_k = \sigma_{t\bar{t}}^{\text{prod}} \mathcal{A}_k + n_k^{\text{back}} \quad (4.4)$$

where \mathcal{A}_k is the detector acceptance times integrated luminosity of a $t\bar{t}$ pair (that may include decays to charged Higgs as well as W's) in the k^{th} channel.

The SM theoretical expectation of the $t\bar{t}$ production cross section is $\sigma_{t\bar{t}}^{\text{theo prod}} = 6.7_{-0.9}^{+0.7}$ pb [5, 6]. In this dissertation we assume the inclusion of the Higgs sector does not modify the value of the $t\bar{t}$ production cross section, and set it to $\sigma_{t\bar{t}}^{\text{prod}} = 6.7 \pm 0.9$ pb, where the errors are taken to be symmetric for simplicity. There are certain MSSM scenarios in which the production cross section is expected to differ from the SM one. These scenarios involve low mass stops and in general are not used in this dissertation. In addition, a larger width of the top quark, such as that obtained by including the decay $t \rightarrow H^+b$, may also result in an increase of the production

cross section as the parton distribution function will tend to produce more lower mass quarks.

We also assume that the backgrounds associated with the inclusion of the Higgs sector are negligible compared to the SM backgrounds in each channel. Hence we take the background expectation n_k^{back} from Table 4.6. This assumption is supported by the fact that current searches of non-SM particles have yielded null results, and by the fact that in many theoretical frameworks the production rate of such non-SM particles is expected to be very low.

The only piece missing to compute the number of expected events in channel k , μ_k , is the acceptance \mathcal{A}_k , which is described next. We assume that the charged Higgs boson can decay only to $c\bar{s}$, $\bar{\tau}\nu$, $t^*\bar{b}$ or W^+h^0 , leading to five possible decay modes for a single top quark: (1) $t \rightarrow W^+b$, (2) $t \rightarrow H^+b$, $H^+ \rightarrow c\bar{s}$, (3) $t \rightarrow H^+b$, $H^+ \rightarrow \bar{\tau}\nu$, (4) $t \rightarrow H^+b$, $H^+ \rightarrow t^*\bar{b}$ and (5) $t \rightarrow H^+b$, $H^+ \rightarrow W^+h^0$, $h^0 \rightarrow b\bar{b}$. Charge conjugated decays are implied. The decay of a pair of top quarks can result in up to 25 modes, but only 15 are different if charged conjugated modes are considered the same.

Allowing for a non-zero $\text{BR}(t \rightarrow H^+b)$, the acceptance of the detector for channel k is

$$\mathcal{A}_k = \sum_{i,j=1}^5 B_i \cdot B_j \cdot \epsilon_{ij,k}(\Gamma_t, \Gamma_{H^\pm}, m_{H^\pm}, m_{h^0}) \quad (4.5)$$

where B_i (B_j) represent the branching fractions of the top quark (anti-quark) to decay via mode i (j) as listed above, and $\epsilon_{ij,k}$ is the efficiency times integrated luminosity to detect a $t\bar{t}$ event in which top quarks decay via modes i and j in channel k .

In the narrow width approximation, in which the width of the charged Higgs is assumed small, the branching ratios B_2 to B_5 can be factorized as $B_i = \text{BR}(t \rightarrow H^+b) \times \text{BR}(H^+ \rightarrow X_i)$, where X_i represents the decay products of the charged Higgs. As shown in the table below, the 5 branching ratios

B_i can be written in terms of $\text{BR}(t \rightarrow H^+b)$, $\text{BR}(H^+ \rightarrow c\bar{s})$, $\text{BR}(H^+ \rightarrow t^*\bar{b})$, $\text{BR}(H^+ \rightarrow W^+h^0)$ and $\text{BR}(h^0 \rightarrow b\bar{b})$, were we have used the additional constraint that the branching fraction of the charged Higgs summed over its four possible decay modes adds up to unity, $\sum_i \text{BR}(H^+ \rightarrow X_i) \equiv 1$.

B_1	$1 - \text{BR}(t \rightarrow H^+b)$
B_2	$\text{BR}(t \rightarrow H^+b) \times \text{BR}(H^+ \rightarrow c\bar{s}b)$
B_3	$\text{BR}(t \rightarrow H^+b) \times \text{BR}(H^+ \rightarrow \bar{\tau}\nu b)$
B_4	$\text{BR}(t \rightarrow H^+b) \times \text{BR}(H^+ \rightarrow t^*\bar{b}b)$
B_5	$\text{BR}(t \rightarrow H^+b) \times \text{BR}(H^+ \rightarrow W^+h^0b) \times \text{BR}(h^0 \rightarrow b\bar{b})$

Explicitly expanding the sum in Equation 4.5 results in

$$\mathcal{A}_k = \{ \alpha^2 \epsilon_{HH,k} + 2\alpha(1 - \alpha)\epsilon_{HW,k} + (1 - \alpha)^2 \epsilon_{WW,k} \}$$

where $\alpha \equiv \text{BR}(t \rightarrow H^+b)$ and $\epsilon_{HH,k}(\epsilon_{HW,k})$ is the efficiency times luminosity of a $t\bar{t}$ pair decaying to $HbHb$ ($HbWb$) in the k channel. α plays here the role of a probability, distributing the $t\bar{t}$ events into the different decay modes. As desired, when $\alpha = 0$ we recover the SM acceptance $\epsilon_{WW,k}$ of Equation 4.1.

The efficiencies $\epsilon_{WW,k}$, $\epsilon_{HW,k}$, and $\epsilon_{HH,k}$ can be written as

$$\begin{aligned}
\epsilon_{WW,k} &= \epsilon_{\mathbf{W}\mathbf{W},k} \\
\epsilon_{HW,k} &= \text{BR}(H \rightarrow c\bar{s}) \epsilon_{HW \rightarrow c\bar{s}W,k} \\
&+ \text{BR}(H \rightarrow \bar{\tau}\nu) \epsilon_{HW \rightarrow \bar{\tau}\nu W,k} \\
&+ \text{BR}(H \rightarrow Wb\bar{b}) \epsilon_{HW \rightarrow Wb\bar{b}W,k} \\
&+ \text{BR}(H \rightarrow W^+h^0) \epsilon_{HW \rightarrow W^+h^0W,k} \\
\epsilon_{HH,k} &= \text{BR}^2(H \rightarrow c\bar{s}) \epsilon_{HH \rightarrow c\bar{s}c\bar{s},k} \\
&+ \text{BR}^2(H \rightarrow \bar{\tau}\nu) \epsilon_{HH \rightarrow \bar{\tau}\nu\bar{\tau}\nu,k} \\
&+ \text{BR}^2(H \rightarrow Wb\bar{b}) \epsilon_{HH \rightarrow Wb\bar{b}Wb\bar{b},k} \\
&+ \text{BR}^2(H \rightarrow W^+h^0) \epsilon_{HH \rightarrow W^+h^0W^-h^0,k} \\
&+ 2 \text{BR}(H \rightarrow c\bar{s}) \text{BR}(H \rightarrow \bar{\tau}\nu) \epsilon_{HH \rightarrow c\bar{s}\bar{\tau}\nu,k} \\
&+ 2 \text{BR}(H \rightarrow c\bar{s}) \text{BR}(H \rightarrow Wb\bar{b}) \epsilon_{HH \rightarrow c\bar{s}Wb\bar{b},k} \\
&+ 2 \text{BR}(H \rightarrow c\bar{s}) \text{BR}(H \rightarrow W^+h^0) \epsilon_{HH \rightarrow c\bar{s}W^+h^0,k} \\
&+ 2 \text{BR}(H \rightarrow \bar{\tau}\nu) \text{BR}(H \rightarrow Wb\bar{b}) \epsilon_{HH \rightarrow \bar{\tau}\nu Wb\bar{b},k} \\
&+ 2 \text{BR}(H \rightarrow \bar{\tau}\nu) \text{BR}(H \rightarrow W^+h^0) \epsilon_{HH \rightarrow \bar{\tau}\nu W^+h^0,k} \\
&+ 2 \text{BR}(H \rightarrow Wb\bar{b}) \text{BR}(H \rightarrow W^+h^0) \epsilon_{HH \rightarrow Wb\bar{b}W^+h^0,k}
\end{aligned} \tag{4.6}$$

This decomposition explicitly shows the 15 independent efficiencies needed to compute \mathcal{A}_k . These efficiencies are obtained from Monte Carlo simulation and are parametrized as a function of Γ_t , Γ_{H^\pm} , m_{H^\pm} , and m_{h^0} as detailed in Section 4.3.1. The total acceptance \mathcal{A}_k depends then only on the unknown nine following quantities:

- Γ_t
- Γ_{H^\pm}
- m_{H^\pm}

- m_{h^0}
- $\text{BR}(t \rightarrow H^+b)$
- $\text{BR}(H^+ \rightarrow c\bar{s})$
- $\text{BR}(H^+ \rightarrow t^*\bar{b})$
- $\text{BR}(H^+ \rightarrow W^+h^0)$
- $\text{BR}(h^0 \rightarrow b\bar{b})$

Once these quantities are specified, the acceptance \mathcal{A}_k , and therefore the expected number of events μ_k , can be calculated for each exclusive channel. Any model that predicts these nine quantities can be tested against data. It should be noted that quantities that were input to the calculation, other than these nine, (e.g. $\sigma_{t\bar{t}}^{\text{prod}}$) have associated errors. The consideration of these errors will result in a distribution of μ_k for each channel k , rather than a single value. This will be discussed in section 4.4.1.

4.3.1 The efficiencies

For a particular cross section analysis k each of the fifteen efficiencies in Equation 4.6 can be written as (dropping the ij subindices for simplicity):

$$\epsilon_k = \sum_{i=1}^{N_k} a_i L_i \quad (4.7)$$

where i runs over the N_k different categories of the k^{th} analysis, a_i is the acceptance and L_i is the integrated luminosity associated with that category. The dependence of $\epsilon_{ij,k}$ on Γ_t , Γ_{H^\pm} , m_{H^\pm} , and m_{h^0} is omitted in this section. All the categories in all four analyses are associated with one of the following

four luminosities, as previously explained in Table 3.4:

$$\begin{aligned}
L_{noSi-noCMX} &= 193.5 \pm 11.6 \text{ pb}^{-1} \\
L_{noSi-CMX} &= 175.3 \pm 10.5 \text{ pb}^{-1} \\
L_{Si-noCMX} &= 161.6 \pm 9.7 \text{ pb}^{-1} \\
L_{Si-CMX} &= 149.8 \pm 9.0 \text{ pb}^{-1}
\end{aligned}
\tag{4.8}$$

obtained by requiring or ignoring that the silicon and/or CMX detectors were in good working condition. The lepton+jets analyses always require good silicon conditions, while the dilepton analysis requires it only for some categories, and the lepton+ τ_h analysis does not require the silicon detector at all. The acceptances a_i can, in turn, be written as

$$a_i = \epsilon_{\text{common}} \cdot \epsilon_i \tag{4.9}$$

where ϵ_{common} gathers the efficiencies and scale factors that are common to all the categories in the channel, and ϵ_i are the efficiencies and scale factors specific to the category. We further factorize the common efficiency as¹

$$\epsilon_{\text{common}} = \epsilon_{Z0} \cdot \epsilon_{\text{trk}} \cdot \epsilon_{ISR/FSR} \cdot \epsilon_{PDF} \cdot \epsilon_{\text{jet-scale}} \cdot \epsilon_{\text{generator}} \tag{4.10}$$

where ϵ_{Z0} and ϵ_{trk} are scale factors introduced to account for known differences between MC simulation of the detector response and that observed in data. The factor ϵ_{Z0} takes into account the difference in the distribution of the position of the primary vertex $Z0$ between data and Monte Carlo. The factor ϵ_{trk} takes into account differences between observed and simulated tracking reconstruction. The other quantities introduce the systematic uncertainties associated with the modeling of initial and final state radiation ($\epsilon_{ISR/FSR}$), the parton distribution functions (ϵ_{PDF}), the jet energy modeling ($\epsilon_{\text{jet-scale}}$), and the dependence on the generator used to perform the

¹Note that efficiencies and scale factors are labeled with the same greek letter ϵ .

	dilepton	lepton+jets	lepton+ τ_h	Correlations (%)
ϵ_{Z0}	0.948 ± 0.003	0.948 ± 0.003	0.948 ± 0.003	100
ϵ_{trk}	0.996 ± 0.004	0.996 ± 0.004	0.996 ± 0.004	100
$\epsilon_{ISR/FSR}$	1.0 ± 0.017	1.0 ± 0.026	1.0 ± 0.099	100
ϵ_{PDF}	1.0 ± 0.057	1.0 ± 0.057	1.0 ± 0.057	100
$\epsilon_{\text{jet-scale}}$	1.0 ± 0.029	1.0 ± 0.029	1.0 ± 0.029	100
$\epsilon_{\text{generator}}$	1.0 ± 0.055	1.0 ± 0.014	1.0 ± 0.07	100

Table 4.7: Common terms for the efficiency. These terms are needed to compute ϵ_{common} for each cross section analysis. The degree of correlation between the analyses is given in the last column. The width of the common Gaussian in 100% correlated variables is taken to be the smallest relative error of the three analyses.

simulation ($\epsilon_{\text{generator}}$). These efficiencies have a central value of 1.0 and only contribute to the systematic error via their uncertainties. The values of all efficiencies are shown in Table 4.7. As expressed before, ϵ_{common} is common to all categories of one analysis, however the values of ϵ_{common} of different analyses are in general correlated, and this will also be taken into account when computing μ_k in section 4.4.1.

The category-specific efficiencies ϵ_i are built for the lepton+jets analyses as

$$\epsilon_i = \epsilon_i^{MC} \cdot \epsilon_i^{trg} \cdot \epsilon_i^{\text{lepton}} \quad (4.11)$$

for the lepton+ τ_h analysis as

$$\epsilon_i = \epsilon_i^{MC} \cdot \epsilon_i^{trg} \cdot \epsilon_i^{\text{lepton}} \cdot \epsilon^{\text{TauId's}} \quad (4.12)$$

and for the dilepton analysis as

$$\epsilon_i = \epsilon_{jk}^{MC} (\epsilon_j^{trg} + \epsilon_k^{trg} - \epsilon_j^{trg} \times \epsilon_k^{trg}) \cdot \epsilon_j^{\text{lepton}} \cdot \epsilon_k^{\text{lepton}} \quad (4.13)$$

where j and k label the two leptons in the category i . The ϵ_i^{MC} is the efficiency obtained from direct application of the event selection to Monte

Carlo simulated events. All channels use data samples collected with a lepton trigger, and thus the trigger efficiency for a specified lepton ϵ_i^{trg} is included. For the lepton+ τ_h channel a factor associated with the difference of the tau identification efficiency in MC and data of $\epsilon^{TausId's} = 0.95 \pm 0.10$ is used. In addition, each type of lepton has associated specific corrections $\epsilon_i^{\text{lepton}}$. The $\epsilon_i^{\text{lepton}}$ can be obtained by multiplying the last four columns in Table 4.8. With the exception of ϵ^{trg} , all efficiencies are interpreted as correction factors to the Pythia predictions for the final number of events passing all the analysis' cuts. The term ϵ^{id} represents the ratio of the identification efficiency in data and Monte Carlo, the term ϵ^{rec} the ratio of the reconstruction efficiency, the term $\epsilon^{conv/veto}$ the ratio of the conversion-veto efficiency and ϵ^{mod} the ratio in efficiency due to differences in the E_T resolution and the amount of material in the calorimeter for electrons and the P_T resolution and understanding of the muon sub-detector geometry for muons. More detailed information about these quantities can be found in [7].

The only term missing to fully calculate efficiencies in Equation 4.11, 4.12, and 4.13 are the “raw” Monte Carlo efficiencies $\epsilon_{j,k}^{MC}$ and ϵ_i^{MC} . These efficiencies depend on Γ_t , Γ_{H^\pm} , m_{H^+} , and m_{H^0} and introduce the dependence of $\epsilon_{i,j,k}$ on these parameters.

4.3.2 Calculation of the raw Monte Carlo efficiencies

The raw Monte Carlo efficiencies are calculated by applying the selection criteria of the four channels on the Monte Carlo datasets of different m_t and m_{H^\pm} combinations. The datasets contain decays to all possible modes and are therefore called “all-inclusive”. Generator level information is used to identify the decay mode on an event-by-event basis. In each channel the output of the selection code is, for each of the 15 different modes, the original number of events in that mode and the number of events passing

Lepton i	ϵ^{trg}	ϵ^{id}	ϵ^{rec}	$\epsilon^{conv/veto}$	ϵ^{mod}
CEM	0.965 ± 0.002	0.990 ± 0.008	1 ± 0	1 ± 0.014	1 ± 0.00327
PHX	0.92 ± 0.01	0.986 ± 0.004	1 ± 0	1 ± 0	1 ± 0
CMUP	0.89 ± 0.009	0.937 ± 0.011	0.927 ± 0.01	1 ± 0.010	1 ± 0.012
CMX	0.966 ± 0.007	1.015 ± 0.013	0.992 ± 0.011	1 ± 0.010	1 ± 0.012
NICEM	0.965 ± 0.002	0.78 ± 0.07	1 ± 0	1 ± 0.014	1 ± 0.00327
PEM	0	0.96 ± 0.05	1 ± 0	1 ± 0	1 ± 0
NICMUP	0.890 ± 0.009	0.85 ± 0.09	0.927 ± 0.01	1 ± 0.010	1 ± 0.012
NICMX	0.966 ± 0.007	0.85 ± 0.09	0.992 ± 0.011	1 ± 0.010	1 ± 0.012
CMU	0	0.97 ± 0.02	0.898 ± 0.021	1 ± 0.010	1 ± 0.012
NICMU	0	0.85 ± 0.09	0.898 ± 0.021	1 ± 0.010	1 ± 0.012
CMP	0	0.96 ± 0.02	0.920 ± 0.016	1 ± 0.010	1 ± 0.012
NICMP	0	0.85 ± 0.09	0.920 ± 0.016	1 ± 0.010	1 ± 0.012
CMIO	0	1.0 ± 0	1 ± 0	1 ± 0.010	1 ± 0.012

Table 4.8: Lepton-specific terms for the efficiency. This table allows the computation of $\epsilon_i^{\text{lepton}}$ by multiplying the elements in the last four columns of the row. The factorization is done to show the contribution of each sub efficiency.

each category. For example the lepton+jets selection code gives for the $t\bar{t} \rightarrow W^+bW^-\bar{b}$ mode the following output:

lepton+jets $W^+bW^-\bar{b}$	
Category	Number of events
INITIAL	117514
CEM+JETS	2372
CMUP+JETS	1405
CMX+JETS	545

The efficiencies are then calculated in each category, and the error is taken to be binomial.

4.3.3 Interpolation of the raw Monte Carlo efficiencies

The datasets provide efficiency values for a discrete number of points in the (m_t, m_{H^\pm}) plane. In general it is desirable to know the efficiency at intermediate values too. There are many interpolation methods available to do this, however, because the efficiencies do not change much between dataset points, the simplest one is used: the double linear interpolation.

The points A,B,C, and D in Figure 4.2 represent available datasets from which the efficiencies for a particular mode in a particular channel can be obtained. To obtain the efficiency at an intermediate point “K” in the (m_t, m_{H^\pm}) plane, the double linear interpolation method first interpolate between A and B at constant m_t obtaining α , and between C and D at constant m_t , obtaining β . Then interpolate between α and β at constant m_{H^\pm} . As long as ABDC forms a rectangle it can be proved that the result obtained at K is the same as if we were to interpolate first at constant m_{H^\pm} and then at constant m_t . From now the raw MC efficiency will be regarded as a continuous function in the plane (m_t, m_{H^\pm}) .

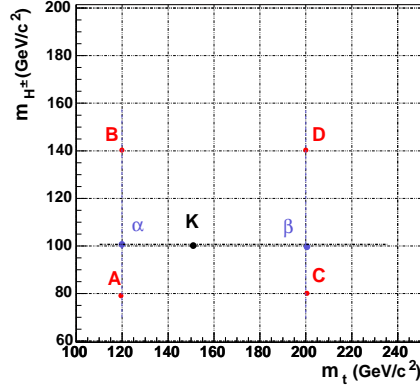


Figure 4.2: Double linear interpolation method for the efficiencies in the (m_t, m_{H^\pm}) plane. The points A,B,C,D represents the efficiency obtained for one particular mode from the datasets, the points α and β are the interpolation of A and B, and C and D respectively. The efficiency at K is the linear interpolation between α and β .

4.3.4 Width related corrections to the raw MC efficiencies

The all-inclusive datasets were generated with fixed widths of $\Gamma_{H^\pm} = 1 \text{ GeV}/c^2$ and $\Gamma_t = 1.38 \text{ GeV}/c^2$. These widths can be predicted by the model under consideration, and in the specific case of the MSSM the widths depend on the parameters m_{H^\pm} and $\tan(\beta)$ as shown previously in Section 2.3.5, Figure 2.8. The difference between the width predicted by the model and that generated in the dataset could result in different efficiencies. Thus, the efficiencies obtained from the all-inclusive datasets need to be corrected according to the expected width distributions of both particles.

A particular (theoretical) model can predict the invariant mass spectrum of the Higgs and top quark. The mass spectrum of the top, $\mathcal{W}^t(m_t)$, can be parameterized as a function of the effective width Γ_t of the top quark and its nominal mass m_t^0 , $\mathcal{W}^t(m_t, \Gamma_t, m_t^0)$. As shown in Section 2.3.5 the width of the top in turn depends on the mass of the charged Higgs, and therefore

the top mass spectrum is a function of it as well, $\mathcal{W}^t(m_t, m_{H^\pm}, m_t^0)$.

The Higgs mass spectrum $\mathcal{W}^H(m_{H^\pm})$ depends on $m_{H^\pm}^0$ and its width Γ_{H^\pm} that does not depend on the mass of the top quark. We parametrize the mass spectrum of the Higgs as a function of its nominal mass and its width $\mathcal{W}^H(m_{H^\pm}, m_{H^\pm}^0, \Gamma_{H^\pm})$. The efficiency for a particular set of nominal masses $(m_t^0, m_{H^\pm}^0)$ is corrected by integration as follows:

$$\begin{aligned}
\epsilon(m_t^0, m_H^0) &= \int_0^\infty \int_0^\infty \epsilon(m_t, m_{H^\pm}) \mathcal{W}^t(m_t, m_{H^\pm}, m_t^0) \mathcal{W}^H(m_{H^\pm}, m_{H^\pm}^0) dm_H dm_t \\
&= \int_0^\infty \mathcal{W}^H(m_{H^\pm}, m_{H^\pm}^0) \left(\int_0^\infty \epsilon(m_t, m_{H^\pm}) \mathcal{W}^t(m_t, m_{H^\pm}, m_t^0) dm_t \right) dm_{H^\pm} \\
&\simeq \int_{m_{H^\pm}^0 - 3\Gamma_{H^\pm}}^{m_{H^\pm}^0 + 3\Gamma_{H^\pm}} \mathcal{W}^H(m_{H^\pm}, m_{H^\pm}^0) \left(\int_{m_t^0 - 3\Gamma_t}^{m_t^0 + 3\Gamma_t} \epsilon(m_t, m_{H^\pm}) \mathcal{W}^t(m_t, m_{H^\pm}, m_t^0) dm_t \right) dm_{H^\pm}
\end{aligned} \tag{4.14}$$

where it is assumed that both \mathcal{W} 's are normalized and the quantities Γ_t and Γ_{H^\pm} are calculated at m_t^0 and $m_{H^\pm}^0$. The last term shows the approximation used in this dissertation in which the integral is cut off outside the $\pm 3\Gamma$ region. In a Gaussian-distributed shape this amounts to 99.74% of the area. The integration is computed numerically using a Gauss-Legendre quadrature of the 5th order as described in Appendix A.

The top mass spectrum

In the $t\bar{t}$ MC production process the mass of the top is first taken from a Breit-Wigner (BW) shape with $\Gamma_t = 1.38 \text{ GeV}/c^2$. These masses determine the phase space for the decay, and this phase space is sampled to find the kinematic variables \hat{t} and \hat{s} . Then the parton distribution functions of the proton and antiproton are sampled to evaluate the probability that they would yield the \hat{t} and \hat{s} variables. Based on all these probabilities a final weight is computed, which decides whether that particular event survives.

Through this procedure the Breit-Wigner distribution is deformed by the parton distribution functions.

The top mass spectrum is assumed to follow a Breit-Wigner distribution with a nominal mass of $m_t^0 = 175 \text{ GeV}/c^2$ and Γ_t as predicted by the model under consideration. This spectrum has yet to be deformed by the parton distribution function as in the real decay. In order to include this effect four MC $t\bar{t}$ datasets with $\Gamma_t = 1.38 \text{ GeV}/c^2$, $5 \text{ GeV}/c^2$, $10 \text{ GeV}/c^2$, and $15 \text{ GeV}/c^2$ have been generated. For each dataset the top mass spectrum is reconstructed from generator level information as shown in Figure 4.3. As expected the mean of the distributions becomes smaller at higher Γ_t , due to the higher probabilities of the parton distribution functions to generate lower mass top quarks. Note however that the peak is consistently at $175 \text{ GeV}/c^2$.

The resulting top mass spectra are parametrized as a function of the original width by fitting Breit-Wigner functions at either side of the peak, with the nominal mass fixed at $175 \text{ GeV}/c^2$ and the constraint that the functions match at $175 \text{ GeV}/c^2$. The fit returns three parameters; the widths of both Breit-Wigner functions (Γ_t^{lower} and Γ_t^{higher}) and an unimportant overall normalization parameter. The fits are shown as solid lines in Figure 4.3. Figure 4.4 shows the fitted width versus the original width used in the Monte Carlo generation, for the lower and higher Breit-Wigner functions. A linear parametrization is extracted from that figure obtaining:

$$\begin{aligned}\Gamma_{t,\text{PDF}}^{lower} &= -0.617 + 1.212 \times \Gamma_t \\ \Gamma_{t,\text{PDF}}^{higher} &= 0.394 + 0.786 \times \Gamma_t\end{aligned}\quad (4.15)$$

Note that for a somewhat large Γ_t (say $\geq 4 \text{ GeV}/c^2$) the offset terms in Equation 4.15 are negligible and the top mass spectrum can be parametrized with $\text{BW}(\Gamma_{\text{PDF}} \simeq 1.21 \times \Gamma_t)$ below $175 \text{ GeV}/c^2$ and with a $\text{BW}(\Gamma_{\text{PDF}} \simeq 0.79 \times \Gamma_t)$ above $175 \text{ GeV}/c^2$. This study however uses the full parametrization which is indeed good up to $\pm 3 \Gamma_t$ away from the peak as shown in Fig-

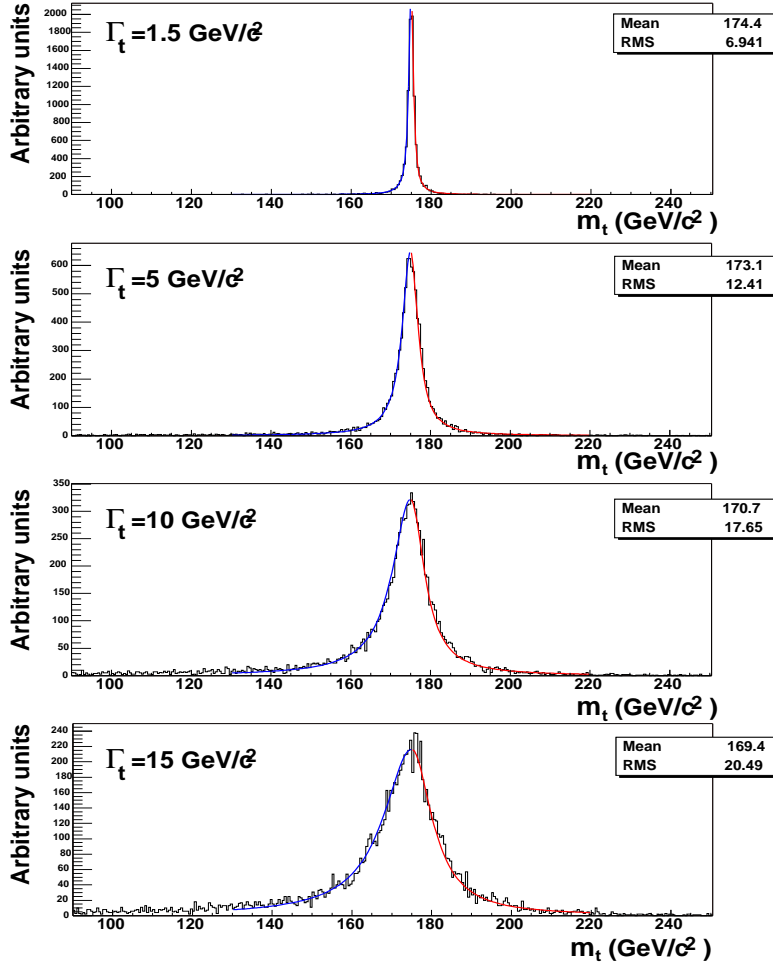


Figure 4.3: Top mass spectrum for top quarks with $m_t = 175 \text{ GeV}/c^2$ and $\Gamma_t^{ori} = 1.38 \text{ GeV}/c^2$, $5 \text{ GeV}/c^2$, $10 \text{ GeV}/c^2$ and $15 \text{ GeV}/c^2$. The original Breit-Wigner top mass distribution gets modified by the parton distribution function. The modified mass spectrum is then fitted by two Breit-Wigner functions at low and high mass regions with the requirement to match exactly at $m_t = 175 \text{ GeV}/c^2$. The histogram is what was obtained from Pythia MC simulation, the blue (red) solid line is the fit below (above) $175 \text{ GeV}/c^2$.

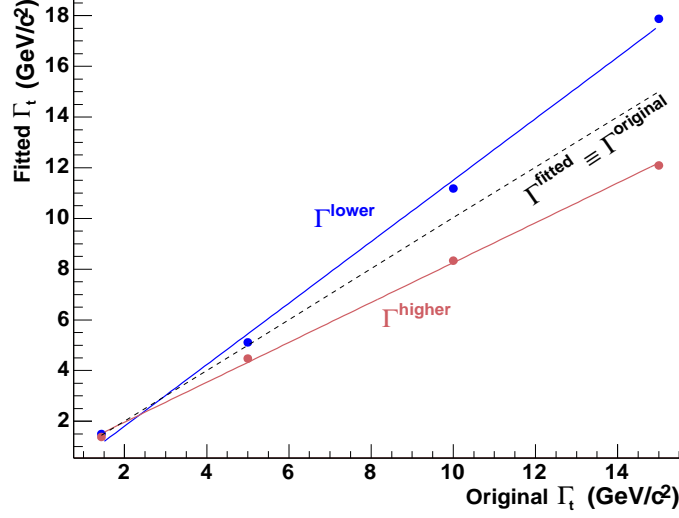


Figure 4.4: Breit-Wigner fitted width versus the original top width. The plot shows the fitted versus the original width as extracted from Figure 4.3. The dashed line represents the $\Gamma^{\text{fitted}} \equiv \Gamma^{\text{generated}}$ and is there only for reference.

ure 4.3. Given a theoretical width of Γ_t , the parton-distribution-corrected width given by $\Gamma_{t,\text{PDF}}^{\text{lower}}$ and $\Gamma_{t,\text{PDF}}^{\text{higher}}$ is obtained according to Equation 4.15. These $\Gamma_{t,\text{PDF}}$'s enter Equation 4.14.

Results of width-related corrections.

The table below shows the efficiency for $m_t = 165 \text{ GeV}/c^2$ and $185 \text{ GeV}/c^2$ divided by the efficiency at $m_t = 175 \text{ GeV}/c^2$ for the three channels.

$t\bar{t} \rightarrow W^+bW^-b\bar{b}$			
	m_t (GeV/ c^2)		
	165	175	185
$\epsilon/\epsilon_{m_t=175}$			
dilepton	0.94	$\equiv 1$	1.12
lepton +jets,=1 tags	0.96	$\equiv 1$	1.10
lepton+ τ_h	0.93	$\equiv 1$	1.09

Note that the relative change in efficiency at $185 \text{ GeV}/c^2$ (12% in the dilepton channel) is larger than that for $165 \text{ GeV}/c^2$ (6% in the dilepton channel). This means that if the top width were a perfectly symmetric function then we would expect the width-corrected efficiency to be higher. However the top width distribution is skewed to low masses, so there is cancellation between the two effects. Since the width distributions of the top and the Higgs are roughly symmetrical around their nominal masses, and the efficiencies change only by a few percent in a large range of top masses we do not expect a significant change in the absolute efficiency after width corrections. We quantify the effect of width corrections to the efficiency by showing, in the following table, the efficiency in the lepton+jets analysis as a function of the width of the top quark, relative to the efficiency obtained at $\Gamma_t = 1.38 \text{ GeV}/c^2$.

$t\bar{t} \rightarrow W^+bW^-\bar{b}$, lepton+jets				
$\Gamma_t (\text{ GeV}/c^2)$				
	1.38	5	10	15
$\epsilon_{\Gamma_t}/\epsilon_{\Gamma_t=1.38 \text{ GeV}/c^2}$	$\equiv 1$	1.002	1.003	1.005

The overall effect of the top width correction is very small, with relative differences of less than 1% for Γ_t up to $15 \text{ GeV}/c^2$. Note that Γ_t is the full width half maximum of the Breit-Wigner distribution, thus a Γ_t of $15 \text{ GeV}/c^2$ would be roughly equivalent to Gaussian of width $\simeq 7.5 \text{ GeV}/c^2$. The sharpness of the peak together with the slow change in efficiency are the determining factors for the almost null overall change in efficiency. This analysis has been repeated for different modes obtaining relative differences always less than 1%. A similar study over the width of the Higgs, assuming a low Γ_t , over the different channels and modes reveals that the corrections are of the order of $< 1\%$. However, when both widths are simultaneously large, $\Gamma \geq 15 \text{ GeV}/c^2$, the corrections done according to Equation 4.14 result

in efficiency changes of up to 1.5%. These changes are taken into account to fully account for width corrections.

4.3.5 Efficiencies summary

In summary, the efficiencies $\epsilon_{ij,k}$ for each of the 25 modes in each channel are shown in Table 4.9. These efficiencies include the luminosity and are obtained from Monte Carlo simulation assuming $\Gamma_t = 1.4 \text{ GeV}/c^2$, $\Gamma_{H^\pm} = 1 \text{ GeV}/c^2$, $m_{H^\pm} = 120 \text{ GeV}/c^2$ and $m_{h^0} = 80 \text{ GeV}/c^2$. In the dilepton and lepton+ τ_h channels the efficiency for any mode in which a top decays via $t \rightarrow H^+b$ with $H^+ \rightarrow c\bar{s}$ is zero due to the generator level requirement that the two leptons or one lepton and one hadronic tau come from the bosons of the $t\bar{t}$ decay. As expected the lepton+jets channels show an extremely low efficiency only when both top decays to $t \rightarrow H^+b$ with $H^+ \rightarrow c\bar{s}$.

4.4 Data-expectation comparison method

The expected number of events in each of the four channels can be calculated for any model that predicts the nine quantities listed in Section 4.3. This section describes the method of comparison between the expected and observed number of events in each channel that ultimately allows us to set limits on the model. As was previously mentioned, considering the errors associated to inputs in the calculation of the expected number of events results in a distribution of values of μ_k , rather than in a single value for each channel. The comparison then can be regarded as performed, for each of the four channels, between a distribution of the expected number of events and the single number observed in data. This is done by using Bayesian statistics and the method of Monte Carlo integration.

In the next sub-section the idea and implementation of the Monte Carlo integration method is detailed. The following sub-sections explain the limit-

dilepton					
$\epsilon_{ij}(pb^{-1})$	$i = t \rightarrow Wb$	$t \rightarrow Hb \rightarrow c\bar{s}b$	$t \rightarrow Hb \rightarrow \bar{\tau}\nu b$	$t \rightarrow Hb \rightarrow t^*\bar{b}b$	$t \rightarrow Hb \rightarrow Wh^0b$
$j = t \rightarrow Wb$	1.23 ± 0.05	0.00 ± 0.00	0.73 ± 0.03	1.11 ± 0.04	0.42 ± 0.05
$t \rightarrow Hb \rightarrow c\bar{s}b$	0.00 ± 0.00	0.00 ± 0.00	0.00 ± 0.00	0.00 ± 0.00	0.00 ± 0.00
$t \rightarrow Hb \rightarrow \bar{\tau}\nu b$	0.73 ± 0.03	0.00 ± 0.00	0.36 ± 0.03	0.63 ± 0.03	0.32 ± 0.04
$t \rightarrow Hb \rightarrow t^*\bar{b}b$	1.11 ± 0.04	0.00 ± 0.00	0.63 ± 0.03	0.90 ± 0.04	0.27 ± 0.04
$t \rightarrow Hb \rightarrow W^+h^0b$	0.42 ± 0.05	0.00 ± 0.00	0.32 ± 0.04	0.27 ± 0.04	0.02 ± 0.01

lepton+jets, = 1 tag					
$\epsilon_{ij}(pb^{-1})$	$i = t \rightarrow Wb$	$t \rightarrow Hb \rightarrow c\bar{s}b$	$t \rightarrow Hb \rightarrow \bar{\tau}\nu b$	$t \rightarrow Hb \rightarrow t^*\bar{b}b$	$t \rightarrow Hb \rightarrow Wh^0b$
$j = t \rightarrow Wb$	4.99 ± 0.22	3.18 ± 0.14	2.82 ± 0.13	4.85 ± 0.21	3.45 ± 0.19
$t \rightarrow Hb \rightarrow c\bar{s}b$	3.18 ± 0.14	0.00 ± 0.00	1.95 ± 0.09	2.64 ± 0.12	0.62 ± 0.06
$t \rightarrow Hb \rightarrow \bar{\tau}\nu b$	2.82 ± 0.13	1.95 ± 0.09	1.53 ± 0.08	3.07 ± 0.14	2.86 ± 0.17
$t \rightarrow Hb \rightarrow t^*\bar{b}b$	4.85 ± 0.21	2.64 ± 0.12	3.07 ± 0.14	4.52 ± 0.21	3.01 ± 0.17
$t \rightarrow Hb \rightarrow W^+h^0b$	3.45 ± 0.19	0.62 ± 0.06	2.86 ± 0.17	3.01 ± 0.17	1.02 ± 0.09

lepton+ τ_h					
$\epsilon_{ij}(pb^{-1})$	$i = t \rightarrow Wb$	$t \rightarrow Hb \rightarrow c\bar{s}b$	$t \rightarrow Hb \rightarrow \bar{\tau}\nu b$	$t \rightarrow Hb \rightarrow t^*\bar{b}b$	$t \rightarrow Hb \rightarrow Wh^0b$
$j = t \rightarrow Wb$	0.16 ± 0.02	0.00 ± 0.00	0.93 ± 0.05	0.10 ± 0.01	0.00 ± 0.00
$t \rightarrow Hb \rightarrow c\bar{s}b$	0.00 ± 0.00	0.00 ± 0.00	0.00 ± 0.00	0.00 ± 0.00	0.00 ± 0.00
$t \rightarrow Hb \rightarrow \bar{\tau}\nu b$	0.93 ± 0.05	0.00 ± 0.00	0.74 ± 0.05	0.75 ± 0.04	0.00 ± 0.00
$t \rightarrow Hb \rightarrow t^*\bar{b}b$	0.10 ± 0.01	0.00 ± 0.00	0.75 ± 0.04	0.05 ± 0.01	0.00 ± 0.00
$t \rightarrow Hb \rightarrow W^+h^0b$	0.00 ± 0.00	0.00 ± 0.00	0.00 ± 0.00	0.00 ± 0.00	0.00 ± 0.00

lepton+jets, ≥ 2 tags					
$\epsilon_{ij}(pb^{-1})$	$i = t \rightarrow Wb$	$t \rightarrow Hb \rightarrow c\bar{s}b$	$t \rightarrow Hb \rightarrow \bar{\tau}\nu b$	$t \rightarrow Hb \rightarrow t^*\bar{b}b$	$t \rightarrow Hb \rightarrow Wh^0b$
$j = t \rightarrow Wb$	1.32 ± 0.07	0.85 ± 0.04	0.75 ± 0.04	2.00 ± 0.09	2.51 ± 0.15
$t \rightarrow Hb \rightarrow c\bar{s}b$	0.85 ± 0.04	0.00 ± 0.00	0.55 ± 0.03	1.07 ± 0.05	0.43 ± 0.05
$t \rightarrow Hb \rightarrow \bar{\tau}\nu b$	0.75 ± 0.04	0.55 ± 0.03	0.35 ± 0.03	1.35 ± 0.07	1.75 ± 0.12
$t \rightarrow Hb \rightarrow t^*\bar{b}b$	2.00 ± 0.09	1.07 ± 0.05	1.35 ± 0.07	2.57 ± 0.13	2.56 ± 0.15
$t \rightarrow Hb \rightarrow W^+h^0b$	2.51 ± 0.15	0.43 ± 0.05	1.75 ± 0.12	2.56 ± 0.15	1.30 ± 0.10

Table 4.9: Efficiency summary. The table shows the efficiency for the 25 different decay modes for each of the search channels. The values are given in units of pb^{-1} since the efficiencies include the luminosity.

setting procedures for three specific models; the MSSM, the tauonic Higgs model, and the branching ratio independent model.

4.4.1 Bayesian statistics and Monte Carlo integration

In this dissertation a Bayesian statistic is used to set limits on a parameter of interest, generally called p . The parameter of interest, together with a generic set of constant parameters ρ , allows in a specific model the determination of the nine quantities needed to calculate the predicted number of events in each channel. The posterior probability density distribution of p given the observed number of events is given by Bayes' theorem

$$\mathcal{P}\left(p, \rho | \{N_{channel}^{obsv}\}\right) = \frac{L(\{N_{channel}^{obsv}\} | p, \rho) \pi(p)}{\int_{p_{min}}^{p_{max}} L(\{N_{channel}^{obsv}\} | p', \rho) \pi(p') dp'} \quad (4.16)$$

where $\{N_{channel}^{obsv}\}$ represents the set of four numbers given by the observed events in each channel, L is the likelihood, or probability of obtaining the four observed channels given p and ρ , and $\pi(p)$ is the prior probability on the parameter of interest p . The prior probability introduces the prior knowledge of the parameter of interest. In general, the only information we have on the parameter of interest is that it should lie between two known values, p_{min} and p_{max} , that represent the limits in the allowed range of p . The prior is taken to be constant between these values and zero elsewhere. The denominator is a normalization factor that insures that the integral of the probability density \mathcal{P} between p_{min} and p_{max} results in unity.

The likelihood L is computed as follows:

$$L\left(\{N_{channel}^{obsv}\} | p, \rho\right) = \int \dots \int \prod_{k=1}^4 P(N_k^{obsv}, \mu'_k) \prod_{j=1}^N D_j(\epsilon'_j, \epsilon_j) d\epsilon'_j \quad (4.17)$$

where the integrals run over the allowed values of each of the N independent inputs (ϵ' 's) that enter the calculation of the μ_k 's, $D_j(\epsilon', \epsilon)$ is the probability distribution of the variable ϵ' with mean at ϵ , and $P(N_k^{obsv}, \mu'_k)$ is the Poisson

probability of observing N_k^{obsv} events in channel k when the mean expected value is μ'_k . The value of μ'_k is calculated based on the values of ϵ' , p , and ρ .

The number of integrals is very large, as each of the variables in Table 4.8 have an associated distribution due to its error. The standard method to evaluate such a multidimensional integral is by the method of Monte Carlo integration [8]. The method calculates the likelihood using the following expression:

$$L\left(\{N_{channel}^{obsv}\}|p, \rho\right) = \frac{1}{M} \sum_{i=1}^M \prod_{k=1}^4 P(N_k^{obsv}, \mu'_k) \quad (4.18)$$

where M is the number of iterations. In each iteration (i.e. each step of the sum) different values for the independent inputs ϵ' are taken, the four μ'_k 's are calculated and the product of the Poisson's is evaluated. In each step all the luminosities in Equation 4.8 are sampled from a single Gaussian distribution with mean one and width 6%. The ϵ_{common} of Equation 4.10 is calculated by sampling each variable in Table 4.7 from a common Gaussian distribution with appropriate mean and error for all the three channels, with the uncertainty taken to be the smaller of the three values. The ϵ^{lepton} of Equation 4.11, 4.12 and 4.13 are calculated by sampling the variables in Table 4.8 from Gaussian distributions with appropriate mean and errors. The μ'_k 's are finally calculated using Equation 4.9, 4.7, 4.5 and 4.4.

It can be shown that for large values of M the likelihood obtained with Equation 4.18 converges to that obtained with Equation 4.17. The number of iterations to be performed in the MC integration is an important limitation in this analysis. The time required for a single MC iteration has to be multiplied by the product of the number of bins in other scanned variables. The time taken to performed a MC integration has to be multiplied typically by at least 20,000 and up to a million times. Figure 4.5 shows the value of the likelihood as a function of the number of iterations. A particular set of the nine quantities was used to fully determine \mathcal{A}_k . Based on that figure

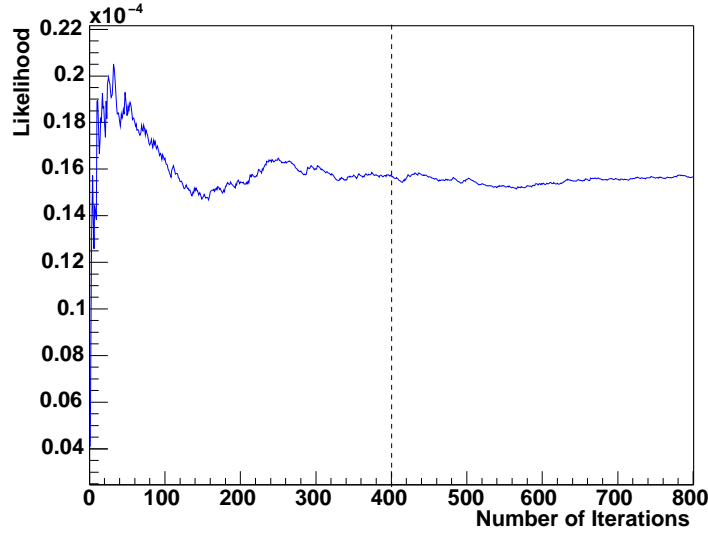


Figure 4.5: Likelihood versus the number of iterations in the Monte Carlo integration. Based on this plot we chose 400 as a compromise in computing time and accuracy.

we choose 400 as the number of iterations used to do the MC integration. The convergence of the Monte Carlo integration procedure is not expected to change with different values of \mathcal{A}_k .

The likelihood calculation can be repeated for any value of p and the posterior probability \mathcal{P} is obtained from Equation 4.16. Limits on the parameter p are obtained by integrating the posterior probability distribution over the maximum density region until reaching the desired confidence level, α . This is

$$\int_{p1}^{p2} \mathcal{P}(p, \rho) = \alpha \quad (4.19)$$

where $p1$ and $p2$ are the limits obtained in the integration. Because the integration is over the maximum density posterior probability $p1$ and $p2$ satisfy $\mathcal{P}(p1, \rho) = \mathcal{P}(p2, \rho)$. By construction both, $p1$ and $p2$, lie in the allowed range of the parameter of interest $[p_{\min}, p_{\max}]$. Values of p less than

$p1$, or greater than $p2$ are excluded at the α confidence level.

4.4.2 MSSM

In the context of the MSSM we consider $\tan(\beta)$ the parameter of interest. For a given mass of the charged Higgs, the exclusion region is obtained by scanning over $\tan(\beta)$ calculating the posterior probability given the observed candidates and the rest of the benchmark MSSM parameters. The tools described in section 2.3.5, specifically the calculations done in Appendix B and the program CPsuperH, are used to predict the quantities needed to obtain μ_k at each point.

For a given benchmark scenario (ρ) and mass of the Higgs, we obtain

$$\mathcal{P}(\tan(\beta), \rho | \{N_k^{obsv}\}) = \frac{L(\{N_k^{obsv}\} | \tan(\beta), \rho) \pi(\tan(\beta))}{\int_{\tan(\beta)} L(\{N_k^{obsv}\} | \tan(\beta) \prime, \rho) \pi(\tan(\beta) \prime) d\tan(\beta) \prime} \quad (4.20)$$

where $\pi(\tan(\beta))$ is the prior which we take to be flat in $\log_{10}(\tan(\beta))$, and zero in the theoretically inaccessible region as determined by CPsuperH (see Section 2.3.5). The choice of a flat prior in $\log_{10}(\tan(\beta))$ was determined after the results obtained in Section 2.3.5, Figure 2.7, where it is shown that a smooth behavior of the top and charged Higgs branching ratios is obtained as a function of $\log_{10}(\tan(\beta))$.

This probability is integrated over the maximum density region until obtaining the 95% area, defining the minimum and maximum values of $\tan(\beta)$. The values of $\tan(\beta)$ below the minimum or above the maximum are excluded at 95% confidence level. The procedure is repeated for masses of the charged Higgs between $80 \text{ GeV}/c^2$ and $160 \text{ GeV}/c^2$ in steps of $10 \text{ GeV}/c^2$, and the final exclusion region is obtained in the $(m_{H^\pm}, \tan(\beta))$ plane for the benchmark used.

It's interesting to see the behavior of the number of expected events for each channel as a function of $\tan(\beta)$. This is shown in Figure 4.6(a) for

$m_{H^\pm}=120 \text{ GeV}/c^2$. A strong suppression of events is evident at low $\tan(\beta)$, where the decay to $H^+ \rightarrow c\bar{s}$ is dominant. At intermediate values of $\tan(\beta)$ $\text{BR}(t \rightarrow H^+b)$ is very low (see Figure 2.7), and we recover the SM predictions of candidates marked by a constant dashed line in Figure 4.6. At high values of $\tan(\beta)$ the suppression is again strong for the dilepton and lepton+jets analyses, while the number of expected lepton+ τ_h events is much higher. The local peak at about $\tan(\beta) \simeq 1$ in that channel is due to the rise of the $\text{BR}(H^+ \rightarrow \bar{\tau}\nu)$ and the fall of $\text{BR}(t \rightarrow H^+b)$ as we move from low to high $\tan(\beta)$ values as shown in Figure 2.7.

The probability density results for $m_{H^\pm}=120 \text{ GeV}/c^2$ are obtained when the number of observed events are used in Equation 4.20. This is done in the Chapter 5 where the final results are shown. An idea of how this distribution is expected to look like can be obtained when using the number of SM expected events in the equation. This essentially compares the number of MSSM expected events to the number of SM expected events, and the results are called “sensitivity” results. The sensitivity result for the posterior probability is shown in Figure 4.6(b) for $m_{H^\pm}=120 \text{ GeV}/c^2$. The posterior is integrated over $\tan(\beta)$ to obtain the 95% confidence region as shown in the figure.

With respect to previous searches, one of the improvements performed in this analysis is the separation of lepton+jets with one or more b-tags into two channels, one with exactly one b-tag and another with two or more b-tags. This is particularly important for large Higgs masses in which the charged Higgs decay to $Wb\bar{b}$ is enhanced. The gain is evident in the Figure 4.7, where the number of expected events is shown for the four channels as a function of $\tan(\beta)$ for $m_{H^\pm}=140 \text{ GeV}/c^2$ in benchmark 1. The figure clearly shows that, at low $\tan(\beta)$, the number of expected events in the one tag and two or more tags samples are below and above the standard model expectation

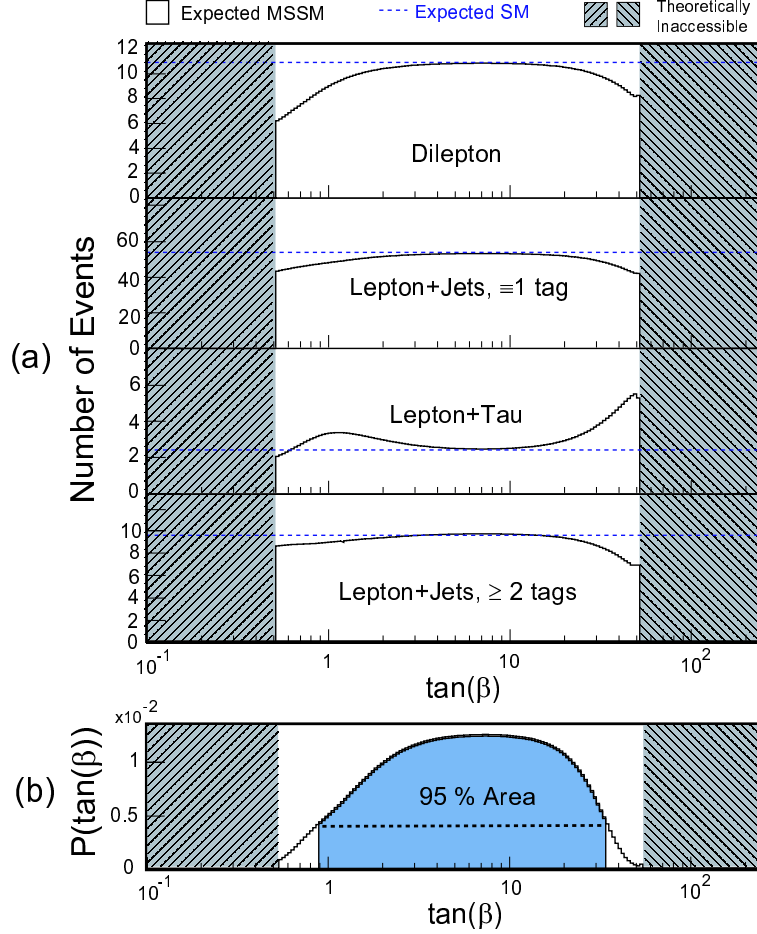


Figure 4.6: (a) MSSM expected number of events in each of the four search channels for $m_{H^\pm} = 120 \text{ GeV}/c^2$ as a function of $\tan(\beta)$. The regions $\tan(\beta) < 0.505$ and $\tan(\beta) > 51$ are theoretically inaccessible. In each histogram the SM prediction of the number of events is marked by the dashed line. (b) Posterior probability density obtained when comparing the MSSM expected number of events with SM expectations. A flat prior in $\log_{10}(\tan(\beta))$ is used. Other relevant MSSM parameters are given by benchmark 1 defined in Section 2.3.6.

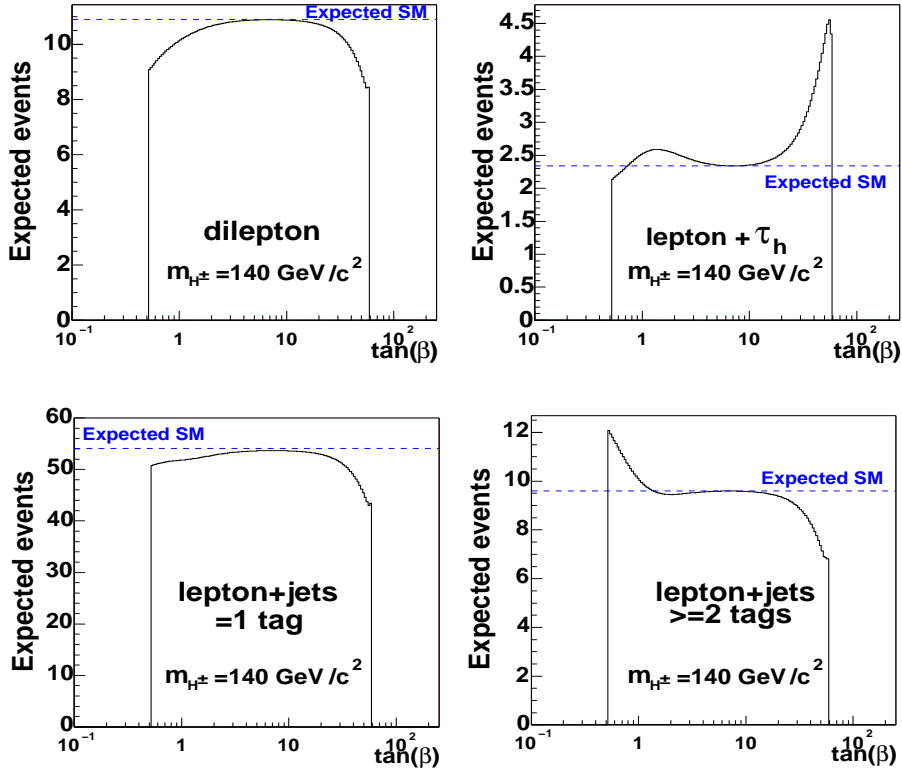


Figure 4.7: Number of expected events as a function of $\tan(\beta)$ for $m_{H^\pm} = 140 \text{ GeV}/c^2$. In each histogram the SM-predicted number of events is marked by the dashed line. Note that at low $\tan(\beta)$ the number of expected events tends to decrease for the exactly one tag channel and to increase for the two or more tags channel.

respectively. At $\tan(\beta) \simeq 0.5$ the one tag predicts about 3 events less than the SM, but the two or more tags predicts about 3 events more; if we were to use the one or more tags (which is effectively the sum of both channels) we would get about the same amount as expected with the SM, and the sensitivity of the analysis would be reduced. The difference between these two channels is enhanced at low $\tan(\beta)$ for larger charged Higgs masses.

4.4.3 Tauonic Higgs model

As discussed in Section 2.4.2, theoretical considerations and the latest LEP results seem to favor large values of $\tan(\beta)$, in which the charged Higgs decays to $\bar{\tau}\nu$ 100% of the time. This is called the ‘‘tauonic Higgs model’’. In this model we consider the $\text{BR}(t \rightarrow H^+b)$ the parameter of interest. The posterior is calculated as follow,

$$\mathcal{P}(\alpha|\{N_k^{obsv}\}) = \frac{L(\{N_k^{obsv}\}|\alpha)\pi(\alpha)}{\int_{\alpha} L(\{N_k^{obsv}\}|\alpha)\pi(\alpha)d\alpha} \quad (4.21)$$

where $\alpha = \text{BR}(t \rightarrow H^+b)$ has been used to avoid clutter in the notation. For a given m_{H^\pm} we scan the $\text{BR}(t \rightarrow H^+b)$ from 0 to 0.99 in steps of 0.01. In each bin in $\text{BR}(t \rightarrow H^+b)$ we compute the posterior probability density assuming $\text{BR}(H^+ \rightarrow \bar{\tau}\nu)=1$. The latter is achieved by setting the other 7 variables needed to compute \mathcal{A}_k to:

- $\text{BR}(H^+ \rightarrow c\bar{s}) \equiv 0$
- $\text{BR}(H^+ \rightarrow t^*\bar{b}) \equiv 0$
- $\text{BR}(H^+ \rightarrow W^+h^0) \equiv 0$
- $\text{BR}(h^0 \rightarrow b\bar{b})$ is irrelevant
- $\Gamma_t = 1.38/(1.0 - \text{BR}(t \rightarrow H^+b)) \text{ GeV}/c^2$
- $\Gamma_{H^\pm} = 1 \text{ GeV}/c^2$

- m_{h^0} is irrelevant

The posterior is then integrated over the maximum density region until the 95% area is obtained, resulting in a 95% CL limit in $\text{BR}(t \rightarrow H^+b)$. The posterior probability density obtained using the number of SM expected candidates is shown in Figure 4.8 for $m_{H^\pm}=80 \text{ GeV}/c^2$. The dashed line indicates the upper 95% CL in the $\text{BR}(t \rightarrow H^+b)$. This procedure is repeated for different charged Higgs masses, and the results using the observed number of events are presented as exclusion regions in the $(m_{H^\pm}, \text{BR}(t \rightarrow H^+b))$ plane in Chapter 5. It should be noted that for $\text{BR}(t \rightarrow H^+b) > 0.9$ the width of the top is greater than $15 \text{ GeV}/c^2$, and the narrow width approximation used in section 4.3 does not accurately hold. In particular the scan is performed only up to 0.99 to avoid the Γ_t divergence when $\text{BR}(t \rightarrow H^+b) = 1$. The top width Γ_t assumes its largest value of $138 \text{ GeV}/c^2$ when $\text{BR}(t \rightarrow H^+b) = 0.99$. The width correction mechanism described previously, cannot precisely correct the efficiency for such a large width, but the extremely large number of events predicted in each channel makes the likelihood value at that $\text{BR}(t \rightarrow H^+b)$ very small. The mechanism of width corrections regains its accuracy for values of $\text{BR}(t \rightarrow H^+b) \leq 0.96$.

4.4.4 Branching ratio independent model

In the tauonic Higgs Model we assumed the charged Higgs decays to $\bar{\tau}\nu$ 100% of the time. For each mass of the charged Higgs we obtained a posterior probability in $\text{BR}(t \rightarrow H^+b)$, from which we took 95% C.L. limits. In principle this can be repeated assuming any other combination of branching ratios, for example $\text{BR}(H^+ \rightarrow c\bar{s}) = 0.3$, $\text{BR}(H^+ \rightarrow t^*\bar{b}) = 0.5$ and $\text{BR}(H^+ \rightarrow \bar{\tau}\nu) = 0.2$.

For a certain charged Higgs mass the branching ratio independent model takes all possible combinations of the different branching ratios of the Higgs,

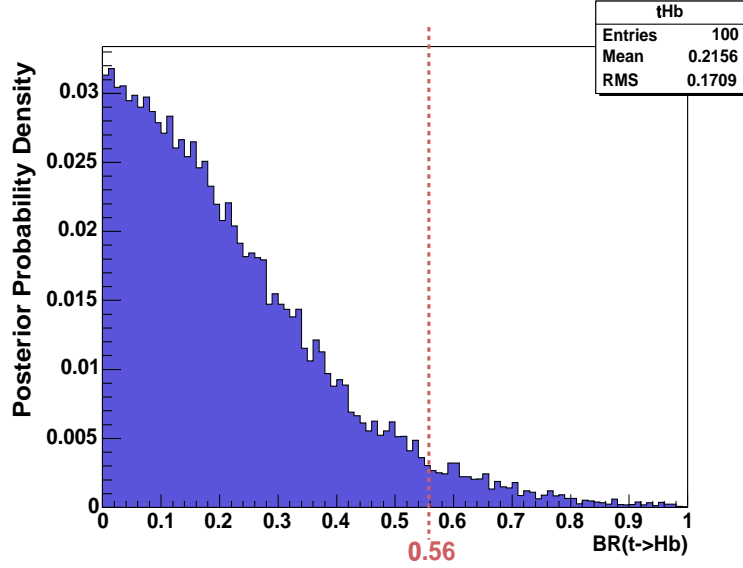


Figure 4.8: The sensitivity results for the posterior probability density of $\text{BR}(t \rightarrow H^+ b)$ for $m_{H^\pm} = 80 \text{ GeV}/c^2$. The 95% C.L. is indicated by the dashed line.

producing for each combination a 95% CL limit in $\text{BR}(t \rightarrow H^+ b)$. For a specific charged Higgs mass the branching ratio parameter space is divided such that the branching ratios of each of the four decays $H^+ \rightarrow c\bar{s}$, $H^+ \rightarrow t^*\bar{b}$, $H^+ \rightarrow \bar{\tau}\nu$, and $H^+ \rightarrow W^+ h^0$ is divided into 21 bins. This results in 1771 possible combinations subject to the relation $\sum_i \text{BR}(H^+ \rightarrow X_i) \equiv 1$, where the index i runs over the four charged Higgs decay modes considered. For each combination we scan $\text{BR}(t \rightarrow H^+ b)$ from 0 to 0.99, in steps of 0.01. For each point in the scan the rest of the relevant parameters to calculate \mathcal{A}_k are given by

- $\text{BR}(h^0 \rightarrow b\bar{b}) \equiv 0.9$
- $\Gamma_t = 1.38/(1.0 - \text{BR}(t \rightarrow H^+ b)) \text{ GeV}/c^2$
- $\Gamma_{H^\pm} = 1 \text{ GeV}/c^2$
- m_{h^0} is set to $70 \text{ GeV}/c^2$.

Figure 4.9 shows the distribution of the 1771 limits obtained for $m_{H^\pm}=120 \text{ GeV}/c^2$ when the SM expected number of events is used. The least-stringent limit is quoted as the result for that mass. Since we place limits on $\text{BR}(t \rightarrow H^+b)$ that hold for any combination of charged Higgs branching ratios the results are independent of the charged Higgs branching ratios. The figure shows that the least-stringent limit is $\text{BR}(t \rightarrow H^+b)=0.88$, indicating that for $m_{H^\pm}=120 \text{ GeV}/c^2$ we expect to exclude $\text{BR}(t \rightarrow H^+b) \geq 0.88$ at 95% C.L. The distribution of Figure 4.9 also indicates that the best obtainable limit is $\text{BR}(t \rightarrow H^+b)=0.23$ for a particular BR combination and with the used search channels, methodology and amount of data collected. This analysis is repeated for different charged Higgs masses between $80 \text{ GeV}/c^2$ and $160 \text{ GeV}/c^2$, and the results using the observed number of events are presented as exclusion regions in the $(m_{H^\pm}, \text{BR}(t \rightarrow H^+b))$ plane in Chapter 5. As before, it should be remembered that the narrow width approximation starts to break down for $\text{BR}(t \rightarrow H^+b) > 0.9$.

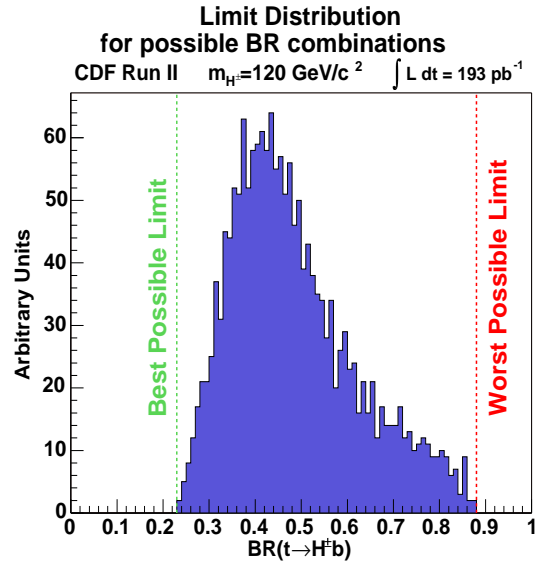


Figure 4.9: The distribution of the 95% CL limits obtained from the 1771 combinations of branching ratios. The limits were obtained using the SM expected number of events. The plot is made for $m_{H^\pm}=120 \text{ GeV}/c^2$ assuming $m_{h^0}=70 \text{ GeV}/c^2$ and $\text{BR}(h^0 \rightarrow b\bar{b}) \equiv 0.9$. The least-stringent limit obtained is $\text{BR}(t \rightarrow H^+ b)=0.88$ and is shown by the red dotted line.

Bibliography

- [1] D. Acosta et al. Measurement of the $t\bar{t}$ production cross section in $p\bar{p}$ collisions at $\sqrt{s} = 1.96$ TeV using dilepton events. *Phys. Rev. Lett.*, 93:142001, 2004.
- [2] Sarah Demers. *A Measurement of $BR(t \rightarrow \tau + \nu + quark)$* . PhD thesis, University of Rochester, 2005.
- [3] D. Acosta et al. Measurement of the $t\bar{t}$ production cross section in $p\bar{p}$ collisions at $\sqrt{s} = 1.96$ TeV using lepton + jet events with secondary vertex b-tagging. *Phys. Rev.*, D71:052003, 2005.
- [4] Sarah Demers et al. Measurement of $t\bar{t}$ in the $e - \tau_{had}$ and $\mu - \tau_{had}$ dilepton channels. *CDF note 6921*, 2004.
- [5] Nikolaos Kidonakis and Ramona Vogt. Next-to-next-to-leading order soft-gluon corrections in top quark hadroproduction. *Phys. Rev.*, D68:114014, 2003.
- [6] M. Cacciari, S. Frixione, M. L. Mangano, P. Nason, and G. Ridolfi. The t anti- t cross-section at 1.8-TeV and 1.96-TeV: A study of the systematics due to parton densities and scale dependence. *JHEP*, 04:068, 2004.
- [7] K. Bloom et al. $t\bar{t}$ event selection and detection efficiency for summer 2003 lepton+jets analyses. *CDF note 6574*, 2003.
- [8] John Conway. Efficiency uncertainties : A Bayesian prescription. *CDF note 5894*, 2002. See also “<http://www.taygeta.com/rwalks/node5.html>” to get a basic description of the Monte Carlo integration procedure.

Chapter 5

Results and Conclusions

The results of the search for charged Higgs bosons are presented in the first section of this chapter. The comparison of the results with expected sensitivity limits and with previous results is also shown. The dissertation finishes with concluding remarks and future prospects in the last section of this chapter.

5.1 Results

The results of this dissertation are obtained when the number of candidates observed in data are used to calculate the posterior probability density of the parameters of interest for the three models used. The posterior probability is then integrated to obtain limits at the 95% C.L. for the MSSM, the tauonic Higgs model, and the Higgs branching ratio independent model.

5.1.1 MSSM

The results obtained by using the observed number of candidates in each channel are shown in Figure 5.1, 5.2 for the four benchmarks developed in Section 2.3.6, and in Figure 5.3 for the two LEP benchmarks. Each figure contains limits for two benchmarks, and the exclusion limits for the six benchmarks are shown.

The plots for the six benchmarks show exclusion limits in the $(m_{H^\pm}, \tan(\beta))$

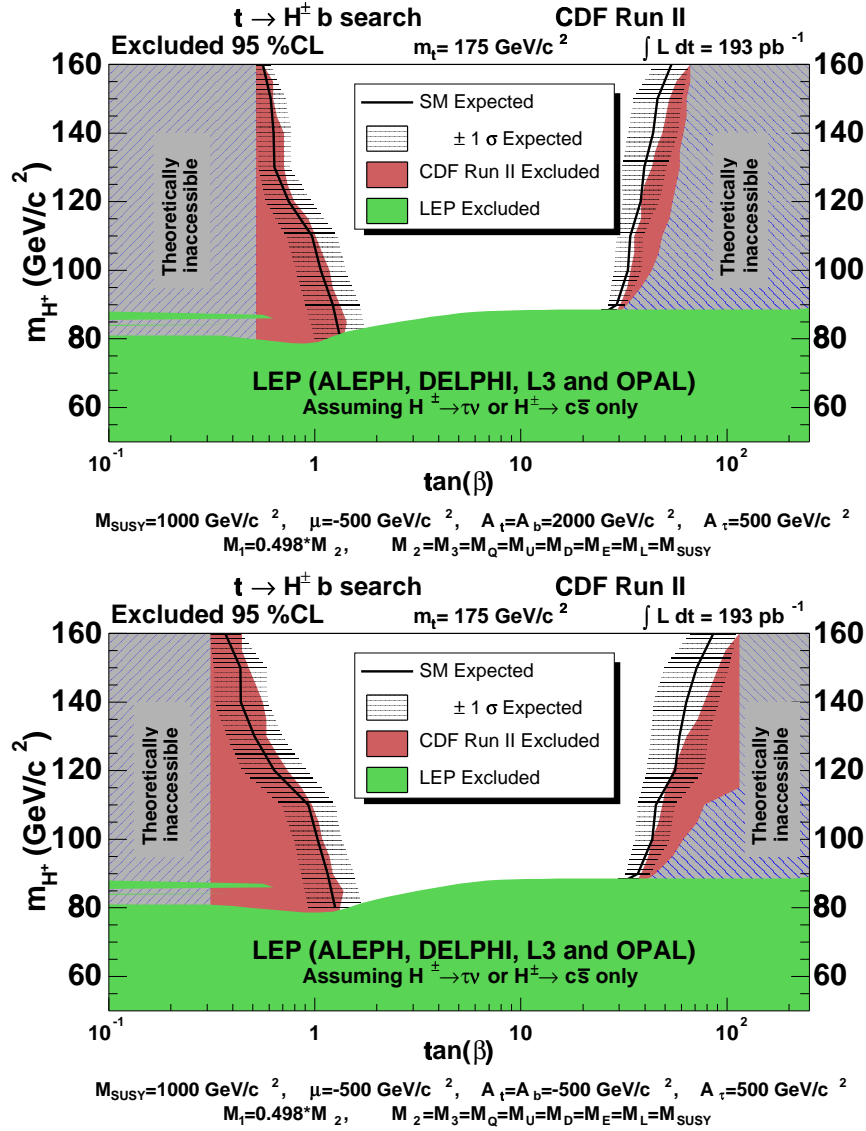


Figure 5.1: The MSSM results obtained with 193 pb^{-1} at CDF for benchmark 1 (top) and 2 (bottom). The expected exclusion limits are indicated by a black solid line and the 1-sigma confidence band around it is obtained by throwing pseudo-experiments. The contour of the red solid region indicates the observed limits. The red solid region represents the area excluded at the 95% CL. The lower green region is the LEP combined results from direct searches.

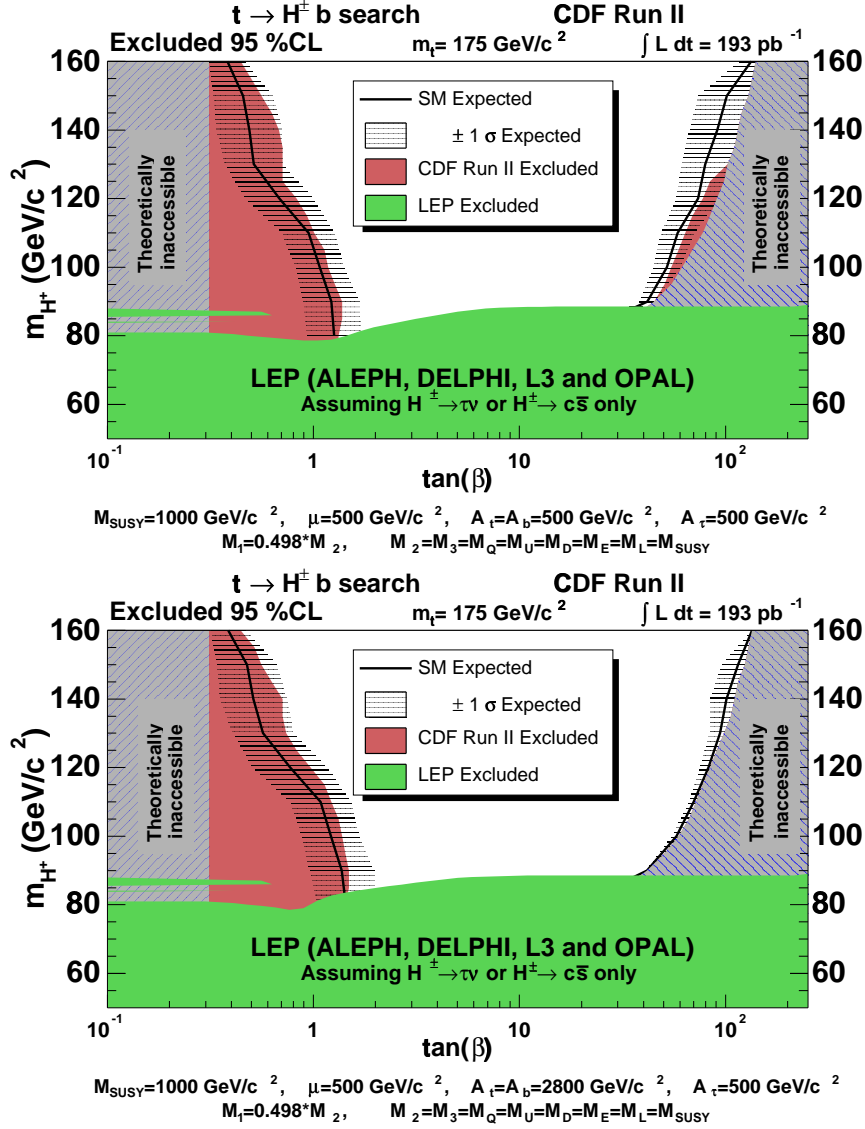


Figure 5.2: The MSSM results obtained with 193 pb^{-1} at CDF for benchmark 3 (top) and 4 (bottom). The expected exclusion limits are indicated by a black solid line and the 1-sigma confidence band around it is obtained by throwing pseudo-experiments. The contour of the red solid region indicates the observed limits. The red solid region represents the area excluded at the 95% CL. The lower green region is the LEP combined results from direct searches.

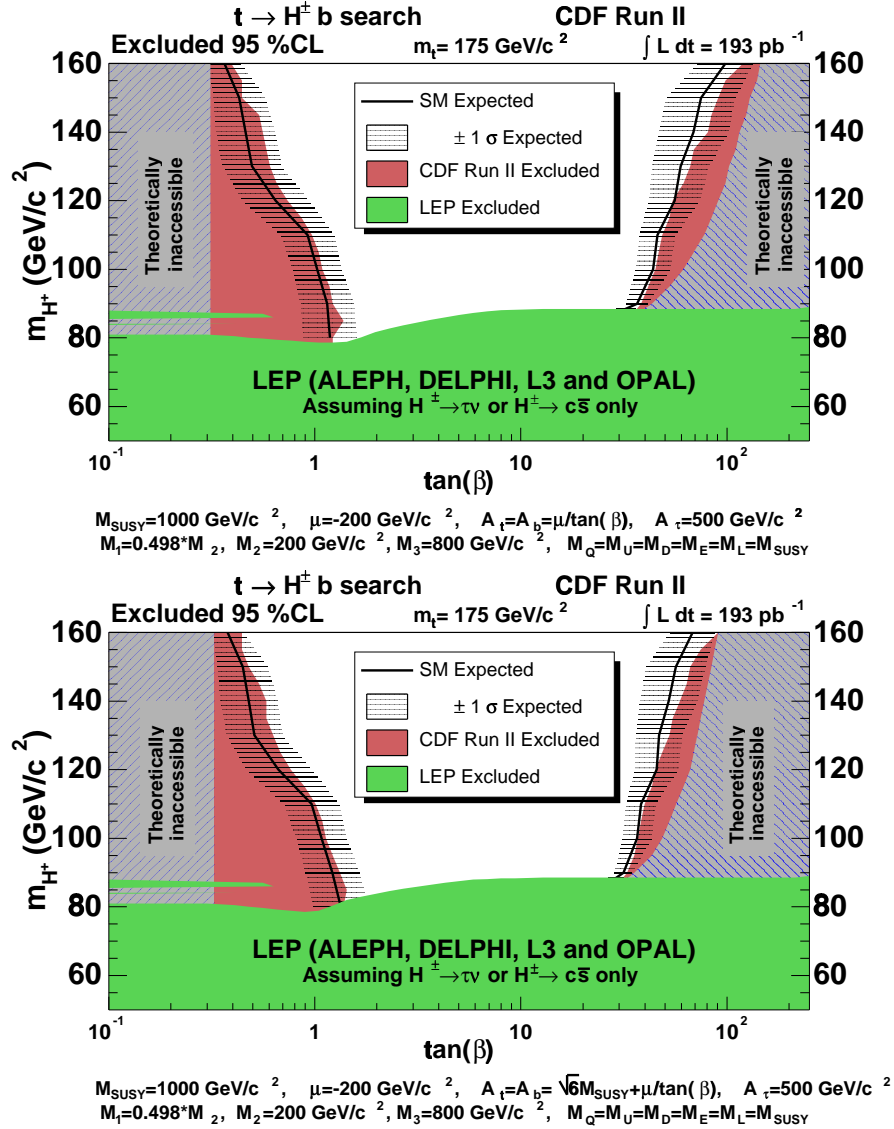


Figure 5.3: The MSSM results obtained with 193 pb^{-1} at CDF for the minimal LEP benchmark (top) and maximal LEP benchmark (bottom). The expected exclusion limits are indicated by a black solid line and the 1-sigma confidence band around it is obtained by throwing pseudo-experiments. The contour of the red solid region indicates the observed limits. The red solid region represents the area excluded at the 95% CL. The lower green region is the LEP combined results from direct searches.

plane and share similar characteristics. The lower excluded Higgs mass region is given by the combined LEP result, obtained from direct search studies as previously mentioned in Section 2.4.2 and Figure 2.11(right). The hatched regions at high and low values of $\tan(\beta)$ are considered theoretically inaccessible as determined by CPsuperH and previously described in Section 2.3.5. The solid (red) regions in the $(m_{H^\pm}, \tan(\beta))$ plane, labeled “CDF Run II Excluded” in the legend, are the results of this dissertation for the MSSM. These regions are excluded at 95% C.L. and were obtained using the observed number of candidates in Equation 4.20. The sensitivity bands, labeled “SM $\pm 1 \sigma$ Expected” in the legend, are obtained by throwing pseudo-experiments where the number of candidates were Poisson-fluctuated around the SM-expected number of events in each channel. The band represents the RMS in the limits obtained from the ensemble of pseudo-experiments. The continuous, solid line labeled “SM Expected” is the mean value of the limits obtained from the ensemble of pseudo-experiments.

The sensitivity bands give an idea of how the obtained limits compare to SM expectations. If signal were present in our sample the sensitivity band would move a certain number of standard deviations away from the actual observed limits. In an exclusion plot the signal always manifests itself as a discrepancy with respect to the limits that would be obtained in the context of the SM.

In all the MSSM benchmarks considered in this dissertation, the charged Higgs decay to W^+h^0 is predicted to have its largest branching fraction in the region around $\tan(\beta) \approx 1$, as demonstrated in Figure 2.6 for benchmark 1.

Benchmarks 1 and 2, for which results are shown in Figure 5.1, differ only in the value of A_t , or equivalently X_t since both benchmarks have the same value of μ (see Equation 2.61). As described in Section 2.3.6 this results in

different predictions of the mass of the neutral h^0 boson, and thus different $\text{BR}(H^+ \rightarrow W^+h^0)$ for the two benchmarks. Benchmark 1, described in Section 2.3.6, was developed to satisfy the maximal m_{h^0} condition at $\tan(\beta) \approx 1$, thus predicting large m_{h^0} values. Benchmark 2 was developed to satisfy the minimal m_{h^0} condition, thus resulting in a smaller m_{h^0} . Since the coupling strength of the Higgs boson increases with the mass of the decaying particles, benchmark 1 predicts a larger $\text{BR}(H^+ \rightarrow W^+h^0)$ than benchmark 2. The difference in the exclusion regions at low $\tan(\beta)$ of these two benchmarks is representative of the dependence of the analysis on $\text{BR}(H^+ \rightarrow W^+h^0)$. Figure 5.1 demonstrates that this dependence is small, as both exclusion regions are very similar. This is because the charged Higgs branching ratio to W^+h^0 is relatively small for both benchmarks. Taking $m_{H^\pm} = 120 \text{ GeV}/c^2$ as an example, the first benchmark predicts $\text{BR}(H^+ \rightarrow W^+h^0) = 0.10$ (see Figure 2.6), and $\text{BR}(H^+ \rightarrow W^+h^0) = 0.15$ is predicted for benchmark 2.

The discussion in the previous paragraph applies as well for the comparison between the exclusion regions of benchmark 3 and 4 in the low $\tan(\beta)$ region. As before, the branching ratio $H^+ \rightarrow W^+h^0$ is small for both benchmarks, and the difference in the low $\tan(\beta)$ exclusion limits between benchmark 3 and 4 is small. These benchmarks, although with different values of μ and A_t , satisfy the same maximal and minimal m_{h^0} conditions that benchmark 1 and 2 do, and since the value of μ does not play a significant role at low $\tan(\beta)$, the four exclusion regions are found to be very similar.

In the low $\tan(\beta)$ region, the largest difference between the exclusion regions of benchmarks 1 and 2, appears at $m_{H^\pm} = 160 \text{ GeV}/c^2$. This is because the theoretically inaccessible region at low $\tan(\beta)$ is smaller in the second benchmark than in the first. As a consequence, the integration region is larger in the second benchmark and the limits are obtained at lower values of $\tan(\beta)$. This dependence with the integration region arises at large m_{H^\pm} ,

where the $\text{BR}(t \rightarrow H^+b)$ is strongly suppressed (see Figure 2.7), and the sensitivity of the method becomes small.

The similarities between the four benchmarks end in the large $\tan(\beta)$ region. In this region the charged Higgs boson decays mostly to $\bar{\tau}\nu$, and the decay is governed by the top quark branching ratio to charged Higgs and a b quark. This branching ratio strongly depends on the values of μ and A_t for large values of $\tan(\beta)$. Benchmarks 1 and 2 have a value of $\mu = -500 \text{ GeV}/c^2$ resulting in a $\text{BR}(t \rightarrow H^+b)$ that quickly grows with $\tan(\beta)$ as seen in Figure 2.4. Having the same value of μ , the difference between benchmark 1 and 2 is attributed to the different values of A_t .

The shape of the theoretically inaccessible area in the high $\tan(\beta)$ region of benchmark 2 is due to two effects. For masses of the charged Higgs below $115 \text{ GeV}/c^2$ the program CPsuperH is unable to successfully diagonalize the mass matrices, and a consistent MSSM theory cannot be achieved. For masses above $115 \text{ GeV}/c^2$ the vertical region is determined by the bottom Yukawa coupling exceeding a value of 4, and a perturbation theory cannot be achieved at higher energies.

The exclusion region obtained at low $\tan(\beta)$ in the four benchmarks can be compared with the lines of constant $\text{BR}(t \rightarrow H^+b)$ shown in Figure 2.4. The comparison indicates that this region roughly follows the contour of $\text{BR}(t \rightarrow H^+b) = 0.4$ for $m_{H^\pm} \leq 120 \text{ GeV}/c^2$. For higher charged masses the exclusion region follows the contours of lower $\text{BR}(t \rightarrow H^+b)$. In the large $\tan(\beta)$ region the exclusion limit roughly follow the lines of $\text{BR}(t \rightarrow H^+b) = 0.2$ in each benchmark. The difference between the exclusion region in the low and high $\tan(\beta)$ region in terms of the $\text{BR}(t \rightarrow H^+b)$, arises from the fact that the method is more sensitive at high $\tan(\beta)$ values where the charged Higgs decays to τ_h 's, than at low values, where the charged Higgs decays to a mixture of final states.

From the results presented in the four benchmarks, the first and second yield the largest exclusion regions due to the enhanced $\text{BR}(t \rightarrow H^+b)$. In contrast, the parameters of benchmark 3 and 4 strongly suppress the $\text{BR}(t \rightarrow H^+b)$, and the excluded region is expected to be very limited. The choice of A_t for benchmark 3 allows a small exclusion region to be placed for large values of $\tan(\beta)$. However, the choice of A_t for benchmark 4 allows no exclusion limit to be placed in the high $\tan(\beta)$ region due to the strong suppression of $\text{BR}(t \rightarrow H^+b)$. This is in strong contrast with previous experiments in which an exclusion region was obtained as shown in Section 2.4.3, Figure 2.12(left). It is fundamental to consider radiative corrections in the determination of the exclusion region. Our result shows that for high $\tan(\beta)$ values no limit can be placed that hold for any combination of MSSM values.

For completeness, the results obtained for the minimal and maximal LEP benchmarks are shown in Figure 5.3. The low $\tan(\beta)$ regions are very similar between the two, and also similar to the other four benchmarks developed in this dissertation. The large $\tan(\beta)$ region are only slightly different, showing that in this region there is not a large difference in the prediction of $\text{BR}(t \rightarrow H^+b)$. This is a consequence of the fact that the LEP benchmarks were not designed for charged Higgs searches, and have very similar phenomenologies for the $t \rightarrow H^+b$ decay.

The contours of the exclusion region in the six benchmarks overlap with their respective sensitivity bands obtained using pseudo-experiments. This indicates that the exclusion regions closely resemble what would be obtained if no charged Higgs signal is present. The maximum deviation between the exclusion region contour and the sensitivity band is of order of 1 standard deviation in $\tan(\beta)$, and can be seen, for example, in benchmark 3, for $m_{H^\pm} = 135 \text{ GeV}/c^2$ and $\tan(\beta) = 0.7$.

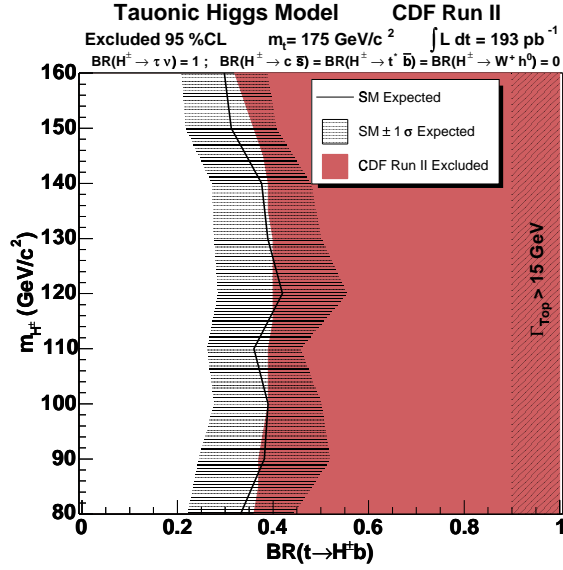


Figure 5.4: The red solid region represent the CDF Run II excluded region in the $(m_{H^\pm}, BR(t \rightarrow H^+b))$ plane, assuming $BR(H^+ \rightarrow \tau\nu) \equiv 1$. The band represent the expected limit obtained by generating pseudo-experiments in which the number of candidates is Poisson-fluctuated around SM expectations. The region $BR(t \rightarrow H^+b) > 0.9$ where the narrow width approximation starts to break is indicated by the hatched region.

5.1.2 Tauonic Higgs model

The posterior probability density of $BR(t \rightarrow H^+b)$ for a given charged Higgs mass is computed from Equation 4.21 using the observed number of candidates in each channel. The 95% upper confidence limit is obtained and the procedure repeated for Higgs masses between $80 \text{ GeV}/c^2$ and $160 \text{ GeV}/c^2$. The results are shown in the $(m_{H^\pm}, BR(t \rightarrow H^+b))$ plane in Figure 5.4. The solid (red) region, labeled “CDF Run II Excluded” in the legend, are the results of this dissertation for the tauonic Higgs model. This region is excluded at 95% C.L. and was obtained using the observed number of candidates. The sensitivity bands are labeled “SM $\pm 1\sigma$ Expected” and are

obtained by generating pseudo-experiments in which the number of candidates is Poisson-fluctuated around the SM-expected number of events in each channel. The band represents the RMS in the limits obtained from the ensemble of pseudo-experiments. The mean value of the limits obtained from the ensemble of pseudo-experiments is the solid line labeled “SM Expected”.

Figure 5.4 shows that the $\text{BR}(t \rightarrow H^+b) \geq 0.4$ can be excluded at 95% C.L. in the tauonic Higgs model, with only a small dependence of the excluded branching ratio on the mass of the charged Higgs. The exclusion of $\text{BR}(t \rightarrow H^+b) \geq 0.4$ doubles the value of $\text{BR}(t \rightarrow H^+b) \geq 0.2$ obtained from a translation of the MSSM results to $\text{BR}(t \rightarrow H^+b)$ in the large $\tan(\beta)$ region, as described in the previous section. This is a consequence of different limit-setting procedures for both cases.

5.1.3 BR independent model

For a given charged Higgs mass, and each possible branching ratio combination of the charged Higgs decays, the posterior probability density of $\text{BR}(t \rightarrow H^+b)$ is obtained from Equation 4.21. From each posterior the 95% C.L. limit is obtained, and the least-stringent limit is quoted for the given charged Higgs mass. This procedure is repeated for different charged Higgs masses. The results of the charged Higgs Branching ratio independent results are shown in Figure 5.5.

Figure 5.5 shows that the $\text{BR}(t \rightarrow H^+b) \geq 0.9$ can be excluded at 95% C.L. in the BR independent model, with a strong dependence of the excluded branching ratio on the mass of the charged Higgs. The least stringent Higgs branching ratio combination, for all the masses in the $80 - 160 \text{ GeV}/c^2$ range, is found to be one in which the charged Higgs dominantly decays $t^* \bar{b} \rightarrow Wb\bar{b}$, thus mimicking the decay $t \rightarrow W^+b$. The least stringent limit is obtained for $m_{H^\pm} = 100 \text{ GeV}/c^2$. A charged Higgs of $m_{H^\pm} = 100 \text{ GeV}/c^2$

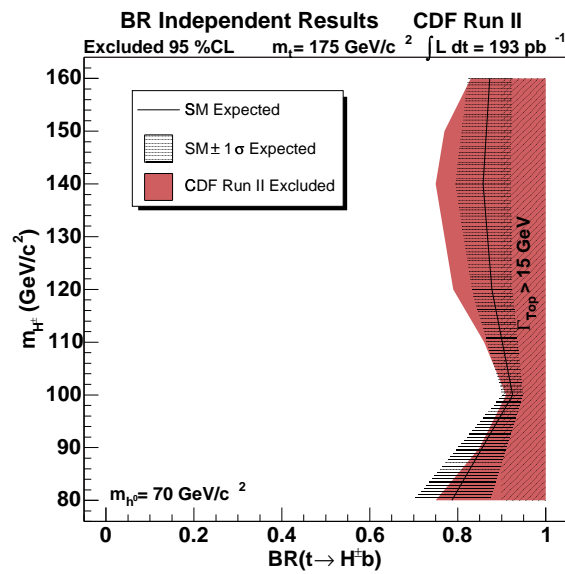


Figure 5.5: The exclusion region in the $(m_{H^\pm}, BR(t \rightarrow H^+b))$ plane. At each value of m_{H^\pm} the worst limit is shown for all possible combination of branching ratios. The region $BR(t \rightarrow H^+b) > 0.9$ where the narrow width approximation starts to break is indicated by the hatched region.

effectively produces an $80 \text{ GeV}/c^2$ W boson and a pair of soft b quarks, and the kinematics of the decay are very similar to the $t \rightarrow W^+b$ counterpart. The most stringent limit is obtained for $m_{H^\pm} = 80 \text{ GeV}/c^2$ and $140 \text{ GeV}/c^2$, in which this decay shows a stronger difference with respect the SM decay.

It should be noted that the results shown in Figure 5.5 were obtained using $m_{h^0} = 70 \text{ GeV}/c^2$. This value is chosen to allow the decay $H^+ \rightarrow W^+h^0$ even for values of m_{H^\pm} as low as $80 \text{ GeV}/c^2$. The results are not sensitive to small deviations from that mass, as the observed limits are driven by the charged Higgs decay to $t^*\bar{b} \rightarrow Wb\bar{b}$. If higher values of m_{h^0} were used, the decay $H^+ \rightarrow W^+h^0$ would be kinematically forbidden for $m_{H^\pm} \leq m_{h^0}$, and the limits below m_{h^0} would only get stricter.

5.2 Conclusions

This dissertation reports the results of a search for a charged Higgs boson in the decays of top quarks produced in $p\bar{p}$ collisions at a center-of-mass energy of 1.96 TeV. The data sample, consisting of $t\bar{t}$ candidates decaying to four different decay channels, was collected by the upgraded Collider Detector at Fermilab and corresponds to an integrated luminosity of up to 193 pb^{-1} .

The search for charged Higgs is based on the number of events observed in the four channels. No evidence for charged Higgs production is found, allowing 95% C.L. limits to be placed for different charged Higgs decay scenarios.

It is demonstrated in Section 2.3.5 that the possibility for the charged Higgs decays to W^+h^0 and W^+A^0 is significant, and these decays are therefore considered in this analysis. The effects due to large widths of the top and charged Higgs are also considered, although are found to be very small (see Section 4.3.4).

In the context of MSSM, results are presented for the first time including

radiative corrections. The consideration of these corrections results in a narrower region of theoretically accessible values than originally thought in previous studies (see Section 2.4.3). In addition, it is shown that the set of benchmarks developed at LEP is not optimal for the search for charged Higgs (Section 5.1.1), and a set of four benchmark scenarios was specifically developed for this purpose (Section 2.3.6). This dissertation finds that large regions of $\tan(\beta)$ cannot be excluded regardless of the MSSM parameters, as the radiative corrections strongly modify the $\text{BR}(t \rightarrow H^+b)$ predictions. The region of low values of $\tan(\beta)$ is similarly excluded in all the benchmarks used (Section 5.1.1).

In the context of the tauonic Higgs model, values of $\text{BR}(t \rightarrow H^+b) \geq 0.4$ are excluded at 95% C.L. This exclusion region surpasses previously obtained results (see Section 2.4.3) and constitute the best limits to date.

The charged Higgs branching ratio independent method has been developed. For the first time, a limit is placed that considers all the significant charged Higgs branching ratios. Values of $\text{BR}(t \rightarrow H^+b) \geq 0.9$ are excluded at 95% C.L.

5.3 Future prospects

With an integrated luminosity of 193 pb^{-1} , the measurements of the $t\bar{t}$ production cross section in each of the four channels is dominated by the statistical uncertainties in the numbers of expected events. Therefore, the limits in the results of this dissertation are also of a statistical nature, as they are based in the results of the production cross section measurement in the four channels. This error is expected to decrease only with the square root of the integrated luminosity, and a reduction of 30% in the error is expected when 2 fb^{-1} of data are collected.

The Large Hadron Collider (LHC), a proton-proton accelerator machine

Channel	Events expected in 200 pb ⁻¹		
	S/B	μ^{expected}	n^{back}
dilepton	10	1600	160 ± 13
lepton+jets, = 1 tag	28	4540	163 ± 15
lepton+jets, ≥ 2 tags	78	740	22 ± 2
lepton+ τ_h	10	290	29 ± 5

Table 5.1: Expected $t\bar{t}$ events in the ATLAS detector at LHC. The numbers are expected with 200 pb⁻¹. The values were extracted from the study performed in [2], where the μ^{expected} and n^{back} columns were scaled to 200 pb⁻¹.

located at CERN, is scheduled to start taking data in 2007. With a center-of-momentum energy of 14 TeV the $t\bar{t}$ production cross section calculated at next to leading order is $\sigma_{t\bar{t}}^{\text{prod}} = 833 \pm 83$ pb (see [1]). This large $t\bar{t}$ production rate would allow the study of the top properties and production in detail, and this knowledge would be crucial for most searches of new physics in which top production is considered background.

A series of detectors are located at the colliding points in the LHC ring. For one of them, called ATLAS, a thorough study of the expected number of events in each of the four search channels has been performed in [2]. The analysis performed in this dissertation is extrapolated to the ATLAS detector, and limits are obtained assuming only 200 pb⁻¹ of data taken with the ATLAS detector for comparison. According to the luminosity expectation to be delivered by the LHC accelerator, the ATLAS detector would collect 200 pb⁻¹ of data in a single week of nominal data-taking. The limits obtained from this extrapolation are, therefore, just a glimpse into the LHC potential.

The theoretical production cross section is used, together with the numbers provided in [2] and Table 5.1 to predict the achievable limits for the

ATLAS detector. The results are shown in Figure 5.6 in the $(m_{H^\pm}, \tan(\beta))$ plane for benchmark 1, and in Figure 5.7 for $\text{BR}(t \rightarrow H^+b)$ in the tauonic Higgs model. The method used in this dissertation, applied to data col-

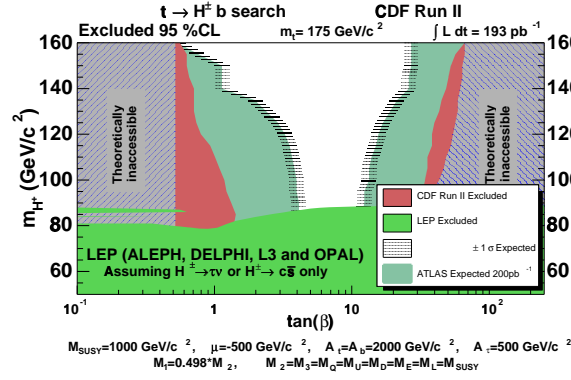


Figure 5.6: Expected limits for benchmark 1 using 200 pb⁻¹ from the ATLAS detector.

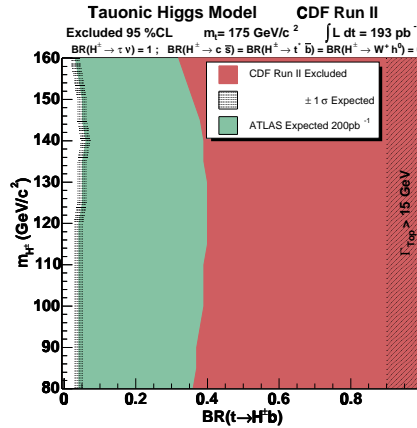


Figure 5.7: ATLAS expectation for the tauonic Higgs model. With 200 pb⁻¹ values of $\text{BR}(t \rightarrow H^+b) \geq 0.05$ are expected to be excluded.

lected during a week with the ATLAS detector at LHC, is expected to set very strict limits in the $(m_{H^\pm}, \tan(\beta))$ plane for benchmark 1. In the tauonic Higgs model, values of $\text{BR}(t \rightarrow H^+b) \geq 0.05$ are expected to be excluded at 95% C.L.

The current constraints on the top quark properties and decays, and in general on the mechanism of electro-weak symmetry breaking, are still not strong. Deviations from SM expectation can still be large, and yet lie within the experimental error of the measurements. In the years to come, with more data collected from the Tevatron and the turn-on of the LHC, physicists will have a unique opportunity. The opportunity to noticeably strengthen these constraints, and possibly force nature to reveal the mechanism of electro-weak symmetry breaking, and with it, help answer the fundamental questions of contemporary particle physics.

Bibliography

- [1] Roberto Bonciani, Stefano Catani, Michelangelo L. Mangano, and Paolo Nason. Nll resummation of the heavy-quark hadroproduction cross-section. *Nucl. Phys.*, B529:424–450, 1998.
- [2] I. Borjanovic et al. Investigation of top mass measurements with the atlas detector at lhc. *Eur. Phys. J.*, C39S2:63–90, 2005.

Appendix A

Numeric integration

In order to numerically compute the integrals in Equation 4.14 we employ a Gauss-Legendre quadrature of the 5th order. The working scheme of the quadrature states that

$$I = \int_a^b \mathcal{F}(x)dx \simeq m \sum_{i=1}^N w_i \mathcal{F}(c + mt_i) \quad (\text{A.1})$$

Where $c = \frac{a+b}{2}$ and $m = \frac{b-a}{2}$. And N is the number of points we wish to use in the integration; the larger the better. The w_i and t_i represent the weights and points to which we need to weight and evaluate our function, are standard tabulated and depend on the number N. In our case we use N=5, and the w_i 's and t_i 's are :

Gauss-Legendre quadrature 5 th order		
i	w_i	t_i
1	0.23697	-0.90618
2	0.47862	-0.53847
3	0.56888	0.0
4	0.47862	+0.53847
5	0.23697	+0.90618

As a cross check let's apply this method to the integration of a Gaussian between $\pm 3\sigma$. The result should be close to 0.9974 (= 1 - 2 * 0.0013).

$$\begin{aligned}
I &= \frac{1}{\sigma\sqrt{2\pi}} \int_{-3\sigma}^{3\sigma} e^{-\frac{u^2}{2\sigma^2}} du \simeq m \sum_{i=1}^N w_i \mathcal{F}(c + mt_i) \\
&\simeq \frac{3\sigma}{\sigma\sqrt{2\pi}} \left[0.56888 + 2 \times 0.4786 e^{-\frac{(3 \times 0.5385)^2}{2}} \right. \\
&\quad \left. + 2 \times 0.23697 e^{-\frac{(3 \times 0.90618)^2}{2}} \right] \\
&\simeq \frac{3}{\sqrt{2\pi}} [0.56888 + 0.259587 + 0.0117735] = 1.005
\end{aligned} \tag{A.2}$$

This indicates that the numeric integration has an relative error of less than 0.8%, which is more than adequate for our purposes¹.

¹The same calculation with a 3th order quadrature yields a relative error of about 15%

Appendix B

Radiative corrections to

$$\Gamma(t \rightarrow H^+ b)$$

The first part of Section B.1 shows the tree level and standard model QCD corrections to the decay rate $t \rightarrow H^+ b$. The corrections are performed to full one-loop order. The second part of this section shows improved results in which the resummation of next-to-leading logarithms is included. This resummation is performed in the context of the operator product expansion (OPE) over an effective, soft, SUSY-breaking Lagrangian. Section B.2 introduces the modifications needed in order to account for SUSY-QCD and SUSY-EW corrections. The final formulae is shown in Section B.3. Section B.4 shows the conclusions of this appendix.

B.1 QCD corrections

The one-loop QCD corrections are taken directly from [1] and reproduced below for reference. The authors used the renormalization mass scale of the decaying (top) quark and have used dimensional regularization working in $d=4-2\omega$ dimensions in order to overcome the divergences due to the emission of soft and collinear gluons. The virtual gluon contribution is also included.

Let's introduce dimensionless parameters based on the pole masses,

$$\epsilon = \frac{m_b}{m_t}, \chi = \frac{m_H}{m_t}, \omega = \frac{m_W}{m_t} \quad (\text{B.1})$$

and further define a and b for a Type II 2HDM as follows:

$$a = \cot(\beta) + \epsilon \tan(\beta)$$

$$b = \cot(\beta) - \epsilon \tan(\beta)$$

We can use the variables above to define,

$$\begin{aligned} \bar{P}_0 &\equiv \frac{1}{2}(1 - \chi^2 + \epsilon^2) \\ \bar{P}_3 &\equiv \frac{1}{2}\sqrt{1 + \chi^4 + \epsilon^4 - 2(\chi^2 + \epsilon^2 + \chi^2\epsilon^2)} \\ \bar{P}_\pm &\equiv \bar{P}_0 \pm \bar{P}_3 \\ \bar{Y}_p &\equiv \frac{1}{2}\ln\left(\frac{\bar{P}_+}{\bar{P}_-}\right) \\ \bar{W}_0 &\equiv \frac{1}{2}(1 + \chi^2 - \epsilon^2) \\ \bar{W}_\pm &\equiv \bar{W}_0 \pm \bar{P}_3 \\ \bar{Y}_w &\equiv \frac{1}{2}\ln\left(\frac{\bar{W}_+}{\bar{W}_-}\right) \end{aligned}$$

We are now going to define four more functions based on the previous,

$$\begin{aligned} \mathcal{H} &= 4\bar{P}_0 \left[Li_2(\bar{P}_+) - Li_2(\bar{P}_-) - 2Li_2\left(1 - \frac{\bar{P}_-}{\bar{P}_+}\right) + \bar{Y}_p \ln\left(\frac{4\bar{P}_3^2\chi}{\bar{P}_+^2}\right) - \bar{Y}_w \ln(\epsilon) \right] \\ &+ 2\bar{Y}_w(1 - \epsilon^2) + \frac{2}{\chi^2}\bar{P}_3 \ln(\epsilon)(1 + \chi^2 - \epsilon^2) \\ G_0 &= -6\bar{P}_0\bar{P}_3 \ln \epsilon \\ G_- &= \mathcal{H} + \bar{P}_3 \left[6 - 4\ln\left(\frac{4\bar{P}_3^2}{\epsilon\chi}\right) \right] + \frac{1}{\chi^2}\bar{Y}_p (1 - \chi^2 - 2\epsilon^2 + \epsilon^4 - 3\chi^2\epsilon^2) \\ G_+ &= \bar{P}_0\mathcal{H} + \bar{P}_0\bar{P}_3 \left[\frac{9}{2} - 4\ln\left(\frac{4\bar{P}_3^2}{\epsilon\chi}\right) \right] \\ &+ \frac{1}{4\chi^2}\bar{Y}_p (2 - \chi^2 - 4\chi^4 + 3\chi^6 - 2\epsilon^2 - 2\epsilon^4 + 2\epsilon^6 - 4\chi^2\epsilon^2 - 5\chi^2\epsilon^4) \end{aligned}$$

where the Li_2 is the dilogarithm function

$$Li_2(z) = \sum_{k=1}^{\infty} \frac{z^k}{k^2}$$

The width of the decay is now constructed from two terms,

$$\Gamma^0(t \rightarrow H^+b) = \frac{G_F m_t^3}{4\sqrt{2}\pi} |V_{tb}|^2 [\bar{P}_0(a^2 + b^2) + \epsilon(a^2 - b^2)] \bar{P}_3 \quad (\text{B.2})$$

$$\begin{aligned} \Gamma^{(1)}(t \rightarrow H^+b) = \frac{\alpha_s}{6\pi^2} \frac{G_F m_t^3 |V_{tb}|^2}{\sqrt{2}} & [(a^2 + b^2)G_+ \\ & + (a^2 - b^2)\epsilon G_- + abG_0] \quad (\text{B.3}) \end{aligned}$$

Finally, the total width is then

$$\Gamma(t \rightarrow H^+b) = \Gamma^0(t \rightarrow H^+b) + \Gamma^{(1)}(t \rightarrow H^+b) \quad (\text{B.4})$$

B.1.1 Renormalization Group improvement

The full one-loop QCD corrections to the top decay shown in the previous section contains the summation of the leading logarithms

$$\alpha_s^n \log^n \left(\frac{Q}{m_b} \right)$$

However, as indicated in [2], a consistent use of the one-loop corrected expressions requires also the summation of the next-to-leading logarithms

$$\alpha_s^{n+1} \log^n \left(\frac{Q}{m_b} \right)$$

because all these terms are of the same order as the one-loop finite terms.

This is done in [2] for large values of $\tan(\beta)$ obtaining

$$\begin{aligned} \Gamma_{QCD}^{imp}(t \rightarrow bH^+) \stackrel{\tan(\beta) \geq 10}{=} & \frac{g^2}{64\pi M_W^2} m_t (1 - \chi^2)^2 \bar{m}_b^2(m_t^2) \tan^2(\beta) \times \\ & \left\{ 1 + \frac{\alpha_s(m_t^2)}{\pi} \left[7 - \frac{8\pi^2}{9} - 2\log(1 - \chi^2) + 2(1 - \chi^2) \right. \right. \\ & \left. \left. + \left(\frac{4}{9} + \frac{2}{3} \log(1 - \chi^2) \right) (1 - \chi^2)^2 \right] \right\} \quad (\text{B.5}) \end{aligned}$$

where $\alpha_s(m_t^2)$ and $\bar{m}_b(m_t^2)$ are the running coupling constant and mass evaluated in $\bar{M}S$ -scheme, so there is an implicit scheme conversion in going from the high $\tan(\beta)$ limit of Equation B.4 to Equation B.5.

In order to include the next-to-leading summation for large values of $\tan(\beta)$ in the standard QCD corrections of Equation B.4 we simply strip Equation B.4 of those terms proportional to $\tan^2(\beta)$ and add the improved results of Equation B.5 resulting in our final QCD corrections,

$$\Gamma_{QCD}^{impr}(t \rightarrow H^+b) = \Gamma^{\tan^2(\beta)}(t \rightarrow H^+b) + \Gamma^{\cot^2(\beta)}(t \rightarrow H^+b) + \Gamma^{indep}(t \rightarrow H^+b) \quad (B.6)$$

where $\Gamma^{\tan^2(\beta)}$, $\Gamma^{\cot^2(\beta)}$ and Γ^{indep} are the terms proportional to $\tan^2(\beta)$, $\cot^2(\beta)$ and independent of $\tan(\beta)$ respectively.

$$\begin{aligned} \Gamma^{\tan^2(\beta)}(t \rightarrow H^+b) &= \frac{G_F m_t}{4\sqrt{2}\pi} |V_{tb}|^2 [\bar{m}_b^2(m_t^2) \tan^2(\beta) 2\bar{P}_0] \bar{P}_3 \times \\ &\left\{ 1 + \frac{\alpha_s(m_t^2)}{\pi} \left[7 - \frac{8\pi^2}{9} - 2\log(1 - \chi^2) + 2(1 - \chi^2) \right. \right. \\ &\left. \left. + \left(\frac{4}{9} + \frac{2}{3}\log(1 - \chi^2) \right) (1 - \chi^2)^2 \right] \right\} \quad (B.7) \end{aligned}$$

$$\Gamma^{\cot^2(\beta)}(t \rightarrow H^+b) = \frac{G_F m_t^3}{2\sqrt{2}\pi} |V_{tb}|^2 \cot^2(\beta) \left[\bar{P}_0 \bar{P}_3 + \frac{2\alpha_s}{6\pi} (2G_+ + G_0) \right] \quad (B.8)$$

$$\Gamma^{indep}(t \rightarrow H^+b) = \frac{G_F m_t^3}{\sqrt{2}\pi} |V_{tb}|^2 \epsilon^2 \left[\bar{P}_3 + \alpha_s \frac{2}{3\pi} G_- \right] \quad (B.9)$$

Equations B.7, B.8 and B.9 contain the better results at high $\tan(\beta)$ obtained in [2] and the one-loop correction without the summation of sub-leading logarithms at low $\tan(\beta)$. Note that $\Gamma^{\cot^2(\beta)}$ and Γ^{indep} contain the bottom pole mass while the term $\Gamma^{\tan^2(\beta)}$ contains the running mass of the b at the renormalization scale of the top. The full formulae for the calculation of the running b mass for arbitrary renormalization scale is found in [2] and yields approximately $\bar{m}_b = \bar{m}_b(m_{top}) \simeq [2.863 - 0.001166(m_{top} - 175)]$ GeV.

B.2 SUSY corrections

In the supersymmetric limit down-like (up-like) quarks couple only to Φ_d^0 (Φ_u^0), however when supersymmetry is broken a small coupling of the down-

like (up-like) quarks to Φ_u^0 (Φ_d^0) can arise from the one-loop Yukawa vertex corrections. The results can be summarized by an effective Lagrangian that describes the coupling of the Higgs bosons to the third generation quarks, thus implying a modification of the tree-level relations between the Yukawa coupling and the quark masses [3, 4] as follows:

$$\begin{aligned} m_b &= \frac{h_b v}{\sqrt{2}} \cos(\beta) \left(1 + \frac{\delta h_b}{h_b} + \frac{\Delta h_b \tan(\beta)}{h_b} \right) \equiv \frac{h_b v}{\sqrt{2}} \cos(\beta) (1 + \Delta_b) \\ m_t &= \frac{h_t v}{\sqrt{2}} \sin(\beta) \left(1 + \frac{\delta h_t}{h_t} + \frac{\Delta h_t \cot(\beta)}{h_t} \right) \equiv \frac{h_t v}{\sqrt{2}} \sin(\beta) (1 + \Delta_t) \end{aligned}$$

where $v \simeq 174$ GeV. Note that the correction to m_b (m_t) is enhanced by a large (small) $\tan(\beta)$. The variable Δ_b encodes all the SUSY corrections to the b quark, and can effectively be included in the calculations by replacing the mass m_b with $\frac{\tilde{m}_b}{1 + \Delta_b}$. The same applies to Δ_t .

In general the quantities $\frac{\Delta h_q}{h_q}$ and $\frac{\delta h_q}{h_q}$ can in turn be obtained from [5]:

$$\frac{\delta h_d}{h_d} = -\frac{2\alpha_s}{3\pi} M_{\tilde{g}} A_d I(m_{\tilde{d}_1}, m_{\tilde{d}_2}, |M_{\tilde{g}}|) - \frac{|h_u|^2}{16\pi^2} |\mu|^2 I(m_{\tilde{u}_1}, m_{\tilde{u}_2}, |\mu|) \quad (\text{B.10})$$

$$\begin{aligned} \frac{\Delta h_d}{h_d} &= \frac{2\alpha_s}{3\pi} M_g \mu I(m_{\tilde{d}_1}, m_{\tilde{d}_2}, M_{\tilde{g}}) + \frac{h_u^2}{16\pi^2} \mu A_u I(m_{\tilde{u}_1}, m_{\tilde{u}_2}, \mu) \\ &\quad - \frac{g^2}{16\pi^2} \mu M_2 [\cos^2 \theta_{\tilde{u}} I(m_{\tilde{u}_1}, M_2, \mu) + \sin^2 \theta_{\tilde{u}} I(m_{\tilde{u}_2}, M_2, \mu)] \\ &\quad - \frac{g^2}{16\pi^2} \mu M_2 \frac{1}{2} [\cos^2 \theta_{\tilde{d}} I(m_{\tilde{d}_1}, M_2, \mu) + \sin^2 \theta_{\tilde{d}} I(m_{\tilde{d}_2}, M_2, \mu)] \end{aligned} \quad (\text{B.11})$$

where d and u represent the up-like and down-like quarks and the function I is defined as:

$$I(a, b, c) = \frac{1}{(a^2 - b^2)(b^2 - c^2)(a^2 - c^2)} \left(a^2 b^2 \log \frac{a^2}{b^2} + b^2 c^2 \log \frac{b^2}{c^2} + c^2 a^2 \log \frac{c^2}{a^2} \right) \quad (\text{B.12})$$

Equations B.10 and B.11 contain threshold radiative effects assuming negligible mixing between the different generation of squarks. Analog quantities for $\frac{\delta h_d}{h_d}$ and $\frac{\Delta h_d}{h_d}$ are obtained by interchanging u and \tilde{u}_i by d and \tilde{d}_i in

Equation B.10, B.11. In terms of the third generation quarks the terms in the the right hand side of the equations above represent (from left to right) the sbottom-gluino (SUSY-QCD), the charged higgsino-stop, the charged wino-stop and the neutral wino-sbottom contributions. The bino effects have been neglected due to its small numerical effects [2].

B.3 Final Formulas

The final formulas are then built by introducing the SUSY corrected top and bottom masses to Equations B.7, B.8 and B.9. This amounts, for every mass brought in the equation by the Yukawa coupling, to replace $\bar{m}_b(m_{top})$ by $\frac{\bar{m}_b(m_{top})}{(1+\Delta_b)}$ and m_t by $\frac{m_t}{(1+\Delta_t)}$ in Equation B.7, B.8, and B.9, yielding the final formulae:

$$\begin{aligned} \Gamma^{\tan^2(\beta)}(t \rightarrow H^+b) &= \frac{G_F m_t}{4\sqrt{2}\pi} |V_{tb}|^2 \left[\frac{\bar{m}_b^2(m_t^2)}{(1+\Delta_b)^2} \tan^2(\beta) 2\bar{P}_0 \right] \bar{P}_3 \times \\ &\quad \left\{ 1 + \frac{\alpha_s(m_t^2)}{\pi} \left[7 - \frac{8\pi^2}{9} - 2\log(1-\chi^2) + 2(1-\chi^2) \right. \right. \\ &\quad \left. \left. + \left(\frac{4}{9} + \frac{2}{3}\log(1-\chi^2) \right) (1-\chi^2)^2 \right] \right\} \quad (\text{B.13}) \end{aligned}$$

$$\begin{aligned} \Gamma^{\cot^2(\beta)}(t \rightarrow H^+b) &= \frac{G_F m_t}{4\sqrt{2}\pi} \frac{m_t^2 |V_{tb}|^2}{(1+\Delta_t)^2} \cot^2(\beta) \times \\ &\quad \left[2\bar{P}_0 \bar{P}_3 + \frac{4\alpha_s}{6\pi} (2G_+ + G_0) \right] \quad (\text{B.14}) \end{aligned}$$

$$\Gamma^{indep}(t \rightarrow H^+b) = \frac{G_F}{\sqrt{2}\pi} \frac{|V_{tb}|^2}{m_t} \frac{m_t^2 m_b^2}{(1+\Delta_t)(1+\Delta_b)} \left[\bar{P}_3 + \alpha_s \frac{2}{3\pi} G_- \right] \quad (\text{B.15})$$

As before note that the bottom pole mass is used in the definitions of the Equation B.15 as it is implicit in all the terms \bar{P}_i and G_i . The running bottom mass at the energy of the top quark is used only explicitly in Equation B.13.

B.4 Conclusions

We have derived, in the context of the MSSM with a type II Higgs sector, the $\Gamma(t \rightarrow H^+b)$, including full QCD, SUSY-QCD and SUSY-EW corrections. These expressions are valid to all values of $\tan(\beta)$ in which perturbative expansion is allowed. The formulas are derived from an effective lagrangian that modifies the tree-level relation between the bottom Yukawa coupling and the bottom mass. The resummation of leading and next to leading order logarithms which are dominant in the high $\tan(\beta)$ regime are also included.

Bibliography

- [1] Andrzej Czarnecki and Sacha Davidson. Qcd corrections to the charged higgs decay of a heavy quark. *Phys. Rev.*, D48:4183–4187, 1993.
- [2] Marcela Carena, David Garcia, Ulrich Nierste, and Carlos E. M. Wagner. Effective lagrangian for the anti-t b h+ interaction in the mssm and charged higgs phenomenology. *Nucl. Phys.*, B577:88–120, 2000.
- [3] Lawrence J. Hall, Riccardo Rattazzi, and Uri Sarid. The top quark mass in supersymmetric so(10) unification. *Phys. Rev.*, D50:7048–7065, 1994.
- [4] Ralf Hempfling. Yukawa coupling unification with supersymmetric threshold corrections. *Phys. Rev.*, D49:6168–6172, 1994.
- [5] M. Carena, John R. Ellis, S. Mrenna, A. Pilaftsis, and C. E. M. Wagner. Collider probes of the mssm higgs sector with explicit cp violation. *Nucl. Phys.*, B659:145–178, 2003.

Appendix C

Adding the $H^+ \rightarrow t^* \bar{b} \rightarrow W b \bar{b}$

Decay to Pythia

The first part of this appendix describes the technical details of the addition of the decay $H^+ \rightarrow t^ \bar{b} \rightarrow W b \bar{b}$ to Pythia. The second part describes the analysis performed to cross check its proper implementation.*

C.1 Adding the decay to Pythia

In this dissertation the code *Pythia* version 6.216 is used to generate $t\bar{t}$ events in which one or both top quarks can decay to a charged Higgs and a b quark. Details of the Pythia code can be found in [1]. This version of the code includes the decay $t \rightarrow H^+ b$, but lacks the decay $H^+ \rightarrow t^* \bar{b} \rightarrow W b \bar{b}$.

It can be argued that a 3-body decay can be simulated by generating $H^+ \rightarrow W^+ h^0$ in which the h^0 decays to $b\bar{b}$ as long as the mass of the h^0 is low. This type of decay populates the available phase space homogeneously. However, the matrix element of the decay $H^+ \rightarrow t^* \bar{b} \rightarrow W b \bar{b}$ deforms the population of the available phase space, making the kinematic properties of the two decays different. Therefore, in order to properly simulate the decay $H^+ \rightarrow t^* \bar{b} \rightarrow W b \bar{b}$ the full matrix element is introduced in a custom-modified version of Pythia. The modification is done in two steps. First the $W^+ b \bar{b}$ are included as decay products of the charged Higgs in the Pythia

decay tables. This is accomplished by including the line “*-channelIndex=511 -products=24,5,-5*” in the tcl configuration file. This enables the charged Higgs to decay to $W^+b\bar{b}$, but the decay is still simulated with an homogeneously populated phase space. Second the matrix element is introduced in the routine `pytbdf`. The matrix element is used to weight the phase space and is obtained from [2], where it was calculated at tree level and is reproduced here for reference :

$$\frac{\Gamma_{H^+ \rightarrow W^+b\bar{b}}}{ds_{\bar{b}}ds_b} = \frac{3g^4m_t^4\cot^2(\beta)}{256\pi^3m_{H^\pm}^34m_W^4(m_t^2 - s_{\bar{b}})} [m_W^2(s_W - 2m_b^2) + (s_{\bar{b}} - m_b^2 - m_W^2)(s_b - m_b^2 - m_W^2)]$$

where $s_b = (P_{H^\pm} - P_b)^2$ and $s_{\bar{b}} = (P_{H^\pm} - P_{\bar{b}})^2$ are the square of the four-momentum transferred to the b and \bar{b} quarks.

It can be shown however that SUSY corrections, as those to the bottom Yukawa coupling described in Appendix B, will not deform the topology of the kinematics in the phase space, but will enter as an overall factor affecting the branching ratio. The datasets used in this analysis have fixed branching ratios, and thus SUSY corrections do not affect the obtained efficiencies.

C.2 Cross check of the implementation

Several cross checks have been done to assure that our implementation of Pythia works correctly. First, the kinematic phase space of the decay is populated from the generated dataset. For each event the variables s_b , and $s_{\bar{b}}$ are calculated and an entry in the plot is made. This plot, known as Dalitz plot, is shown in Fig. C.1(left) for a dataset with $m_{H^\pm} = 140 \text{ GeV}/c^2$.

The density of the points is non-uniform because the phase space is weighted by the square of the matrix element. A fit was performed to the matrix element function defined in [2] obtaining excellent agreement. As a second cross check the total width $\Gamma_{H^+ \rightarrow Wb\bar{b}}$ was obtained by integrating the

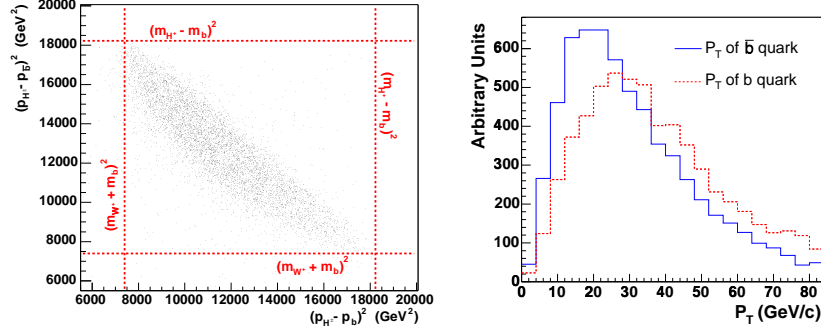


Figure C.1: $H^+ \rightarrow t^* \bar{b} \rightarrow W b \bar{b}$ decay for a mass of the charged Higgs of 140 GeV/ c^2 . Left : Kinematic phase space Right : P_T spectrum of the b and \bar{b} quarks.

matrix element over the available phase space, yielding the correct branching fractions predicted by [2]. This shows that the available phase space and the value of the matrix element are implemented correctly. It is worth mentioning that the matrix element is not a strong function of the phase space variables as can be seen in the Figure.

As an additional check the P_T of the b quarks are compared. In the decay $H^+ \rightarrow t^* \bar{b} \rightarrow W b \bar{b}$ the P_T spectrum of the b quark should be higher than that of the \bar{b} quark. This is because the b quark comes from a virtual top, which tends to be as close as the mass of the top as possible. This is verified for $m_{H^\pm}=140$ GeV/ c^2 in Figure C.1(right).

Bibliography

- [1] Torbjorn Sjostrand et al. High-energy-physics event generation with pythia 6.1. *Comput. Phys. Commun.*, 135:238–259, 2001.
- [2] Ernest Ma, D. P Roy, and Jose Wudka. Enhanced three-body decay of the charged higgs boson. *Phys. Rev. Lett.*, 80:1162–1165, 1998.